



**UNIVERSITÀ  
DEGLI STUDI  
DI TRIESTE**

UNIVERSITÀ DEGLI STUDI DI TRIESTE

---

DIPARTIMENTO DI FISICA

XXXVII Ciclo del Dottorato di Ricerca in Fisica

**A NOVEL ANALYSIS OF  
 $B \rightarrow D\ell\nu_\ell$  AND  $B \rightarrow D^*\ell\nu_\ell$  DECAYS AT BELLE II**

Settore scientifico-disciplinare: FIS/04

Ph.D. student:  
Michele Mantovano

Ph.D. program Coordinator:  
Prof. Francesco Longo

Thesis Supervisor:  
Dr. Mirco Dorigo

---

ANNO ACCADEMICO 2023–2024







## Abstract

This particle physics thesis presents the first simultaneous analysis of the  $B \rightarrow D\ell\nu_\ell$  and  $B \rightarrow D^*\ell\nu_\ell$  decays at the Belle II experiment, where  $\ell$  denotes either an electron or a muon. The analysis uses electron-positron collision data produced by the SuperKEKB collider at the  $\Upsilon(4S)$  resonance and collected by Belle II between 2019 and 2022. The Belle II experiment is designed to reconstruct the decays of  $B$  and  $D$  mesons and  $\tau$  leptons, to provide high-precision measurements that test the heavy-flavour sector of the Standard Model of particle physics.

The  $B \rightarrow D\ell\nu_\ell$  and  $B \rightarrow D^*\ell\nu_\ell$  decays are reconstructed from about 387 million  $B\bar{B}$  pairs. I analyse the dynamics of these decays using novel observables, defined for the first time in this thesis, that enable a number of key results. The most significant of these is a precise measurement of the weak coupling strength between beauty and charm quarks,  $|V_{cb}|$ , a fundamental Standard Model parameter of the quark weak interactions. Additional measurements include four signal decay branching fractions and, for the  $B \rightarrow D^*\ell\nu_\ell$  decay, the lepton forward-backward asymmetry  $A_{\text{FB}}$ , and the  $D^*$  longitudinal polarisation  $F_L^{D^*}$ .

The analysis is performed on simulated and control-data samples and will be applied to the signal sample upon approval from the Belle II Collaboration following internal review. At the time of this writing, the measurement values remain blinded. The anticipated precisions are competitive with those of world's best results, and the expected outcomes are:

$$\begin{aligned}
 |V_{cb}| &= (XXX \pm 0.29 \pm 0.64 \pm 0.45) \times 10^{-3}, \\
 \mathcal{B}(B^+ \rightarrow \bar{D}^0 \ell^+ \nu_\ell) &= (XXX \pm 0.01 \pm 0.06)\%, \\
 \mathcal{B}(B^+ \rightarrow \bar{D}^{*0} \ell^+ \nu_\ell) &= (XXX \pm 0.02 \pm 0.13)\%, \\
 \mathcal{B}(B^0 \rightarrow D^- \ell^+ \nu_\ell) &= (XXX \pm 0.01 \pm 0.05 \pm 0.02)\%, \\
 \mathcal{B}(B^0 \rightarrow D^{*-} \ell^+ \nu_\ell) &= (XXX \pm 0.02 \pm 0.12 \pm 0.05)\%, \\
 A_{\text{FB}} &= (XXX \pm 0.5 \pm 0.4)\%, \\
 F_L^{D^*} &= (XXX \pm 0.7 \pm 0.6)\%,
 \end{aligned}$$

where the first uncertainty is statistical, the second systematic, and the third, when present, is related to theoretical inputs or assumptions.

In addition, by assuming isospin symmetry, I obtain from the same analysis a new measurement of  $f_{+-}/f_{00}$ , the ratio of the branching fractions of  $\Upsilon(4S)$  decays into charged and neutral  $B$ -meson pairs. The expected result,

$$f_{+-}/f_{00} = XXX \pm 0.007 \pm 0.025 \pm 0.024,$$

is also competitive with the best measurements of this quantity. Improving the precision on  $f_{+-}/f_{00}$  enhances the accuracy of all measurements of  $B$  branching fractions at Belle II.



# Contents

<b>Introduction</b>	<b>1</b>
<b>1 Beauty to charm: <math> V_{cb} </math> in the Standard Model</b>	<b>5</b>
1.1 A model with eighteen free parameters . . . . .	5
1.2 The remaining four parameters . . . . .	8
1.3 Constraining the CKM matrix . . . . .	10
1.4 The need to go beyond . . . . .	12
1.5 The matrix element $ V_{cb} $ . . . . .	13
<b>2 A novel approach</b>	<b>17</b>
2.1 Exclusive semileptonic $B$ decays: generalities . . . . .	17
2.2 The $B \rightarrow D^{(*)}\ell\nu_\ell$ decays . . . . .	19
2.3 Current status . . . . .	21
2.3.1 Branching fractions measurements . . . . .	21
2.3.2 $ V_{cb} $ and form factors . . . . .	23
2.3.3 Production rates of charged versus neutral $B$ -meson pairs . . . . .	25
2.4 Open challenges . . . . .	27
2.4.1 Challenges in lattice calculations . . . . .	29
2.5 A novel approach: model-independent observables for a global analysis . . . . .	31
2.5.1 Analysis overview . . . . .	32
<b>3 The Belle II experiment at the SuperKEKB collider</b>	<b>35</b>
3.1 The SuperKEKB collider . . . . .	35
3.2 The Belle II detector . . . . .	39
3.2.1 Tracking system . . . . .	43
3.2.1.1 Silicon-pixel vertexing detector . . . . .	43
3.2.1.2 Silicon-strip vertexing detector . . . . .	43
3.2.1.3 Central drift chamber . . . . .	44
3.2.2 Electromagnetic calorimeter . . . . .	45
3.2.3 Particle identification . . . . .	47
3.2.3.1 Time-of-propagation detector . . . . .	47
3.2.3.2 Aerogel ring-imaging Cherenkov counter . . . . .	48
3.2.3.3 $K_L^0$ and muon detection system . . . . .	48
3.2.4 Trigger and data acquisition system . . . . .	49
3.3 Reconstruction of stable particles . . . . .	50
3.3.1 Charged-particle reconstruction . . . . .	50
3.3.2 Charged-particle identification . . . . .	52
3.4 Instrumental asymmetries . . . . .	55
3.4.1 $A_{det}$ from $D$ control decays . . . . .	56

3.4.2	Sample selection . . . . .	57
3.4.3	Asymmetry determination . . . . .	57
3.4.4	Dependencies of $A_{det}$ . . . . .	59
3.4.5	Weighting method . . . . .	60
3.4.6	Closure tests . . . . .	60
3.4.7	$A_{det}$ for a target decay . . . . .	64
3.4.8	Summary . . . . .	65
<b>4</b>	<b>Data samples and selection</b>	<b>67</b>
4.1	Experimental and simulated data . . . . .	67
4.1.1	Corrections to the data . . . . .	69
4.1.1.1	Track momentum scale . . . . .	70
4.1.1.2	Photon energy bias . . . . .	70
4.1.1.3	Electron bremsstrahlung . . . . .	71
4.1.1.4	Lepton and hadron PID . . . . .	71
4.1.1.5	Tracking efficiency . . . . .	71
4.1.2	Sample components . . . . .	72
4.2	Event selection . . . . .	73
4.2.1	Skim selection . . . . .	74
4.2.2	Final selection . . . . .	75
4.3	Signal efficiency . . . . .	78
4.4	Expected sample composition . . . . .	78
<b>5</b>	<b>Background modelling</b>	<b>81</b>
5.1	Fake- $D$ and continuum backgrounds . . . . .	81
5.2	Real- $D$ background . . . . .	84
5.3	$X\ell\nu_\ell$ background . . . . .	88
5.3.1	Corrections on the cascade decays background . . . . .	88
5.4	Background control region . . . . .	92
<b>6</b>	<b>Novel approach: the global fit</b>	<b>95</b>
6.1	Accessing the differential decay rates . . . . .	95
6.2	The $\chi^2$ fit . . . . .	97
6.2.1	Signal . . . . .	99
6.2.1.1	Dynamical signal templates . . . . .	101
6.2.2	$X\ell\nu_\ell$ background . . . . .	102
6.2.3	Real- $D$ background . . . . .	104
6.2.4	Fake- $D$ and continuum . . . . .	104
6.2.5	Fit parameters . . . . .	105
6.3	Fit to the control region . . . . .	107
6.4	Fit to a simulated Run I data set . . . . .	111
6.5	Check of the fit properties . . . . .	116
<b>7</b>	<b>Systematic uncertainties and final measurements</b>	<b>119</b>
7.1	Systematic uncertainties . . . . .	119
7.1.1	External inputs . . . . .	120
7.1.2	Analysis assumptions . . . . .	120
7.2	Measurement of $f_{+-}/f_{00}$ . . . . .	122
7.3	Measurement of the model-independent observables . . . . .	124
7.4	Measurement of branching fractions . . . . .	127

7.5	Measurements of $A_{\text{FB}}$ and $F_L^{D^*}$ . . . . .	128
7.6	Summary of the results . . . . .	130
<b>8</b>	<b>Measurement of <math> V_{cb} </math></b>	<b>133</b>
8.1	Fit to the model-independent observables . . . . .	133
8.1.1	BGL fit . . . . .	134
8.1.2	Expected uncertainties . . . . .	138
	<b>Summary</b>	<b>141</b>
<b>A</b>	<b>Form-factor parametrisations</b>	<b>145</b>
A.1	$B \rightarrow D^* \ell \nu_\ell$ . . . . .	145
A.2	$B \rightarrow D \ell \nu_\ell$ . . . . .	147
<b>B</b>	<b>Control region checks</b>	<b>149</b>
<b>C</b>	<b>Signal-only Asimov fit</b>	<b>157</b>
<b>D</b>	<b>Validation of the systematic uncertainty on the <math>D^{**}</math> decays</b>	<b>159</b>
<b>E</b>	<b>Interpretation with the BGL and CLN parametrisations</b>	<b>161</b>
E.1	Form factors and $ V_{cb} $ using the BGL parametrisation . . . . .	161
E.2	Form factors and $ V_{cb} $ using the CLN parametrisation . . . . .	162
<b>F</b>	<b>Pull distributions</b>	<b>165</b>
F.1	Asimov fit . . . . .	165
F.2	Direct fit (BGL parametrisation) . . . . .	168
F.3	A posteriori fit (BGL parametrisation) . . . . .	172
F.4	A posteriori fit (BGL parametrisation): configuration 2 . . . . .	176
F.5	Direct fit (CLN parametrisation) . . . . .	179
F.6	A posteriori fit (CLN parametrisation) . . . . .	183
	<b>Bibliography</b>	<b>187</b>



# Introduction

The Standard Model (SM) of elementary particles and their interactions is the currently accepted theory of particle physics. It is widely recognised as the ultimate success of the reductionist paradigm for describing physics at its most fundamental level. Using about twenty parameters, the SM accurately describes thousands of measurements involving processes mediated by the electromagnetic, weak, and strong interactions, covering more than ten orders of magnitude in energy. However, theoretical considerations and, possibly, experimental evidence suggest that the SM may be an *effective theory*: one that is valid at the energies tested thus far but embedded within a yet-unknown, more comprehensive framework. Extending the SM is the principal goal of today's particle physics.

*Direct* approaches, which broadly involve searching for decay products of non-SM particles produced in high-energy collisions, provide an unequivocal means of discovering and characterising new particles. However, their current reach is limited by the collision energy of today's accelerators and by the large investments needed to advance it in the future. Complementary approaches involve comparing precise measurements with equally precise predictions of lower-energy processes where virtual non-SM particles could contribute. A consistent pattern of deviations from SM predictions would reveal new phenomena. The reach of these *indirect* approaches is not limited by collision energy but rather by the precision achievable in both measurements and theoretical predictions.

Belle II is an experiment designed to test the SM *indirectly* by analysing billions of decays of particles containing the quarks *beauty* and *charm* (heavier counterparts of the *down* and *up* quarks, which make up atomic nuclei) and of the  $\tau$  lepton (a heavier counterpart of the electron) produced in electron-positron collisions at energies near 10.58 GeV. Since the start of data taking in March 2019, Belle II collected a sample containing about 387 million of  $B\bar{B}$  mesons (a  $B$  meson is a bound states of a *beauty* antiquark and either an *up* or *down* quark). Run II started in March 2024, after a 1.5-year shutdown to upgrade the detector and collider, and will continue until a second shutdown for a new upgrade, expected around 2027, with the goal of collecting a sample significantly larger than that of Run I.

This thesis presents a simultaneous analysis of two decays of the  $B$  mesons,  $B \rightarrow D\ell\nu_\ell$  and  $B \rightarrow D^*\ell\nu_\ell$ , where  $\ell$  can be either an electron or a muon, using Belle II Run I data. I analyse their decay dynamics with a novel method that enables several key measurements, the most significant being a precise determination of the weak-interaction coupling strength between *beauty* and *charm* quarks,  $|V_{cb}|$ . This measurement is crucial as it provides one of the SM fundamental parameters related to quark weak interactions.

Accurate knowledge of  $|V_{cb}|$  is essential for precisely predicting rates of processes highly sensitive to physics beyond the SM, thereby enhancing the discovery potential of indirect searches. Over the past two decades, measurements of  $|V_{cb}|$  have been conducted using two main analysis categories based on theoretically distinct yet equally valid approaches: the *inclusive* and *exclusive* methods. Both methods achieve a similar precision, approximately

2%. However, the  $|V_{cb}|$  values obtained differ by approximately 5%, and this discrepancy currently limits the knowledge of  $|V_{cb}|$ .

The primary decay modes used in the exclusive method are  $B \rightarrow D\ell\nu_\ell$  and  $B \rightarrow D^*\ell\nu_\ell$ , precisely those studied in this thesis. The determination of  $|V_{cb}|$  with these decays follows from measurements of their branching fractions and form factors—functions that encode the strong-interaction effects binding *beauty* and *charm* quarks in mesons. To extract  $|V_{cb}|$  theoretical calculations of the form factors are necessary, as well as a model to extrapolate them to the entire phase space of the decay. Recent results from various collaborations present some tensions regarding the  $B \rightarrow D^*\ell\nu_\ell$  form factors, further complicating the  $|V_{cb}|$  extraction.

In this thesis, I propose a measurement of model-independent observables, defined here for the first time, sensitive to the  $B \rightarrow D\ell\nu_\ell$  and  $B \rightarrow D^*\ell\nu_\ell$  decay dynamics, from which  $|V_{cb}|$  can be determined *a posteriori* using any input calculation and model for the form factors. These observables facilitate improved determinations of  $|V_{cb}|$  using any future advancements on the theoretical side, and mark the first element of novelty of my work. From the same observables, I also obtain the  $B \rightarrow D\ell\nu_\ell$  and  $B \rightarrow D^*\ell\nu_\ell$  branching fractions and, for  $B \rightarrow D^*\ell\nu_\ell$  decays, the forward-backward asymmetry of the lepton  $A_{\text{FB}}$ , and the longitudinal polarisation of the  $D^*$  meson  $F_L^{D^*}$ . The latter encode information on the decay dynamics that helps shedding light on the form-factor calculations.

My analysis targets both  $B \rightarrow D\ell\nu_\ell$  and  $B \rightarrow D^*\ell\nu_\ell$  decays *simultaneously*, accounting for correlations between uncertainties in the extraction of  $|V_{cb}|$ . To this end, in  $B \rightarrow D^*\ell\nu_\ell$  decays, the  $D^*$  decay is partially reconstructed from  $D\ell$  candidates. This global approach represents the second novel aspect of my work, as the two decays have previously been analysed separately at Belle II.

The partial reconstruction of the  $D^*$  decay eliminates a major systematic uncertainty affecting previous measurement of  $|V_{cb}|$  from  $B \rightarrow D^*\ell\nu_\ell$  decays, the uncertainty associated with the slow-pion reconstruction efficiency in  $D^* \rightarrow D\pi_{\text{slow}}$ . However, the analysis becomes more sensitive to background modelling, with a dangerous background being feed-down from semileptonic decays involving excited charm states, whose production rates remain poorly known. I conduct a detailed study to constrain this background with data, identifying a control region enriched of these decays that I analyse simultaneously with the signal sample. This is another element of novelty of my work.

Finally, my analysis also provides an important byproduct. By assuming isospin symmetry, I also perform a new measurement of  $f_{+-}/f_{00}$ , the ratio of the branching fractions of  $\Upsilon(4S)$  decays into charged and neutral  $B$ -meson pairs, eliminating another significant source of systematic uncertainty on  $|V_{cb}|$ . The value of  $f_{+-}/f_{00}$  in use at Belle II comes from an analysis of  $B \rightarrow J/\psi K$  decays, which is affected by a 5% theoretical uncertainty to cover isospin-breaking in these decays. For semileptonic decays, isospin breaking should contribute a smaller uncertainty, offering a more precise way to measure  $f_{+-}/f_{00}$ . The improvement of the precision on  $f_{+-}/f_{00}$  has a pivotal importance in Belle II, as its uncertainty affects all measurements of  $B$  branching fractions.

The analysis, while fully completed on simulation and control data, is not yet applied to the signal sample, because it is still under Belle II internal review. The full analysis will be applied to the real data after the review and carefully defining an *unblinding* procedure. Nevertheless this thesis fully demonstrates the potential of the novel method proposed.

The thesis is structured as follows. Chapter 1 introduces the parameters of the SM, focusing on  $|V_{cb}|$ . In Chapter 2, I give an overview of the methods and challenges for the exclusive  $|V_{cb}|$  determination from  $B \rightarrow D\ell\nu_\ell$  and  $B \rightarrow D^*\ell\nu_\ell$  decays, discussing also my new analysis approach and defining the model-independent observables, the target of my

measurement. Chapter 3 describes the Belle II experiment, reporting also an important service work I conducted during my first Ph.D. year, the measurement of instrumental asymmetries for kaons and pions. The reconstruction of the signal decays from Belle II data and their selection is discussed in Chapter 4, where I also introduce the sample composition. Chapter 5 focuses on a detailed description of the backgrounds and the strategies to model and constrain them directly from data. The core of the analysis, a global fit to the data, is detailed in Chapter 6, with the final measurements and their associated uncertainties discussed in Chapter 7. Finally,  $|V_{cb}|$  and form-factors parameters are determined in Chapter 8. A final summary concludes the document.

Charge-conjugate processes are implied throughout the document unless specified otherwise. Generic particle symbols ( $B$ ,  $D$ , ...) indicate either charged or neutral particles.



# Chapter 1

## Beauty to charm: $|V_{cb}|$ in the Standard Model

*The current theory of fundamental particles and interactions, the Standard Model of particle physics, relies on about twenty parameters that determine the physics we observe. Their values are not predicted by the model and must be measured experimentally. Knowledge of one of these parameters is limited by the current uncertainty in the magnitude of the bottom-to-charm quark coupling,  $|V_{cb}|$ . My thesis aims to improve its measurement. In this chapter, I concisely review the Standard Model by discussing its fundamental parameters, with a focus on quark-flavour mixing and its role in exploring physics beyond the Standard Model. I conclude with a brief overview of the current knowledge of  $|V_{cb}|$ .*

### 1.1 A model with eighteen free parameters

The Standard Model (SM) of particle physics is an effective quantum field theory that offers the most fundamental description of nature known to date. It describes the fundamental interactions between the elementary particles of matter, except for gravity [1–6]. The model relies on about twenty free parameters, which are *a priori* arbitrary and must be determined experimentally. Given the values of these parameters, the theory can explain, in principle, all phenomena in our daily lives and all data observed in accelerator-based experiments. In its minimal representation, the SM has eighteen free parameters: three for the gauge couplings of the strong, electromagnetic and weak interactions; two for the Higgs sector; and thirteen for the fermion masses and mixing.<sup>1</sup>

The first three parameters are related to the gauge groups. The SM is based on the symmetry group

$$SU(3)_C \otimes SU(2)_W \otimes U(1)_Y,$$

where  $SU(3)_C$  is the standard unitary group that describes the strong interactions (quantum chromodynamics, QCD); the product  $SU(2)_W \otimes U(1)_Y$  describes the combination of the weak and electromagnetic interactions, with  $SU(2)_W$  being the standard unitary group of weak isospin doublets, and  $U(1)_Y$  the unitary group of hypercharge. Three coupling constants,  $g_1$ ,  $g_2$  and  $g_3$ , are associated with these groups:  $g_1$  and  $g_2$  mix and give the couplings of the weak and electromagnetic interactions;  $g_3$  is the coupling constant of the strong interaction. They vary according to known functions with the energy scale due to the effects of renormalisation [7] and are free parameters in the SM.

---

<sup>1</sup>Hereafter the minimal version of the SM, which assumes massless neutrinos and  $CP$ -conserving strong interaction, is considered.

Spin-1 particles called *gauge bosons* mediate the interactions. Strong interactions are mediated by *gluons*, eight massless particles corresponding to the generators of  $SU(3)_C$ . They carry a combination of two charges, called *colour* and *anti-colour*, which can be each of three kinds (red, blue, and green). Weak interactions are mediated by two charged massive bosons,  $W^\pm$ , and a neutral massive boson,  $Z^0$ . Electromagnetic interactions occur between particles carrying electric charge and are mediated by a neutral massless boson, the photon  $\gamma$ . The electroweak bosons  $W^\pm$ ,  $Z^0$ , and  $\gamma$ , arise from linear combinations of  $SU(2)_W \otimes U(1)_Y$  generators through the Weinberg angle  $\theta_W$ , which is a function of  $g_1$  and  $g_2$ :

$$\sin \theta_W = \frac{g_1}{\sqrt{g_1^2 + g_2^2}}, \quad \cos \theta_W = \frac{g_2}{\sqrt{g_1^2 + g_2^2}}.$$

The  $W^\pm$  mass depends on the  $Z^0$  mass via  $\theta_W$ , as  $m_Z = m_W / \cos \theta_W$ . The electromagnetic coupling constant  $e$  is given in terms of the weak coupling constant  $g_2$  as

$$e = g_2 \sin \theta_W,$$

and the Fermi constant of weak interactions is given by

$$G_F = \frac{\pi \alpha}{\sqrt{2}(M_Z \cos \theta_W \sin \theta_W)^2},$$

where  $\alpha = e^2/4\pi$ . Measuring the electromagnetic and weak couplings, the Weinberg angle, and the masses of the  $Z^0$  and  $W^\pm$  bosons provides a test of this sector of the SM. Any deviation from the predicted values could indicate the presence of new physics beyond it, making precision measurements crucial. Such tests also probe the internal consistency of the electroweak theory, offering a stringent check on radiative corrections and potential contributions from unknown particles or forces.

The  $SU(2)_W \otimes U(1)_Y$  symmetry of the electroweak interactions does not manifest itself at low energies and it is spontaneously broken by the vacuum expectation value of a field, mediated by a spin-0 particle. The simplest implementation of this spontaneous symmetry-breaking is given by an Higgs doublet

$$H = \begin{pmatrix} H^+ \\ H^0 \end{pmatrix}$$

with a potential

$$V(H) = \frac{\lambda}{4} \left( H^\dagger H - \frac{v^2}{2} \right)^2,$$

where  $v$  is the vacuum expectation value and  $\lambda$  denotes the scalar Higgs-Higgs coupling strength. These are other two free parameters of the model. Assigning a vacuum expectation value to the Higgs field results in the desired spontaneous breakdown of  $SU(2)_W \otimes U(1)_Y$ , which produces the gauge-invariant mass terms in the SM. For instance, the  $Z^0$  mass is related to  $v$  through  $M_{Z^0} = (\sqrt{g_1^2 + g_2^2}/2)v$ . The value of  $v$  can thus be inferred to be about 246 GeV, as  $\sqrt{2}G_F = 1/v^2$ . The Higgs mass is related to the vacuum expectation value by

$$m_H = \sqrt{2\lambda}v.$$

The observation of the Higgs boson with a mass of about  $125 \text{ GeV}/c^2$  at LHC in 2012 [8] made the last missing step for the completion of the measurement of all SM parameters.

The remaining thirteen free parameters of the model are related to matter particles, which also acquire mass via the interaction with the Higgs field. Most of the richness and

complexity of the model, allowing for chemistry and life itself, resides in the values of these parameters. Matter particles correspond to excitations of spin- $\frac{1}{2}$  fields, the *fermions*. Their masses are generated through their Yukawa couplings to the Higgs field,

$$m_f = y_f \frac{v}{2}$$

where  $m_f$  is the mass of the fermion and  $y_f$  is the Yukawa coupling. The masses (or the couplings) are free parameters to be measured.

Fermions are classified into two classes: quarks, which are the fundamental constituents of nuclear matter, and leptons. Each fermion is also associated with an antiparticle. Quarks are massive and organised in three families, each composed of an up-type quark with charge  $\frac{2}{3}e$ , and a down-type quark with charge  $-\frac{1}{3}e$ ,

$$\begin{pmatrix} u \\ d \end{pmatrix} \begin{pmatrix} c \\ s \end{pmatrix} \begin{pmatrix} t \\ b \end{pmatrix}.$$

They couple with both the strong and electroweak interactions. Each quark has colour and a *flavour* quantum number, which comes in six varieties and is conserved in the electromagnetic and strong interactions, but not in the weak interactions. Due to colour confinement free quarks are not observable<sup>2</sup>. They are only observed in their colourless bound states, which include mesons, typically composed of a quark and an anti-quark, and baryons, composed of three quarks. Baryons are assigned a quantum number, called baryon number, found to be conserved.

Leptons are also grouped in three families, composed each by a neutral massless neutrino and a massive particle with electric charge  $-e$ ,

$$\begin{pmatrix} \nu_e \\ e \end{pmatrix} \begin{pmatrix} \nu_\mu \\ \mu \end{pmatrix} \begin{pmatrix} \nu_\tau \\ \tau \end{pmatrix}.$$

They couple only with the electroweak interaction. Each lepton has a lepton-family quantum number; their sum in a process, called global lepton number, is found to be conserved in all interactions, although no symmetry of the dynamics prescribes that. Individual lepton numbers are not conserved in neutrino oscillations (this fact also leads to neutrino masses).

Only left-chiral fermions (and right-chiral antifermions) engage in the charged weak interaction. Interactions involving right-handed or opposite-handed fermions do not occur. This implies that weak interactions, in contrast to strong and electroweak interactions, violates parity ( $P$ ), the transformation that inverts all spatial coordinates. In the SM, this feature is implemented through left- and right-handed fields of quark and lepton transforming differently under  $SU(2)_W$ : right-handed fields are singlet; left-handed field are doublets. Weak interaction also violates  $CP$ , the combined transformation of parity and charge-conjugation ( $C$ , which inverts all quantum numbers of a particle);  $CP$  violation is established only in the quark sector. While the electromagnetic interaction is  $CP$  symmetric, the strong interaction could violate  $CP$  symmetry too, but no experimental evidence of that has ever been observed. All interactions are symmetric under the combined  $CPT$  transformation, where  $T$  inverts the time axis. This is prescribed by foundational axioms

---

<sup>2</sup>To a good approximation, the attractive force between quarks grows linearly with distance. As two quarks are separated, putting energy into the bounded system, it becomes energetically favourable for a new quark-antiquark pair to appear, rather than extending the distance further. As a consequence new bound states are generated instead of separated and free quarks.

of field theory [9], and results in particles and antiparticles having the same mass and lifetime.

Along with six parameters for the quark masses and three parameters for the lepton masses, there are four additional free parameters. They concern the mixing between the quark flavours, governed by the Cabibbo-Kobayashi-Maskawa matrix, which I present in detail in the next section.

## 1.2 The remaining four parameters

The role of flavour in shaping the SM has been central since the early days of particle physics. In the early 1960s, during the crucial years for the theoretical development of the SM, there was an apparent inconsistency between weak coupling constants measured in muon decay, neutron decay, and strange-particle decays. Such inconsistency was first addressed by Gell-Mann and Levy [10] and then Cabibbo [11], who postulated differing mass and weak eigenstates for down-type quarks. This was achieved by introducing a mixing angle between the  $s$  quark and  $d$  quark, the only two down-type quarks known at the time.

While Cabibbo's theory efficiently addressed the difference in weak coupling constants, it also predicted a rate for kaon decays involving neutral-current transition inconsistent with the experimental limits at the time. Glashow, Iliopoulos, and Maiani addressed the conundrum by postulating the existence of a fourth quark, the charm, of about  $2 \text{ GeV}/c^2$  mass, whose contribution to the decay amplitude suppresses the branching fraction down to values consistent with experimental limits [12].<sup>3</sup> The charm quark was then discovered four years after its prediction.

In 1973, when only three quarks were known, Kobayashi and Maskawa generalised Cabibbo's theory from a four-quark model to a six-quark model to accommodate the phenomenon of  $CP$  violation observed in 1964 [13]. They introduced a complex unitary matrix to describe the relations between mass (unprimed) and weak (primed) interaction eigenstates of quarks as seen by  $W^\pm$  bosons. This is known as the Cabibbo-Kobayashi-Maskawa (CKM) quark-mixing matrix denoted as  $V_{\text{CKM}}$ ,

$$\begin{pmatrix} d' \\ s' \\ b' \end{pmatrix} = \begin{pmatrix} V_{ud} & V_{us} & V_{ub} \\ V_{cd} & V_{cs} & V_{cb} \\ V_{td} & V_{ts} & V_{tb} \end{pmatrix} \begin{pmatrix} d \\ s \\ b \end{pmatrix} .$$

Each  $V_{ij}$  matrix element encapsulates the weak-interaction coupling between an up-type  $i$  and down-type  $j$  quarks; for instance, the  $V_{cb}$  matrix element governs the weak-interaction coupling between the beauty and charm quarks. A general quark-mixing matrix has dimension  $N \times N$  and  $(N-1)^2$  free parameters, where  $N$  is the number of quark families<sup>4</sup>. If  $N = 2$ , the only free parameter is a single angle (the Cabibbo angle  $\theta_C$ ), whereas if  $N = 3$ , the free parameters are three Euler angles and a complex phase; the latter allows for  $CP$ -violating couplings [14]. There are three families of quarks in the SM, thus four parameters making up the CKM matrix: these complete the set of the eighteen free parameters of the SM.

<sup>3</sup>Nowadays we know that also the top quark contributes to the amplitude, with a GIM factor which is proportional to the squared ratio of the top and  $W$  masses  $m_t^2/m_W^2$ ; this contribution is suppressed by the smallness of the quark-mixing couplings involved.

<sup>4</sup>A generic  $N \times N$  complex matrix  $U$  is defined with  $2N^2$  free parameters. The unitary condition  $UU^\dagger = 1$  eliminates  $N^2$  degrees of freedom. We can then redefine  $(N-1)$  quark fields to absorb  $2N-1$  free parameters. We end up with  $2N^2 - N^2 - (2N-1) = (N-1)^2$  free parameters.

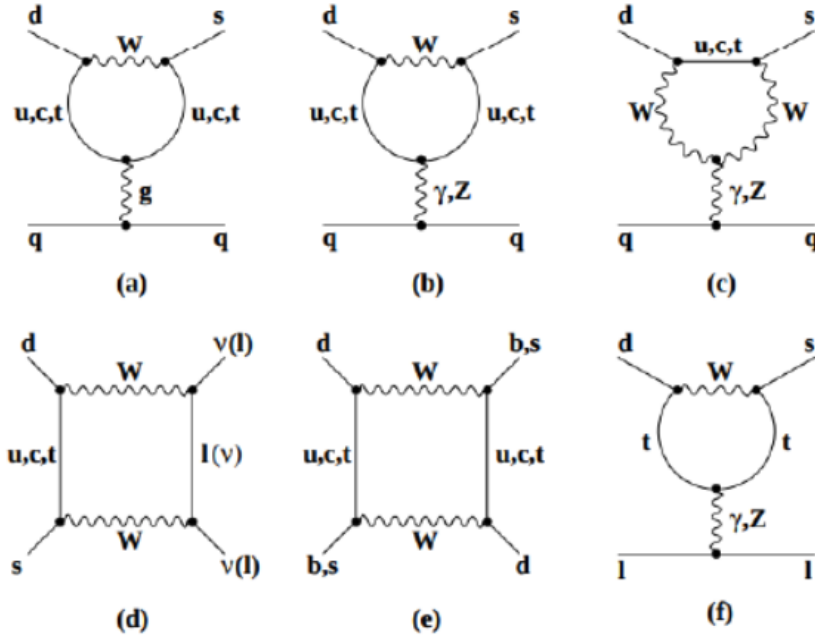


Figure 1.1: Examples of leading FCNC diagrams.

The CKM matrix is most conveniently written in the so-called *Wolfenstein parametrisation*, which is an expansion in the small parameter  $\lambda = \sin \theta_C \approx 0.23$  that makes explicit the observed hierarchy between its elements [15],

$$V_{\text{CKM}} = \begin{pmatrix} 1 - \lambda^2/2 & \lambda & A\lambda^3(\rho - i\eta) \\ -\lambda & 1 - \lambda^2/2 & A\lambda^2 \\ A\lambda^3(1 - \rho - i\eta) & -A\lambda^2 & 1 \end{pmatrix} + \mathcal{O}(\lambda^4).$$

The four free SM parameters of the quark-mixing sector are thus  $\lambda$ ,  $A$ ,  $\rho$  and  $\eta$ . The parameter  $\lambda$  expresses the mixing between the first and second quark generations,  $A$  and  $\rho$  are real parameters, and  $\eta$  is the parameter that introduces  $CP$  violation. The parameter  $A$  enters at both  $\lambda^2$  and  $\lambda^3$  levels, with the  $\lambda^3$  contribution being more suppressed. Consequently,  $A$  is primarily determined by the contributions at  $\lambda^2$ , specifically from the  $|V_{cb}|$  and  $|V_{ts}|$  elements. However, the measurement of  $|V_{cb}|$  is favoured over  $|V_{ts}|$  because it is obtained at tree-level rather than at loop-level. Thus, a precise measurement of the matrix element  $|V_{cb}|$  directly leads to an accurate determination of the Wolfenstein parameter  $A$ , given that the Cabibbo angle is known with an uncertainty of only 0.2%. In this context, the measurement of  $|V_{cb}|$  yields a fundamental SM parameter.

With the Wolfenstein parametrisation, a clear hierarchy of the matrix elements becomes evident. Transitions within the same family are favoured; then, those to the nearest family; finally, transitions that skip a family are the most suppressed. The origin of hierarchy of the CKM-matrix elements is unknown and remains an open conundrum to this day.

Quark-mixing occurs through the emission of a  $W^\pm$  boson; therefore, a change of quark charge by one unit. This process is called flavour-changing charge current. In contrast, flavour-changing neutral currents (FCNC) are processes in which the quark flavour changes, but the electric charge remains the same. Such kind of processes are suppressed in the SM, because they occur only through second-order amplitudes involving the internal exchange of a  $W^\pm$  bosons (“loop amplitudes”), as shown in Fig. 1.1. Such amplitudes are naturally

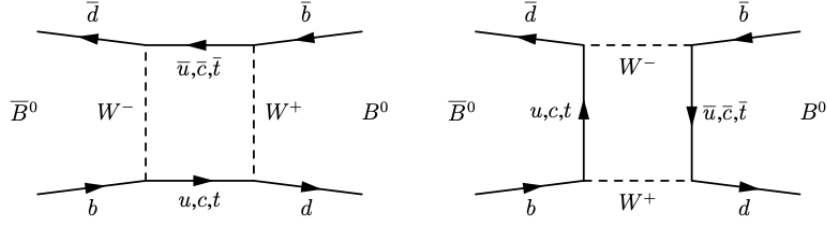


Figure 1.2: Leading order Feynman diagrams contributing to neutral  $B^0 - \bar{B}^0$  mixing.

sensitive to non-SM contributions, since any particle with proper quantum numbers and nearly arbitrary mass can replace the SM-quark closed-line in these diagrams thus altering the rate. FCNC are therefore powerful in identifying contributions from non-SM particles if rate enhancements or suppressions with respect to SM expectations are observed.

A peculiar FCNC process which enriches significantly the phenomenology of neutral mesons is the phenomenon of flavour oscillations. Flavour quantum numbers are conserved in strong interactions and thus flavour eigenstates are eigenstates of strong interactions. Weak interactions do not conserve flavour, allowing a neutral meson to undergo a transition into its own antiparticle (or vice versa), which changes flavour by two units. Because the full Hamiltonian contains strong and weak interactions, its eigenstates (which are the particles we observe, with definite masses and lifetimes) are linear superposition of flavour eigenstates. As an example, Fig. 1.2 shows the leading-order Feynman diagrams contributing to neutral  $B^0 \bar{B}^0$  mixing. Flavour oscillations are suppressed in the SM, and provide strong constraints on model building for SM extensions.

### 1.3 Constraining the CKM matrix

The unitarity condition of the CKM matrix,  $V_{\text{CKM}} V_{\text{CKM}}^\dagger = \mathbb{1}$ , yields nine relations, which are sums of three complex numbers each. Six equations sum to zero prompting a convenient geometric representation in the complex plane in terms of the so-called *unitarity triangles*. A notable triangle, referred to as “the unitarity triangle” (UT) and shown in Fig. 1.3, comes from the equation that has all elements of similar magnitudes,

$$V_{ub}^* V_{ud} + V_{cb}^* V_{cd} + V_{tb}^* V_{td} = 0. \quad (1.1)$$

Conventionally, side sizes are normalised to the length of the base,  $V_{cb}^* V_{cd}$ , and the three angles are labelled  $\alpha$  (or  $\phi_2$ ),  $\beta$  (or  $\phi_1$ ), and  $\gamma$  (or  $\phi_3$ ).

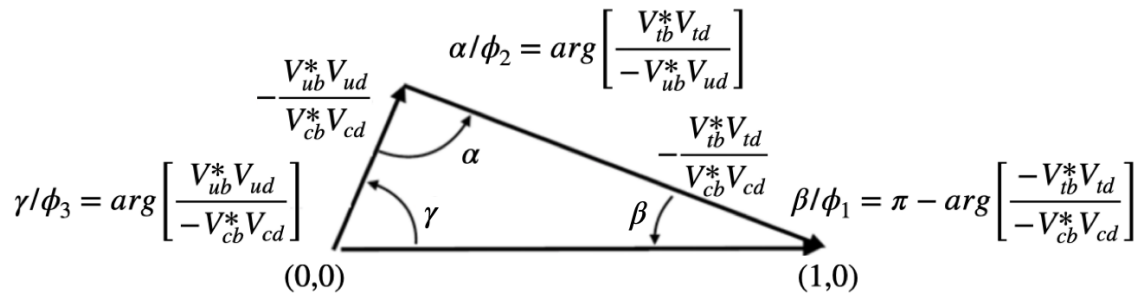


Figure 1.3: Graphical representation of the Unitarity Triangle.

By measuring the size of the sides and angles, the triangle can be overconstrained to test the consistency of the CKM mechanism. This can reveal effects beyond the SM if a disagreement between lengths of the sides of the UT and its angles is found.

The sides are constrained by the magnitudes of CKM matrix elements, which are usually measured with semileptonic or fully leptonic decays, including charged current quark transitions. The measured decay rates of the respective flavour-changing transitions are proportional to the coupling strength  $|V_{ij}|^2$ . This is the case for the matrix element  $|V_{cb}|$ , the focus of this thesis, which is extracted by analysing  $B \rightarrow X_c \ell \nu_\ell$  transitions, where  $X_c$  is a hadron containing a  $c$  quark and  $\ell$  is either an electron or a muon (this will be expanded in Chapter 2). Similarly, the smallest CKM matrix element  $|V_{ub}|$  is determined from  $B \rightarrow X_u \ell \nu_\ell$  processes;  $|V_{us}|$  from  $K \rightarrow \pi \ell \nu_\ell$  decays, and  $|V_{cd}|$  from  $D \rightarrow \pi \ell \nu_\ell$ , while the best way to measure  $|V_{cs}|$  is through the fully leptonic decay  $D_s \rightarrow \ell \nu_\ell$ . The element  $|V_{ud}|$  is measured from nuclear  $\beta$  decays.

Not all magnitudes are best measured with semileptonic decays. The combination  $|V_{td}V_{tb}^*|$  can be extracted precisely by measuring the difference of neutral  $B$  mass eigenstates,  $\Delta m_d$ , which is proportional to  $|V_{td}V_{tb}^*|^2$ . This quantity gives the frequency of  $B^0\bar{B}^0$  oscillations. Due to significantly reduced theory uncertainties, the ratio of mass differences for neutral  $B$  and  $B_s$  meson  $\Delta m_d/\Delta m_s$  (proportional to  $|V_{td}V_{tb}^*|^2/|V_{ts}V_{tb}^*|$ ) is often used as a better constraint.

All measurements of  $|V_{ij}|$  elements require input from theoretical calculations to factor out the strong interaction from the decay rate as the quarks involved are bound in hadrons. Therefore, improvements on the determination of the matrix-element strengths require advancements both on the experimental measurements and QCD calculations. The current status confirms the almost diagonal hierarchical structure of the CKM matrix:

$$V_{\text{CKM}} = \begin{pmatrix} 0.97446 \pm 0.00010 & 0.22452 \pm 0.00044 & 0.00365 \pm 0.00012 \\ 0.22438 \pm 0.00044 & 0.97359^{+0.00010}_{-0.00011} & 0.04214 \pm 0.00076 \\ 0.00896^{+0.00024}_{-0.00023} & 0.04133 \pm 0.00074 & 0.999105 \pm 0.000032 \end{pmatrix}.$$

The UT angles can be determined by measurements of  $CP$ -violating observables. The angle  $\beta = \arg(-V_{cd}V_{cb}^*/V_{td}V_{tb}^*)$  can be determined from time dependent decay rates of  $B^0$  and  $\bar{B}^0$  to the same final state  $f$ , here the  $B^0/\bar{B}^0$  meson can either directly decay to the final state  $f$  or first oscillate into its antiparticle  $\bar{B}^0/B^0$ , and then decay to  $f$ . Since the two paths have a phase difference (weak and strong phase difference), interference can occur and results in a time dependent asymmetry. If  $f$  is a  $CP$  eigenstate and amplitudes with one CKM phase dominate the decay, the time-dependent  $CP$  symmetry is given by:

$$A_{CP} = \frac{\Gamma(\bar{B}^0(t) \rightarrow f) - \Gamma(B^0(t) \rightarrow f)}{\Gamma(\bar{B}^0(t) \rightarrow f) + \Gamma(B^0(t) \rightarrow f)} = \eta_f \sin(2\beta) \sin(\Delta m_d t), \quad (1.2)$$

where  $\eta_f$  is the  $CP$  eigenvalue of  $f$ . A measurement of  $\sin(2\beta)$  can be obtained from  $b \rightarrow \bar{c}cs$  transitions, such as  $B^0 \rightarrow J/\psi K_{S/L}^0$ ,  $b \rightarrow \bar{c}cd$  transitions like  $B^0 \rightarrow J/\psi \pi^0$  and  $b \rightarrow \bar{c}ud$  transitions as  $B^0 \rightarrow \bar{D}^0 h^0$ . The angle  $\alpha = \arg(-V_{td}V_{tb}^*/V_{ud}V_{ub}^*)$  is measured using time-dependent  $CP$  asymmetries from  $b \rightarrow \bar{u}ud$  decay dominated modes such as  $B \rightarrow \pi\pi$ ,  $\rho\pi$  and  $\rho\rho$  decays. Unlike  $\alpha$  and  $\beta$ , the angle  $\gamma = \arg(-V_{ud}V_{ub}^*/V_{cd}V_{cb}^*)$  does not depend on CKM elements involving the top quark and can therefore directly be measured in tree-level decays using  $B \rightarrow D\pi$  and  $B \rightarrow DK$  decays.

Measurements of parameters associated with quark-flavour physics have been performed in many dedicated, or general-purpose, experiments in the last three decades. All measure-

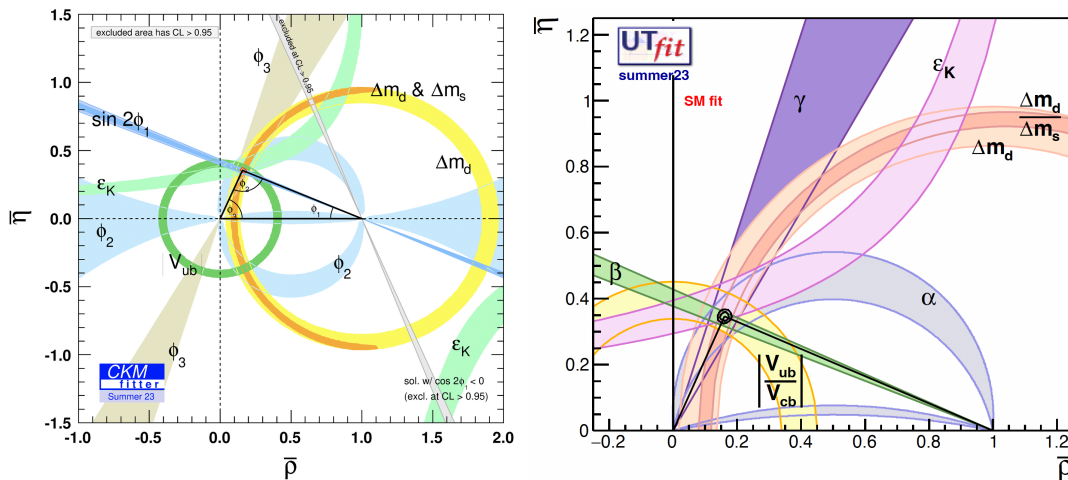


Figure 1.4: Global fits to the CKM parameters  $\bar{\rho}$ ,  $\bar{\eta}$ ,  $A$  and  $\lambda$  from the CKMfitter and UTfit collaborations as of Summer 2023.

ments can be combined in a global fit imposing SM constraints. There are two collaborations that combine experimental data with theory predictions for hadronic matrix elements using different approaches: the CKMfitter and UTfit collaborations [16, 17]. Both of them provide similar results and the constraints implied by unitarity significantly reduce the allowed range for some of the CKM elements. A comparison of the apex of the unitarity triangle from the global fits obtained by both collaborations is shown in Fig 1.4. Their results of the global fits are in excellent agreement with each other.

The resulting global picture is that the CKM interpretation of quark-flavour phenomenology is the dominant mechanism at play in the dynamics. Despite this remarkable consistency, possible deviations of up to 20% are still unconstrained, especially those associated to FCNC processes. It is especially promising that most of the relevant measurements are currently dominated by statistical uncertainties, offering therefore fruitful opportunities for future experiments.

The LHCb experiment started taking data in its Upgrade I incarnation in 2023 and is expected to accumulate 50 times more data than what collected so far. Belle II should also enlarge the Belle data set by an order of magnitude or more within a similar timescale. Furthermore, a second upgrade of LHCb has been proposed [18], as well as an upgrade of Belle II [19]. Further in the future, beyond 2040, the FCC-ee phase of a future circular collider [20] is generating much interest in the flavour community: unprecedented statistics could be attainable at the  $Z$  pole ( $O(5 \times 10^{12})$   $Z$  decays) which can be used for flavour physics measurements, exploiting both a clean experimental environment (similar to Belle II) and the production of all species of heavy flavours with a large boost (similar to LHCb).

## 1.4 The need to go beyond

The SM framework was completed in the 1970s and has been successfully tested since in thousands of measurements, some of which have reached fractional uncertainties of one part per trillion [14]. A minimal extension of the model can accommodate the evidence for neutrino masses and mixing angles from the observation of their oscillations. This necessitates introducing new physics, such as right-handed neutrinos or mechanisms such

as the Seesaw model [21], to explain the small but non-zero masses of neutrinos and their oscillatory behaviour. Even with this extension, observations and theoretical considerations suggest that the SM is likely to be an effective field theory, valid at the eV-TeV energies probed so far, which should be completed by a more general full theory valid over a broader range of high energies. Clear phenomenological evidences come from cosmology and astrophysics. For instance, the SM lacks an explanation for a dynamical origin of the observed asymmetry between matter and antimatter in the universe, and has no candidate for the postulated large amounts of non-interacting matter (dark matter) introduced to justify cosmological observations. In addition, gravity must be eventually included.

Besides these unresolved questions, there are fundamental puzzles that reside within the SM itself. We currently have no clue about the origin of the free fundamental parameters. There is no explanation for why there are three families of quarks and leptons, or why they have the specific masses and mixing couplings that they do. This is known as the *flavour puzzle*. Solving the puzzle requires a more general theory, manifesting at some high energy scale, which can explain the observed patterns and hierarchies in the flavour sector. The flavour puzzle remains one of the central challenges in theoretical physics, driving ongoing research and experimentation.

Extending the SM in an attempt to address these and other open issues is the main goal of today's particle physics. Current strategies can broadly be classified into two synergistic approaches. The energy-frontier, a *direct* approach that aims at using high-energy collisions to produce new particles not included in the SM, and detect directly their decay products, thus gaining direct evidence of their existence. This offers striking experimental evidence of new phenomena, when energetically accessible, but its reach is limited by the maximum energy available at colliders. The intensity-frontier, an *indirect* approach that broadly consists in searching for significant differences between precise measurements and equally precise SM predictions in lower-energy processes sensitive to non-SM contributions. Experimental evidence is typically harder to establish, but the reach is not bounded by the maximum collision energy reachable by experiments.

Precision tests of forbidden or suppressed processes in the SM are powerful probes for the indirect search of physics beyond the SM. The structure of the SM implies several accidental features (*i.e.*, properties that are not postulated but arise automatically) which can be challenged to look for new phenomena. Among these, there is the baryon number conservation, the universality of the gauge couplings for the three charged leptons, and the absence of FCNC at tree level. Quark flavour physics offers a rich phenomenology to probe these (and other) accidental SM properties. Considering the experimental opportunities ahead, assessing the factors that will limit the sensitivity of golden quark-flavour probes is critical. It turns out that, in several FCNC processes, a major limitation of the theoretical predictions is due to the current knowledge of the  $|V_{cb}|$  matrix element.

## 1.5 The matrix element $|V_{cb}|$

In phenomenological analyses where flavour measurements bound physics beyond the SM, a precise determination of CKM parameters from tree-level measurements, where new contribution is very unlikely, is essential. Several studies identify the uncertainty on  $|V_{cb}|$ , together with that on hadronic matrix elements, as the bottleneck for the comparison of SM predictions with future high-precision measurements. The experimental uncertainties in the rates of several rare processes, which are sensitive to potential beyond-SM contributions, are expected to decrease to below a few percent (or at most 10% in the next decade). See for instance Refs. [22–24]. These rates, such as the one for  $K \rightarrow \pi\nu\nu$  [25], are proportional

to  $A^4$ ; an uncertainty as small as 5% on  $A$  would lead to a 20% uncertainty on the SM prediction for the rate of these processes.

The current precision on  $|V_{cb}|$ , which directly affects that on  $A$ , is indeed around 5% due to a long-standing discrepancy between two measurement methods that needs to be resolved. The measurements exploit semileptonic decays of  $B$  mesons that proceed through the electroweak transition  $b \rightarrow c\ell\nu_\ell$ : these are governed by  $|V_{cb}|$ , since the intermediate  $W$  boson decays leptonically and does not involve any other CKM matrix elements. The decay amplitudes of these processes can be factorised into hadronic and leptonic currents, as explained in more detail in the next chapter. The primary challenge in extracting  $|V_{cb}|$  lies in determining the matrix element of the hadronic current. To address this, two different theoretical approaches have been developed: the *inclusive* and *exclusive* methods.

The *inclusive method* considers all possible hadronic final states with charm into which the  $B$  meson can decay. In this method, the partonic level of the  $B \rightarrow X_c\ell\nu_\ell$  decays is the only relevant process to consider, thanks to the quark-hadron duality [26]. This approach eliminates any long-distance dependence (*i.e.*, non-perturbative QCD) of the decay amplitude for the final state, while the short-distance correction (*i.e.*, perturbative QCD) can be computed in terms of an expansion of the strong coupling constant at the  $b$  quark mass scale,  $\alpha_s(m_b) \sim 0.2$ . The remaining long-distance corrections related to the initial  $B$  meson can be expanded in powers of  $\Lambda_{QCD}/m_b \sim 0.1$ , where  $\Lambda_{QCD}$  is the hadronic scale of order  $m_B - m_b \sim 0.5 \text{ GeV}/c^2$ . This approximation is called *heavy quark expansion*: it systematically expresses the decay rate in terms of non-perturbative parameters that describe universal properties of the  $B$  meson.

The *exclusive method* considers the decay of the  $B$  meson into a final state with a specific charm meson. Two decay channels are considered  $B \rightarrow D\ell\nu_\ell$  and  $B \rightarrow D^*\ell\nu_\ell$ , with the latter providing the best sensitivity. In this method, the hadronic matrix element is parametrised in terms of form factors, which are non-perturbative functions of the recoil energy of the charm meson in the  $B$  rest frame. Form factors encapsulate the non-perturbative dynamics of the transition between the initial and final states, providing essential insights into the underlying strong interactions. So, in  $B \rightarrow D\ell\nu_\ell$  decays, they describe the transition between the  $B$  and the  $D$ ; similarly, in  $B \rightarrow D^*\ell\nu_\ell$  decays, that from the  $B$  to the  $D^*$  state. Precise theoretical calculations using lattice QCD methods, and experimental information on the dependence of the form factors on the recoil energy, are crucial for extracting  $|V_{cb}|$ .

These two methods rely on different experimental techniques as well, complementing each other and providing largely independent determinations (of comparable accuracy) of  $|V_{cb}|$ . This feature would provide a crucial cross-check on our understanding of semileptonic  $B$  decays. Unfortunately, it turned out to be the major limitation in the determination of  $|V_{cb}|$ . The two methods, although reaching individually high precision (about 2% uncertainty), provide values of  $|V_{cb}|$  that differ by about 5% as shown in Fig.1.5, completely spoiling the knowledge of this CKM element.

The discrepancy must be resolved to obtain the ultimate precision on  $|V_{cb}|$ . My work aims to provide new inputs to improve the *exclusive* determination by performing the first simultaneous analysis of  $B \rightarrow D\ell\nu_\ell$  and  $B \rightarrow D^*\ell\nu_\ell$  decays at Belle II. In the next chapter, I provide more details on the theoretical description of these decays and present my novel approach for their experimental analysis.

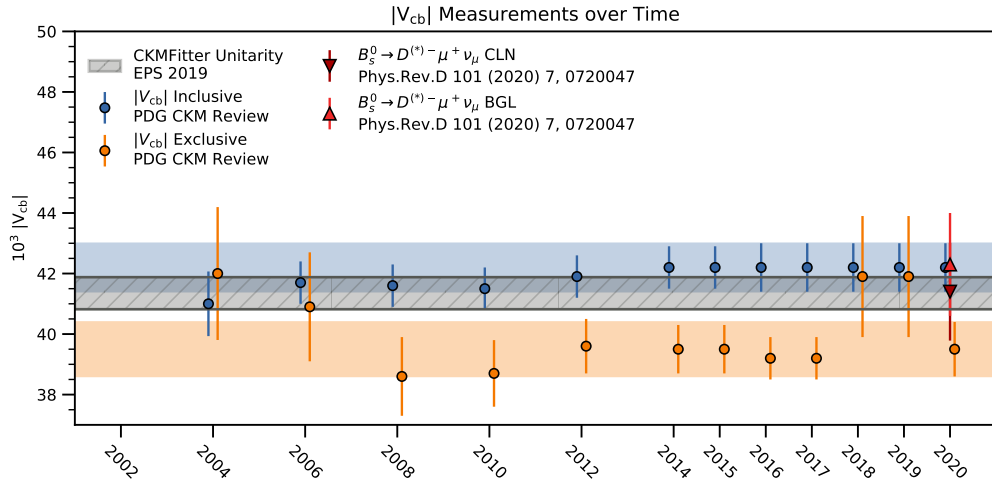


Figure 1.5: Measurements of  $|V_{cb}|$  over the last two decades. Blue points are the averages of the inclusive measurements, orange points are those of the exclusive measurements. The bands are the latest averages. The red points are measurements done with  $B_s^0$  decays, while all the others are done with  $B^+$  and  $B^0$  decays. The grey band is the indirect determination from all other constraints on the unitarity triangle provided by the CKMFitter Collaboration. The plot is taken from Ref. [27].



## Chapter 2

# A novel approach

The primary decay modes used in the exclusive determination of  $|V_{cb}|$  are  $B \rightarrow D\ell\nu_\ell$  and  $B \rightarrow D^*\ell\nu_\ell$ . In this chapter, I introduce the phenomenology of these decays and review the current status of measurements regarding their branching fractions, form factors and  $|V_{cb}|$ . After discussing the open challenges associated with their study, I present my analysis method and the definition of the model-independent observables, the target of my measurement, and all derived quantities. The chapter concludes with an overview of the analysis.

### 2.1 Exclusive semileptonic $B$ decays: generalities

Semileptonic decays of a *bottom* meson  $B$  into a *charm* meson, a lepton  $\ell$ , and a neutrino  $\nu_\ell$  proceed through the electroweak decay  $b \rightarrow c\ell^-\bar{\nu}_\ell$  (Fig. 2.1). The CKM matrix element  $|V_{cb}|$  is the only quark-mixing coupling at play. The other quark making the  $B$  meson (a  $d$  quark for the  $B^0$  and  $u$  quark for  $B^+$ ) does not engage in the electroweak transition and it is usually referred to as the *spectator* quark.

The decay width  $d\Gamma$  in a phase-space interval can be decomposed as the product of two currents,  $L^\mu$  and  $H_\mu$ , by integrating out the contribution of the  $W$  boson at tree level, since  $m_b \ll m_W$ ; the decay width takes the form

$$d\Gamma \propto G_F^2 |V_{cb}|^2 |L^\mu H_\mu|^2, \quad (2.1)$$

where  $G_F = 1.16637 \times 10^{-5} \text{ GeV}^{-2}$  is the Fermi constant,  $L^\mu$  is the leptonic current and  $H_\mu$  the hadronic current, and  $\mu$  are Lorentz indexes. The leptonic current can be exactly calculated at the elementary-particle level, as it involves only leptons. On the other hand, the hadronic current cannot be, as the quarks are bounded in mesons. Indeed, the spectator

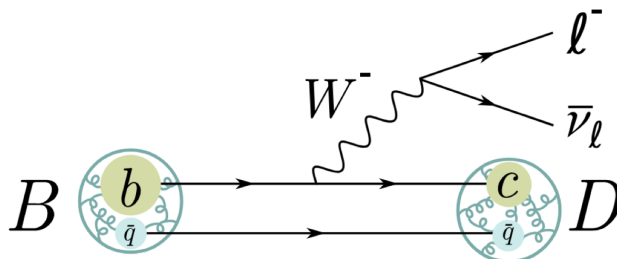


Figure 2.1: Feynman diagram of semileptonic  $B \rightarrow D\ell\nu_\ell$  decays. A decay involving a  $D^*$  meson has the same diagram. The green curly lines represent the exchange of soft gluons between the heavy ( $b$  and  $c$ ) and the light spectator quark ( $\bar{q}$ ).

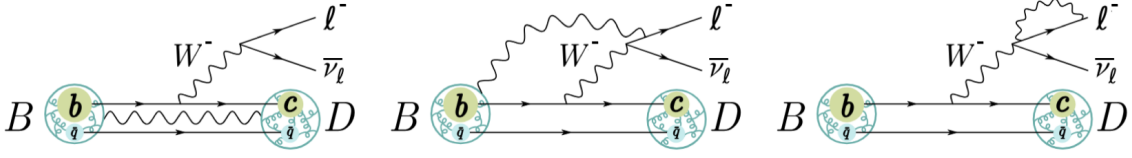


Figure 2.2: Photonic terms contributing to the leading order electroweak correction.

quark can be considered as such only for the weak interaction; it interacts strongly with the other quark exchanging soft gluons in the  $B$  and  $D$  mesons.

While the leptonic and hadronic current do not interact at tree level, higher orders can add terms with exchange of a photon,  $W$ ,  $Z$ , or Higgs bosons. The largest impact at the leading order is due to the electromagnetic interactions depicted in Fig. 2.2, the so-called *radiative corrections*. The leading-order correction gives

$$|L^\mu H_\mu|^2 \rightarrow |L^\mu H_\mu|^2 \eta_{\text{EW}} \quad (2.2)$$

where  $\eta_{\text{EW}} = (1 + (\alpha/\pi) \ln(m_Z/\mu))$ , and  $\alpha = e^2/4\pi$  is the fine-structure constant,  $m_Z$  is the mass of  $Z$  boson,  $\mu$  is the mass scale characterising the process at hand. Using the calculations from Ref. [28] one gets  $\eta_{\text{EW}} \approx 1.0066$ . This value only encapsulates the leading-order correction and is often termed as ‘‘Sirlin factor’’. Contributions outside this factor are more difficult to calculate and subject of debate within the phenomenological community.<sup>1</sup> An approach is to inflate the uncertainty on the Sirlin factor to conservatively account for higher-order corrections (see for instance Chapter 3 of Ref. [30]).

In the exclusive approach, the hadronic current is parametrised in terms of form factors, non-perturbative functions of the squared transferred momentum  $q_{D^{(*)}}^2$  between the  $B$  and  $D^{(*)}$  mesons. This momentum is related to the recoil variable  $w_{D^{(*)}}$ , the scalar product of four-velocities of the two mesons:

$$w_{D^{(*)}} = v_B \cdot v_{D^{(*)}} = \frac{m_B^2 + m_{D^{(*)}}^2 - q_{D^{(*)}}^2}{2m_B m_{D^{(*)}}}, \quad (2.3)$$

where  $m_B$  and  $m_{D^{(*)}}$  are the masses of the two mesons. The minimum value,  $w_{D^{(*)}} = 1$ , corresponds to zero recoil of the  $D^{(*)}$  meson in the  $B$  rest frame, *i.e.*, the largest kinematically allowed value of  $q_{D^{(*)},\text{max}}^2$ . In the following, I use the notation  $w$  to denote both  $w_D$  and  $w_{D^*}$  when the intended variable is clear from context; similarly with  $q^2$  for  $q_D^2$  and  $q_{D^{(*)}}^2$ . The form factors can be computed by employing lattice QCD, a non-perturbative method that adapts continuous equations derived from the original QCD Lagrangian in a discrete space, and then solves them numerically. However, these numerical calculations require intense CPU power and time, which limit the accessible phase-space region and achievable precision.

The form factors can be calculated only for a few  $q^2$  values close to  $q_{\text{max}}^2$ , and usually have 1-2% uncertainty only at  $q_{\text{max}}^2$  [31–33]. Approximated analytical methods (light cone sum rules) are also used [34], but they yield much less precise results; their advantage consists in providing values of the form factors at low  $q^2$ , to complement lattice-QCD calculations.

Form factors can also be measured experimentally by analysing the differential decay rate as a function of  $q^2$ . However only the ‘‘shape’’ of the function can be accessed, *i.e.*, only the relative variations of the form factors are measurable. As the decay rate is the

<sup>1</sup>For instance, see Ref. [29] for a recent work on QED contributions for inclusive measurements.

product of  $|V_{cb}|$  and the form factor (both squared), to disentangle them, the value of the form factor must be known at least for one  $q^2$  value. Although any  $q^2$  point could work, usually that with maximum precision is used (*i.e.*, the value of the form factors at  $q_{\max}^2$  from lattice QCD).

Parametrisations of the form factors are used to extrapolate them at any  $q^2$  value, allowing to obtain precise predictions for decay rates. There are different parametrisations, named after the physicists who proposed them. The two most commonly used are:<sup>2</sup>

- **The Boyd-Grinstein-Lebed (BGL) parametrisation** [37]. The form factors are expanded in a power series of a variable  $z$ , a function of  $q^2$ , which takes values much smaller than 1, such that the series converges within a few terms. The series are constructed to satisfy basic constraints imposed by unitarity and flavour symmetries. The free parameters are the coefficients of the powers of  $z$  of the series (see Eq. A.21 and Eqs. A.8-A.10 in Appendix A). This is the most generic functional description of the form factors and has an arbitrary number of parameters depending on the truncation order of the series [38, 39].
- **The Caprini-Lellouch-Neubert (CLN) parametrisation** [40]. The form factors are also expanded in  $z$ , but imposing more restrictive theoretical constraints to reduce the number of free parameters. For this reason, it has been the preferred parametrisation used in experimental analyses until few years ago. Phenomenologists have strongly criticised its use [41, 42], as the assumptions made do not allow for enough flexibility to fit the data; resulting uncertainties associated with the form factor parameters and  $|V_{cb}|$  are also considered to be underestimated in this approach.

Once the form factors of the decay are known, the value of  $|V_{cb}|$  can be determined by a measurement of its branching fraction. This measurement can be differential as a function of the kinematic variables which characterise the decay rate, in order to gain experimental sensitivity from the form factor shape and its knowledge over the phase space. In the next section I will discuss the differential decay rate of the  $B \rightarrow D\ell\nu_\ell$  and  $B \rightarrow D^*\ell\nu_\ell$  decays.

## 2.2 The $B \rightarrow D^{(*)}\ell\nu_\ell$ decays

In the limit of negligible lepton masses (*i.e.*, for an electron or a muon), the differential decay rate of the  $B \rightarrow D\ell\nu_\ell$  decay as a function of  $w$  can be written as<sup>3</sup>

$$\frac{d\Gamma(B \rightarrow D\ell\nu_\ell)}{dw} = \frac{G_F^2 m_D^3}{48\pi^3} (m_B + m_D)^2 \eta_{EW}^2 |V_{cb}|^2 (w^2 - 1)^{3/2} |\mathcal{G}(w)|^2, \quad (2.4)$$

and it depends only on one form factor, encoded in the function  $\mathcal{G}(w)$  [43]. The form factor is  $f_+(w)$  and its relation to  $\mathcal{G}(w)$  is

$$|\mathcal{G}(z)|^2 = \frac{4r}{(1+r)^2} |f_+(z)|^2, \quad (2.5)$$

where  $r = m_D/m_B$  is the ratio of the  $D$  and  $B$  masses, and the conformal variable  $z$  is defined as

$$z \equiv \frac{\sqrt{w+1} - \sqrt{2}}{\sqrt{w+1} + \sqrt{2}}. \quad (2.6)$$

---

<sup>2</sup>The list is not exhaustive as there are also other parametrisations available, such as BCL or BSW parametrisations [35, 36].

<sup>3</sup>Here I focus solely on  $w_D$  for the  $B \rightarrow D\ell\nu_\ell$  decay, although the lepton helicity angle can also be defined for this process.

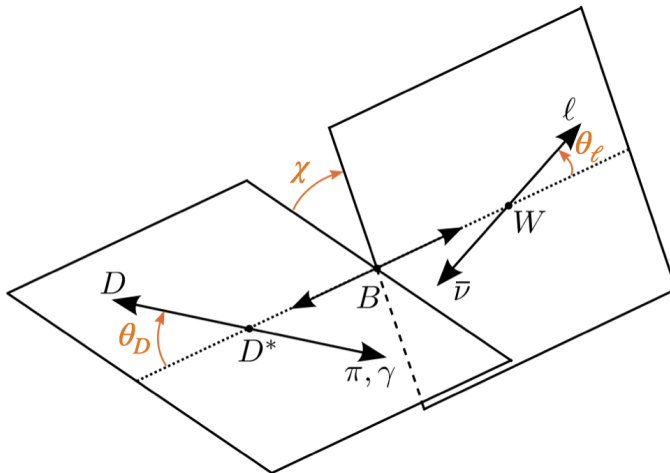


Figure 2.3: Graphical representation of the helicity angles in the  $B \rightarrow D^* \ell \nu_\ell$  decay. The definitions are provided in the text.

The BGL and CLN parametrisations of  $f_+(w)$  are discussed in Appendix A. The main goal of my analysis is to measure the product of  $|V_{cb}|$  and  $\mathcal{G}(w)$  in bins of  $w$ , as I explain in more detail in Sect. 2.5.

The differential decay rate of the  $B \rightarrow D^* \ell \nu_\ell$  decay is more complex than that of  $B \rightarrow D \ell \nu_\ell$ , due to the spin-1  $D^*$  meson which results in a richer phenomenology that manifests in the angular distributions of the decay products. The lepton pair in the decay originates from the virtual  $W$  decay: the  $B$  decay can be described as the transition of a spin-0 particle (the  $B$  meson) into two spin-1 particles (the  $D^*$  and the  $W$ ). The decay amplitude  $\mathcal{A}$  can be expressed in terms of three helicity amplitudes,  $H_+(w)$ ,  $H_-(w)$ , and  $H_0(w)$ , which correspond to the three polarisation states of the  $D^*$  meson, two transverse and one longitudinal, allowed by angular-momentum conservation. The helicity states are characterised by different angular distributions of the final-state particles, which depend on the  $D^*$  decay (different for  $D^* \rightarrow D\pi$  and  $D^* \rightarrow D\gamma$ ).

The kinematics of the full decay can be described by four variables, the recoil energy  $w$  and three helicity angles, displayed in Fig. 2.3. These angles are:  $\theta_\ell$ , the angle between the direction of the lepton in the virtual  $W$  rest frame and the direction of the  $W$  in the  $B$  rest frame;  $\theta_D$ , the angle between the direction of the  $D$  meson in the  $D^*$  rest frame and the direction of the  $D^*$  meson in the  $B$  rest frame;  $\chi$ , the angle between the decay planes formed by the  $W$  and the  $D^*$  meson in the  $B$  rest frame.

In the massless lepton limit, the four-dimensional differential decay rate is [44]

$$\frac{d^4\Gamma(B \rightarrow D^* \ell \nu_\ell)}{dw d \cos \theta_\ell d \cos \theta_D d \chi} = \frac{3}{16\pi} \Gamma_0(w) |V_{cb}|^2 |\mathcal{A}(w, \theta_\ell, \theta_D, \chi)|^2, \quad (2.7)$$

where  $\Gamma_0(w) = \eta_{\text{EW}}^2 m_B m_{D^*}^2 G_F^2 \sqrt{w^2 - 1} (1 - 2rw + r^2) / (4\pi^3)$ , with  $r = m_{D^*} / m_B$ . The decay amplitude  $\mathcal{A}$  can be expressed in terms of the helicity amplitudes  $H_+(w)$ ,  $H_-(w)$ , and  $H_0(w)$  as

$$|\mathcal{A}(w, \theta_\ell, \theta_D, \chi)|^2 = \sum_{i=1}^6 \mathcal{H}_i(w) k_i(\theta_\ell, \theta_D, \chi), \quad (2.8)$$

where  $\mathcal{H}_i$  and  $k_i$  terms are defined in the Table 2.1.

Since in my analysis the  $D^*$  decay is not completely reconstructed, I can solely access the  $\theta_\ell$  angle and the two-dimensional decay rate as a function of  $w$  and  $\cos \theta_\ell$ . In this case, the

$i$	$\mathcal{H}_i(w)$	$k_i(\theta_\ell, \theta_D, \chi)$	
		$D^* \rightarrow D\gamma$	$D^* \rightarrow D\pi$
1	$H_+^2$	$\frac{1}{2}(1 + \cos^2 \theta_D)(1 - \cos \theta_\ell)^2$	$\sin^2 \theta_D(1 - \cos \theta_\ell)^2$
2	$H_-^2$	$\frac{1}{2}(1 + \cos^2 \theta_D)(1 + \cos \theta_\ell)^2$	$\sin^2 \theta_D(1 + \cos \theta_\ell)^2$
3	$H_0^2$	$2 \sin^2 \theta_D \sin^2 \theta_\ell$	$4 \cos^2 \theta_D \sin^2 \theta_\ell$
4	$H_+ H_-$	$4 \sin^2 \theta_D \sin^2 \theta_\ell \cos 2\chi$	$-2 \sin 2\theta_D \sin^2 \theta_\ell \cos 2\chi$
5	$H_+ H_0$	$\sin 2\theta_D \sin \theta_\ell(1 - \cos \theta_\ell) \cos \chi$	$-2 \sin 2\theta_D \sin \theta_\ell(1 - \cos \theta_\ell) \cos \chi$
6	$H_- H_0$	$-\sin 2\theta_D \sin \theta_\ell(1 + \cos \theta_\ell) \cos \chi$	$2 \sin 2\theta_D \sin \theta_\ell(1 + \cos \theta_\ell) \cos \chi$

Table 2.1: Functions describing the differential decay rate of  $B \rightarrow D^* \ell \nu_\ell$  decays, separately for the cases in which the  $D^*$  meson decays to  $D\gamma$  or  $D\pi$ .

mixed terms ( $i = 4, 5, 6$ ) of the decay rate listed in Tab. 2.1 are zero for both  $D^* \rightarrow D\gamma$  and  $D^* \rightarrow D\pi$ . Furthermore, by integrating over  $\cos \theta_D$ , the terms with  $i = 1, 2, 3$  are identical for the two transitions, and the two-dimensional decay rates the same for  $D^* \rightarrow D\gamma$  and  $D^* \rightarrow D\pi$  decays.

The helicity amplitudes encode the form factors, which are expressed as functions of  $w$ . Depending on the assumed parametrisation, there are different functions related to them. For example, a common basis used for the BGL expansion defines the following ‘‘helicity’’ form factors:

$$g(w) = \frac{H_-(w) - H_+(w)}{2m_B^2 r \sqrt{w^2 - 1}}, \quad (2.9)$$

$$f(w) = \frac{H_+(w) + H_-(w)}{2}, \quad (2.10)$$

$$\mathcal{F}_1(w) = m_B H_0(w) \sqrt{1 - 2rw + r^2}. \quad (2.11)$$

The important point to make is that form factors are functions of the helicity amplitudes. A measurement of the helicity amplitudes as functions of  $w$  gives access to the form factors. The three form factors can be expressed using either the BGL or CLN parametrisations; details are given in Appendix A. In my analysis, I target a measurement of model-independent observables that are combinations of  $|V_{cb}|^2$  and the helicity amplitudes squared, in bins of  $w$ . This is explained in Sect. 2.5.

## 2.3 Current status

From the knowledge of the branching fractions and the form factors,  $|V_{cb}|$  can be determined. I will briefly review the current experimental status of these ingredients for both  $B \rightarrow D \ell \nu_\ell$  and  $B \rightarrow D^* \ell \nu_\ell$  decays.

### 2.3.1 Branching fractions measurements

Measurements of the  $B \rightarrow D \ell \nu_\ell$  properties have been reported by various experiments, with the most recent results coming from the Belle [45]. The Heavy Flavour Averaging Group (HFLAV) [46] performs a comprehensive combination of all available measurements for the  $B \rightarrow D \ell \nu_\ell$  decays. Table. 2.2 shows these measurements for  $B^0 \rightarrow D^- \ell^+ \nu_\ell$  and

Experiment	$\mathcal{B}(B^0 \rightarrow D^- \ell^+ \nu_\ell)[\%]$	$\mathcal{B}(B^+ \rightarrow \bar{D}^0 \ell^+ \nu_\ell)[\%]$
ALEPH [47]	$2.17 \pm 0.18 \pm 0.35$	—
CLEO [48]	$2.10 \pm 0.13 \pm 0.15$	$2.14 \pm 0.13 \pm 0.17$
BABAR [49]	$2.15 \pm 0.11 \pm 0.14$	$2.16 \pm 0.08 \pm 0.12$
Belle [45]	$2.33 \pm 0.04 \pm 0.11$	$2.46 \pm 0.04 \pm 0.12$
Average	$2.24 \pm 0.04 \pm 0.08$	$2.30 \pm 0.03 \pm 0.08$

Table 2.2: Measurements of various experiments and the averages of  $B^0 \rightarrow D^- \ell^+ \nu_\ell$  and  $B^+ \rightarrow \bar{D}^0 \ell^+ \nu_\ell$  branching fractions. The first uncertainty is statistical and the second is systematic. The measurements are rescaled to the latest values of the input parameters (mainly branching fractions of charmed mesons). Taken from Ref. [50].

$B^+ \rightarrow \bar{D}^0 \ell^+ \nu_\ell$  decays. The averages read:

$$\mathcal{B}(B^0 \rightarrow D^- \ell^+ \nu_\ell) = (2.24 \pm 0.04 \pm 0.08)\%, \quad (2.12)$$

$$\mathcal{B}(B^+ \rightarrow \bar{D}^0 \ell^+ \nu_\ell) = (2.30 \pm 0.03 \pm 0.08)\%, \quad (2.13)$$

where the first uncertainty is statistical and the second is systematic. The main systematic uncertainties on these measurements are the lepton-identification efficiency and the modelling of the backgrounds; these affect also the  $|V_{cb}|$  determination from these decays.

The first observation of the  $B \rightarrow D^* \ell \nu_\ell$  decay was reported in 1997 by ALEPH [47], while the most recent measurement comes from Belle II [51].

Experiment	$\mathcal{B}(B^0 \rightarrow D^{*-} \ell^+ \nu_\ell)[\%]$	$\mathcal{B}(B^+ \rightarrow \bar{D}^{*0} \ell^+ \nu_\ell)[\%]$
ALEPH [47]	$5.45 \pm 0.26 \pm 0.33$	—
OPAL [52]	$6.13 \pm 0.28 \pm 0.57$	—
OPAL [52]	$5.12 \pm 0.20 \pm 0.36$	—
DELPHI [53]	$4.95 \pm 0.14 \pm 0.35$	—
DELPHI [54]	$5.08 \pm 0.20 \pm 0.42$	—
CLEO [55]	$6.09 \pm 0.19 \pm 0.37$	$6.20 \pm 0.20 \pm 0.26$
Belle [56]	$4.83 \pm 0.02 \pm 0.15$	—
BABAR [57, 58]	$4.41 \pm 0.04 \pm 0.32$	$5.30 \pm 0.15 \pm 0.33$
BABAR [59]	$5.17 \pm 0.16 \pm 0.31$	$5.00 \pm 0.08 \pm 0.31$
Belle II [60]	$4.60 \pm 0.05 \pm 0.48$	—
Belle II [51]	$4.51 \pm 0.41 \pm 0.52$	—
Average	$4.97 \pm 0.02 \pm 0.12$	$5.58 \pm 0.07 \pm 0.21$

Table 2.3: Measurements of various experiments and the averages of  $B^0 \rightarrow D^{*-} \ell^+ \nu_\ell$  and  $B^+ \rightarrow \bar{D}^{*0} \ell^+ \nu_\ell$  branching fractions. The first error is statistical and the second one is systematic. The measurements are rescaled to the latest values of the input parameters (mainly branching fractions of charmed mesons). Taken from Ref. [50]

The averages of the branching fractions (see Tab. 2.3) for  $B^0 \rightarrow D^{*-}\ell^+\nu_\ell$  and  $B^+ \rightarrow \bar{D}^{*0}\ell^+\nu_\ell$  are [50]:

$$\mathcal{B}(B^0 \rightarrow D^{*-}\ell^+\nu_\ell) = (4.97 \pm 0.02 \pm 0.12)\%, \quad (2.14)$$

$$\mathcal{B}(B^+ \rightarrow \bar{D}^{*0}\ell^+\nu_\ell) = (5.58 \pm 0.07 \pm 0.21)\%, \quad (2.15)$$

where also in this case, the first uncertainty is statistical and the second is systematic. The measurements are all limited by the systematic uncertainties, whose principal sources are the lepton-identification efficiency [56] and the track-reconstruction efficiency. The greatest contribution is given by that for the soft pion in the  $D^*$  decay [51, 56]. These very sources of systematic uncertainty affect also  $|V_{cb}|$ .

### 2.3.2 $|V_{cb}|$ and form factors

Measurements of  $|V_{cb}|$  are obtained by assuming a parametrisation of the form factors. Due to its reduced set of parameters, the CLN has been the parametrisation used in all measurements till about 2017. For the  $B \rightarrow D\ell\nu_\ell$  decays, the form-factor parameter  $\rho_D^2$  (see Appendix A for more details) is measured and then the rate at zero recoil ( $w = 1$ ) is extracted to determine  $\eta_{\text{EW}}\mathcal{G}(1)|V_{cb}|$ , where  $\mathcal{G}(1)$  is the value of  $\mathcal{G}(w)$  at  $w = 1$ . These measurements are obtained from both  $B^0 \rightarrow D^-\ell^+\nu_\ell$  and  $B^+ \rightarrow \bar{D}^0\ell^+\nu_\ell$  decays, assuming isospin symmetry, *i.e.*, the equality of the semileptonic decay width for  $B^0$  and  $B^+$  decays. A summary of the measurements of these parameters are shown in Tab. 2.4.

HFLAV performs a fit on all these measurements taking into account correlated statistical and systematic uncertainties [50]. The result of the fit is

$$\eta_{\text{EW}}\mathcal{G}(1)|V_{cb}| = (41.53 \pm 0.98) \times 10^{-3}, \quad (2.16)$$

$$\rho_D^2 = 1.129 \pm 0.033, \quad (2.17)$$

where the uncertainties include both the statistical and systematic contributions. To obtain  $|V_{cb}|$ , the input value for the form factor normalisation is required. The best known value from averages of lattice-QCD calculations is [61]

$$\mathcal{G}(1) = 1.0541 \pm 0.0083, \quad (2.18)$$

and with  $\eta_{\text{EW}} = 1.0066 \pm 0.0050$ , HFLAV obtains

$$|V_{cb}| = (39.14 \pm 0.92 \pm 0.36) \times 10^{-3}, \quad (2.19)$$

where the first error combines the statistical and systematic uncertainties from the experimental measurements and the second is theoretical (lattice-QCD calculations and electroweak correction).

When experimental data on the  $w$  spectrum are available, a fit allows to use a different parametrisation and to include available lattice-QCD data at  $w > 1$  to improve the extrapolation to  $w = 1$ . Spectra of  $w$  have been published by BaBar [49] and Belle [45]. However, the BaBar result does not include the full covariance matrix of the measured data, preventing a combined fit.

Similarly, for the  $B \rightarrow D^*\ell\nu_\ell$  decays the CLN parameter  $\rho_{D^*}^2$  (and in some cases also  $R_1(1)$  and  $R_2(1)$ , see Appendix A for more details) is measured and then the rate at zero recoil ( $w = 1$ ) is extracted to determine  $\eta_{\text{EW}}h_{A_1}(1)|V_{cb}|$ , where  $h_{A_1}(1)$  is the value of the form factor at  $w = 1$ . HFLAV performs a four-dimensional fit of  $\eta_{\text{EW}}h_{A_1}(1)|V_{cb}|$ ,  $\rho_{D^*}^2$ ,

Experiment	$\eta_{\text{EW}}\mathcal{G}(1) V_{cb} [10^{-3}]$	$\rho_D^2$
ALEPH [47]	$36.19 \pm 9.38 \pm 6.83$	$0.814 \pm 0.821 \pm 0.419$
CLEO [48]	$44.17 \pm 5.68 \pm 3.46$	$1.270 \pm 0.214 \pm 0.121$
Belle [45]	$41.83 \pm 0.60 \pm 1.20$	$1.090 \pm 0.036 \pm 0.019$
BABAR [62]	$42.55 \pm 0.71 \pm 2.06$	$1.194 \pm 0.034 \pm 0.060$
BABAR [49]	$42.54 \pm 1.71 \pm 1.26$	$1.200 \pm 0.088 \pm 0.043$
Average	$41.53 \pm 0.44 \pm 0.88$	$1.129 \pm 0.024 \pm 0.023$

Table 2.4: Measurements of  $\eta_{\text{EW}}\mathcal{G}(1)|V_{cb}|[10^{-3}]$  and the CLN parameter  $\rho_D^2$  in the  $B \rightarrow D\ell\nu_\ell$  decays. The first error is statistical and the second is systematic. Taken from Ref. [50].

$R_1(1)$  and  $R_2(1)$  with the measurements shown in Tab. 2.5, assuming isospin symmetry between  $B^0$  and  $B^+$  decays.

The results of the fit are [50]:

$$\eta_{\text{EW}}h_{A_1}(1)|V_{cb}| = (35.00 \pm 0.36) \times 10^{-3}, \quad (2.20)$$

$$\rho_{D^*}^2 = 1.121 \pm 0.024, \quad (2.21)$$

$$R_1(1) = 1.269 \pm 0.026, \quad (2.22)$$

$$R_2(1) = 0.853 \pm 0.017. \quad (2.23)$$

The uncertainties include both the statistical and systematic contributions.

To convert this result into  $|V_{cb}|$ , theory input for the form-factor normalisation is required. The recent lattice-QCD result from Ref. [63, 64] is

$$\eta_{\text{EW}}h_{A_1}(1) = 0.910 \pm 0.013, \quad (2.24)$$

from which  $|V_{cb}|$  can be extracted using  $\eta_{\text{EW}} = 1.0066 \pm 0.0050$ ,

$$|V_{cb}| = (38.46 \pm 0.40 \pm 0.55) \times 10^{-3}, \quad (2.25)$$

where the first uncertainty combines the statistical and systematic uncertainties from the experimental measurements and the second is theoretical (lattice-QCD calculations and electroweak correction). This number is in agreement with  $|V_{cb}|$  obtained from  $B \rightarrow D\ell\nu_\ell$  decays given in Eq. 2.19.

Similar combinations can be done using recent results with the BGL parametrisation. Both Belle [56] and BaBar [65] have recently published analyses of  $B \rightarrow D^*\ell\nu_\ell$  decays that employ the BGL parametrisation. However, while Belle performs an extraction of  $|V_{cb}|$ , the BaBar analysis only fits the BGL parameters taking the normalisation as an external input. Due to the limited set measurements, HFLAV currently does not perform a combination of the BGL parameters and  $|V_{cb}|$ . However, the result of  $|V_{cb}|$  from Belle and Babar analyses using BGL is in agreement with that obtained by HFLAV with the CLN parametrisation.

Experiment	$\eta_{EW}h_{A_1}(1) V_{cb} [10^{-3}]$	$\rho_{D^*}^2$
ALEPH [47]	$31.38 \pm 1.80 \pm 1.24$	$0.488 \pm 0.226 \pm 0.146$
CLEO [55]	$40.16 \pm 1.24 \pm 1.54$	$1.363 \pm 0.084 \pm 0.087$
OPAL [52]	$36.20 \pm 1.58 \pm 1.47$	$1.198 \pm 0.206 \pm 0.153$
OPAL [52]	$37.44 \pm 1.20 \pm 2.32$	$1.090 \pm 0.137 \pm 0.297$
DELPHI [53]	$35.52 \pm 1.41 \pm 2.29$	$1.139 \pm 0.123 \pm 0.382$
DELPHI [54]	$35.87 \pm 1.69 \pm 1.95$	$1.070 \pm 0.141 \pm 0.153$
Belle [56]	$34.82 \pm 0.15 \pm 0.55$	$1.106 \pm 0.031 \pm 0.008$
BABAR [57]	$33.37 \pm 0.29 \pm 0.97$	$1.182 \pm 0.048 \pm 0.029$
BABAR [58]	$34.55 \pm 0.58 \pm 1.06$	$1.124 \pm 0.058 \pm 0.053$
BABAR [49]	$35.45 \pm 0.20 \pm 1.08$	$1.171 \pm 0.019 \pm 0.060$
Average	$35.00 \pm 0.11 \pm 0.34$	$1.121 \pm 0.014 \pm 0.019$

Table 2.5: Measurements of  $\eta_{EW}h_{A_1}(1)|V_{cb}|[10^{-3}]$  and the CLN parameter  $\rho_{D^*}^2$  in  $B \rightarrow D^*\ell\nu_\ell$  decays. The first error is statistical and the second is systematic. Since most analyses does not measure  $R_1(1)$  and  $R_2(1)$ , only  $\eta_{EW}h_{A_1}(1)|V_{cb}|$  and  $\rho_{D^*}^2$  are shown. Taken from Ref. [50].

### 2.3.3 Production rates of charged versus neutral $B$ -meson pairs

The ratio  $f_{+-}/f_{00}$  measures the production rates of charged ( $B^+B^-$ ) versus neutral ( $B^0\bar{B}^0$ )  $B$ -meson pairs in  $\Upsilon(4S)$  decays. Precise measurements of this ratio are essential as the production rates directly affect the knowledge of the branching-fractions of all  $B$  decays (and also  $|V_{cb}|$ ) measured at  $B$ -factories.

Experimentally,  $f_{+-}/f_{00}$  is determined by reconstructing  $B$ -meson decays in specific final states and correcting for detection efficiencies and reconstruction biases. The challenge lies in designing a measurement strategy that minimises reliance on strong assumptions, such as the equality of decay widths between charged and neutral  $B$  mesons, used to cancel the dependence on the branching fractions of the  $B$  decays employed. For instance,  $B^+ \rightarrow J/\psi K^+$  and  $B^0 \rightarrow J/\psi K^*(892)^0$  are used to count the relative yields of  $B^+$  and  $B^0$  in the same amount of data: to determine  $f_{+-}/f_{00}$ , one would need the ratio of branching fractions of these decays as external inputs. By considering isospin symmetry, instead, one can impose an equality between the ratio of branching fractions and that of the  $B$  lifetimes,  $\mathcal{B}(B^0 \rightarrow J/\psi K^*(892)^0)/\mathcal{B}(B^+ \rightarrow J/\psi K^+) = \tau(B^0)/\tau(B^+)$ . The major challenge of this approach is to correctly assign a systematic uncertainties for possible isospin-breaking effects. In addition, these approaches assume a negligible fraction of  $\Upsilon(4S)$  decaying into a different final state than  $B\bar{B}$ , *i.e.*,  $f_{+-} + f_{00} = 1$ .

A precise measurement of  $f_{+-}/f_{00}$  using these assumptions has been performed by BABAR. The measured value of  $f_{+-}/f_{00}$  is  $1.06 \pm 0.02(\text{stat}) \pm 0.03(\text{syst})$  [66]. Values reported from earlier measurements feature uncertainties of approximately 10%. These results initially suggested only minor deviations from the isospin-symmetric expectation of unity. However, these studies neglected or underestimated uncertainties related to isospin-breaking effects, such as differences in electromagnetic corrections and phase space between charged and neutral  $B$ -mesons. A significant advance was achieved very recently by the Belle experiment, which provided a detailed measurement of  $f_{+-}/f_{00}$ , yielding  $1.065 \pm 0.012(\text{stat}) \pm 0.019(\text{syst}) \pm 0.047(\text{th})$  [67]. This analysis was the first to rigorously

Experiment	Measurement
	$f_{+-}/f_{00}$
CLEO [72]	$1.04 \pm 0.07 \pm 0.04$
BABAR [66]	$1.06 \pm 0.02 \pm 0.03$
Belle [67]	$1.065 \pm 0.012 \pm 0.019 \pm 0.047$
CLEO [73]	$1.058 \pm 0.084 \pm 0.136$
Belle [74]	$1.01 \pm 0.03 \pm 0.09$
	$f_{00}$
BABAR [70]	$0.487 \pm 0.010 \pm 0.008$
	$f_{\mathcal{B}}$
CLEO [75]	$-0.0011 \pm 0.0143 \pm 0.0107$
BABAR, Belle [76–78]	$\geq 0.00264 \pm 0.00021$
Average	$f_{+-}/f_{00} = 1.052 \pm 0.031$

Table 2.6: Measurements of  $f_{+-}/f_{00}$ ,  $f_{00}$  and  $f_{\mathcal{B}} = 1 - f_{+-} - f_{00}$  used in the HFLAV combination. The first uncertainty is statistical, the second systematic, and the third, when present, arises from isospin-breaking assumptions. Taken from Ref. [71].

incorporate the impact of isospin breaking (the uncertainty denotes as “th”), considering both electromagnetic and hadronic effects. These corrections must be taken into account and depend on the specific decays used to measure  $f_{+-}/f_{00}$ . By addressing these limitations, the Belle measurement set a new standard in the field, providing a value that aligns well with theoretical expectations [68, 69] and improving the reliability of  $f_{+-}/f_{00}$  as a benchmark for  $B$ -factory experiments. From now on, I consider the Belle measurement the best accurate determination of  $f_{+-}/f_{00}$  from a single experiment, as it correctly accounts the systematic effect due to isospin-breaking assumptions.

A different and promising approach is the double-tagging method, which avoids both the isospin symmetry assumption and that of  $f_{+-} + f_{00} = 1$ , by simultaneously reconstructing both the signal-side and tag-side  $B$  mesons in the same decay channel, to measure  $f_{00}$  [70]. This method provides a direct and assumption-free measurement, although with the drawback of significantly reduced reconstruction efficiency, hence the need for large data samples. By using this method, BaBar obtained  $f_{00} = 0.487 \pm 0.010(\text{stat}) \pm 0.008(\text{syst})$ .

HFLAV [46] has recently performed an average of all results, taking into account correlations of the systematic uncertainties due to the common input of  $\tau(B^+)/\tau(B^0)$  and due to the isospin-symmetry assumption. They also include the measurement of  $f_{00}$  and the constraints on the fraction of  $\Upsilon(4S)$  decays to a non  $B\bar{B}$  final state ( $f_{\mathcal{B}}$ ). They obtain a value  $f_{+-}/f_{00} = 1.052 \pm 0.031(\text{stat} + \text{syst})$  [71]. The measurements used in the combination are shown in Tab. 2.6.

It is important to note that the ratio  $f_{+-}/f_{00}$  varies with centre-of-mass energy due to the different phase space of  $B^+B^-$  and  $B^0\bar{B}^0$  pairs. This may introduce an additional uncertainty, which is not included in the combination provided by HFLAV, due to potential variation during data-taking of the centre-of-mass energies in the different experiments. For this reason, an independent measurement of  $f_{+-}/f_{00}$  at Belle II is crucial to account for this effect, thus providing a more reliable value for Belle II branching-fraction measurements.

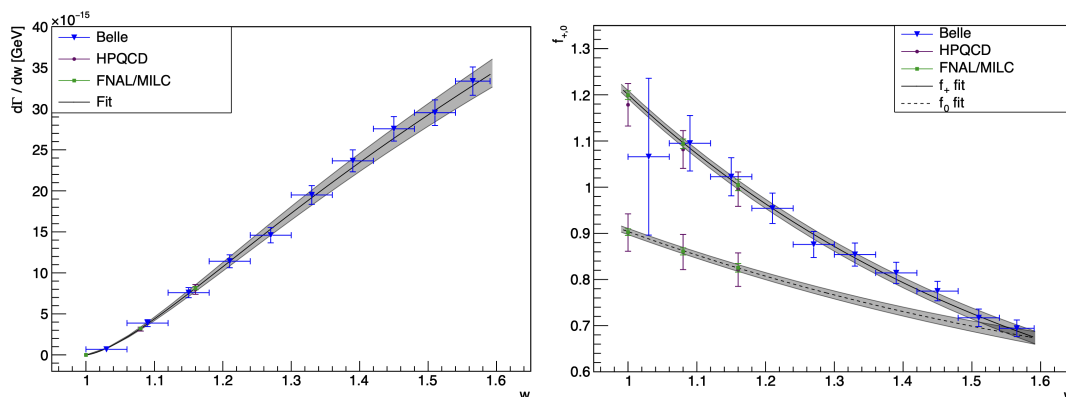


Figure 2.4: (Left) Measured differential decay rate as a function of  $w$  and (right) form factors of the decay  $B \rightarrow D l \nu_\ell$  and result of the combined fit to experimental and lattice QCD (FNAL/MILC and HPQCD) data [45]. The BGL series is truncated after the cubic term. The points with error bars are Belle and lattice-QCD data. For Belle data, the uncertainties are represented by the vertical error bars and the bin widths by the horizontal bars. The solid curve is the  $f_+$  form factor and the dashed curve represents  $f_0$ . The shaded areas around these curves indicate the uncertainty in the coefficients of the BGL expansion.

The ratio  $f_{+-}/f_{00}$  will be one of the key observables in my analysis, which will be explained in more detail in Sect. 2.5.1.

## 2.4 Open challenges

The results reported in Tab. 2.4 and 2.5 are extracted by combining measurements that assume the CLN parametrisation, which has been criticised by several phenomenological papers in recent years [41, 42], due to restrictive theoretical assumptions used to decrease the number of free parameters. The general prejudice is that measurement uncertainties using this parametrisation are underestimated. For this reason, recent experimental analyses consider a different paradigm. First, the more general model given by the BGL parametrisation should be employed. Second and more important, whenever possible, the outcome of the measurement should be *model-independent* observables that can be reanalysed using any model for the form factors.

Regarding the BGL parametrisation, although it provides a more general model, its results may depend on an arbitrary choice either—specifically, the truncation order [38, 39, 43, 79, 80]. The form factors are indeed expressed as a series expansion in the conformal variable  $z$  (see Eq. 2.6). However, since this series is infinite, it must be truncated after a finite number of terms for practical applications. This truncation typically occurs after a few terms, such as  $z^2$  or  $z^3$ , to maintain a balance between accuracy and simplicity. The truncation introduces approximations, as omitting higher-order terms assumes their contribution is minimal within the relevant kinematic range. On the other hand, going at high orders introduce a larger number of parameters with the risk of overfitting. The truncation choice directly affects the precision of the form factor description, and ultimately that on  $|V_{cb}|$ , making careful consideration essential.

Regarding model-independent observables, an example is the measurement of the  $w$  spectrum reported in Fig. 2.4. The first analysis to use this approach for  $B \rightarrow D l \nu_\ell$  decays has been Ref. [45]. In this paper, a BGL analysis is carried out using lattice-QCD data at that time, but a different parametrisation (or a BGL with a different truncation order)

and new lattice data could be employed to fit the provided spectrum and extract the form factor  $f_+(w)$  along with  $|V_{cb}|$ .

A main challenge associated with model-independent variables, such as the  $w$  spectrum, is *unfolding*. This technique consists in correcting for the distortions introduced by the measurement resolution and selection inefficiency, allowing to reconstruct the true physical distributions from the observed experimental data, to enable direct phenomenological analyses. Unfolding is based on an accurate simulation of the experimental apparatus and techniques. By comparing the observed distributions with simulated models reproducing experimental data, one can quantify the distortions introduced by the detector resolution and selection efficiency, and apply corrections using dedicated algorithms. These algorithms, which may include matrix inversion techniques [81], aim to reverse the the experimental effects to recover the underlying true distributions. Once the data is corrected, physical parameters can be extracted.

Measurement resolution is not trivial in semileptonic  $B$  decays, as the undetected neutrino in the final state prevents fully reconstructing the decay kinematics. At  $e^+e^-$  machines operating at the  $\Upsilon(4S)$ -mass energy, information from the  $\Upsilon(4S) \rightarrow B\bar{B}$  decay is used to recover the missing quadrimomentum of the neutrino. The full decay of the  $B$  meson accompanying the  $B$  signal can be reconstructed (so-called *B tagging*), *i.e.*, by using hadronic  $B$  decays [82]. The neutrino reconstruction is accurate in this case, providing good resolution on the measurement of the signal kinematics variables. However, this approach features low efficiency (generally smaller than 1%) and requires large data sets for obtaining impactful measurements. In addition, the efficiency of  $B$ -tagging algorithms must be calibrated on data, and the associated uncertainty is usually too large for a precision measurement such that of  $|V_{cb}|$ .

*Untagged* analyses, instead, approximate the kinematics of the signal decay by using the information of the rest of the event in an inclusive way, *i.e.*, estimating the other  $B$  momentum by the sum of the other visible particles in the event other than those of the signal. Other constraints can be imposed, *i.e.*, from the angular distribution of the  $B$  mesons produced in  $\Upsilon(4S)$  decays [83]. Untagged methods are very efficient, although they provide lower resolution on the measurement of the signal kinematics. In this case, the analysis must rely on a good description of the rest-of-event particles to properly compute resolutions through the migration matrices used to unfold experimental effects from the data.

Differential decay rates can be provided as one-dimensional or multidimensional distributions. One-dimensional distributions are simpler to obtain but may miss important correlations between different kinematic variables, diluting the information on the decay dynamic. In contrast, multi-dimensional distributions allows for a more comprehensive analysis. This is particular important for  $B \rightarrow D^*\ell\nu_\ell$  decays. However, binning in more dimensions requires, again, large data sets, and it has not been attempted yet. The first analysis reporting model-independent observables for  $B \rightarrow D^*\ell\nu_\ell$  is that in Ref. [84] from 2017, which was updated in 2019 [56]. In this analysis, Belle obtains one-dimensional distributions of  $w$  and the helicity angles  $\theta_\ell$ ,  $\theta_D$ , and  $\chi$ . This is also done in a refined analysis from Belle using  $B$  tagging in Ref. [85] (see Fig. 2.5). Despite the approximation of marginalising the four-dimensional decay rate, the four independent one-dimensional distributions enable reanalysis of the data *a posteriori* assuming a different form-factor model for describing the differential decay rate compared to that used by Belle.

A different approach to provide model-independent observables that encodes the full four-dimensional information has been also pursued very recently [85]. In this approach, angular coefficients of the decay rate as functions of  $w$  are measured: from those coefficients

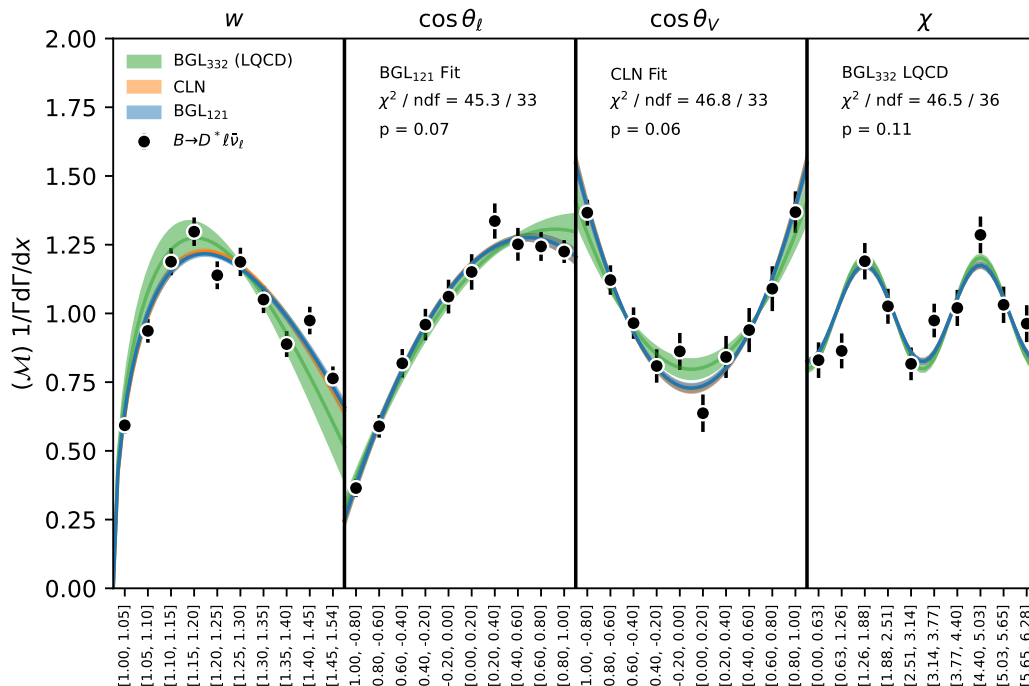


Figure 2.5: Unfolded distributions of  $w$ ,  $\cos\theta_\ell$ ,  $\cos\theta_D$  and  $\chi$  from Ref. [85]. Black points are the measured data, which are fitted with both BGL (blue) and CLN (orange) parametrisations.

the full four-dimensional decay rate can be recovered. This type of analysis requires large data samples though, as  $B$ -tagging is used to achieve best resolution for unfolding the data to measure the coefficients.

My work explores yet another method to access the information on the differential decay rates, for both  $B \rightarrow D\ell\nu_\ell$  and  $B \rightarrow D^*\ell\nu_\ell$  decays, through the definition of other model-independent observables presented in Sect. 2.5, which are conceptually similar to the  $w$  spectrum for  $B \rightarrow D\ell\nu_\ell$  and to the angular coefficients for  $B \rightarrow D^*\ell\nu_\ell$ . Before addressing these new observables, I provide an overview of the current theoretical challenges on the form factors, focusing on lattice QCD.

### 2.4.1 Challenges in lattice calculations

Theoretical challenges involve calculating the hadronic matrix element governed by the dynamics of strong interactions between quarks at low energies (see Sect. 2.1). This is where lattice QCD [86] becomes essential, offering a first-principles approach to calculating these matrix elements. Nonetheless, lattice-QCD calculations themselves carry uncertainties. These stem from discretisation errors due to the finite lattice spacing, statistical noise from the Monte Carlo simulations, and systematic errors in the tuning of quark masses. These uncertainties are particularly significant at large recoil, where lattice results for  $B \rightarrow D^{(*)}\ell\nu_\ell$  decays become less precise.

In recent years, there has been significant progress on lattice-QCD calculations of the form factors for both  $B \rightarrow D\ell\nu_\ell$  and  $B \rightarrow D^*\ell\nu_\ell$  decays. The calculations for the  $B \rightarrow D\ell\nu_\ell$  decays are now fairly established, with different collaborations providing consistent results for the form factors over a range of  $q^2$  [63]. Those calculations, along with the experimental

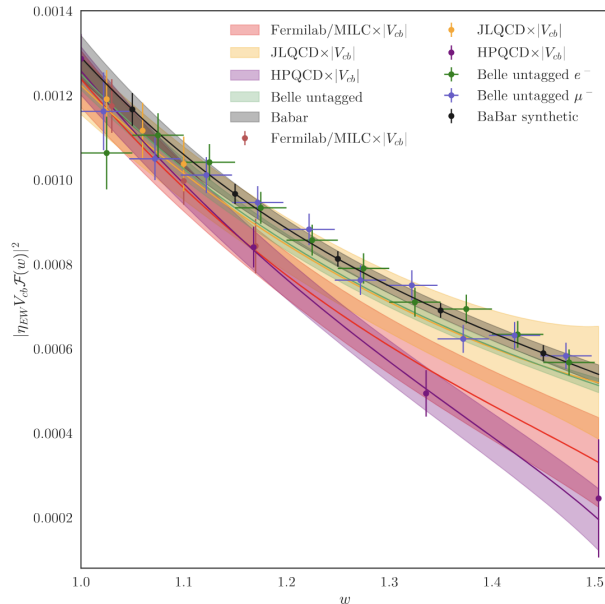


Figure 2.6: Comparison of recent lattice calculations of  $B \rightarrow D^* \ell \nu_\ell$  form factors with experiments (figure from Ref. [87]). The differential decay rate without some kinematical factors,  $|\eta_{EW} V_{cb} \mathcal{F}(w)|^2$ , is plotted as a function of the recoil parameter  $w$ . The orange, magenta and red bands show results from JLQCD [31], HPQCD [32] and Fermilab/MILC [33], respectively, whereas experimental data from Belle (BaBar) are plotted by the green (grey) band.

data, have allowed for a solid extraction of  $|V_{cb}|$  from  $B \rightarrow D \ell \nu_\ell$  decays.

For  $B \rightarrow D^* \ell \nu_\ell$ , the situation is more fluid. The leading form-factor is calculated precisely at  $q_{\max}^2$  [63]; however, due to the additional complexity of this channel, calculations over a range of  $q^2$  have lagged behind those for  $B \rightarrow D \ell \nu_\ell$ . The gap has been recently filled, with results now available from three collaborations, JLQCD, HPQCD and Fermilab/MILC [31–33].

Some of these results are puzzling though, yielding form factors that have different shapes for the three calculations, which differ also with respect to those extracted from experimental data. This is represented in Fig. 2.6, which shows a function of  $w$  proportional to the  $B \rightarrow D^* \ell \nu_\ell$  differential decay rate, comparing recent lattice calculations with results from experimental data. Data from Fermilab/MILC shows a steeper slope than that observed in experimental data from Belle and BaBar; HPQCD calculations indicate an even steeper slope, creating tension with data on the calculated longitudinally-polarised fraction. In contrast, results from JLQCD demonstrate good consistency with experimental findings. Specific combinations of form-factors enhance some of these differences, as reported in Ref. [88]. The source of these tensions is not yet clarified. As experimental precision improves, the differences between lattice results and data have become more evident, underscoring the need for refined methods on both the theoretical and experimental fronts to achieve a more consistent description.

## 2.5 A novel approach: model-independent observables for a global analysis

In this thesis, to address some of the experimental challenges presented in the previous chapter, I present model-independent observables for both  $B \rightarrow D\ell\nu_\ell$  and  $B \rightarrow D^*\ell\nu_\ell$  decays, which enable an *a posteriori* determination of  $|V_{cb}|$  using any form-factor model and lattice-QCD inputs. The approach combines the benefits of unfolded distributions—without the approximations introduced by one-dimensional projections for  $B \rightarrow D^*\ell\nu_\ell$  decays—and the angular coefficients of  $B \rightarrow D^*\ell\nu_\ell$  decays, while avoiding  $B$ -tagging to enhance efficiency. The analysis targets both decays simultaneously, reconstructing them together from Belle II data, to leverage correlations that offer a more comprehensive understanding of the underlying dynamics and reduce uncertainties in extracting  $|V_{cb}|$ . To this extend, in  $B \rightarrow D^*\ell\nu_\ell$ , the  $D^*$  decay is partially reconstructed from  $D\ell$  candidates.

For  $B \rightarrow D^*\ell\nu_\ell$  decays, the idea is to measure a combination of the helicity amplitudes  $H_i(w)$ . Since the  $D^*$  decay is partially reconstructed, I can only access the two-dimensional decay rate

$$\frac{d^2\Gamma}{dw d\cos\theta_\ell} = \frac{1}{2}\Gamma_0(w)|V_{cb}|^2\{a(w) + b(w)\cos\theta_\ell + c(w)\cos^2\theta_\ell\}, \quad (2.26)$$

where

$$a(w) = H_+^2(w) + H_-^2(w) + 2H_0^2(w), \quad (2.27)$$

$$b(w) = 2[H_-^2(w) - H_+^2(w)], \quad (2.28)$$

$$c(w) = H_+^2(w) + H_-^2(w) - 2H_0^2(w). \quad (2.29)$$

and  $\Gamma_0(w) = \eta_{\text{EW}}^2 m_B m_{D^*}^2 G_F^2 \sqrt{w^2 - 1}(1 - 2rw + r^2)/(4\pi)^3$ .

A measurement of the coefficients  $a(w)$ ,  $b(w)$  and  $c(w)$  yields the three helicity amplitudes squared: the form factors  $g(w)$ ,  $f(w)$ , and  $\mathcal{F}_1(w)$  can be measured through Eqs. 2.9–2.11.<sup>4</sup> Considering  $N$  bins of  $w$ , I define  $3N$  model-independent observables:

$$a'_n = |V_{cb}|^2 a'_n \equiv |V_{cb}|^2 a(\bar{w}_n), \quad (2.30)$$

$$b'_n = |V_{cb}|^2 b'_n \equiv |V_{cb}|^2 b(\bar{w}_n), \quad (2.31)$$

$$c'_n = |V_{cb}|^2 c'_n \equiv |V_{cb}|^2 c(\bar{w}_n), \quad (2.32)$$

where  $\bar{w}_i$  is the average value of  $w$  in the bin  $n$ , with  $n = 1, \dots, N$ .

Similarly, for the  $B \rightarrow D\ell\nu_\ell$  decay the idea is to measure the form factor  $\mathcal{G}(w)$ . In this case, the one-dimensional decay rate reads

$$\frac{d\Gamma}{dw} = \Gamma'_0(w)|V_{cb}|^2|\mathcal{G}(w)|^2, \quad (2.33)$$

where  $\Gamma'_0(w) = G_F^2 \eta_{\text{EW}}^2 m_D^3 (m_B + m_D)^2 (w^2 - 1)^{3/2}/(4\pi)^3$ . I define the  $M$  model-independent observables as

$$G'_m = |V_{cb}| G_m \equiv |V_{cb}| \mathcal{G}(\bar{w}_m), \quad (2.34)$$

<sup>4</sup>Note that the helicity amplitudes can be determined from the angular coefficients  $a(w)$ ,  $b(w)$ , and  $c(w)$ , up to an ambiguity in their signs, resulting in multiple solutions for the helicity form factors. Based on previous experimental and theoretical information, I can resolve the ambiguity and choose all positive helicity amplitudes to obtain the form factors. This choice will be implemented in the fit to the measured model-independent observables explained in Chapter 8 to extract  $|V_{cb}|$ .

for the bin  $m = 1, \dots, M$ .

I target a measurement of the model-independent observables  $a'_n, b'_n, c'_n$  and  $G'_m$  from a global analysis of  $B \rightarrow D\ell\nu_\ell$  and  $B \rightarrow D^*\ell\nu_\ell$  decays. From these measurements, assuming a form-factor parametrisation and also using lattice-QCD data, I can obtain a novel measurement of  $|V_{cb}|$ , which combines information from both decays accounting for correlations and common systematic uncertainties. This is the first of such an analysis at Belle II.

From the model-independent observables, I can also obtain several key measurements: the branching fractions of  $B \rightarrow D\ell\nu_\ell$  and  $B \rightarrow D^*\ell\nu_\ell$  decays and their ratio, and, for  $B \rightarrow D^*\ell\nu_\ell$  decays, the lepton forward-backward asymmetry ( $A_{\text{FB}}$ ) and the  $D^*$  longitudinal polarisation ( $F_L^{D^*}$ ), both in bins of  $w$ . The latter are derived from the following relations:

$$A_{\text{FB}}(\bar{w}_n) \equiv \frac{\int_0^1 \frac{d^2\Gamma}{dw d\cos\theta_\ell} d\cos\theta_\ell - \int_{-1}^0 \frac{d^2\Gamma}{dw d\cos\theta_\ell} d\cos\theta_\ell}{\int_{-1}^1 \frac{d^2\Gamma}{dw d\cos\theta_\ell} d\cos\theta_\ell} = \frac{3b'_n}{6a'_n + 2c'_n}, \quad (2.35)$$

$$F_L^{D^*}(\bar{w}_n) \equiv \frac{H_0^2(w)}{H_0^2(w) + H_+^2(w) + H_-^2(w)} = \frac{a'_n - c'_n}{3a'_n + c'_n}. \quad (2.36)$$

The asymmetry  $A_{\text{FB}}$  gives the difference in the probability that the lepton  $\ell$  is emitted in the direction of the  $D^*$  meson (forward) versus the opposite direction (backward) in the  $B$  rest frame. The polarisation fraction  $F_L^{D^*}$  gives the probability that the  $D^*$  meson is emitted with the spin aligned with its momentum, in the  $B$  rest frame. Branching fractions,  $A_{\text{FB}}$  and  $F_L^{D^*}$  values can also be measured separately for the electron and muons decays. Their comparison enables tests of the universality of the weak coupling for light charged leptons, and accidental SM symmetry that could be violated in several new-physics models [89, 90].

### 2.5.1 Analysis overview

Current measurements of  $|V_{cb}|$  are dominated by systematic uncertainties, and the analysis presented in this thesis is no exception. However, there are original aspects considered in this work to suppress important sources of systematic uncertainties. Experimentally, a simultaneous analysis of  $B \rightarrow D\ell\nu_\ell$  and  $B \rightarrow D^*\ell\nu_\ell$  decays is complementary to separate analyses of each decay, offering several advantages.

The partial reconstruction of the  $D^*$  decay eliminates a major systematic uncertainty affecting the measurement of  $|V_{cb}|$  from  $B \rightarrow D^*\ell\nu_\ell$  decays: the uncertainty associated with the slow-pion reconstruction efficiency in  $D^* \rightarrow D\pi_{\text{slow}}$ . At Belle II, this contributes a 1.5% uncertainty on  $|V_{cb}|$  [91]. In addition, partial  $D^*$  reconstruction allows access to the decay rate at values closer to  $w = 1$ ; however, the analysis becomes more sensitive to background modelling in this kinematic region. A dangerous background is given by feed-down from semileptonic decays with excited charm states whose rates are still poorly known. I conduct a detailed study to constrain with data the modelling of this background. Specifically, I identify a control region enriched of these decays that I analyse simultaneously with the signal sample (see Sect. 5.4).

Another dominant uncertainty on  $|V_{cb}|$  determinations is cancelled in the global analysis: that from  $f_{+-}/f_{00}$ , the ratio of the branching fractions of  $\Upsilon(4S)$  decays into charged and neutral  $B$ -meson pairs. At Belle II, this contributes a systematic uncertainty of about 1.3% on  $|V_{cb}|$  [91]. By assuming isospin symmetry, I can also measure  $f_{+-}/f_{00}$  directly from my analysis, both eliminating a significant source of systematic uncertainty on  $|V_{cb}|$  and potentially improving the current knowledge of  $f_{+-}/f_{00}$ . The Belle determination of this ratio, which properly accounts for the isospin-breaking effect between  $B^+$  and  $B^0$ ,

uses  $B \rightarrow J/\psi K$  decays and is affected by approximately 5% theoretical uncertainty due to the isospin assumption for these decays [67]. For semileptonic decays, isospin breaking should contribute a smaller uncertainty, offering a more precise way to measure  $f_{+-}/f_{00}$ . The improvement of the precision on  $f_{+-}/f_{00}$  has a pivotal importance in Belle II, as its uncertainty affects all measurements of  $B$ -decay branching fractions.

The global analysis is performed using the Run I data set collected by Belle II, which comprises about 387 million  $B\bar{B}$  pairs. The data are selected through requirements optimised on simulation to favour purity over signal significance, as to limit the impact of uncertainties associated with the background modelling. Simulation is corrected for known discrepancies with data, such as those related to particle-identification and tracking efficiencies.

Instead of attempting a reconstruction of kinematic variables such as  $w$  and  $\cos\theta_\ell$ , I use *proxy variables*, fully reconstructed from the visible particles of the signal final state, that preserve information on the decay dynamics and give access to the model-independent observables. The core of the analysis is a least-square fit to the three-dimensional distribution of the proxy variables, using histograms obtained from simulation (templates) to model the data. The dependence of signal templates on the model-independent observables is implemented through a weighting technique that enables to obtain templates independently from the model used in the simulation (see Chapter 6).

The analysis, while fully completed on simulation and control data, is not yet applied to the signal sample, because it is still under Belle II internal review. The full analysis will be applied to the real data data after carefully defining an *unblinding* procedure. Nevertheless this thesis fully demonstrates the potential of the novel method proposed.



## Chapter 3

# The Belle II experiment at the SuperKEKB collider

*The data used in this work are collected by the Belle II experiment operating at the SuperKEKB collider. This chapter outlines SuperKEKB and the Belle II detector. In addition, in the second part of this chapter, I report a service work for the Collaboration that I carried out during the first year of my Ph.D. course: the measurement of the detection asymmetries of kaons and pions, which provides important inputs for high-precision measurements of CP-violating asymmetries at Belle II.*

### 3.1 The SuperKEKB collider

SuperKEKB is an electron-positron ( $e^+e^-$ ) energy-asymmetric collider, designed to produce more than 600  $B\bar{B}$  pairs per second via decays of  $\Upsilon(4S)$  mesons produced at threshold [92] ( $B^0\bar{B}^0$  and  $B^+B^-$  in approximately equal proportions). Such colliders are called ‘ $B$ -factories’, and were proposed in the 1990s for the dedicated exploration of  $CP$ -violation in  $B$  mesons. The main goal of  $B$ -factories is to produce low-background quantum-correlated  $B\bar{B}$  pairs at high rates.

Intense beams of electrons and positrons are brought to collision at the energy corresponding to the  $\Upsilon(4S)$  meson mass, 10.58 GeV, which is just above the  $B\bar{B}$  production kinematic threshold. The great majority of collisions yield electroweak processes ( $e^+e^- \rightarrow e^+e^-$ ,  $e^+e^- \rightarrow \gamma\gamma$ , etc.) that are scarcely interesting and straightforwardly discarded using global event quantities (see Fig. 3.1). More interesting for flavour physics are the collisions that produce hadrons (hadronic events). In these, the finely tuned collision energy is key. The production of  $\Upsilon(4S)$  mesons, which decay in  $B\bar{B}$  pairs more than 96% of the time with little available energy to produce additional particles, suppresses backgrounds from competing nonresonant hadron production. In addition, colliding beams of point-like particles allow for knowing precisely the collision energy, which sets stringent constraints on the collision’s kinematic properties, thus offering means of further background suppression. Since bottom mesons are produced in a strong-interaction decay, flavour is conserved, and the null net bottom content of the initial state implies production of a flavourless  $B\bar{B}$  pair. Even though  $B^0$  and  $\bar{B}^0$  undergo flavour oscillations before decaying, their time-evolution is quantum-correlated in such a way that no  $B^0B^0$  or  $\bar{B}^0\bar{B}^0$  pairs are present at any time. Angular-momentum conservation implies that the decay of a spin-1 particle in two spin-0 particles yields total angular momentum  $J = 1$ . Because the simultaneous presence of two identical particles in an antisymmetric state would violate Bose

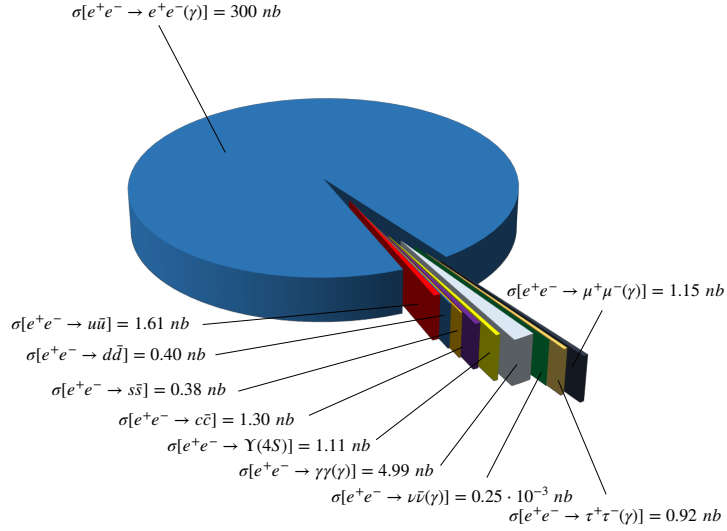


Figure 3.1: Cross sections of the main final states produced in  $e^+e^-$  collision at the  $\Upsilon(4S)$  centre-of-mass energy.

statistics, the system evolves coherently as an oscillating  $B^0\bar{B}^0$  particle-antiparticle pair until either one decays. This allows identification of the bottom (or antibottom) content of one meson at the time of decay of the other, if the latter decays in a final state accessible only by either bottom or antibottom states. This important capability is called ‘flavour tagging’ and allows measurements of flavour-dependent decay rates, as needed in many determinations of  $CP$ -violating quantities.

Figure 3.2 shows the hadron-production cross-section in  $e^+e^-$  collisions as functions of the final-state mass.

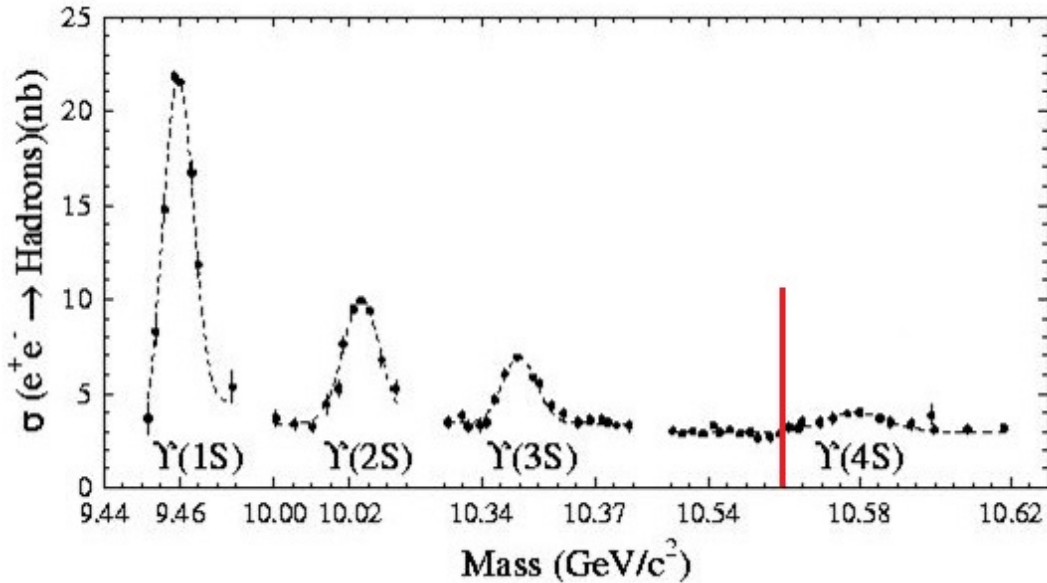


Figure 3.2: Hadron production cross section from  $e^+e^-$  collisions as a function of the final-state mass. The vertical red line indicates the  $B\bar{B}$  production threshold.

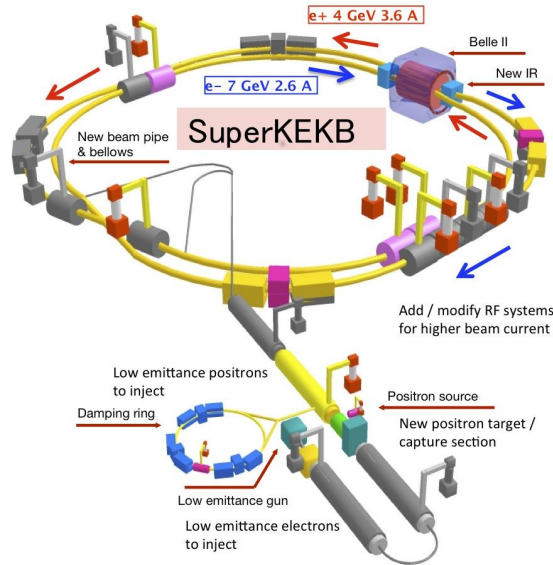


Figure 3.3: Illustration of the SuperKEKB collider.

The various peaks are radial excitations of the  $\Upsilon$  meson overlapping the nearly uniform background at about 4 nb which represents the so-called continuum of lighter-quark pair-production,  $e^+e^- \rightarrow q\bar{q}$ , where  $q$  identifies a  $u$ ,  $d$ ,  $c$ , or  $s$  quark.

Because the  $\Upsilon(4S)$  mesons are produced at threshold, they would be nearly at rest in the laboratory frame in an energy-symmetric collider. The resulting  $B$  mesons too would be produced with low momentum ( $\approx 10 \text{ MeV}/c$ ) in the laboratory, because of the  $21 \text{ MeV}/c^2$  difference between the  $\Upsilon(4S)$  mass and the  $B\bar{B}$  pair mass. With such low momenta they would only travel approximately  $1 \mu\text{m}$  before decaying rendering the  $10 \mu\text{m}$  typical spatial resolution of vertex detectors insufficient to separate  $B$ -decay vertices and enable the study of the decay-time evolution. Asymmetric beam energies are used to circumvent this limitation. By boosting the collision centre-of-mass along the beam in the laboratory frame, they achieve  $B$ -decay vertex separations resolvable with current vertex detectors [93]. SuperKEKB (Fig. 3.3) implements a 7-on-4 GeV energy-asymmetric double-ring design, which achieves a vertex displacement of about  $130 \mu\text{m}$ .

Electrons are produced in a thermionic gun with a barium-impregnated tungsten cathode, then accelerated to 7 GeV with a linear accelerator (linac) and injected in the high-energy ring (HER). Positrons are produced by colliding electrons on a tungsten target, then isolated by a magnetic field, accelerated to 4 GeV with the linac and injected in the low-energy ring (LER).

The electrons and positrons continuously collide at a single interaction point, around which the Belle II detector is installed. To achieve high luminosities, a nano-beam, large crossing-angle collision scheme is implemented [94]. This is an innovative configuration based on keeping small horizontal and vertical emittance and large crossing angle, as shown in Figure 3.4. This is obtained with a final-focus superconducting-quadrupole-magnet system (QCS), made of magnets, corrector coils, and compensation solenoids; a QCS magnet is installed at each longitudinal end of the interaction region. Conceptually the nano-beam scheme mimics a collision with many short micro-bunches, allowing great advantages in luminosity with respect to previous standard schemes. The reduction of the luminous volume size to about 5% with respect to the predecessor KEKB, combined with doubling of

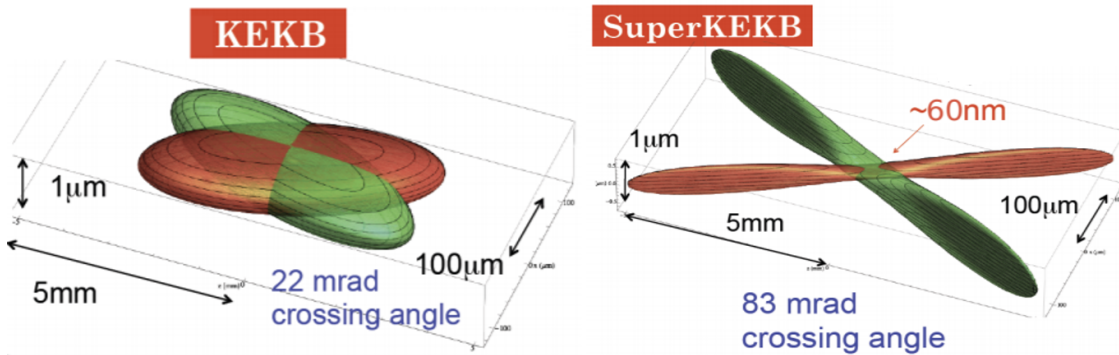


Figure 3.4: Two-dimensional sketch of the nano-beam mechanism implemented in SuperKEKB (right) compared with the previous KEKB collision scheme (left).

beam currents, is expected to yield a factor 40 gain in intensity.

The performance of the SuperKEKB collider is characterised in terms of the luminosity  $\mathcal{L}$ , which is a measure of collision intensity. The rate of any given process

$$\text{rate [events s}^{-1}] = \mathcal{L} [\text{cm}^{-2} \text{s}^{-1}] \times \sigma [\text{cm}^2],$$

is the product of its cross-section,  $\sigma$ , and the instantaneous luminosity  $\mathcal{L}$ ,

$$\mathcal{L} = \frac{\gamma_{\pm}}{2er_e} \left(1 + \frac{\sigma_y^*}{\sigma_x^*}\right) \frac{I_{\pm}\xi_{y\pm}}{\beta_{y\pm}^*} \cdot \frac{R_{\mathcal{L}}}{R_{\xi_y}},$$

where  $\gamma$  is the relativistic Lorentz factor,  $e$  is the absolute value of the electron charge,  $r_e$  is the classical radius of electron,  $\sigma_x^*$  and  $\sigma_y^*$  are the widths of the bunch at the interaction point (IP) on the plane orthogonal to the beam direction (transverse plane),  $I$  is the current of the beam,  $\beta_y^*$  is the vertical betatron function at the IP,  $\xi_y$  is the vertical beam-beam parameter,  $R_{\mathcal{L}}$  and  $R_{\xi_y}$  are the reduction factors of luminosity and the vertical beam-beam parameter due to non-vanishing crossing angle. The ratio of these reduction factors is close to unity, while the design values for the other parameters are reported in Tab. 3.1.

The integral of instantaneous luminosity over time  $T$ , called integrated luminosity,

$$\mathcal{L}_{int} = \int_0^T \mathcal{L}(t') dt'$$

is a direct measure of the number of produced events of interest  $N = \mathcal{L}_{int} \times \sigma$ .

	Design	Achieved
Energy [GeV]	4.0/7.0	4.0/7.0
$\xi_y$	0.090/0.088	0.0407/0.0279
$\beta_y^*$ [mm]	0.27/0.41	1.0/1.0
$I$ [A]	3.6/2.62	1.321/1.099

Table 3.1: Design and achieved values for SuperKEKB fundamental parameters (LER/HER).

Physics data-taking started in March 2019, and Belle II to date has integrated  $567 \text{ fb}^{-1}$  of luminosity. In 2022, SuperKEKB also broke the instantaneous-luminosity world record,

achieving  $4.7 \times 10^{34} \text{ cm}^{-2}\text{s}^{-1}$ . In spite of these achievements, a number of technological and scientific challenges have significantly reduced SuperKEKB performance compared to design. A number of issues associated with beam injection, collimation, and the capability to reduce the transverse dimensions of the beam without generating uncontrollable beam backgrounds limited the capability to deliver the expected samples of data in its first five years. Consolidation, improvement and development work have been made to overcome these difficulties.

## 3.2 The Belle II detector

Belle II (Fig. 3.6) is a large-solid-angle, multipurpose magnetic spectrometer surrounded by a calorimeter and particle-identification systems, installed around the SuperKEKB interaction point. It is designed to determine energy, momentum, and identity of a broad range of particles produced in 10.58 GeV  $e^+e^-$  collisions. Belle II is approximately a cylinder of about 7 m in length and 7 m in diameter. It employs a right-handed Cartesian coordinate system with origin in the interaction point. The  $z$  axis corresponds to the principal axis of the solenoid, which is approximately parallel to the electron beam direction at the interaction point; the  $y$  axis points vertically upward, and the  $x$  axis is horizontal and pointing outward of the accelerator tunnel. The polar angle,  $\theta$ , is referred to the positive  $z$  axis. The azimuthal angle,  $\phi$ , is referred to the positive  $x$  axis in the  $xy$  plane. The radius,  $r = \sqrt{x^2 + y^2}$ , is defined in cylindrical coordinates and measured from the origin in the  $xy$  plane. Throughout this thesis, *longitudinal* means parallel to the electron beam direction (to the  $z$  axis), and *transverse* means perpendicular to the electron beam direction, *i.e.*, in the  $xy$  plane.

Belle II comprises several subsystems, each dedicated to a specific aspect of event reconstruction. From the interaction point outward, a particle would traverse the beam pipe, a two-layer silicon-pixel vertex-detector (PXD), a four-layer silicon-strip vertex-detector (SVD), a central wire drift-chamber (CDC), a time-of-propagation central Cherenkov counter (TOP) or an aerogel threshold forward Cherenkov counter (ARICH), an array of CsI(Tl) crystals (ECL), a superconducting solenoidal magnet, and multiple layers of resistive plate counters (KLM).

The principal experimental strengths are hermetic coverage, which allows for reconstruction of final states involving neutrinos; efficient and precise reconstruction of charged-particle trajectories (tracks), which provide accurately reconstructed decay-vertices and good momentum resolution; high-purity charged-particle identification and neutral-particle reconstruction. A summary of the technological specifications of the Belle II subsystems is in Tab. 3.2. A detailed description of Belle II and its performance is given in Ref. [95].

In June 2022, both SuperKEKB and Belle II ended operations to enter a long shutdown period (LS1). During LS1, the PXD detector was extracted and replaced with a new PXD that has a complete outer layer of pixels. At the same time the TOP photomultipliers were upgraded. Other minor updates, regarding both the detector and the collider, were performed. In the recent Run II, the PXD was turned off to prevent further damages until more stable data-taking conditions are reached. Run II will go on collecting data until a second long shutdown (LS2), expected in 2027. The complete data sample available today corresponds to an integrated luminosity of  $567 \text{ fb}^{-1}$ , combining both Run I ( $428 \text{ fb}^{-1}$ ) and the initial period of Run II ( $139 \text{ fb}^{-1}$ ), from March to December 2024. This corresponds to a data set that lies between the one collected by the BaBar experiment during its lifetime (9 years) and the one collected by the Belle experiment over approximately 11 years. Of the total Belle II sample, about 85% has been collected at the  $\Upsilon(4S)$  resonance, while the

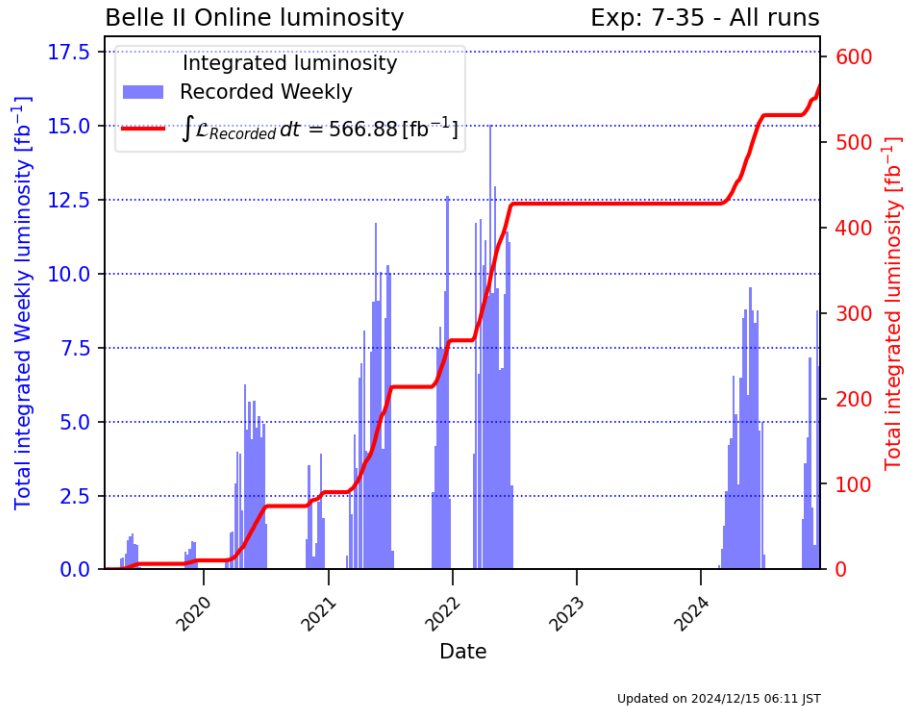


Figure 3.5: Weekly (blue histogram) and total (red line) integrated luminosity recorded using the Belle II detector during 2019-2022 operations of Run I and Run II after the long shutdown [97].

rest with collision energy below or above the  $\Upsilon(4S)$ . The total integrated luminosity as a function of time from January 2019 to June 2024 is shown in Fig. 3.5. To achieve the goal of collecting  $50 \text{ ab}^{-1}$ , SuperKEKB needs to be upgraded during the LS2 in order to reach a peak luminosity of  $\sim 6.5 \times 10^{35} \text{ cm}^{-2} \text{ s}^{-1}$ . An international task force has been formed to provide advice to SuperKEKB on the possible upgrade options, which include a redesign of the interaction region and of the final focusing system. LS2 provides the possibility to upgrade parts of the Belle II detector as well. A new vertex detector might be required to accommodate the new interaction-region design, and other sub-detectors might require improved robustness against increasing machine background [96].

In the following, I focus on the reconstruction and identification of stable particles, which are more relevant for the analysis reported in this thesis.



Purpose	Acronym	Technology	Configuration	Channels	Polar coverage ( $\theta$ )
Beam pipe		Beryllium	Cylindrical, inner radius 10 mm, 10 $\mu\text{m}$ Au, 0.6 mm Be, 1 mm paraffin, 0.4 mm Be		
Tracking	PXD	Silicon pixel	Sensor size: $15 \times (L1\ 136, L2\ 170)$ mm <sup>2</sup> , Pixel size: $50 \times (L1a\ 50, L1b\ 60, L2a\ 75, L2b\ 85)$ $\mu\text{m}^2$ ; two layers at radii: 14, 22 mm	$10^6$	[17°;150°]
	SVD	Silicon strip	Rectangular and trapezoidal, strip pitch: $50(p)/160(n)$ - $75(p)/240(n)$ $\mu\text{m}$ , with one floating intermediate strip; four layers at radii: 38, 80, 115, 140 mm	$2.45 \times 10^5$	[17°;150°]
	CDC	Drift chamber with He-C <sub>2</sub> H <sub>6</sub> gas	14336 wires in 56 layers, inner radius of 160mm outer radius of 1130 mm	$1.4 \times 10^5$	[17°;150°]
	Solenoid	Solenoid coil	Length: 4.41 m. Radius: 1.80 m		
Particle ID	TOP	RICH with quartz radiator	16 segments in $\phi$ at $r \approx 120$ cm, 275 cm long, 2cm thick quartz bars with $4 \times 4$ channel MCP PMTs	$8 \times 10^3$	[31°;128°]
	ARICH	RICH with aerogel radiator	$2 \times 2$ cm thick focusing radiators with different $n$ , HAPD photodetectors	$7.8 \times 10^4$	[14°;30°]
Calorimetry	ECL	CsI(Tl) crystals	Barrel: $r = 125 - 162$ cm, end-cap: $z = -102 - +196$ cm	6624 (Barrel), 1152 (FWD), 960 (BWD)	[12.4°;31.4°], [32.2°;128.7°], [130.7°;155.1°]
Muon ID	KLM	Barrel: RPCs and scintillator strips	2 layers with scintillator strips and 12 layers with 2 RPCs	$\theta\ 1.6 \times 10^4, \phi\ 1.6 \times 10^4$	[40°;129°]
	KLM	End-cap: scintillator strips	12 layers of $(7-10) \times 40$ mm <sup>2</sup> strips	$1.7 \times 10^4$	[25°;40°], [129°;155°]

Table 3.2: Summary of the Belle II subdetectors and their specifications.

### 3.2.1 Tracking system

At Belle II, reconstruction of charged particles and ensuing measurement of their momenta and charges is achieved through an integrated system consisting of six layers of silicon and a drift chamber, surrounding the beam pipe and immersed in a 1.5 T axial magnetic field maintained in a cylindrical volume 3.4 m in diameter and 4.4 m in length. The field is oriented along the  $z$  direction and provided by an aluminum-stabilised superconducting solenoid made of NbTi/Cu alloy.

The solenoid surrounds all the subdetectors up to the KLM. The iron yoke of the detector serves as the return path of the magnetic flux. The beam pipe is a 3 km-long vacuum enclosure to allow beams circulating inside the detector. In the following, I refer only to the straight section of the beam pipe surrounding the interaction point. Multiple Coulomb scattering in the beam-pipe wall of the final-state charged particles would spoil the vertex-position resolution; this dictates a thin beam-pipe wall made of a low- $Z$  material. Moreover, since the vertex resolution is inversely proportional to the distance between the interaction point and the first track sampling, the beam pipe has to be narrow. The possibility for beam-halo to interact with the beam pipe, thus inducing beam backgrounds, and heating of the pipe wall due to charge induction complicates the design. Hence, the beam pipe is constantly cooled and shielded from the vertex detector. The Belle II beam pipe is made of two beryllium cylinders, 0.6 mm thick at radius of 10 mm, and 0.4 mm thick at radius of 12 mm, respectively. A 1.0 mm gap between the inner and outer walls of the pipe is filled with paraffin for cooling. The beam pipe is coated with a 10  $\mu\text{m}$  gold sheet that absorbs low-energy photons, which could damage the silicon detector.

#### 3.2.1.1 Silicon-pixel vertexing detector

The innermost detector is a pixel vertex detector (PXD). Its goal is to sample the trajectories of final-state charged particles in the vicinity of the decay position (vertex) of their long lived ancestors, so that the decay point can be inferred by extrapolation inward.

PXD sensors are based on depleted field-effect transistor technology [98]. They are made of p-channel MOSFET integrated on a silicon substrate, which is fully depleted by applying an appropriate voltage. Incident particles generate electron-hole pairs in the depleted region, and thus induce a current passing through the MOSFET. Sensors are 75  $\mu\text{m}$  thick, which allows on-pixel integration of most of the electronics.

The PXD has two layers at 14 mm and 22 mm radius, respectively, and a full length of 174 mm at the radius of the outer layer. It comprises around 8 million pixels,  $50 \times (50 - 55)\mu\text{m}^2$  (inner layer) and  $50 \times (70 - 85)\mu\text{m}^2$  (outer layer) each. The polar acceptance ranges from  $17^\circ$  to  $150^\circ$ . The design impact-parameter resolution is 12  $\mu\text{m}$ , achieved by weighting the charge deposited in neighbouring pixels. To simplify pattern recognition, tracks are first reconstructed in the outer tracking volume, where lower occupancy aids track finding, and extrapolated to the PXD radius, to define regions of interest around their expected intersection points. If a firing pixel is found inside this region, it is kept in the pattern recognition algorithm, otherwise it is discarded. For the data used in this thesis, the full first pixel layer is used, along with 1/6 of the second layer.

#### 3.2.1.2 Silicon-strip vertexing detector

Around the PXD is SVD [99], a silicon detector aimed at reconstructing decay vertices and low-momentum charged-particle tracks at high resolution.

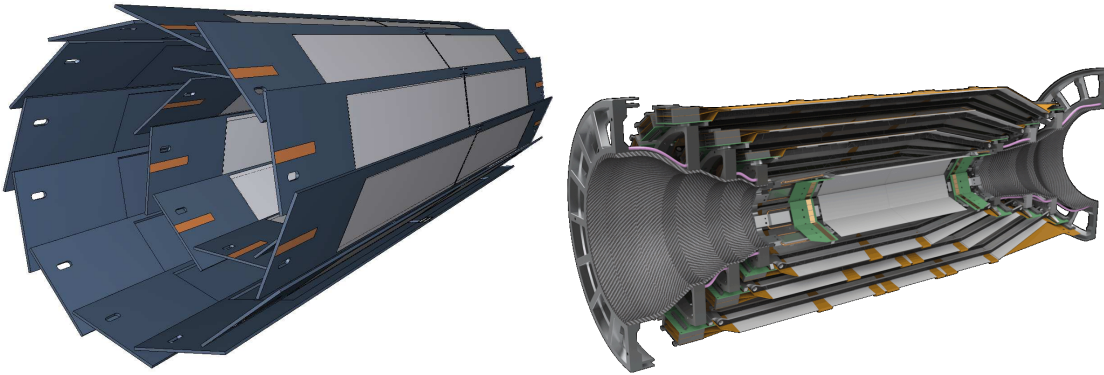


Figure 3.7: (Left) scheme of the PXD detector. (Right) exploded view of a SVD detector half.

SVD uses a double-sided silicon strip technology. Each sensor is made of a silicon n-doped bulk with an highly p-doped implant on one side. A voltage is applied to enhance the depletion region at the p-n junction, and removes intrinsic charge-carriers from the region. Traversing charged particles ionise the silicon, freeing electron-hole pairs that drift due to the electric field, inducing a signal in highly granular strip electrodes implanted at both ends of the depletion region. The fine segmentation of SVD sensors reduces latency, in order to deal with the high rates.

SVD is structured into four concentric layers at radii of 39, 80, 104 and 135 mm, composed by, respectively, 7, 10, 12, and 16 independently-readout modules called ladders, arranged in a cylindrical geometry. As shown in Figure 3.7, SVD has a polar-asymmetric geometry that mirrors the asymmetry in particle density resulting from the centre-of-mass boost. The polar acceptance ranges from  $17^\circ$  to  $150^\circ$ .

Sensors are  $300\ \mu\text{m}$  thick, and the separation between adjacent strips ( $d_{\text{pitch}}$ ) ranges from  $50\ \mu\text{m}$  to  $240\ \mu\text{m}$ . Hence, the spatial resolution  $d_{\text{pitch}}/\sqrt{12}$  varies with the polar angle. Since the charge associated with an incident particle is usually distributed among several strips, position resolution is improved by interpolation.

### 3.2.1.3 Central drift chamber

The CDC [100] is a drift chamber. It samples charged-particle trajectories at large radii, thus providing accurate measurements of momentum and electric charge, trigger signals for events containing charged particles, and information on identification of charged-particle species by measuring their specific-ionisation energy-loss ( $dE/dx$ ).

When a charged particle traverses the CDC volume, it ionises the gas, freeing electrons and positive ions from gas atoms. An applied electric field then moves these charges until they approach the sense wires, where high field gradients cause an abrupt acceleration with secondary ionisations that induce an electric signal whose time is digitised. The particle trajectory is inferred from the time between the collision and the signal.

The CDC inner radius is 16 cm and outer radius is 113 cm. The chamber is composed of 14336  $30\text{-}\mu\text{m}$ -diameter sense wires, divided in 56 layers, immersed in a gaseous mixture of 50% He and 50%  $\text{C}_2\text{H}_6$ , while 42240  $126\text{-}\mu\text{m}$ -diameter aluminum wires shape the electric field. Layers of wires are installed with either “axial” orientation, *i.e.*, aligned with the solenoidal magnetic field, or skewed with respect to the axial wires with a “stereo” orientation. The azimuthal acceptance ranges from  $17^\circ$  to  $180^\circ$ .

The spatial resolution is about  $100\ \mu\text{m}$  and the  $dE/dx$  resolution is 11.9% for an in-

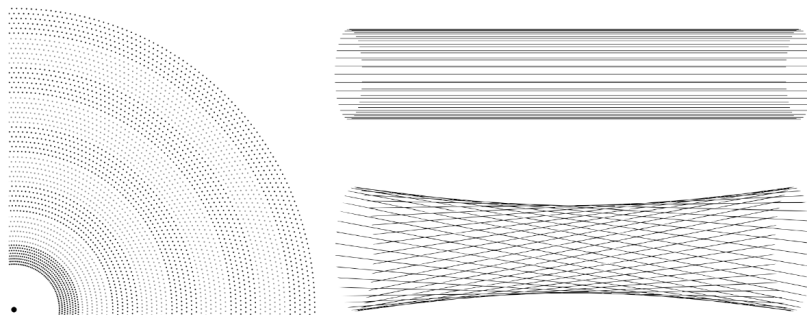


Figure 3.8: A quadrant of a slice of the transverse projection of the drift chamber (left); wire orientation for axial (top right) and stereo (bottom right) layers. The skew is exaggerated for visualization purposes

cident angle of  $90^\circ$ . Figure 3.8 shows a sliced view of the CDC and the possible wires configurations.

### 3.2.2 Electromagnetic calorimeter

The electromagnetic calorimeter (ECL) measures the energy of photons and electrons [101]. High energy photons and electrons entering the calorimeter initiate an electromagnetic shower through bremsstrahlung and electron-positron pair production. The energy is mostly converted to photons, which are collected by the photodiodes. In contrast to hadrons, which pass through the calorimeter with minimal energy loss, most photons and electrons dissipate their entire energy.

The configuration, mechanical structure, and crystals of Belle II ECL are those of the Belle’s calorimeter. The readout electronic boards have been upgraded to cope with SuperKEKB’s higher luminosity. The layout is shown in Fig. 3.9. The ECL consists of three polar compartments: the barrel, the forward endcap, and the backward endcap section. The barrel section is 3.0 m long with 1.25 m of inner radius; the endcaps are located at  $z = +2.0$  m (forward) and  $-1.0$  m (backward) from the interaction point. Tab. 3.3 summarises the geometrical parameters of each section.

Item	$\theta$ coverage	$\theta$ segmentation	$\phi$ segmentation	Number of crystals
Forward endcap	$12.4^\circ$ – $31.4^\circ$	13	48–144	1152
Barrel	$32.2^\circ$ – $128.7^\circ$	46	144	6624
Backward endcap	$130.7^\circ$ – $155.1^\circ$	10	64–144	960

Table 3.3: Summary of ECL parameters.

This requires a segmented calorimeter. The ECL is a highly segmented array of 8736 cesium iodide crystals doped with thallium (CsI(Tl)). Thallium shifts the energy of the excitation light into the visible spectrum. The light is detected by a independent pair of silicon PIN photodiodes [101] and charge-sensitive preamplifiers installed at the outer end of each crystal.

A typical crystal in the barrel section has a  $55 \times 55 \text{ mm}^2$  active surface on the front face and  $65 \times 65 \text{ mm}^2$  on the rear face; the dimensions of the crystals in the endcap sections

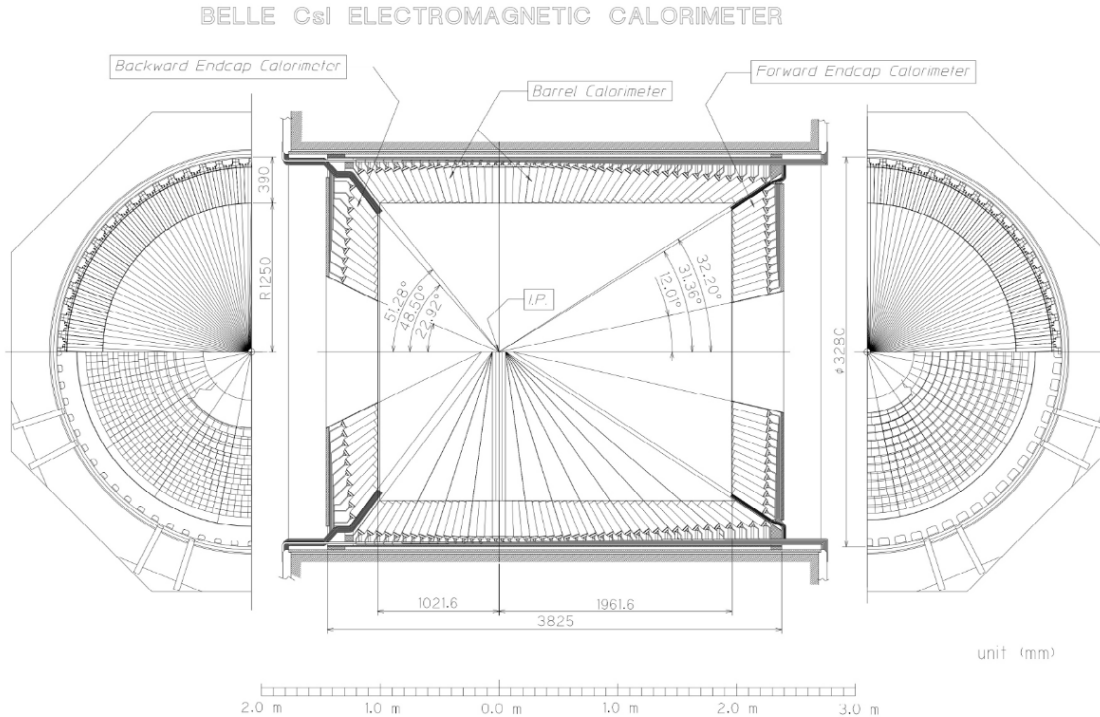


Figure 3.9: ECL layout.

vary from 44.5 to 70.8 mm and from 54 to 82 mm for front and rear faces, respectively. A diagram of an ECL crystal is shown in Fig. 3.10. The 30-cm crystal length, corresponding to  $16.1X_0$ , reduces the fluctuations of shower leakages out of the outermost end of the crystals, which spoils energy resolution. The crystals are designed in such a way that a photon injected at the centre of the crystal would deposit 80% of its energy in the crystal on average. The crystals principal axes do not point exactly to the nominal interaction point, but they are inclined to prevent photons from escaping through gaps between crystals by about  $1.3^\circ$  in the  $\theta$  and  $\phi$  directions in the barrel section, and by about  $1.5^\circ$  and about  $4^\circ$  in the  $\theta$  direction in the forward and backward sections.

Considering the ECL structure—gaps, crystal wrapping, mechanical structure—the fraction of photons that do not leave a detectable signal in the calorimeter is only 0.2%.

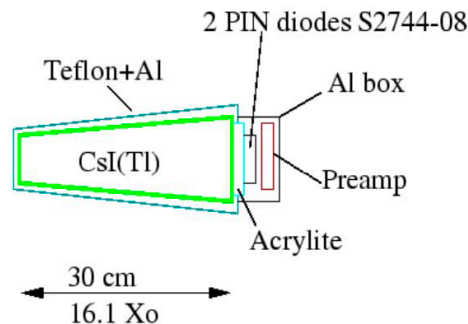


Figure 3.10: Schematic design of a CsI(Tl) crystal with attached readout electronic circuits.

Signals from the photodiodes are sent to two preamplifiers mounted on the rear of the crystal for charge integration.

The two resulting signals are sent to a readout board [101] located outside the Belle II detector. The signal waveforms are analysed using pulse-shape discrimination to improve particle identification, since the signal decay time in CsI(Tl) includes a fast component of around  $0.6 \mu\text{s}$  and a slow component at around  $3.5 \mu\text{s}$ . The fast component is associated with the scintillation response to electromagnetic interactions, while the slow component is associated with the scintillation response to hadronic (*i.e.*, proton or neutron) interactions. This occurs because scintillation in CsI(Tl) for electromagnetic interactions involves the excitation and deexcitation of Tl atoms, while scintillation for hadronic interactions involves the excitation and deexcitation of both Tl and Cs atoms, leading to a longer decay time. The ratio between the intensity of these two decay components varies as a function of the ionising power of the absorbed particle.

The photon emission spectrum peaks at around  $550 \text{ nm}$ , which is convenient for photodiode readout. However, the time for the light in the crystals to decay is relatively long, increasing considerably the overlap of pulses from neighbouring (background) events. This means that scintillation light may be present when a particle from a later event arrives, generating pile-up background.

The ECL also uses Bhabha scattering to measure luminosity. Because the Bhabha cross section is predicted with high accuracy in QED, a precise inference of luminosity is achieved from the measured rate of Bhabha events in a volume of known acceptance.

### 3.2.3 Particle identification

Belle II combines measurements of time-of-propagation, Cherenkov radiation, and ionisation energy loss in the tracker and drift chamber to identify charged particles.

#### 3.2.3.1 Time-of-propagation detector

The time-of-propagation detector (TOP) measures the time of propagation of the Cherenkov photons emitted from charged particles passing through its quartz bars and internally reflected within a radiator [102]. It is made of 16 quartz bars mounted at  $1.2 \text{ m}$  from the IP. Each bar has three main components (Fig. 3.11): a long bar acts as Cherenkov radiator, where photons are generated and propagated; a focusing mirror is mounted at the forward end; and a prism mounted at the backward end collects photons and guides them to a photomultiplier. The polar coverage ranges from  $31^\circ$  to  $128^\circ$ . On average, photons originated from slower particles take more time to reach the photomultipliers, because of the inverse proportionality between  $\beta$  and  $\cos \theta_C$ .

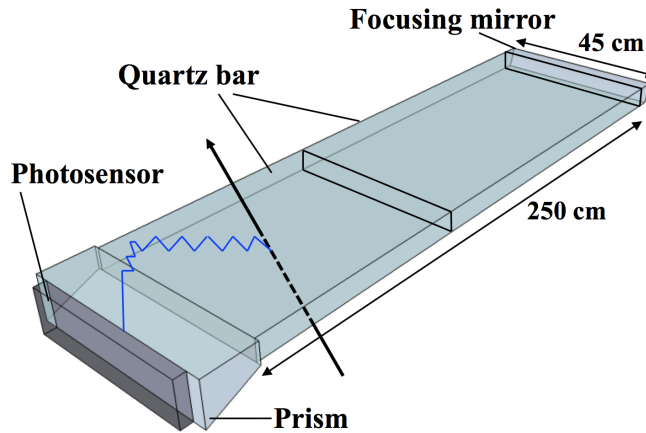


Figure 3.11: Scheme of a TOP bar. A charged particle crossing the radiator and emitting Cherenkov photons, which are collected at the photomultipliers, is also represented.

### 3.2.3.2 Aerogel ring-imaging Cherenkov counter

The aerogel ring-imaging Cherenkov counter detector (ARICH) identifies charged particles by measuring the Cherenkov ring produced when passing through a radiator [103]. It consists of 420 modules for photon detection in seven layers extending from 0.56 to 1.14 m radius, and 248 aerogel tiles installed on the detector end-caps. The aerogel radiator produces Cherenkov photons when traversed by charged particles of a certain momentum range. Next to the radiator is an expansion volume where photons are propagated, to form rings on position-sensitive photodiodes. Photo-cathodes then convert photons into photoelectrons and generate electric signals. Two adjacent radiators with different refraction indexes generate enough photons for achieving sufficient resolution, as shown in Fig. 3.12.

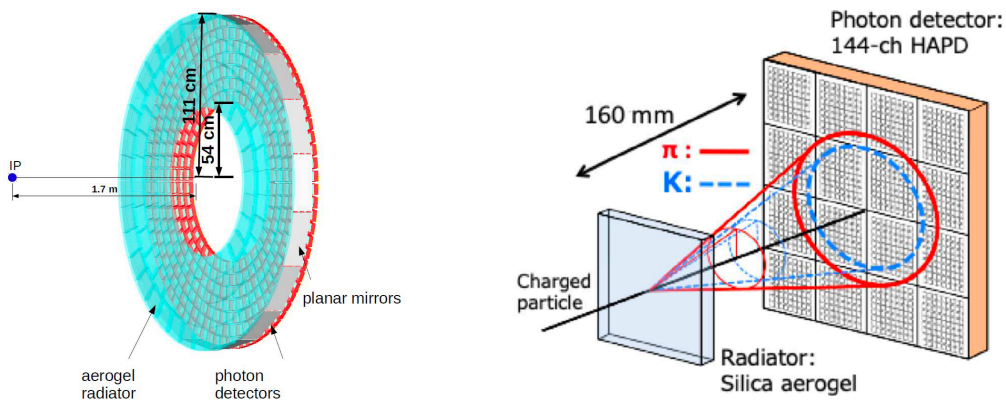


Figure 3.12: Sketch of (left) the ARICH with its main components and (right) diagram of the difference in the photon path for Cherenkov photons from kaons and pions.

### 3.2.3.3 $K_L^0$ and muon detection system

The  $K_L^0$  and muon detection system (KLM) detects muons and neutral particles that do not get absorbed in the inner detectors, such as  $K_L^0$  mesons [104]. It is made of alternating 4.7-cm-thick iron plates and active detector elements. Iron elements act also as magnetic flux returns for the tracking solenoid. In the inner layers, the active material is scintillator, in the outer layers are glass-electrode resistive-plates chambers, with a gas mixture filling

the space between electrodes. When particles traverse the KLM, they produce charges that are collected by applying an appropriate voltage. The barrel section of the detector covers  $45^\circ$  to  $125^\circ$  in polar angle. The end-caps cover  $20^\circ$  to  $45^\circ$  and  $125^\circ$  to  $155^\circ$ .

### 3.2.4 Trigger and data acquisition system

The  $e^+e^-$  collisions at the  $\Upsilon(4S)$  resonance produce a variety of processes. As the events of interest are only a fraction of the total cross section and it would be impossible to record all collisions on permanent memory, an online event-selection system (trigger) is used to distinguish them from background in real time, and to feed only the interesting events to the data acquisition system (DAQ), compatibly with data processing resources. The physics processes of interest include hadronic,  $\mu/\tau$ -pair, Bhabha, and two photon events. Accept rates of Bhabha and  $\gamma\gamma$  events, which have high cross section and can be identified by their distinct signature, are artificially reduced by a factor of 100 to comply with the data acquisition limitations. Preferably discarded events include beam-related background resulting from synchrotron radiation, scattering of the beams on the residual gas, interactions in the beam pipe, and cosmic-ray events.

The Belle II trigger is organised according to a two-level logic, with a level 1 (L1) hardware trigger followed by a software-based, high-level trigger (HLT).

The L1 trigger, designed for a maximum rate of 30 kHz, uses input from four subdetectors: (i) the CDC, that provides three-dimensional track information to suppress tracks not originating from the interaction point; (ii) the ECL, that gives information on total energy deposit and cluster multiplicity; (iii) the TOP, that provides timing and hit topology information; and (iv) the KLM, that gives high-efficiency trigger for muons. These are used to achieve a low-level reconstruction that is fed to the global decision logic, which sends the proper trigger signal if the event passes the selection requirements. The L1 logic is implemented using field-programmable gate arrays that have a fixed latency of  $5\ \mu\text{s}$ , with an uncertainty on the trigger timing (jitter) of approximately 10 ns.

Expected cross sections and trigger accept rates for physics processes of interest at the design instantaneous luminosity of  $8 \times 10^{35} \text{cm}^{-2} \text{s}^{-1}$  are given in Tab. 3.4.

Process	$\sigma$ [nb]	Rate [Hz]
$e^+e^- \rightarrow \Upsilon(4S)$	1.2	960
$e^+e^- \rightarrow q\bar{q}$ ( $q = u, d, s, c$ )	2.8	2200
$e^+e^- \rightarrow \mu^+\mu^-$	0.8	640
$e^+e^- \rightarrow \tau^+\tau^-$	0.8	640
$e^+e^- \rightarrow e^+e^-$ (Bhabha scattering) $\theta_{lab} > 17^\circ$	44	350*
$e^+e^- \rightarrow \gamma\gamma$ $\theta_{lab} > 17^\circ$	2.4	19*
Two photon events ( $\theta_{lab} > 17^\circ$ and $p_T \geq 0.1 \text{ GeV}/c$ )	$\approx 80$	$\approx 1500$

Table 3.4: Expected cross sections and trigger rates of various physics processes at  $8 \times 10^{35} \text{cm}^{-2} \text{s}^{-1}$  luminosity [95]. Bhabha and  $\gamma\gamma$  accept rates (\*) are artificially reduced by a factor of 100 to comply with the data acquisition limitations.

Events selected by the L1 trigger are input to the HLT, that makes a decision using information from all the subdetectors except for PXD. The online software reconstruction is similar to that used offline. A first selection, performed after the first step of the reconstruction and aimed at discarding about half of the events, is based on requirements

on track multiplicity, vertex position, and total ECL energy deposit. After the remaining steps of the standard reconstruction are completed, further physics-level selection are performed. After this stage, the number of events is reduced to about 1/5 of those passing the L1 trigger. The efficiency of the HLT for  $\Upsilon(4S) \rightarrow B\bar{B}$  events is higher than 99%.

Data from the PXD for events that pass the L1 selection are stored in a dedicated online data reduction system. Once an event passes the selection, HLT extrapolates the tracks found by CDC and SVD to the PXD layers, defining regions of interest (ROIs). These are passed to the data reduction system, and only hits matching with a ROI are transmitted to the DAQ system. This keeps the PXD data size to about 100 kB/event.

Fully reconstructed events are stored in DST files. The size of a DST of a typical hadronic event is 100 kB. The large amount of information stored in DST files is reduced into mini-DST to isolate subsets of events of physics processes of interest like hadronic events. The size of a mini-DST of an hadronic event is around 40 kB.

### 3.3 Reconstruction of stable particles

Reconstruction is the process through which raw data collected by the detectors are transformed into manageable physics information, in terms of quantity, quality, and meaningfulness. Several algorithms use low-level objects (detector signals, alignment, and calibration information) combined with our knowledge of relativistic kinematics to produce higher-level objects (tracks, energy deposits, etc). An outline of the essential aspects of the reconstruction of these, along with the associated performance quantities follows.

#### 3.3.1 Charged-particle reconstruction

The ideal trajectories of charged particles in a solenoidal magnetic field are helical, with radius proportional to their transverse momentum. This ideal configuration can be altered by effects such as Coulomb scattering or other energy losses. When reconstructing a track, that is, measuring its momentum and position of closest approach to the interaction point, we need to take into account for these possible effects.

Track reconstruction, or “tracking”, in Belle II [105] consists in the combination of sequences of hits (measurement space-points) into tracks (full trajectories) after a charged particle crosses multiple active layers. The first step is called track finding; the second, track fitting. Tracking relies on PXD, SVD, and CDC information. Due to the different properties of these detectors, specific algorithms are used for each.

As a first step of track finding, hits in the outer tracking volume (CDC), where lower occupancy aids track finding, are filtered and reconstructed by two independent algorithms. One is a global track finding based on the Legendre algorithm [106], that transforms the position of each hit into a  $(\theta, \rho)$  pair, which represents all the circles traversing both the IP and the considered hit. Another is a local algorithm that takes into account possible non-circular trajectories. The global track finding searches for patterns of hits consistent with helical trajectories, accounting for layer inefficiencies, while local track finding detects extended patterns of nearby hits, to complement the global search and detect short tracks and tracks displaced from the IP. The results of both algorithms are merged and the resulting CDC-only tracks are fitted by an iterative fitter based on the Kalman filter technique, that accounts also for possible random perturbations on the trajectory due for example to multiple scattering or energy losses [107].

Then, tracks are extrapolated inward making sure to avoid duplications, and SVD information is added. They are fitted again, before being extrapolated further inward to the PXD

to define regions of interest around their expected intersection points. If an excited pixel is found inside this region, it is included in the pattern recognition algorithm, otherwise it is discarded.

Finally, the parameters of the track are determined thanks to a fitting algorithm and by assuming a mass hypothesis (Fig. 3.13):

- $d_0$ , the distance of the point of the closest approach to the  $z$  axis;
- $\phi_0$ , the angle between the transverse momentum and the  $x$  axis at the point of the closest approach;
- $\omega$ , the track curvature signed according to the particle charge;
- $z_0$ , the  $z$  coordinate at  $d_0$ ;
- $\tan \lambda$ , the tangent of the angle between track momentum and transverse momentum.

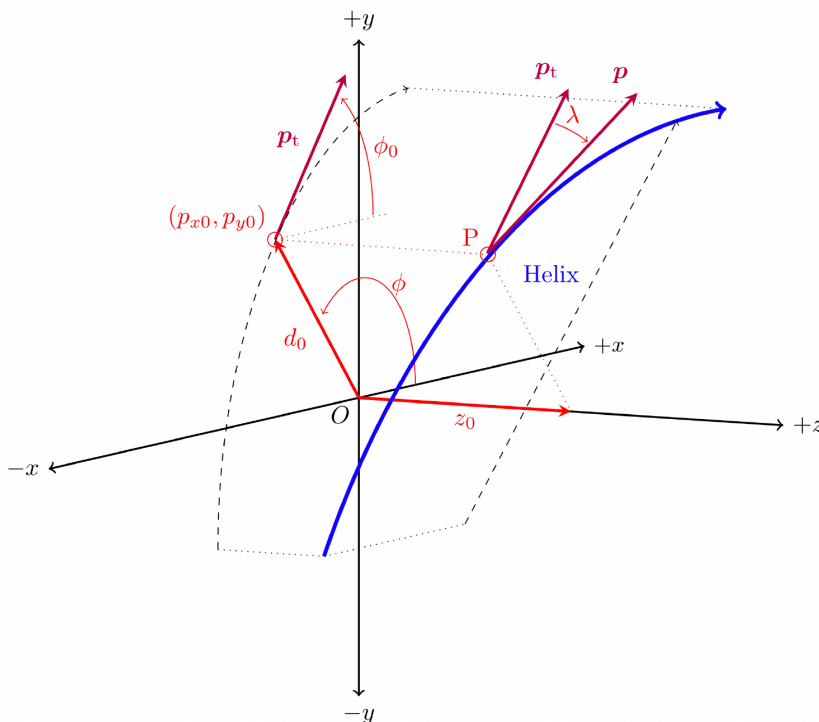


Figure 3.13: Three-dimensional representation of the helical trajectory of a track at the point of closest approach ( $P$ ) to the IP (the origin  $O$ ). Symbol  $p$  is the momentum of the charged particle at the point  $P$ ,  $p_t$  its transverse momentum and  $\lambda$  is the angle between the two vectors.

Track reconstruction is subjected to uncertainties and errors. A track might sometimes be a fake track, if it includes hits from beam-induced background or combines hits from two different particles, or a clone track, if other tracks are reconstructed from the same particle.

Tracking efficiency, that is the efficiency in reconstructing the track of a particle produced after a collision in the detector acceptance, varies from 75% at low transverse momenta ( $\mathcal{O}(10)$  MeV) to 95% around 4 GeV/ $c$ . It degrades the closer the track is to the

beam axis (small or large polar angles), while it is mostly constant around 90% regardless of the azimuthal angle.

The observed transverse momentum resolution is  $\sigma(p_T)/p_T = 0.0011p_T[\text{GeV}/c] \oplus 0.0025/\beta$  as shown in Fig. 3.14. The momentum- and angle-dependent impact parameter resolutions are  $\sigma_{xy} = 10 \oplus 25/(p\beta\sin^{3/2}\theta)\mu\text{m}$  and  $\sigma_z = 15 \oplus 27/(p\beta\sin^{5/2}\theta)\mu\text{m}$  for the transverse and longitudinal projections, respectively.

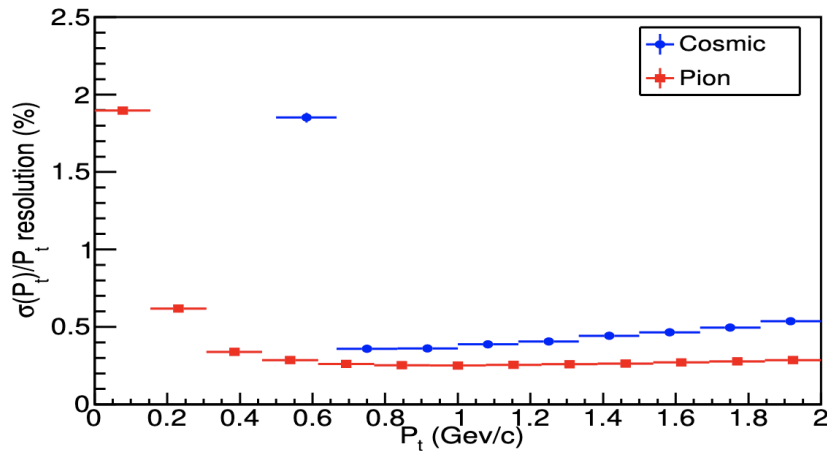


Figure 3.14: Transverse momentum resolution for collision and cosmic ray data.

### 3.3.2 Charged-particle identification

Particle identification is essential in flavour physics as most of the interesting channels are suppressed and therefore affected by signal-like backgrounds that only differ by the identity of some final-state hadrons. Particle identification (PID) at Belle II is achieved by combining information from several subdetectors. The trajectories of charged particles reconstructed by the tracking detectors, PXD, SVD, and CDC, are extrapolated outward to the TOP, ARICH, ECL and KLM detectors, where geometric matching between the tracks and observed signals is attempted. Offline reconstruction associates PID-detector information sensitive to its identity to each matching track. For example, the drift chamber output encodes information on the specific ionisation energy loss associated with each track. The raw information is further processed to provide higher-level quantities that are more convenient for usage in analysis. These are typically ‘likelihood’ values associated to the track. For each of six possible mass hypotheses, kaon, pion, electron, muon, proton and deuteron, the likelihood expresses the probability to observe the reconstructed PID information if the mass hypothesis was true.

For each detector and particle-hypothesis, the likelihood is usually obtained by comparing the expected and the observed value of the raw information, taking into account the uncertainties. For instance, in the CDC such information is  $dE/dx_{\text{obs}}(h)$ , the specific-ionisation energy-loss observed for a charged particle  $h$ , averaged across the CDC wires. The resulting (natural logarithm of) the likelihood is

$$\ln \mathcal{L}_{\text{hyp}}^{\text{CDC}}(h) = -\frac{1}{2} \left[ \frac{\frac{dE}{dx}_{\text{obs}}(h) - \frac{dE}{dx}_{\text{exp-hyp}}(h)}{\sigma_{\text{obs}}(h)} \right]^2, \quad (3.1)$$

where ‘hyp’ represents the particle hypothesis and  $\sigma_{\text{obs}}(h)$  is the observed uncertainty on  $dE/dx_{\text{obs}}(h)$ , which mainly depends on the number of CDC hits associated to  $h$ . The

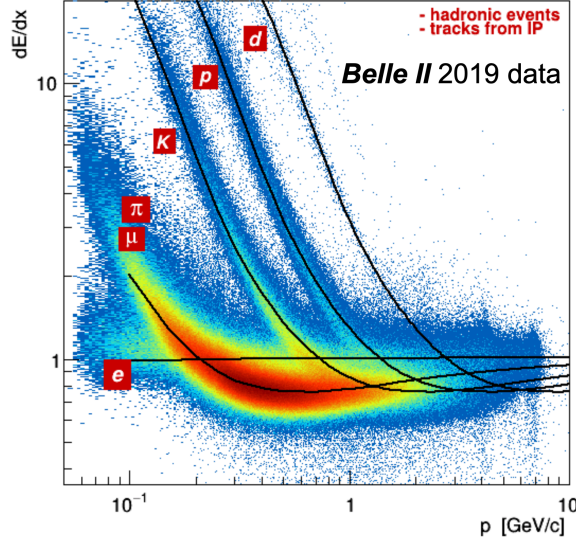


Figure 3.15: Distribution of (points) observed ionisation-energy loss as a function of momentum for charged particles from hadronic events reconstructed in Belle II data, along with average expected values (solid lines). Reproduced from Ref. [110].

expected value  $dE/dx_{\text{exp-hyp}}(h)$  is the average ionisation-energy loss from a charged particle  $h$  that has the observed momentum, assuming the hypothesis ‘hyp’, calculated using the Bethe-Bloch equation [108, 109] modified according to minor empirical adjustments to adapt to the details of the CDC response. Figure 3.15 shows the  $dE/dx_{\text{obs}}(h)$  distribution for various particle species in Belle II data and the expected energy loss for each of the six mass hypotheses considered.

In the TOP, the likelihood is calculated by comparing the observed number of detected photons associated to the charged particle with the photon yield expected from simulation [111, 112],

$$\ln \mathcal{L}_{\text{hyp}}^{\text{TOP}}(h) = \sum_{i=1}^N \ln \left[ \frac{S_{\text{hyp}}(x_i, t_i, h) + B(x_i, t_i)}{N_e(h)} \right] + \ln P_N(N_e(h)), \quad (3.2)$$

where  $x_i$  and  $t_i$  are, respectively, the positions and times of arrival of the  $N$  Cherenkov photons excited by the charged hadron  $h$ . The term  $S_{\text{hyp}}(x, t, h)$  is the signal distribution for the hypothesis ‘hyp’;  $B(x, t)$  is the distribution of background; and  $N_e(h) = N_{\text{hyp}}(h) + N_B$  is the expected number of detected photons, which is the sum of the expected number of signal photons  $N_{\text{hyp}}(h)$  for hypothesis ‘hyp’ and background photons  $N_B$ . The second term in Eq. (3.2) is a probability for a Poisson with mean  $N_e$  to generate  $N$  photons [111]. Figure 3.16 shows an example of the identification of a kaon in the TOP detector: the positions and arrival times of Cherenkov photons are compared with the values expected for a pion or a kaon.

Using the likelihoods for the various mass hypotheses, Belle II algorithms construct a particle identification variable  $\text{PID}_{\text{hyp}}^{\text{det}}$  for every detector,

$$\text{PID}_{\pi}^{\text{det}}(h) = \frac{\mathcal{L}_{\pi}^{\text{det}}(h)}{\mathcal{L}_{\pi}^{\text{det}}(h) + \mathcal{L}_{K}^{\text{det}}(h) + \mathcal{L}_{e}^{\text{det}}(h) + \mathcal{L}_{\mu}^{\text{det}}(h) + \mathcal{L}_{p}^{\text{det}}(h) + \mathcal{L}_{d}^{\text{det}}(h)}, \quad (3.3)$$

which is directly used in physics analyses. As an example, this was the  $\text{PID}_{\text{hyp}}^{\text{det}}$  expression

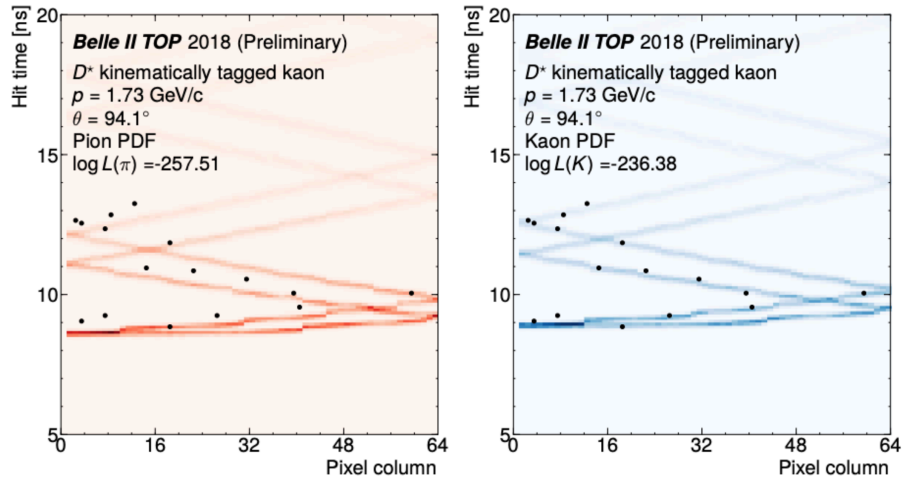


Figure 3.16: Example of kaon identification in the TOP detector. Arrival time of the Cherenkov photons as a function of position is compared with the expectations for (left) a pion and (right) a kaon passing in the TOP [110].

associated with the pion mass hypothesis<sup>1</sup>, but the  $\text{PID}_{\text{hyp}}^{\text{det}}$  values for other mass hypotheses are obtained by replacing the likelihood at the numerator  $\mathcal{L}_{\pi}^{\text{det}}(h)$  with the corresponding hypothesis-specific value  $\mathcal{L}_{\text{hyp}}^{\text{det}}(h)$ . The quantity  $\text{PID}_{\text{hyp}}^{\text{det}}(h)$  is defined similarly to a likelihood ratio  $\mathcal{L}_0/\mathcal{L}_1$ , which is the best-performing quantity to test two alternative simple statistical hypotheses [113]. The  $\text{PID}_{\text{hyp}}^{\text{det}}$  variable assumes values from 0 to 1. The larger the  $\text{PID}_{\text{hyp}}^{\text{det}}$ , the higher the probability of observing the reconstructed track assuming true the chosen mass hypothesis.

Information from individual detectors is combined to improve the identification performance. The detector-specific likelihoods are combined together as a product,

$$\mathcal{L}_{\text{hyp}}(h) = \mathcal{L}_{\text{hyp}}^{\text{TOP}}(h)\mathcal{L}_{\text{hyp}}^{\text{CDC}}(h)\mathcal{L}_{\text{hyp}}^{\text{SVD}}(h)\mathcal{L}_{\text{hyp}}^{\text{ARICH}}(h)\mathcal{L}_{\text{hyp}}^{\text{ECL}}(h)\mathcal{L}_{\text{hyp}}^{\text{KLM}}(h), \quad (3.5)$$

and the result is used in Eq.(3.6) to obtain the detector-combined PID. If a particle does not get reconstructed in a detector because, for instance, it escapes its acceptance, no PID information from that detector is available and the corresponding individual likelihood is set to one.

Of the two main PID detectors, TOP allows separating pions from kaons at 0.4 – 4 GeV/c momenta with kaon identification efficiency of about 85% and pion misidentification rate of about 10%, while the ARICH separates pions from kaons across all their momentum spectrum and discriminates also pions, electrons, and muons below 1 GeV/c with  $4\sigma$  separation or more.

Combining information from all detectors, the electron and muon identification efficiencies are respectively 86% and 88.5% after requiring the binary PID to be larger than 0.9, with pion misidentification rates of 0.4% and 7.3%, respectively. Binary PID is an

<sup>1</sup>In practice, the Belle II software expresses  $\text{PID}_{\text{hyp}}$  using only the natural logarithm of the likelihood values,

$$\text{PID}_{\text{hyp}} = \frac{e^{\ln \mathcal{L}_{\text{hyp}} - \ln \mathcal{L}_{\text{MAX}}}}{\sum_i (e^{\ln \mathcal{L}_i - \ln \mathcal{L}_{\text{MAX}}})} = \frac{e^{\Delta \ln \mathcal{L}_{\text{hyp}}}}{\sum_i (e^{\Delta \ln \mathcal{L}_i})} \quad (3.4)$$

where  $\mathcal{L}_{\text{MAX}}$  is the largest of the likelihood values over the six hypotheses.

additional PID variable that compares only two mass hypotheses, for example

$$\text{PID}_{\mu,\pi}^{\text{det}}(h) = \frac{\mathcal{L}_{\mu}^{\text{det}}(h)}{\mathcal{L}_{\mu}^{\text{det}}(h) + \mathcal{L}_{\pi}^{\text{det}}(h)}. \quad (3.6)$$

Data and simulation agree, except at low momenta where discrepancies within 20% are observed. Performance of kaon identification for a threshold of 0.8 on the kaon-pion binary PID is summarised in Fig. 3.17. Efficiency varies from 95% to around 60%, depending on kaon momentum and polar angle. The pion misidentification varies from about 20% to less than 5%.

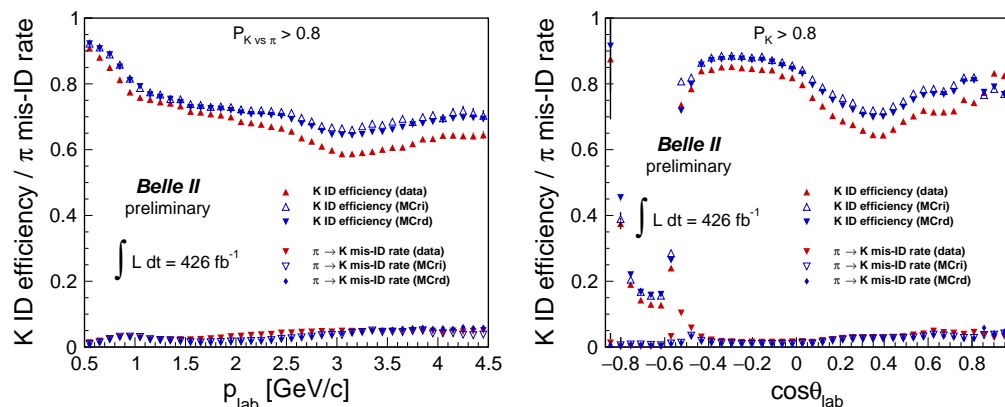


Figure 3.17: Kaon identification efficiencies and pion misidentification rates for events having a binary PID larger than 0.8, in data and simulation (MC) as functions of (left) kaon momentum, and (right) cosine of the polar angle in the laboratory frame.

### 3.4 Instrumental asymmetries

Measurements of charge-parity-violating decay-rate asymmetries,  $A_{CP}$ , are a fundamental goal of the Belle II physics programme. Decay-rate asymmetries are derived from charge-dependent signal yields of reconstructed decay candidates. Such yield asymmetries,  $A_{raw}$ , may be affected by biases due to charge-dependent reconstruction efficiencies of final-state particles. These biases are referred to as detection asymmetries,  $A_{det}$ , and they originate from various sources. For instance, when charged kaons are reconstructed, a detection asymmetry is expected due to the known difference in interaction probabilities between  $K^+$  and  $K^-$  with matter<sup>2</sup>. Other sources of  $A_{det}$  may arise from tracking or particle identification algorithms.

Simulation might not model perfectly all these effects because of a approximated description of detector material budget or simplified modelling of processes related to tracking and particle identification. It is pivotal to carry out auxiliary measurements on abundant samples of control data to determine (or to bound) detection asymmetries, so that measured charge-yields asymmetries can be corrected for to measure genuine  $CP$  asymmetries.

I study the detection asymmetries of kaons and pions using control samples of  $D^0 \rightarrow K^- \pi^+$  and  $D^- \rightarrow K_S^0 \pi^-$  decays. For the first time at Belle II, I investigate the dependencies of instrumental asymmetries on track variables. In addition, I develop a strategy for

<sup>2</sup>The  $\bar{u}$  quark of a  $K^-$  allows a wider variety of interaction processes, such as the production of strange baryons (e.g.  $\Sigma^*(1385)$ ,  $\Lambda(1405)$ ,  $\Sigma(1660)$ ), which is instead forbidden for  $K^+$ .

determining instrumental asymmetries for physics decays based on my measurements in  $D$  control channels.

### 3.4.1 $A_{det}$ from $D$ control decays

To determine  $A_{det}$  from the  $D$  control decays, I measure the signal-yield asymmetries  $A_{raw}$  from the fit of the  $D$ -mass distribution of the reconstructed candidates. The yield asymmetry can be decomposed into three contributions as:

$$A_{raw} = \frac{N - \bar{N}}{N + \bar{N}} = A_{CP} + A_{det} + A_{FB}, \quad (3.7)$$

where  $N$  is the measured signal yield for a charge-specific decay (*i.e.*, number of  $D^0 \rightarrow K^- \pi^+$  or  $D^- \rightarrow K_S^0 \pi^-$  decays) and  $\bar{N}$  for its  $CP$  conjugate. The term  $A_{FB}$  is the forward-backward asymmetry, a known asymmetry in the production of  $D$  and  $\bar{D}$  mesons due to the  $\gamma^*-Z^0$  interference in  $e^+e^- \rightarrow c\bar{c}$  processes [114].

I use these  $D$  control decays because they have null or very well-known values of  $A_{CP}$ . The  $D^0 \rightarrow K^- \pi^+$  decays are governed solely by a Cabibbo-favoured tree amplitude to a very good approximation. The expected  $A_{CP}$ , if any, is smaller than 0.1%, as confirmed by measurements, so I assume  $A_{CP}(D^0 \rightarrow K^- \pi^+) = 0$ . The  $D^- \rightarrow K_S^0 \pi^-$  decays are also expected to exhibit a small  $CP$  asymmetry. The measured value,  $A_{CP}(D^- \rightarrow K_S^0 \pi^-) = (0.41 \pm 0.09)\%$  [14], differs from zero; therefore, this value is subtracted from the measured  $A_{raw}$ .

Knowing the values of  $A_{CP}$  for these control decays, the contribution of  $A_{FB}$  is needed to determine  $A_{det}$  from  $A_{raw}$ . The asymmetry  $A_{FB}$  is known to be antisymmetric as a function of  $\cos \theta_D^*$ , *i.e.*, the cosine of the  $D$  meson polar angle in the centre-of-mass system [114]. Assuming that  $A_{det}$  is not antisymmetric in  $\cos \theta_D^*$ ,  $A_{FB}$  can be cancelled by measuring  $A_{raw}$  in bins of  $\cos \theta_D^*$  and averaging the values obtained in bins with opposite signs of  $\cos \theta_D^*$ :

$$A_{det} = \frac{A'_{raw}(\cos \theta_D^*) + A'_{raw}(-\cos \theta_D^*)}{2}, \quad (3.8)$$

where  $A'_{raw}$  is the charge-yield asymmetry corrected for  $A_{CP}$ . I perform the measurement in four bins of  $\cos \theta_D^*$ :  $[-1,-0.5]$ ,  $[-0.5,0]$ ,  $[0,0.5]$ ,  $[0.5,1]$  obtaining two values of  $A_{det}$ , which are averaged to produce a single final result. In the following, the contribution of  $A_{FB}$  is subtracted using this method.

Using the  $D^0 \rightarrow K^- \pi^+$  sample, I can measure the detection asymmetry  $A_{det}(K^- \pi^+)$ , *i.e.*, that for the particle pair  $K^- \pi^+$ . In contrast, with the  $D^- \rightarrow K_S^0 \pi^-$  decays, I determine the asymmetry of the  $K_S^0 \pi^-$  pair. Assuming that the particle-pair detection asymmetry is the sum of the individual detection asymmetries of each particle, the  $A_{det}$  values for pions and kaons are derived as

$$A_{det}(\pi^-) \simeq A_{det}(D^- \rightarrow K_S^0 \pi^-) \quad (3.9)$$

$$A_{det}(K^-) \simeq A_{det}(D^0 \rightarrow K^- \pi^+) - A_{det}(\pi^+). \quad (3.10)$$

In this calculation the tiny contribution from  $CP$  violation in neutral kaons is neglected (with an associated systematic uncertainty of  $\mathcal{O}(0.2\%)$ ). The subtraction of  $A_{det}(\pi^+)$  ( $= -A_{det}(\pi^-)$ ) in Eq. 3.10 is valid as long as pion kinematic is similar in the  $D^0 \rightarrow K^- \pi^+$  and  $D^- \rightarrow K_S^0 \pi^-$  samples, a fair assumption for these decays.

### 3.4.2 Sample selection

For this study, I use a simulated data set based on the Monte Carlo (MC) approach, which is produced using event generators according to theoretical models of particle kinematic properties and interactions. The MC samples include  $B^0\bar{B}^0$ ,  $B^+B^-$ ,  $u\bar{u}$ ,  $d\bar{d}$ ,  $c\bar{c}$  and  $s\bar{s}$  processes in adequate proportions and correspond to an integrated luminosity of  $300 \text{ fb}^{-1}$  at the  $\Upsilon(4S)$  resonance. The experimental data set corresponds to an integrated luminosity of  $189.26 \text{ fb}^{-1}$ .

The  $D$  meson candidates are reconstructed by filling collections of candidate final-state particles filtered through loose baseline selection criteria and then combine them in kinematic fits consistent with the topologies of the desired decay. For pions and kaons, the following requirements are applied:

- the polar angle between  $17^\circ - 150^\circ$ ;
- at least 1 hits tracks in the central drift chamber (CDC);
- the  $p$ -value of the track fit is required to be greater than 0;
- the distance of the closest approach to the interaction point (IP) in the  $r$ - $\phi$  plane is required to be less than 0.5 cm, and the absolute relative distance in the  $z$  direction to be less than 3 cm.

For  $D^0 \rightarrow K^-\pi^+$  candidates, the particle identification probability of the kaon candidate is required to exceed 0.25, I select the mass range of the  $K\pi$  system to be between  $1.80\text{--}1.95 \text{ GeV}/c^2$  and the momentum of the  $D^0$  candidate in the centre-of-mass frame,  $p^*(D^0)$ , to be greater than  $2.5 \text{ GeV}/c$  to select  $e^+e^- \rightarrow c\bar{c}$  events.

For  $D^- \rightarrow K_S^0\pi^-$  candidates, the  $K_S^0$  flight distance is required to be larger than 44.5 mm, and the mass range of  $K_S^0$  is set to be between  $0.4942\text{--}0.5014 \text{ GeV}/c^2$ . These values resulted from maximising the figure of merit  $S/\sqrt{S+B}$  for simulated candidates, where  $S$  and  $B$  represent signal and background candidates, respectively. The invariant mass of the  $K_S^0\pi$  candidate must be in the range  $1.82\text{--}1.93 \text{ GeV}/c^2$ . I also require for the  $D^-$  momentum in the centre-of-mass,  $p^*(D^-)$ , to be greater than  $2.5 \text{ GeV}/c$  to select  $e^+e^- \rightarrow c\bar{c}$  events.

For 7.5% (1.5%) of the events, there are more than one  $D^0 \rightarrow K^-\pi^+$  ( $D^- \rightarrow K_S^0\pi^-$ ) candidate, with an average multiplicity of 1.08 (1.02). For those events, one random candidate is chosen.

### 3.4.3 Asymmetry determination

To determine  $A_{raw}$  defined in Eq. 3.7, a simultaneous binned fit of the  $D$  and  $\bar{D}$  candidate mass distributions is performed using the following probability density functions (PDFs):

$$\mathcal{P} = \frac{f_{\text{sig}}}{2} (1 - A_{raw}) \mathcal{P}_{\text{sig}} + (1 - \frac{f_{\text{sig}}}{2} (1 - A_{raw})) \mathcal{P}_{\text{bkg}}, \quad (3.11)$$

$$\bar{\mathcal{P}} = \frac{f_{\text{sig}}}{2} (1 + A_{raw}) \mathcal{P}_{\text{sig}} + (1 - \frac{f_{\text{sig}}}{2} (1 + A_{raw})) \mathcal{P}_{\text{bkg}}, \quad (3.12)$$

where the  $D$  ( $\bar{D}$ ) candidates are fitted with  $\mathcal{P}$  ( $\bar{\mathcal{P}}$ ). Here,  $f_{\text{sig}}$  is the total fraction of the signal (summing the  $D$  and  $\bar{D}$  samples), and  $\mathcal{P}_{\text{sig}}$  and  $\mathcal{P}_{\text{bkg}}$  are the PDFs of the signal and background components. I study the models for  $\mathcal{P}_{\text{sig}}$  and  $\mathcal{P}_{\text{bkg}}$  separately in the simulation, selecting samples of signal-only and background-only candidates, and I use

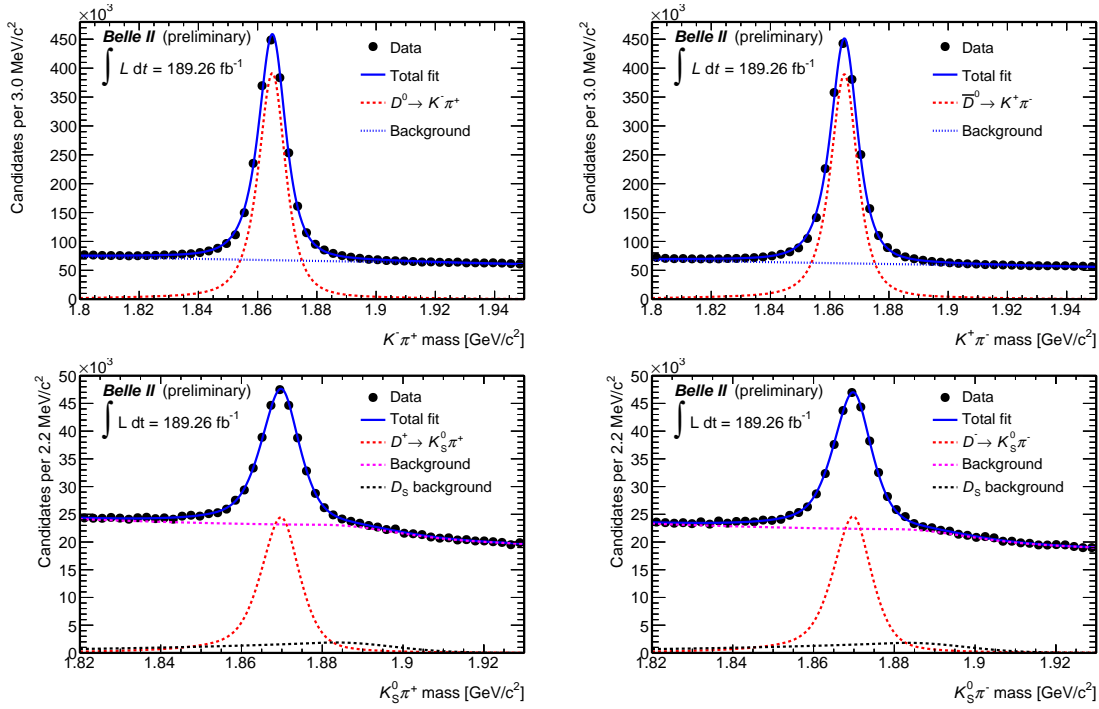


Figure 3.18: Mass distributions for (top left)  $D^0 \rightarrow K^- \pi^+$  candidates and (top right)  $\bar{D}^0 \rightarrow K^+ \pi^-$  candidates. Mass distributions for (bottom left)  $D^+ \rightarrow K_S^0 \pi^+$  candidates and (bottom right)  $D^- \rightarrow K_S^0 \pi^-$  candidates. Fit projections are overlaid.

the same model to fit the  $D$  and  $\bar{D}$  samples. The mass distributions with fit projections overlaid are presented in Fig. 3.18.

For the  $D^0 \rightarrow K^- \pi^+$  decays,  $\mathcal{P}_{\text{sig}}$  is a sum of a Johnson and a Gaussian function, while  $\mathcal{P}_{\text{bkg}}$  is an exponential function. The parameters of  $\mathcal{P}_{\text{sig}}$  are fixed from the fit to the simulation, and two free parameters are used: a shift on the mean and a scale factor for the width of the peak. The slope parameter of  $\mathcal{P}_{\text{bkg}}$  is also free. The sample is composed of about 10.1 million candidates in the full ( $D^0$  and  $\bar{D}^0$ ) sample, with a signal fraction of  $(36.60 \pm 0.02)\%$ .

For the  $D^- \rightarrow K_S^0 \pi^-$  decays,  $\mathcal{P}_{\text{sig}}$  is a sum of a Johnson and a Gaussian function;  $\mathcal{P}_{\text{bkg}}$  is the sum of an exponential function, which models a smooth component dominated by combinatorial background, and a Crystal-Ball function, which models the  $D_s^-$  background peaking around  $1.89 \text{ GeV}/c^2$ . The fraction of the  $D_s^-$  peak found in simulation is about 4.3% of the total background. The parameters of  $\mathcal{P}_{\text{sig}}$  and those of the Crystal-Ball component of  $\mathcal{P}_{\text{bkg}}$  are fixed from the fit to the simulation and two free parameters are used: a common shift on the mean and a common scale factor for the width of the peaks. The slope of the exponential and the fraction of the  $D_s^-$  background in  $\mathcal{P}_{\text{bkg}}$  are also free parameters. The number of candidates in the full ( $D^+$  and  $D^-$ ) sample is about 2.5 million, with a signal fraction of  $(12.72 \pm 0.02)\%$ .

I carry out the measurement of  $A_{\text{raw}}$  in bins of  $\cos \theta_D^*$  and determine the value of  $A_{\text{det}}$  as explained in Sect. 3.4.1, obtaining:

$$A_{\text{det}}^{\text{data}}(K^- \pi^+) = (0.43 \pm 0.06)\%, \quad (3.13)$$

$$A_{\text{det}}^{\text{data}}(\pi^-) = (-0.10 \pm 0.34)\%, \quad (3.14)$$

$$A_{\text{det}}^{\text{data}}(K^-) = (0.33 \pm 0.34)\%. \quad (3.15)$$

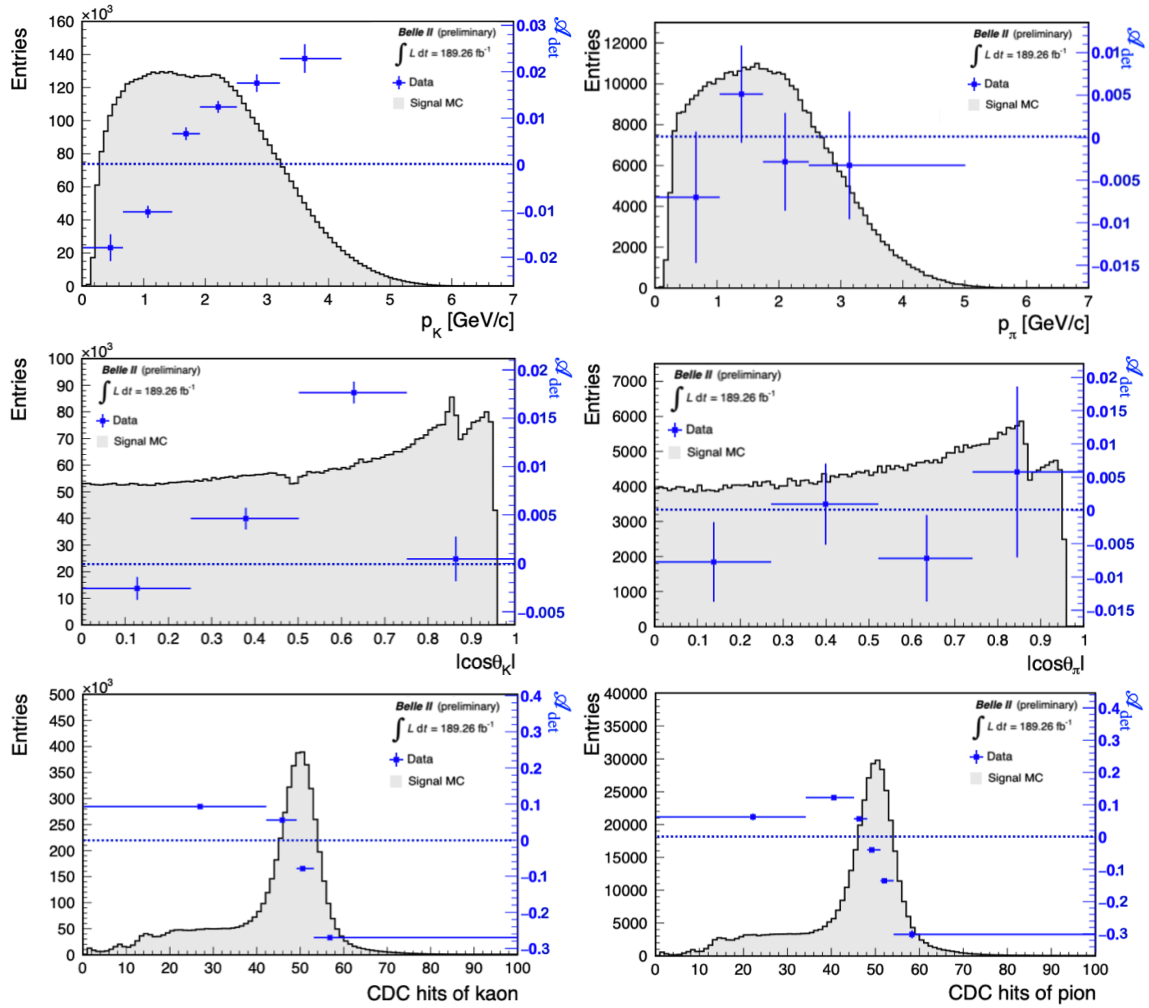


Figure 3.19: (Left column) Measurement of  $A_{det}(K^-\pi^+)$  as a function of (top) kaon momentum  $p(K)$ , (middle) cosine of polar angle  $\cos\theta(K)$ , (bottom) track CDC hits. (Right column) Measurement of  $A_{det}(\pi^-)$  as a function of (top) pion momentum  $p(\pi)$ , (middle) cosine of polar angle  $\cos\theta(\pi)$ , (bottom) track CDC hits. Blue markers show measured values in data. The point are placed at the average of the values in the considered bin. The distributions of the variables for signal decays in simulation (MC) are also drawn as grey histograms.

### 3.4.4 Dependencies of $A_{det}$

In addition to determining  $A_{det}$ , I also investigate its possible dependencies on the particle momentum ( $p$ ), the cosine of the polar angle ( $\cos\theta$ ), and the number of CDC hits. The dependence of  $A_{det}$  on  $p$  and  $\cos\theta$  can be expected because interaction cross-sections depend on particle momentum and because particles traverse different material budgets according to their direction. In addition, asymmetries intrinsic to tracking algorithms might also depend on particle kinematics. The average number of CDC hits varies for tracks of opposite curvature, which might induce also a charge asymmetry as a function of CDC hits. The three variables considered are not independent of each other. Since studying the dependence of  $A_{det}$  in a three-dimensional space is practically difficult, I first investigate the dependence on each individual variable while marginalising over the distributions of the others.

The dependencies are determined by binning the sample in one variable: for each bin, the procedure described in Sect. 3.4.3 to obtain the value of  $A_{det}$  is repeated. The dependencies of  $A_{det}$  as a function of the three variables are reported in Figs. 3.19 for both  $D^0 \rightarrow K^-\pi^+$  and  $D^- \rightarrow K_S^0\pi^-$  decays. I notice a variation of  $A_{det}(K^-\pi^+)$  of about 4% and 2% as a function of  $p(K)$  and  $|\cos\theta(K)|$ , respectively. The largest dependence of  $A_{det}(K^-\pi^+)$  is observed as a function of CDC hits, where the asymmetry spans a range of about 40%. I observe a uniform values of  $A_{det}(\pi^-)$ , with deviations of about 1%, as a function of  $p(\pi)$  or  $|\cos\theta(\pi)|$ . However, similarly to what is observed for  $D^0 \rightarrow K^-\pi^+$ , a large dependence is observed as a function of CDC hits, where  $A_{det}(\pi^-)$  spans a range of about 40%.

### 3.4.5 Weighting method

In this section, I explain the weighting method to determine  $A_{det}$  in order to correct the raw asymmetries for  $A_{CP}$  measurements for any given *target* decay. The instrumental asymmetries can be derived from my control channels; however, target and control decays might feature very different distributions of particle momentum, polar angle, and CDC hits. Given the dependencies observed, the value of  $A_{det}$  changes according to the distributions of those variables (when  $A_{det}$  is averaged over these distributions). To ensure a proper value of  $A_{det}$  to be subtracted from  $A_{raw}$ , the distributions of the control decay must mirror those of the target. Thus, I propose a method based on a weighting procedure that equalises the distributions between the control and the target decays. I then determine the value of  $A_{det}$  from the weighted control sample, which corresponds to the value needed for the target decay. I carry out the procedure in the following steps:

1. Split the control and target samples into  $N$  bins of the CDC hits distribution;
2. For each bin, weight the two-dimensional  $(p, \cos\theta)$  distributions of the control sample to match those of the target decays;
3. In each bin, measure the value of  $A_{det}$  from the weighted control sample, using the procedure outlined in Sect. 3.4.3;
4. Obtain the final value of  $A_{det}$  by taking a weighted average of the  $A_{det}$  measurements in each bin, using the fractions of signal candidates from the target decays in each bin as weights for the average.

This procedure is designed to provide better control over the weighting and is equivalent to a full three-dimensional reweighting of the  $(p, \cos\theta, \text{CDC hits})$  distributions of the control sample, accounting for correlations between these variables.

### 3.4.6 Closure tests

To validate the procedure, I perform a closure test using simulation to verify whether the desired value of  $A_{det}(K^-\pi^+)$  is correctly reproduced for a target decay by using the control  $D^0 \rightarrow K^-\pi^+$  decay. In this test, I use only signal candidates for both the target and control decays.

The simulated sample of  $\overline{B}^0 \rightarrow K^-\pi^+$  serves as the target decay. I reconstruct and select the sample according to the requirements reported in Ref. [115] to simulate a realistic analysis case. In particular, a tight continuum-suppression selection is applied in this analysis. This suppression is achieved using a boosted decision tree (BDT), where the output is required to be greater than 0.95. Additionally, the (global) particle-identification

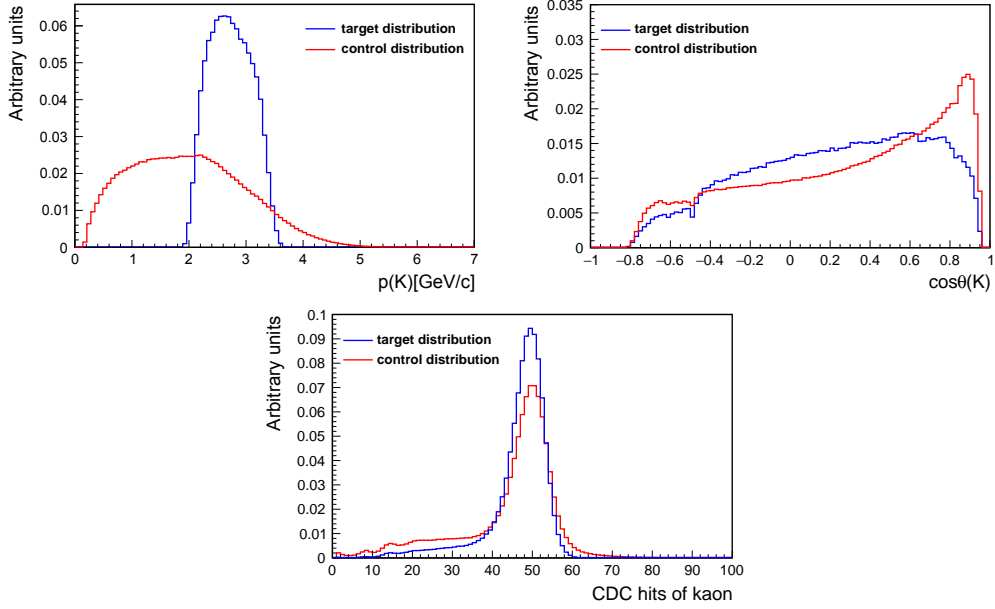


Figure 3.20: (Top left) Kaon momentum,  $p(K)$ , (top right) cosine of polar angle  $\cos\theta(K)$ , and (bottom) CDC hits distributions of the (blue) target  $\bar{B}^0 \rightarrow K^- \pi^+$  and (red) control  $D^0 \rightarrow K^- \pi^+$  decays.

variable for the kaon candidate must exceed 0.25. I obtain the detection asymmetry for the target decay,  $A_{det}^{\text{target}}(K^- \pi^+)$ , by counting the yields of truth-matched signal candidates split by final-state charge (as  $A_{CP} = 0$  in simulation):

$$A_{det}^{\text{target}}(K^- \pi^+) = (0.12 \pm 0.15)\%. \quad (3.16)$$

I select the simulated sample of the  $D^0 \rightarrow K^- \pi^+$  control decay, as described in Sect. 3.4.2. On top of those requirements, a requirement on the continuum-suppression BDT, greater than 0.5, is applied to have a selection closer to that of the target decay. The value of the detection asymmetry in the control channel is:

$$A_{det}^{\text{control}}(K^- \pi^+) = (-0.76 \pm 0.07)\%. \quad (3.17)$$

As expected, the value differs from that of the target. Indeed, the distributions of  $p(K)$ ,  $\cos\theta(K)$ , and CDC hits differ between target and control decays, as reported in Fig. 3.20.

I apply the weighting procedure explained in the previous section, to verify if the control sample value can match with the one of the target sample:

1. 7 bins of CDC hits are considered to split the sample. The range of these bins have been chosen to have approximately the same number of signal events for each bin.
2. For each bin, I weight the two-dimensional  $(p(K), \cos\theta(K))$  distributions of the  $D^0 \rightarrow K^- \pi^+$  decay to match that the  $\bar{B}^0 \rightarrow K^- \pi^+$  decay (note that I carry out the weighting by using only the kaon information since  $A_{det}(K) \gg A_{det}(\pi)$ ). The weights are computed from the ratio of two-dimensional histograms of target and control samples. An example of the  $p(K)$  and  $\cos\theta(K)$  distributions for  $D^0 \rightarrow K^- \pi^+$  and  $\bar{B}^0 \rightarrow K^- \pi^+$  decays, in three different bins of CDC hits, before and after reweighting, is shown in Fig. 3.21. The  $p(K)$  and  $\cos\theta(K)$  distributions of reweighted  $D^0 \rightarrow K^- \pi^+$  channel match the same distributions of  $\bar{B}^0 \rightarrow K^- \pi^+$ .

3. I measure the  $A_{det}$  values in each bins of CDC hits using the weighted control sample. In Fig. 3.22, the  $A_{det}$  values for the control, target and weighted control channel are depicted, in each bins of CDC hits. The  $A_{det}$  values of weighted control channel approach towards  $A_{det}$  values of the target decay in each bin.
4. Finally, I evaluate the integrated value by performing the weighted average of  $A_{det}$  measurements, using as weights the fraction of candidates in each CDC bin of the  $\bar{B}^0 \rightarrow K^- \pi^+$  decays.

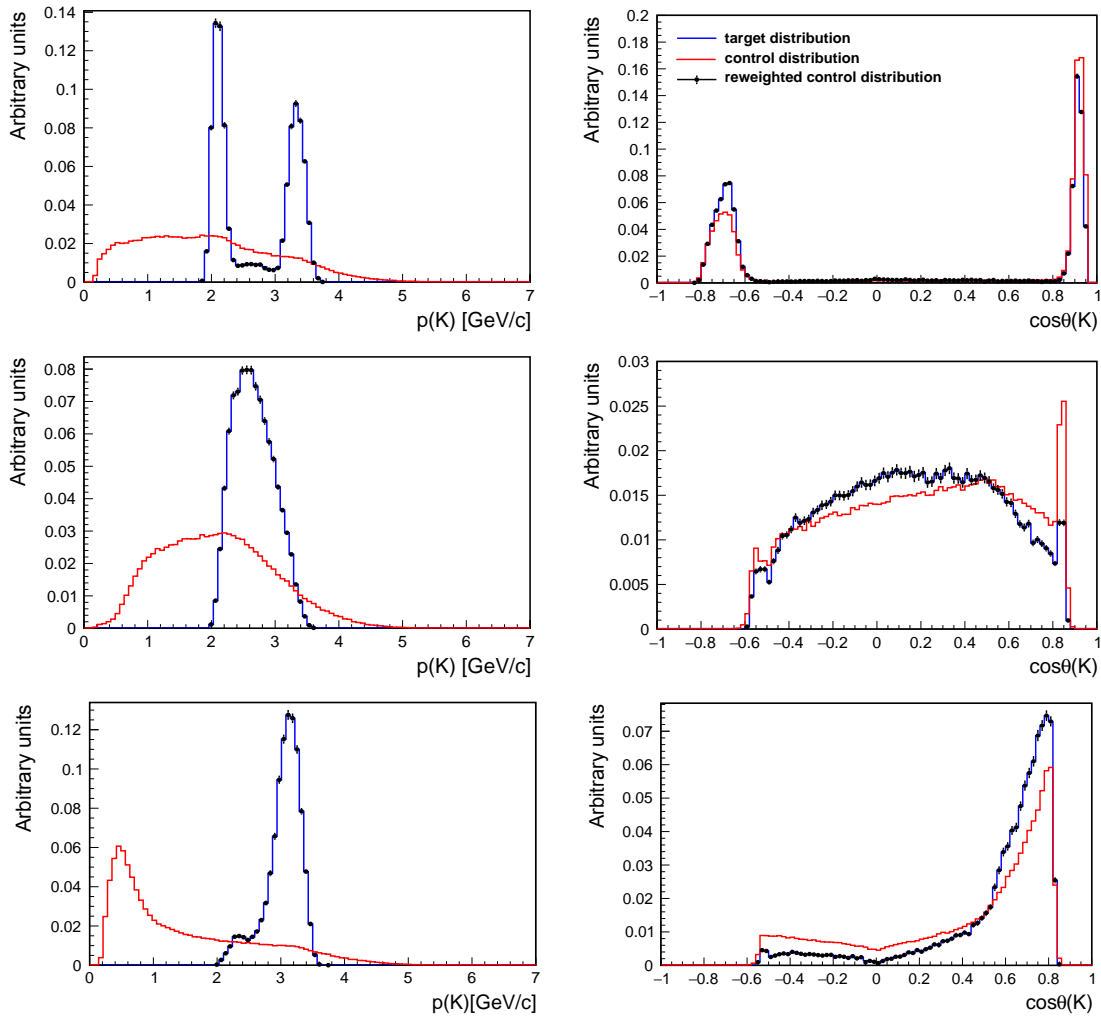


Figure 3.21: (Left) Kaon momentum,  $p(K)$ , and (right) cosine of polar angle,  $\cos\theta(K)$ , distributions of the (blue) target  $\bar{B}^0 \rightarrow K^- \pi^+$ , (red)  $D^0 \rightarrow K^- \pi^+$  control and (black markers) weighted  $D^0 \rightarrow K^- \pi^+$  control channels for three different bins of the CDC-hits distribution, shown as example: (top) bin with 20–43 hits, (middle) 47–49 hits, and (bottom) greater than 54 hits.

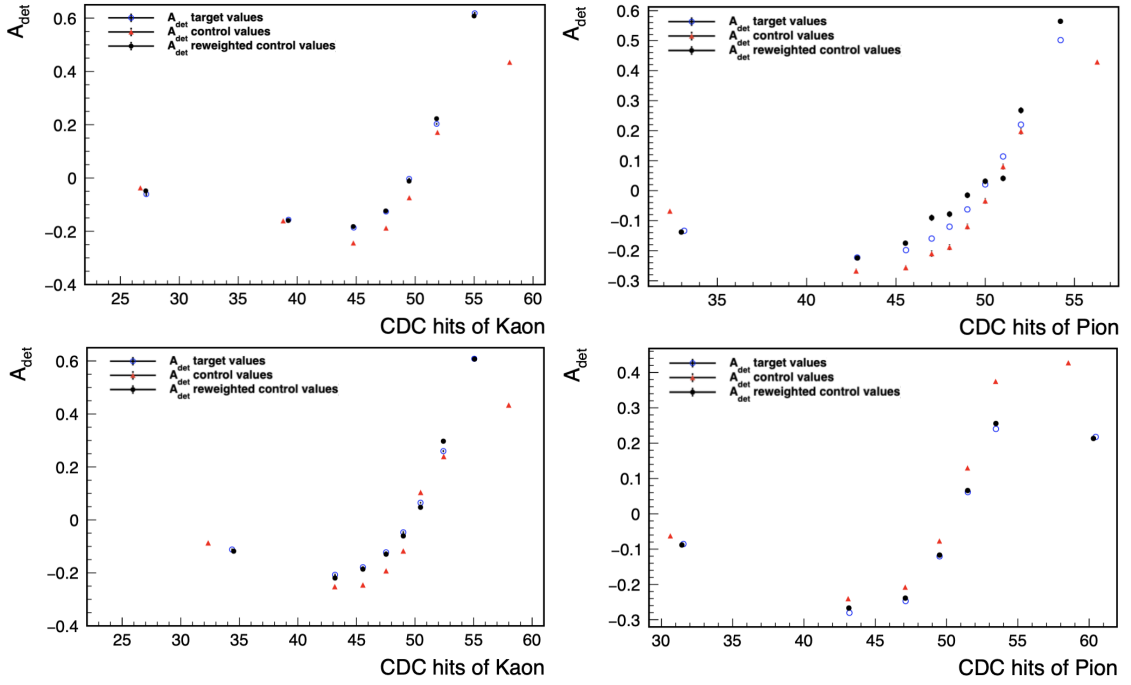


Figure 3.22:  $A_{det}$  values for the (blue markers) target, (red markers) control and (black markers) weighted control decay in each CDC bins. The markers are placed at the average of the CDC-hit values in each bin. The decays considered for the target are: (top-left)  $\bar{B}^0 \rightarrow K^- \pi^+$ , (bottom-left)  $B^- \rightarrow K^- \pi^0$ , (top-right)  $B^- \rightarrow \pi^- \pi^0$ , and (bottom-right)  $B^- \rightarrow \rho^- \rho^0$ .

From the weighting procedure, the value obtained from the control sample is

$$A_{det}^{\text{weighted}}(K^- \pi^+) = (0.27 \pm 0.07)\%, \quad (3.18)$$

That it is in agreement with the target value (see Eq. 3.16).

To check the flexibility of the method, I also perform different closure tests with different target decays using both the  $D^0 \rightarrow K^- \pi^+$  and  $D^- \rightarrow K_S^0 \pi^-$  control decays. I summarise all results in Tab. 3.5. In Fig. 3.22, I also report, the  $A_{det}$  values for the control, target and weighted control channels in each bins of CDC hits.

Target	Asymmetry	$A_{det}^{\text{target}}$ [%]	$A_{det}^{\text{control}}$ [%]	$A_{det}^{\text{weighted}}$ [%]	$\Delta A_{det}$ [%]
$\bar{B}^0 \rightarrow K^- \pi^+$	$A_{det}(K^- \pi^+)$	$0.12 \pm 0.15$	$-0.76 \pm 0.07$	$0.27 \pm 0.07$	$-0.15 \pm 0.17$
$B^- \rightarrow \rho^- \rho^0$	$A_{det}(\pi^-)$	$0.11 \pm 0.14$	$0.58 \pm 0.16$	$0.53 \pm 0.16$	$-0.42 \pm 0.21$
$B^- \rightarrow \pi^- \pi^0$	$A_{det}(\pi^-)$	$-0.02 \pm 0.13$	$0.80 \pm 0.27$	$2.23 \pm 0.27$	$-2.25 \pm 0.30$
$B^- \rightarrow K^- \pi^0$	$A_{det}(K^-)$	$0.16 \pm 0.13$	$1.04 \pm 0.07$	$0.20 \pm 0.27$	$-0.04 \pm 0.30$

Table 3.5: Summary of the closure tests carried out in simulation with different target decays. The last column reports the value of  $\Delta A_{det} \equiv A_{det}^{\text{target}} - A_{det}^{\text{weighted}}$ .

I observe that the weighting method to account for the observed sample-dependence of  $A_{det}$  allows for a reduction in the differences between control and target decays in obtaining the value of  $A_{det}$ , as demonstrated by several closure tests performed in simulation, reported in Tab. 3.5. However, it fails in some cases, where the results depend on the criteria used

to select the control channel. Additionally, there may be other dependencies that need to be considered but are currently neglected.

### 3.4.7 $A_{det}$ for a target decay

The weighting method outlined in Sect. 3.4.5 accounts for the observed sample dependence of  $A_{det}$  and reduces the differences between control and target decays when obtaining the value  $A_{det}$ . However, as explained in the previous section, this method can fail in some cases. To overcome this limitation and to obtain  $A_{det}$  for a given target decay, I propose a strategy that involves using the value measured in  $D$  control channels from data and assessing a systematic uncertainty for possible differences between control and target values of  $A_{det}$ . I outline the proposed strategy in the following operational steps:

1. The control channel to measure  $A_{det}$  is selected with requirements that resemble those of the target decays.
2. The value of  $A_{det}$  is measured in simulation for the target and the control decay, and the difference  $\Delta A_{det}^{MC} = A_{det}^{\text{target,MC}} - A_{det}^{\text{control,MC}}$  is computed.
3. The weighting method (Sect. 3.4.5) is applied to the control channel in simulation, and the difference  $\Delta A_{det}^{\text{reweighted,MC}} = A_{det}^{\text{target,MC}} - A_{det}^{\text{reweighted,MC}}$  is computed.
4. if  $\Delta A_{det}^{\text{reweighted,MC}} < \Delta A_{det}^{MC}$ , the weighting method is applied to measure  $A_{det}^{\text{reweighted,data}} \pm \sigma^{\text{reweighted,data}}$  on the control decay in data, where  $\sigma^{\text{reweighted,data}}$  is the statistical uncertainty of the measurement. The value of  $A_{det}$  to be considered for a target decay is:

$$A_{det}^{\text{reweighted,data}} \pm \sigma^{\text{reweighted,data}} \pm \Delta A_{det}^{\text{reweighted,MC}},$$

where  $\Delta A_{det}^{\text{reweighted,MC}}$  is considered as a systematic uncertainty.

5. if  $\Delta A_{det}^{\text{reweighted,MC}} \geq \Delta A_{det}^{MC}$ , the weighting method should not be applied and the value measured in control channel,  $A_{det}^{\text{control,data}} \pm \sigma^{\text{control,data}}$  (see Eqs. 3.13-3.15), should be considered. The value of  $A_{det}$  to be considered for a target decay is:

$$A_{det}^{\text{control,data}} \pm \sigma^{\text{control,data}} \pm \Delta A_{det}^{MC},$$

where  $\Delta A_{det}^{MC}$  is taken as a systematic uncertainty.

If the systematic uncertainty of  $A_{det}$  limits the precision of the target  $A_{det}$  measurement, one could revisit the control decay selection in the initial step and iterate the procedure to possibly reduce the systematic uncertainty on  $A_{det}$ . On the other hand, if the target  $A_{CP}$  asymmetry measurement is statistically limited, one could choose to stop at step 2 and assign  $\Delta A_{det}^{MC}$  as a systematic uncertainty to the value of  $A_{det}^{\text{control,data}}$  as in step 5.

In step 4, the weights to be used in data are those determined from simulation, although it is known that simulation does not reproduce well the CDC hits distribution observed in data. Therefore, a further data-MC correction must be determined, or an additional systematic uncertainty must be considered. Alternately, one could obtain weights from the data by using background-subtracted distributions of target and control decays.

### 3.4.8 Summary

This work improves over a study conducted on early data by using a larger data set, refining the selection criteria, and correcting for the previously neglected forward-backward production asymmetry of  $D$  mesons. I investigated the dependence of the instrumental asymmetries on the particle momentum, and polar angle, and the number of CDC hits associated with each track, observing a significant variation in  $A_{det}$  as a function of CDC hits.

I developed a method to address the sample dependence resulting from the observed dependencies of the instrumental asymmetries, with the goal of determining the correction values necessary for the measurement of  $A_{CP}$  asymmetries in various  $B$  decays. This method was tested on several control channels using simulation, revealing that the selection criteria applied to the control samples can significantly hinder the accurate determination of the instrumental asymmetries for the target decays. Consequently, this finding indicates that further investigations are required to identify possible other dependencies that have not yet been considered. I also proposed a strategy to assess the systematic uncertainty that accounts for potential discrepancies between the instrumental asymmetry value determined from control channels and the value needed to correct  $A_{CP}$  asymmetries in  $B$  decays. This work has been applied in the analyses of the decays  $B^+ \rightarrow \rho^+ \rho^0$  [116],  $B \rightarrow K\pi$ , and  $B \rightarrow \pi\pi$  [115], as well as in the analysis of  $B \rightarrow K^* \gamma$  (submitted to JHEP). For these analyses, the  $A_{det}$  values were determined using the full Run I data set, corresponding to an integrated luminosity of  $365 \text{ fb}^{-1}$ .



# Chapter 4

## Data samples and selection

*This chapter describes the samples for the analysis. I introduce the experimental and simulated data along with their corrections, provide an overview of the background sources, and outline the requirements to reconstruct and select the signal. As general principle of the selection process, I prioritise higher signal purity over greater efficiency, as the precision on  $|V_{cb}|$  is not expected to be limited by the sample size. I conclude with the calculation of the signal efficiency and a description of the expected sample composition.*

### 4.1 Experimental and simulated data

The Belle II experiment started data taking in March 2019, accumulating electron-positron collision data corresponding to an integrated luminosity of about  $428 \text{ fb}^{-1}$  until July 2022 [117]. This is referred to as the Run I sample. After approximately 1.5 years of shutdown to upgrade both SuperKEKB and Belle II, Run II started in February 2024, with the goal of reaching an instantaneous luminosity of  $2 \times 10^{35} \text{ cm}^{-2}\text{s}^{-1}$ . In this work, I use Run I data ( $365 \text{ fb}^{-1}$ ) collected at the energy of the  $\Upsilon(4S)$  resonance to reconstruct the signal modes, and data ( $43 \text{ fb}^{-1}$ ) collected at an energy of 60 MeV below the  $\Upsilon(4S)$  mass to study the continuum background. This latter sample is henceforth referred to as “off-resonance” data.<sup>1</sup>

Simulated data are also used in physics analyses and play a key role. These data are generally used to study event selections, calculate efficiencies, model distributions, and validate analysis procedures. Simulated samples are based on the Monte Carlo approach. Monte Carlo samples are produced using event generators, which are computer programs that use pseudo-random number generators to produce sets of four-vectors reproducing the final states of  $e^+e^-$  collisions according to theoretical models of particle kinematic properties and interactions.

Figure 4.1 shows a sketch of the generation sequence for a hadronic event in Belle II. The properties of virtual photons, created in the electron-positron annihilation, and their subsequent splitting into a quark-antiquark pair are generated with KKMC [118] followed by PYTHIA8 [119] to simulate their hadronisation which in turn produces the observed hadrons. The decay of the heavy hadron (top right corner in Fig. 4.1), like  $B$  or  $D$  mesons, is simulated according to the EvtGen model [120] for known decays and using PYTHIA8 for unmeasured decays. The relative proportions among decay modes are based on known values or upper limits when available [14], and on arbitrary or educated guesses otherwise.

---

<sup>1</sup>The remaining part of the Run I sample ( $20 \text{ fb}^{-1}$ ) was collected at an energy higher than the  $\Upsilon(4S)$  resonance and it is used for exotic spectroscopy analyses.

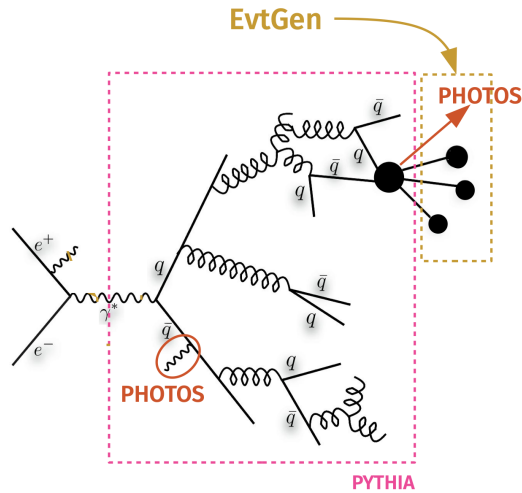


Figure 4.1: Sketch of the various portions of each simulation step of a hadronic event in Belle II. See the description in the text.

The photon emission by final-state charged particles is simulated using PHOTOS [121]. The light quark-antiquark ( $q = u, d, s, c$ ) pairs are generated with PYTHIA8.

Generated data are then subjected to detector simulation, where models of the detector geometry and material are interfaced with models of interactions of particles with matter and signal formation to reproduce the expected values of the raw quantities observed in the detector. These are then processed and subjected to event reconstruction as if they were collision data. The resulting simulated data contain information about reconstructed particles and the generated true particles. By matching these sets of information, we can determine whether particles are reconstructed properly, identify the most frequent misreconstruction occurrences, and ascertain the principal backgrounds. This “truth-matching” procedure is useful for optimising selection requirements, calculating signal efficiencies, classifying sample components, and performing many consistency checks.

Regarding beam interactions, the simulation can be either *run-dependent* or *run-independent*. In run-dependent simulation, the  $e^+e^-$  interactions are modelled based on actual experimental conditions specific to different periods of data-taking. This approach closely mirrors the real conditions of the accelerator during the run. In contrast, run-independent simulation uses an approximation based on the average expected conditions of the experiment, without accounting for variations over time. In my thesis, I use run-dependent simulation to ensure a more accurate representation of the experimental environment.

I use different types of simulation samples in the analysis.

For background and validation studies, I use centrally produced simulated samples corresponding to four times the size of the Run I data set. These include:  $e^+e^- \rightarrow q\bar{q}$ , where  $q = u, d, c, s$ , and  $e^+e^- \rightarrow B\bar{B}$  events. For signal studies, the exclusive samples are filtered from the  $e^+e^- \rightarrow B\bar{B}$  events, with one  $B$  meson constrained to decay into the signal channels  $B \rightarrow D\ell\nu_\ell$  and  $B \rightarrow D^*\ell\nu_\ell$  and while the other  $B$  can undergo all possible decays. These are called signal samples. The different topologies of these two categories of events are shown in Fig 4.2.

In signal samples, the BGL decay model of EvtGen is used for the signal to mirror the most up-to-date measurements of the form factors, assuming the BGL parametrisation [45, 122]. The values of the form factors used in the generation are reported in Tab. 4.1. More

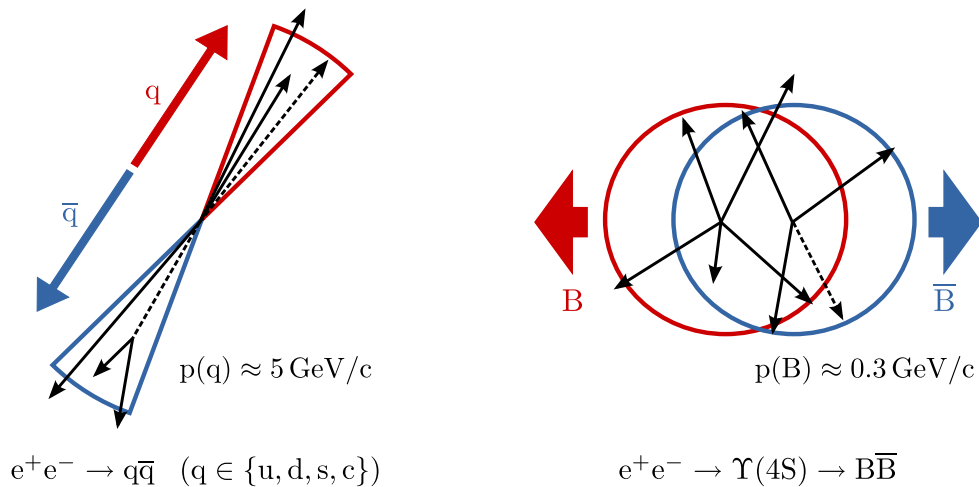


Figure 4.2: Event-shape sketch for the (left) continuum and (right)  $B$ -meson events in the  $\Upsilon(4S)$  frame.

details about the nomenclature used for the form factor can be found in Appendix A.

The charm mesons are forced to decay into their Cabibbo favoured modes,  $\bar{D}^0 \rightarrow K^+\pi^-$  and  $D^- \rightarrow K^+\pi^-\pi^-$ . The  $D^- \rightarrow K^+\pi^-\pi^-$  decay is generated using the `EvtGen` model `D_DALITZ`, which is designed to simulate three-body decays of  $D$  mesons using information from a Dalitz plot analysis [123]. This model employs amplitudes that describe intermediate resonant and non-resonant states which determine the distribution of momenta and directions of the decay products. The  $D^*$  mesons decays into all final states, *i.e.*, a  $\bar{D}^0$  or  $D^-$  with either a pion (charged or neutral) or a photon, with known proportions.

In addition, I use also simplified simulated data (“toy”), which are based on the random generation of few distributions of interest from histograms (“templates”) obtained with the full realistic simulation described above. These simplified data are primarily employed for prototyping the analysis, studying estimator properties, and assessing systematic uncertainties (see Sect. 6.5-7.1).

#### 4.1.1 Corrections to the data

There are two types of corrections that are considered for data. Experimental data can be corrected for known biases in the measurement of particle kinematics, such as the correction to adjust the measured momentum, also known as momentum-scale correction, and the correction to adjust the measured energy of photons, referred to as photon energy bias. These corrections can be considered data calibrations. At Belle II, the momentum-energy scale for tracks, energy bias for photons, and bremsstrahlung correction for electrons are all taken into account.

Another type of corrections concerns the simulation. Differences between simulated and experimental data are a primary source of systematic uncertainties. For instance, requirements on particle identification (PID) often lead to a different selection efficiency between simulated and experimental data due to simulation mismodelling of PID variable distributions. When this occurs, measurements of branching fractions are biased and must be corrected, assigning a systematic uncertainty. To minimise these systematic uncertainties, one approach is to adjust the simulated distributions to better match the data or to directly calculate the efficiencies from the experimental data using control samples. In the

Process	EvtGen model	Branching fraction	Parameters	
$B \rightarrow D\ell\nu_\ell$	BGL	$\mathcal{B}(B^0 \rightarrow D^-\ell^+\nu_\ell) = 2.14\%$	$a_0^{f^+} = 0.0126$	$a_1^{f^+} = -0.094$
		$\mathcal{B}(B^+ \rightarrow \bar{D}^0\ell^+\nu_\ell) = 2.31\%$	$a_2^{f^+} = 0.34$	$a_3^{f^+} = -0.1$
$B \rightarrow D^*\ell\nu_\ell$	BGL	$\mathcal{B}(B^0 \rightarrow D^{*-}\ell^+\nu_\ell) = 5.11\%$ ,	$a_0^g = 0.02596$	$a_1^g = -0.06049$ ,
		$\mathcal{B}(B^+ \rightarrow \bar{D}^{*0}\ell^+\nu_\ell) = 5.49\%$	$a_0^f = 0.01311$	$a_1^f = 0.01713$
			$a_1^{F_1} = 0.00753$	$a_2^{F_1} = -0.09346$
$D^* \rightarrow DX$	PHSP	$\mathcal{B}(D^{*-} \rightarrow \bar{D}^0 X) = 67.7\%$	-	
		$\mathcal{B}(D^{*-} \rightarrow D^- X) = 32.3\%$	-	
$\bar{D}^0 \rightarrow K^+\pi^-$	PHSP	$\mathcal{B}(\bar{D}^0 \rightarrow K^+\pi^-) = 3.95\%$	-	
$D^- \rightarrow K^+\pi^-\pi^-$	DALITZ	$\mathcal{B}(D^- \rightarrow K^+\pi^-\pi^-) = 9.38\%$	-	

Table 4.1: Values used in the generation of the signal samples. The ratio of the branching fractions of the  $\Upsilon(4S)$  decaying to charged and neutral  $B$  mesons,  $f_{+-}/f_{00}$ , is set to 1.066. For the  $B^0$  and  $B^+$  branching decays, isospin symmetry is assumed: their branching fractions are linked by the lifetimes ratio  $\tau_{B^0}/\tau_{B^+} = 0.929$ ; their form-factor parameters (last column) for the BGL model are the same.

Belle II simulation, there are known mismodellings that are corrected for with standard procedures using control channels. These mismodellings pertain to PID, tracking, photon, and  $\pi^0$  reconstruction efficiencies.

Which data and simulation corrections must be applied and which are negligible depends on each specific analysis. Those relevant in this work are the corrections for track momentum scale, photon energy bias, electron bremsstrahlung, lepton and hadron PID and tracking efficiency. They are briefly outlined in what follows. These are applied to the samples in an early stage and propagated through all the analysis. Uncertainties on the corrections are propagated as systematic uncertainties (see Chapter 7).

Finally, simulations can also be corrected for outdated (or incorrect) models or input parameters (such as a branching fraction or a particle lifetime) used in generators. The resulting biases are independent from experimental effects and can be addressed by correcting the inputs and generating new samples or by employing a weighting technique to adjust the simulated data. This will be considered for some specific  $B$  decay modes in Chapter 5.

#### 4.1.1.1 Track momentum scale

To correct for any mismodelling in the magnetic field map, run-period-dependent corrections to track momenta are applied. The corrections are determined by the Belle II tracking group using a control sample of  $D^{*+} \rightarrow D^0[\rightarrow K^-\pi^+]\pi^+$  decays and are applied as a global scale factor of 0.99987 to the experimental data. The corrections have been validated with additional channels  $D^+ \rightarrow K^-\pi^+\pi^+$ ,  $D^0 \rightarrow K^-\pi^+\pi^-\pi^+$ ,  $\Lambda_c^+ \rightarrow p^+K^-\pi^+$ ,  $K_S^0 \rightarrow \pi^+\pi^-$  and  $J/\Psi \rightarrow \ell^+\ell^-$  ( $\ell = e, \mu$ ).

#### 4.1.1.2 Photon energy bias

Photon energy bias corrections are essential to account for systematic deviations in the measured energy of photons, ensuring a more accurate representation of their true energy and improving the agreement between simulation and experimental data. The corrections

of photon energy resolution and bias that need to be applied to the experimental data are provided by the Belle II neutral group, using symmetric decays of  $\pi^0 \rightarrow \gamma\gamma$  and  $\eta \rightarrow \gamma\gamma$ , which cover a photon energy range from 20 MeV to 2 GeV. The latter corrections are applied centrally during the reconstruction process.

#### 4.1.1.3 Electron bremsstrahlung

Due to their small mass, a significant number of electrons can radiate a bremsstrahlung photon while traversing the detector. The bremsstrahlung corrections allow for the adjustment of the electron momentum by adding the momentum carried by the radiated photon, which is reconstructed as an ECL cluster nearby the electron track. This is implemented during the decay reconstruction using an analysis module provided by the Belle II performance group. The corrections are applied to both experimental and simulated data.

While testing their performance, I observe no improvement in the electron energy resolution when applying the bremsstrahlung corrections. On the other hand, I found that these corrections have an impact on two important aspects: (i) it increases the background fraction of the sample; (ii) it sculpts the shape of a background (specifically the one originating from real- $D$  mesons, which will be explained in Sect. 5.2) making it more similar to the signal in some key distributions used to determine the sample composition (through the fit that will be described in Chapter 6). Therefore, after reporting my findings to the Collaboration, I have decided not to apply the bremsstrahlung corrections.<sup>2</sup>

#### 4.1.1.4 Lepton and hadron PID

Corrections to the efficiency of lepton and hadron PID requirements are obtained using control samples where signal tracks are selected without any PID cuts. From these control samples, the corrections are derived as a function of track momentum and polar angle. I use a framework [124] provided by the Belle II PID group, which includes the following control modes:  $J/\psi \rightarrow \ell^\pm \ell^\mp$ ,  $e^+e^- \rightarrow \mu^+\mu^-\gamma$ , and  $e^+e^- \rightarrow (e^+e^-)\ell^\pm \ell^\mp$  to compute efficiency corrections for lepton PID requirements, and  $e^+e^- \rightarrow \tau^\pm[\rightarrow 3\pi^\pm\nu_\tau]\tau^\mp[\rightarrow \ell^\mp\nu_\ell\nu_\tau]$  for misidentification rates (colloquially referred to as fake leptons);  $D^{*+} \rightarrow D^0[\rightarrow K^-\pi^+]\pi^+$  for kaon PID requirements, and  $K_S^0 \rightarrow \pi^+\pi^-$  for misidentification rates (fake pions).<sup>3</sup> The framework has the flexibility to compute the corrections for a given PID requirement and particle species as a function of the track momentum and polar angle. I apply the corrections to my simulated data through per-candidate weights, shown in Fig. 4.3, computed from the framework.

#### 4.1.1.5 Tracking efficiency

The corrections for the tracking efficiency are calculated by the Belle II tracking group using the control decay  $e^+e^- \rightarrow \tau^+\tau^-$  where one tau lepton decays leptonically ( $\tau^\pm \rightarrow \ell^\pm\nu_\ell\bar{\nu}_\tau$ ,  $\ell = e, \mu$ ) while the other decays hadronically into three charged pions ( $\tau^\pm \rightarrow 3\pi^\pm \pm \nu_\tau + n\pi^0$ ). The tracking efficiency is measured to be  $1.0000 \pm 0.0024$  in the momentum range 0.2-3.5 GeV/ $c^2$ . Therefore no correction is applied to the simulated data, while its uncertainty will be taken into account as systematic uncertainty for each track (see Chapter 7). The efficiency is considered independent for each track.

<sup>2</sup>The bremsstrahlung-correction module is now under review by the Collaboration.

<sup>3</sup>There are additional control channels for protons and pions which are not listed here as I do not impose PID selection for those particles.

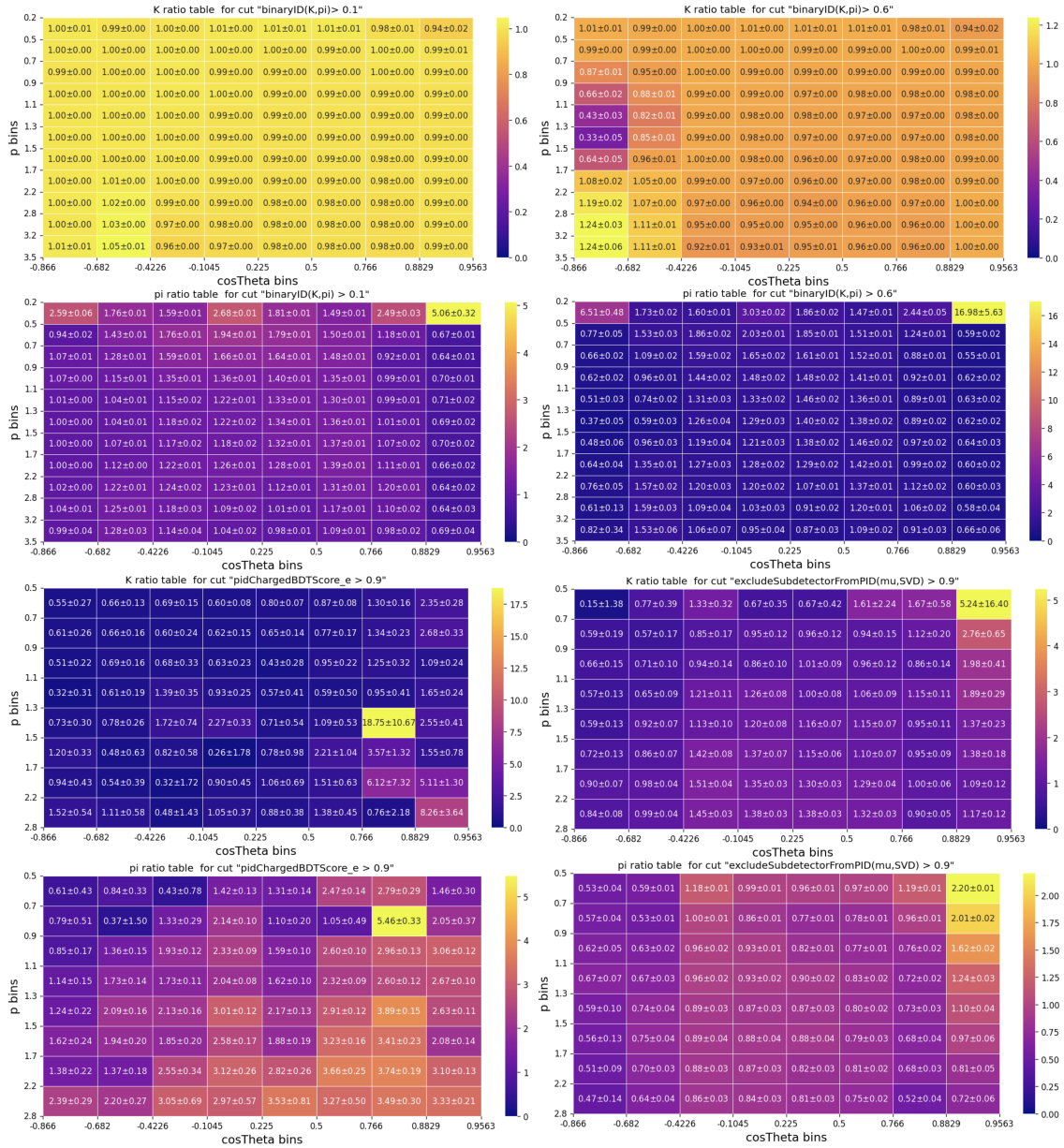


Figure 4.3: Efficiencies and fake rate corrections for the given hadron PID requirements are shown in the top and middle. The last rows display only the fake rate corrections for the lepton PID requirements, but not the efficiencies, as the latter are applied centrally using the tables provided by the Belle II performance group.

#### 4.1.2 Sample components

Before delving into the selection of the sample, I categorise it into components according to the possible origin of the reconstructed particles in the final state. This is useful to tailor possible selections that target a specific background. I have identified five general sample components:

1. **Signal:** the reconstructed particles pertain to the signal decays

$$B^0 \rightarrow D^- [\rightarrow K^+ \pi^- \pi^-] \ell^+ \nu_\ell, \quad B^+ \rightarrow \bar{D}^0 [\rightarrow K^+ \pi^-] \ell^+ \nu_\ell, \quad B^0 \rightarrow D^{*-} [\rightarrow D^- [\rightarrow K^+ \pi^- \pi^-] X] \ell^+ \nu_\ell, \quad \text{and} \quad B^+ \rightarrow \bar{D}^{*0/+} [\rightarrow \bar{D}^0 [\rightarrow K^+ \pi^-] X] \ell^+ \nu_\ell.$$

only partially reconstructed ( $X$  indicates the undetected particle) while the  $D$  mesons are properly reconstructed. The lepton is either an electron or a muon.

2.  **$X\ell\nu_\ell$  background:** the reconstructed particles originate from a semileptonic  $B$  meson decay different from the signal. In this category, I identify:
  - excited charm-meson cascade decays to  $D$  ground states, *i.e.*, a properly reconstructed  $D$  meson not originate from a parent  $B$  but coming from a cascade decay. These are  $B \rightarrow D^{**}\ell\nu_\ell$  decays, where  $D^{**}$  is short-hand for the  $D_0^{*(0,+)}(2300)$ ,  $D_1^{(0,+)}(2420)$ ,  $D_1^{\prime(0,+)}(2430)$  and  $D_2^{*(0,+)}(2460)$  states, the non-resonant  $D^{(*)}\pi(\pi)$  contribution and the  $D^{(*)}\eta$  contribution (see Sect. 5.3.1), unless specified otherwise.
  - semitauconic decays, where the  $\tau$  lepton decays into a muon or an electron. The  $D$  candidates are either coming from a  $B$  meson or from a cascade decay.
  - semileptonic decays as the signal or as those of the above two items, but where the lepton is misidentified.
3. **Real- $D$  background:** combinatorial with a real  $D$  meson, *i.e.*, a random combination of a properly reconstructed  $D$  candidate and either a true or a misidentified lepton. This background is mostly due to the combination of a charm meson and a lepton from two different  $B$  decays and to the combination of a real  $D$  meson and a misidentified lepton, originating from either the same or a different  $B$  decay of the  $D$  candidates (see Sect. 5.2).
4. **Fake- $D$  background:** combinatorial with a fake  $D$  meson, *i.e.*, a random combination of a wrongly reconstructed  $D$  candidate and either a true or a misidentified lepton.
5. **Continuum background:** particles from  $e^+e^- \rightarrow q\bar{q}$ , where  $q$  is either a  $u$ ,  $d$ ,  $c$  or  $s$  quark. The majority of the reconstructed charm candidates comes from  $e^+e^- \rightarrow c\bar{c}$  events, with a small contribution from random combination of tracks. The lepton originates from a secondary decay of an hadron.

This general classification is sufficient to understand the selection requirements described in this chapter; more details on the composition and modelling of the background categories are provided in Chapter 5.

## 4.2 Event selection

Semileptonic  $B$  decays contribute significantly to the total  $B$  decay width: when efficiently reconstructed, they can yield large data samples. Signal events are easily identified through the pairing of a lepton and a charm meson. Signal leptons typically carry large momenta on average, making them distinguishable from leptons originating from secondary semileptonic decays. Additionally, charm decays exhibit narrow peaks in invariant mass distributions, which help discriminate them from combinatorial backgrounds.

However, the signal presents a key experimental challenge. The undetected neutrino leads to incomplete decay kinematics. The only way to access the full kinematics is to reconstruct both the signal and the decay of the accompanying  $B$  meson from  $\Upsilon(4S)$  events. This *tagging* method, however, has a very low efficiency, generally less than 1% [82]. My analysis, instead, is *untagged*: I reconstruct only the signal side to retain a larger sample.

I access the decay kinematics using proxy variables; this latter point will be explained in Chapter 6. Here, I focus on the signal selection.

In addition to providing large samples, untagged analyses are well-suited for measurements of branching fractions, and ultimately  $|V_{cb}|$ , for another reason. Calculating the efficiency of the tagging algorithms is challenging, and the associated uncertainties are often on the order of a few percent, which can significantly affect the precision of branching fraction measurements and, consequently,  $|V_{cb}|$ . On the other hand, while untagged analyses lack powerful discriminating handles, they are more prone to background contamination. Significant background contamination is a concern both for diluting statistical precision and for introducing systematic uncertainties associated with background modelling. To minimise the latter, which might be especially harmful for the signal with partial  $D^*$  reconstruction, I opt for a selection strategy that favours signal purity over efficiency. This principle guides the selection requirements described in the following sections.

### 4.2.1 Skim selection

In Belle II, numerous physics topics are explored, leading to the repeated analysis of data by hundreds of collaborators. To streamline the simultaneous analysis of such a vast data set, several centralised data processing stages are employed.

Initially, raw data undergo central processing to produce summary data, which is more compact and highlights higher-level information pertinent to physics analysis, such as four-momenta, vertices, and particle-identification variables.

The next central step involves applying broad selection criteria to the summary data to create analysis-specific subsets, known as *skims*, which are further reduced in size, with typical retention rate of about 5%. This process allows each collaborator to access and process the data quickly. This is the first selection stage. An optimal skimming is important because any signal inefficiency that occurs at this stage is laborious to recover. After skimming, each collaborator can work with a reduced data sample, which can be easily reprocessed multiple times to refine the selection according to the analysis target.

For my analysis, I devise a skim for untagged  $B \rightarrow D\ell\nu_\ell$  decays. To be considered, an event must pass at least one of the HLT triggers (see Sect. 3.2.4) designed to select only hadronic events. I require tracks have a distance of the closest approach to the interaction point (IP) in the  $r$ - $\phi$  plane of less than 1 cm, an absolute relative distance in the  $z$  direction of less than 3 cm, and to lie within the acceptance range of the central drift chamber (CDC),  $17^\circ$  to  $150^\circ$ . Tracks that pass these conditions are referred to as “good tracks”. They have very high chance to originate from  $e^+e^- \rightarrow Y(4S) \rightarrow B^-B^+$  decays. A pion-mass hypothesis is assigned to calculate the full four-momentum of these tracks.

Tracks must be associated with final-state particles of the signal, where the lepton can either be an electron or a muon. To select electrons candidates, a BDT-based particle identification is used; to select muons, a combination of subdetectors likelihoods; to select kaons, the binary kaon-vs-pion likelihoods. At this stage, the requirements yield nearly 100% signal efficiency while significantly reducing the background.

The  $D$  mesons are reconstructed in the decay modes  $\bar{D}^0 \rightarrow K^+\pi^-$  and  $D^- \rightarrow K^+\pi^-\pi^-$  from the selected kaons and pions candidates. I require the  $D$  meson masses to be between 1.80 and 1.95  $\text{GeV}/c^2$ . This range is large compared to the mass resolution (about 3  $\text{MeV}/c^2$ ), but it allows to retain regions enriched of continuum and fake- $D$  background to study those components, as explained in the next chapter 5. The  $D$  and lepton candidates are combined into a composite system labelled  $Y$ . A kinematic fit, `TreeFitter` [125], is performed on the full  $Y$  decay chain using a Belle II fitter module. The fit must converge

with a  $\chi^2$  probability larger than 1%.

All other good tracks in the event as well as calorimeter clusters are used to form the rest of the event (ROE). Finally, I require the total visible energy, the sum of all energies of the visible particles in the event in the centre-of-mass system, to be greater than 4 GeV and the ratio  $R_2$  between the second and zero-th Fox-Wolfram moments be less than 0.4. The latter is a quantity that captures the geometric features of the spatial distributions of final-state particles to distinguish between continuum collimated jets and the isotropically distributed final-state particles from  $B\bar{B}$  events. It uses information from both signal and ROE. The skim requirements effectively reduce the data set, allowing the signal reconstruction code to be run on the selected data from the full Run I sample in approximately two hours on central processing computers.

### 4.2.2 Final selection

After the skimming the selection needs to be refined. As the main concern is potential large systematic uncertainties from background modelling, the primary target of this final selection is to increase signal purity. Tab. 4.2 summarises all the requirements which are described as follows.

The lepton momentum is required to be larger than 0.8 GeV/ $c$  to reduce contamination from secondary semileptonic decays. I also require the  $D$  meson momentum be larger than 0.5 GeV/ $c$  to reduce the background from hadronic  $B$  decays (Fig. 4.4). I apply tighter requirements on the PID variables for kaons, electrons and muons, as to further reduce the amount of misidentified decays. The specific thresholds are reported in Tab. 4.2. These thresholds correspond to a PID efficiency of approximately 95% for kaons and leptons.

The  $D$  candidates exhibit narrow peaks in the invariant mass distribution. To suppress background from fake- $D$  and continuum events, I select a mass range of approximately twice the mass resolution around the expected mass value. Specifically, the mass ranges are 1.86–1.87 GeV/ $c^2$  for  $m(K\pi)$  and 1.865–1.874 GeV/ $c^2$  for  $m(K\pi\pi)$  (Fig. 4.4). Additionally, for the  $K\pi\pi$  candidates, I require the momentum of the slower pion,  $p_\pi$ , be greater than 0.35 GeV/ $c$ , to reduce systematic uncertainty related to the tracking-efficiency correction for slow tracks. All other tracks have negligible candidates below this momentum threshold, so no additional requirement is necessary.

I require  $m(Y)$ , the invariant mass of the  $D\ell$  system ( $Y$ ), to be greater than 3.2 GeV/ $c^2$ . This selection reduces significantly the fraction of the real- $D$  component in the samples (Fig. 4.4). Knowledge of initial-state energy enables useful kinematic constraints for the selection. The cosine of the angle between the three-momentum of the  $B$  meson and the  $Y$  system,  $\cos\theta_{BY}$ , can be fully determined by assuming only a missing neutrino in the decay. This variable reads

$$\cos\theta_{BY} = \frac{2E_B E_Y - m_B^2 - m_Y^2}{2|\vec{p}_B||\vec{p}_Y|} \quad (4.1)$$

where  $E_B$  is given by half of the measured  $e^+e^-$  energy,  $\sqrt{s}/2$ , and the magnitude of the  $B$  momentum,  $|\vec{p}_B|$ , can be determined by this energy assuming the known value of the  $B$  mass. The momentum and mass of the  $Y$  system are fully determined from the measured four-momenta of the  $D$  and lepton candidates. All quantities in Eq. 4.1 are calculated in the centre-of-mass frame. By construction, for  $B \rightarrow D\ell\nu_\ell$  decays  $\cos\theta_{BY}$  should be constrained to the range between  $-1$  and  $1$ . For  $B \rightarrow D^*\ell\nu_\ell$  decays, the  $\cos\theta_{BY}$  is shifted to lower values, having values that range approximately between  $-2$  and  $1$  due to the presence of the unreconstructed particle in  $D^*$  decays. The distribution for  $X_c\ell\nu_\ell$

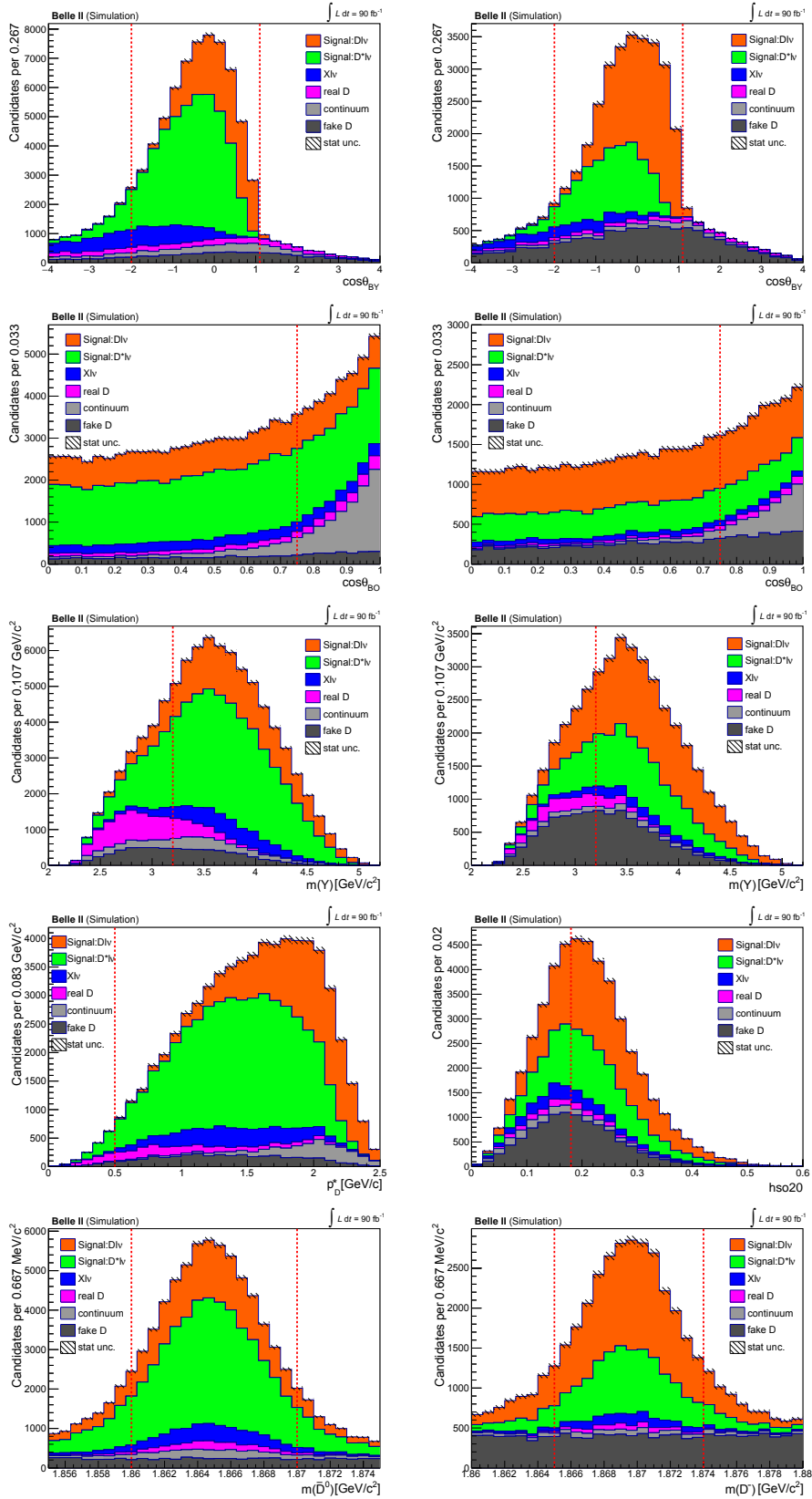


Figure 4.4: Some requirements applied in the final selection for the (left)  $\bar{D}^0 e^+$  and (right)  $(D^- e^+)$  sample. The plots are shown for N-1 requirements, where all but one requirements are applied, allowing for the evaluation of each individual impact. The muon samples are not shown, but exhibit similar features.

Object	Requirement
Signal tracks	$ dr  < 1 \text{ cm}$ $ dz  < 3 \text{ cm}$ polar angle in $[17^\circ, 150^\circ]$
ROE tracks	$ dr  < 1 \text{ cm}$ $ dz  < 3 \text{ cm}$
Hadrons	kaon PID $> 0.1$ ( $0.6$ ) for the $\bar{D}^0$ ( $D^-$ ) sample $p_\pi > 0.35 \text{ GeV}/c$ for the slowest pion of the $D^-$ decay
Leptons	muon PID $> 0.9$ electron PID $> 0.9$ $p^* > 0.8 \text{ GeV}/c$
$D$ mesons	$p^* > 0.5 \text{ GeV}/c$ $m(\bar{D}^0) \in [1.86, 1.87] \text{ GeV}/c^2$ $m(D^-) \in [1.865, 1.874] \text{ GeV}/c^2$
Continuum suppression	$\cos \theta_{BO} < 0.75$ $R2 < 0.4$ Total energy in the event $> 4 \text{ GeV}$ $hso20 > 0.18$ for the $D^-$ sample
$B$ candidate	$m(Y) > 3.2 \text{ GeV}/c^2$ $\cos \theta_{BY} \in [-2, 1.1]$ kinematic fit $\chi^2$ probability $> 1\%$ when multiple, one random candidate selected

Table 4.2: Summary of the selection. See the description in the text for the definition of the variables.

background is further shifted, as extra particles are missing. Other background components feature long tails extending outside the range  $[-2, 1]$  (Fig 4.4). Therefore, I require  $\cos \theta_{BY}$  be bounded between  $-2$  and  $1.1$ . The limit higher than  $1$  accounts for a tails of the signal due to experimental resolution.

To further suppress continuum, I tighten the selection on the cosine of angle between thrust axis of the signal  $B$  meson and ROE thrust axis,  $\cos \theta_{BO}$  (Fig. 4.4). For the  $D^+$  sample, which has a larger continuum component, I also apply a selection on the modified Fox-Wolfram moment  $hso20$  [126] to further reduce this background.

After applying these selections, the fraction of events with more than one  $B$  candidate are reported in Tab. 4.3. All multiplicities are below  $1\%$ . I restrict the samples to one candidate per event by randomly selecting one.

Sample	Data	Simulation
$\bar{D}^0 e^+$	1.003	1.004
$D^- e^+$	1.009	1.007
$\bar{D}^0 \mu^+$	1.003	1.005
$D^- \mu^+$	1.009	1.009

Table 4.3: Candidates multiplicity in data and simulation after the selection.

### 4.3 Signal efficiency

The signal efficiency is calculated using simulated data and is typically defined as the ratio

$$\varepsilon_i^\ell = \frac{N_{i,r}^\ell}{N_{i,g}} \quad (4.2)$$

where  $N_{i,r}^\ell$  is the number of reconstructed signal candidates for the decay  $i$  and lepton  $\ell$  passing the selection (including the truth-matching for the signal), and  $N_{i,g}$  is the number of generated decays of type  $i$ . The latter is the same for electron and muon, because lepton flavour universality is assumed. The number of reconstructed signal candidates is directly evaluated by counting those that pass the truth-matching and the final selection.

For the signal samples, the number of generated decays is set when producing the sample (typically, a few million decays). From the sample of generic  $\Upsilon(4S) \rightarrow B\bar{B}$  decays, the number of generated decays are

$$N_{i,g} = \mathcal{L} \sigma f^j \mathcal{B}_i \mathcal{B}_{i,s}, \quad (4.3)$$

where  $\mathcal{L}$  is the total luminosity of the simulated sample,  $1444 \text{ fb}^{-1}$ ;  $\sigma$  is the cross section of the  $\Upsilon(4S)$  production,  $1.05 \text{ nb}$ ;  $f^j$  is either  $f_{+-}$  or  $f_{00}$ , the decay rates of  $\Upsilon(4S)$  into charged and neutral  $B$ -meson pairs,  $0.515$  and  $0.483$ ;  $\mathcal{B}_i$  is the branching fractions of the signal  $i$ ;  $\mathcal{B}_{i,s}$  is the (product of the) branching fraction(s) of charm meson decays. All branching fractions are reported in Tab. 4.1. Note that for the  $\bar{D}^0 \ell^+ \nu_\ell$  final state, the contributions to consider come specifically from the  $B^+ \rightarrow \bar{D}^0 \ell^+ \nu_\ell$  decays and both  $B^+ \rightarrow \bar{D}^{*0} \ell^+ \nu_\ell$  and  $B^0 \rightarrow D^{*-} \ell^+ \nu_\ell$ , since the  $D^{*-}$  can decay both into a  $\bar{D}^0$  and a  $D^-$  meson. To the  $D^- \ell^+ \nu_\ell$  final state, from the decays  $B^0 \rightarrow D^- \ell^+ \nu_\ell$  and  $B^0 \rightarrow D^{*-} \ell^+ \nu_\ell$ .

The numbers of the generated and reconstructed decays and the signal efficiencies are reported in Tab. 4.4 for both electron and muon samples. I categorize them according to the final state, hence, I sum the  $B^0$  and  $B^+$  contributions for the  $\bar{D}^0 \ell^+ \nu_\ell$  final state.

The difference in efficiency between  $\bar{D}^0$  and  $D^-$  arises from a combination of selection requirements and vertex fit probability. Specifically,  $D^-$  involves three tracks, while  $\bar{D}^0$  has only two, resulting in a lower fit probability for  $D^-$  and consequently reducing the number of reconstructed signal events. Additionally, the difference in efficiency between the electron and muon modes arises because muon tracks are typically easier to identify and reconstruct. In contrast, electron tracks can radiate bremsstrahlung photons, leading to energy loss and making their reconstruction and identification more challenging.

### 4.4 Expected sample composition

After the selection, I obtain samples dominated by signal events, with relative proportions of approximately 80% and 70% for the  $\bar{D}^0 \ell^+$  and  $D^- \ell^+$  samples, respectively. The fractions

Final state	$N_{f,g}$	$N_{f,r}^e$	$N_{f,r}^\mu$	$\varepsilon_f^e$ [%]	$\varepsilon_f^\mu$ [%]
$\overline{D}^0 \ell^+$	746 408	253 457	266 688	$33.96 \pm 0.08$	$35.73 \pm 0.08$
$\overline{D}^{*0} \ell^+$	2 818 431	838 238	945 934	$29.74 \pm 0.04$	$33.56 \pm 0.04$
$D^- \ell^+$	1 540 010	208 147	218 968	$13.52 \pm 0.03$	$14.22 \pm 0.03$
$D^{*-} \ell^+$	1 187 773	121 587	135 955	$10.24 \pm 0.03$	$11.45 \pm 0.03$

Table 4.4: Number of generated and reconstructed signal decays into the final state  $f$  with lepton  $\ell$  ( $N_{f,g}$  and  $N_{f,r}^\ell$ ), and signal efficiencies ( $\varepsilon_f^\ell$ ). The uncertainty on the efficiency is statistical.

of each component are illustrated in the pie charts of Fig. 4.5. The  $\overline{D}^0 \ell^+$  sample contains a high proportion of  $D^*$  events. This is due to the mixture of decays from  $\overline{D}^{*0}$  and  $D^{*-}$ . The analysis involving partially reconstructed  $D^*$  mesons leads to a significant number of  $D^*$  decays, allowing for the first simultaneous analysis of the  $D$  and  $D^*$  samples at Belle II. Fake- $D$  candidates contribute the largest background fraction in the  $D^- \ell^+$  sample. This is due to a larger number of possible fake combinations with three tracks compared to two tracks. However, despite the relatively large size, this background can be constrained directly from data, as explained in Chapter 5. Continuum can be also constrained from data, as described in the same Chapter. Contribution from real- $D$  candidates represents a small fraction of the total background, while the dominant or second-dominant background arises from  $X\ell\nu_\ell$  candidates. A dedicated study to model these backgrounds will be discussed in Chapter 5. The devised selection allows me to work with samples expected to be rich in signal decays, with backgrounds that either constitute a small fraction of the signal or can be directly constrained from the data.

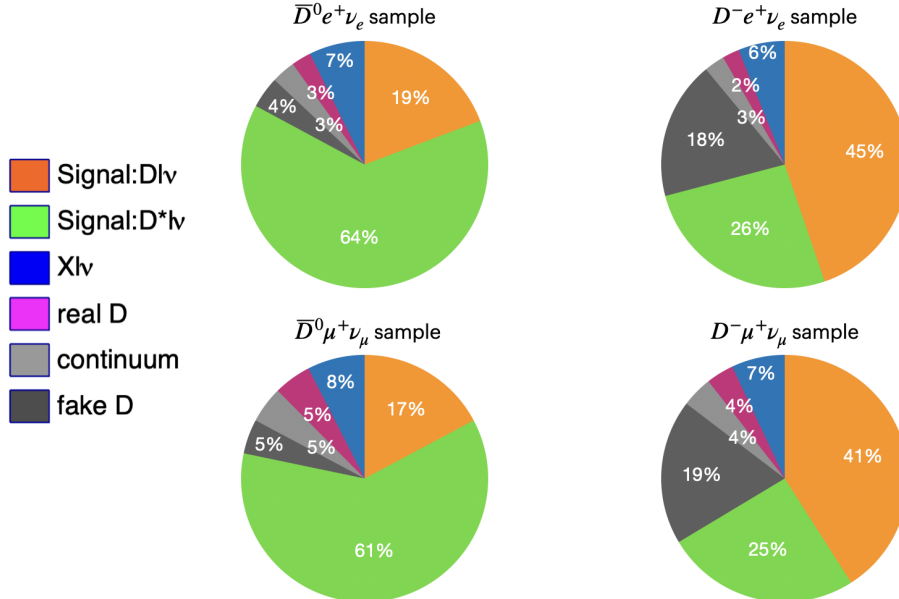


Figure 4.5: Composition of all the samples after the selection:  $B \rightarrow D\ell\nu_\ell$  in orange,  $B \rightarrow D^*\ell\nu_\ell$  in green, continuum processes in light grey, fake- $D$  mesons in dark grey, real- $D$  mesons in magenta and the  $X\ell\nu_\ell$  background in blue.



## Chapter 5

# Background modelling

The world's best measurements of  $|V_{cb}|$  are currently limited by systematic uncertainties, with background knowledge and modelling being major contributors to these limitations. A detailed study of the background composition is therefore crucial for developing strategies to constrain its contribution. In this chapter, I present a comprehensive analysis of each background component, along with the methods used to constrain them, both through control regions in the data and from previous measurements.

### 5.1 Fake- $D$ and continuum backgrounds

The fake- $D$  and continuum backgrounds can be constrained by using specific regions of the  $D$ -mass distribution that lie outside the signal peak, referred to as *sidebands*. In these regions, the fake- $D$  background is the dominant component, with the continuum background being the second most significant. Other components contribute small tails, leaking from the  $D$  peaks.

The sidebands are defined by the ranges 1.810–1.825  $\text{GeV}/c^2$  and 1.910–1.940  $\text{GeV}/c^2$  for both the  $D^- \ell^+$  and  $\bar{D}^0 \ell^+$  samples. These ranges are shown in the  $D$ -mass distributions in Fig. 5.1 for simulated data of the electron channels; the muon samples are not shown,

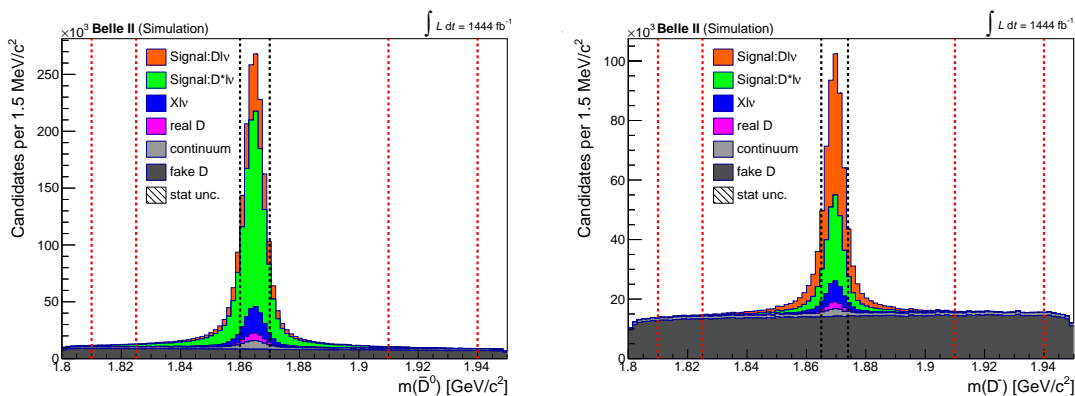


Figure 5.1: Distributions of the  $D$  mass for the (left)  $\bar{D}^0 e^+$  and (right)  $D^- e^+$  samples. The dashed red lines indicate the sidebands, which are used to constrain the contributions from fake- $D$  and continuum backgrounds, following the strategy outlined in the text. The dashed black lines denote the signal regions, as defined by the requirements detailed in the previous chapter. Muon samples exhibit very similar distributions.

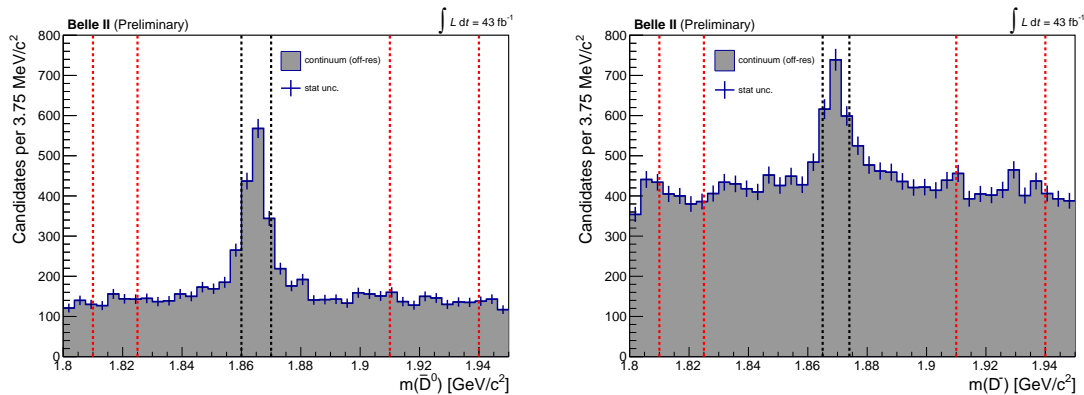


Figure 5.2: Distributions of the  $D$  mass of the off-resonance data for (left)  $\bar{D}^0 e^+$  and (right)  $D^- e^+$  sample. The dashed red (black) lines indicate the sidebands (signal regions).

but exhibit very similar distributions. A mixture of the left and right sidebands is used to mimic the kinematics of the background in the signal region. The left sideband is chosen to avoid a region polluted by background sources distinct from the fake- $D$  component in the signal region, primarily due to partially reconstructed  $D$  decays. Its range is also smaller, to minimise contamination from the tail of the  $D$  peaks. Sideband data are used to determine both the yields and the distributions of the fake- $D$  and continuum backgrounds in the signal region. To this end, certain corrections to the sideband data are applied.

First, the contributions from other components must be subtracted. This primarily concerns the left sideband of the electron and muon samples, which contains approximately 13% and 11% of signal  $B \rightarrow D^{(*)} \ell \nu_\ell$  candidates, respectively, due to the tail from the  $D$  peak. In contrast, the right sideband of both samples contains much smaller signal contributions, about 1% or less. The tail contributions are subtracted using simulated candidates, based on the known  $B \rightarrow D^{(*)} \ell \nu_\ell$  branching fractions [50]. While this introduces a potential circularity in the analysis, as the signal branching fractions are among the quantities being measured, the correction is small enough—even considering the uncertainty on the input branching fractions—to have no significant impact on the final results. Other contributions, apart from fake- $D$ , continuum backgrounds, and the signal, are sufficiently small in the sidebands and can therefore be safely neglected.

Second, the number of sideband candidates must be scaled. A scaling factor is calculated from simulation, as the width of the sideband is different from that of the signal region: 4.5 times larger for  $m(\bar{D}^0)$  and 5 times larger for  $m(D^-)$ . In addition, the background is not uniformly distributed: a slight slope is observed when moving from the left to the right sideband, as shown in Fig. 5.1. To determine the scaling factors for the two sidebands we use the simulation. We fit the 3D distribution of  $(\cos \theta_{BY}, p_\ell^*, p_D^*)$  of the signal-region background (fake- $D$  and continuum) with templates built from the sideband candidates<sup>1</sup>. The fit provides the fractions of the two sidebands required to model the signal region, which we use as scaling factors.

Finally, a missing contribution in the sideband must be accounted for. This is the peak in the signal region caused by candidates with a real- $D$  meson produced in  $e^+ e^- \rightarrow c\bar{c}$  events. To include this component, I use off-resonance data. I define the same sidebands and signal regions for the off-resonance data. Using the sidebands, I subtract the flat background contribution from the signal region to isolate the peak (see Fig. 5.2). Then,

<sup>1</sup>The variables are those used in the nominal fit of the analysis described in Chapter 6.

Sample	Fake- $D$ + continuum
$\bar{D}^0 e^+$	$26153 \pm 305$
$D^- e^+$	$25328 \pm 187$
$\bar{D}^0 \mu^+$	$33315 \pm 360$
$D^- \mu^+$	$29388 \pm 218$

Table 5.1: Expected yields of fake- $D$  and continuum backgrounds in the signal region for the different samples.

I apply a scaling factor to the peak yield to correct for the different sizes of the on- and off-resonance samples. Based on their integrated luminosities, this factor is  $8.55 \pm 0.06$ .<sup>2</sup>

Through these corrections, the expected contributions in the signal region from fake- $D$  and continuum backgrounds amount to the values reported in Tab. 5.1. These backgrounds are combined into a single sample component.

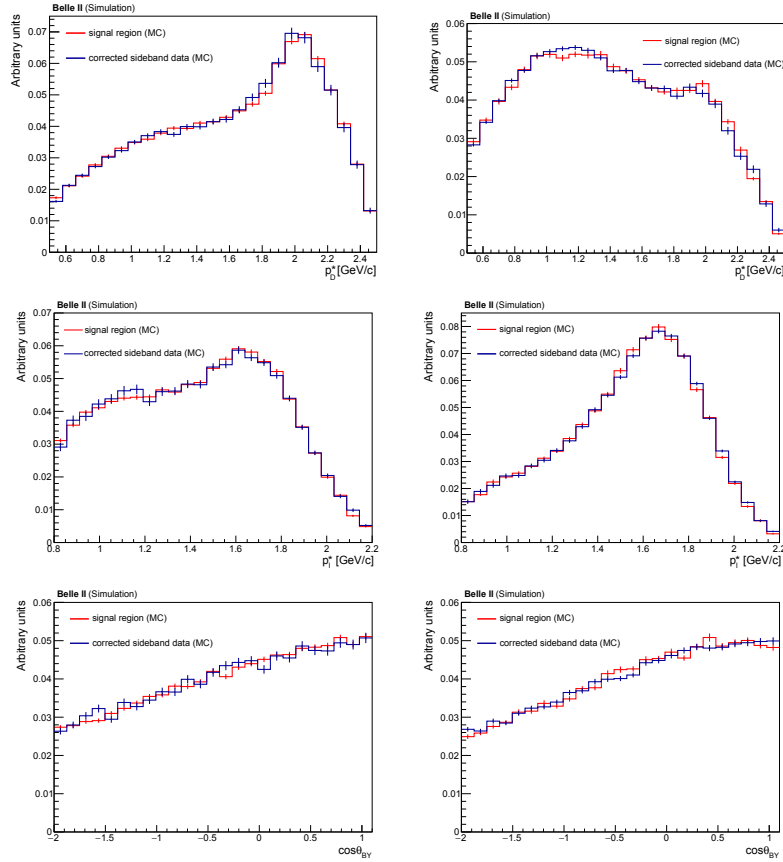


Figure 5.3: Comparisons between the fake- $D$  and continuum backgrounds of (from top to bottom)  $p_D^*$ ,  $p_l^*$  and  $\cos \theta_{BY}$  for the (left)  $\bar{D}^0 e^+$  and (right)  $D^- e^+$  samples, using (blue line) the strategy to build the templates explained in the text and (red line) the candidates in the signal region, all obtained using simulation. The muon samples show similar comparisons.

<sup>2</sup>Another scaling factor is the ratio of the  $e^+e^- \rightarrow c\bar{c}$  cross-sections between the on- and off-resonance samples, but this factor is much smaller: 0.989.

To validate the approach, I use simulations of the on- and off-resonance samples, apply the corrections, and compare the resulting distributions with those from the signal region for several key variables of the analysis. This comparison is shown in Fig. 5.3. I find a reasonable agreement; any differences will be accounted for as a systematic uncertainty, as explained in Chapter 7.

## 5.2 Real- $D$ background

In several analyses [91, 127], to test the modelling of the combinatorial background from real- $D$  mesons, unphysical particle combinations are reconstructed. These are candidates where the lepton charge is intentionally opposite to that expected from the  $D$  flavour, *i.e.*,  $D^- \ell^-$  and  $\bar{D}^0 \ell^-$ .<sup>3</sup> I refer to these combinations as *wrong-charge* (WC) samples; in turn, signal samples are referred to as *right-charge* (RC) samples. Since WC combinations are primarily composed of correctly reconstructed  $D$  candidates, WC samples should provide valuable information for studying the real- $D$  component in the RC samples.

I reconstruct WC samples for each lepton and  $D$  meson flavour in both experimental and simulated data, applying the requirements described in Chapter 4. In the simulation, I categorise the candidates using the same components defined in the RC samples (Sect. 4.1.2). The real- $D$  component is dominant. The  $p_D^*$  and  $p_\ell^*$  distributions of the WC candidates are shown in Fig. 5.4 for the  $\bar{D}^0 e^-$  sample; however, the simulation does not reproduce the experimental data. The  $D^- e^-$  and muon samples exhibit similar distributions and data-simulation disagreements.

I conduct a detailed study to investigate the possible causes of this disagreement and to determine whether it could impact the real- $D$  component in the RC samples. To this end, I split the real- $D$  background into three categories, in both the WC and RC samples, based on the origin of the lepton:

- **primary lepton:** a genuine lepton (referred to as a “true lepton”) originating directly from a  $B$  decay, distinct from the  $B$  decay of the  $D$  candidate;

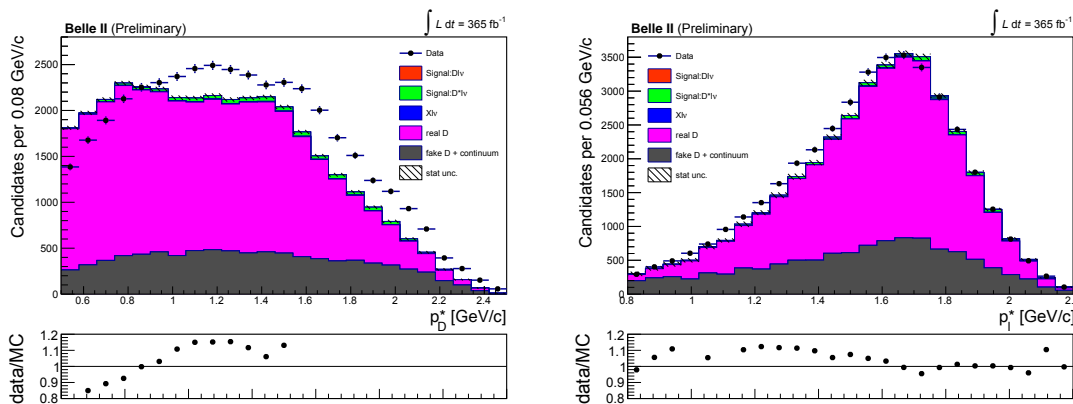


Figure 5.4: Comparison of experimental and simulated data in the WC of the  $\bar{D}^0 e^-$  sample for (left)  $p_D^*$  and (right)  $p_\ell^*$ . The disagreement is also observed for the other samples ( $D^- e^-$ ,  $\bar{D}^0 \mu^-$  and  $D^- \mu^-$ ).

<sup>3</sup>There may be physical  $\bar{D}^0 \ell^-$  combinations due to either  $D^0 - \bar{D}^0$  mixing or the doubly Cabibbo-suppressed  $D^0 \rightarrow K^+ \pi^-$  decay being reconstructed as the favoured  $\bar{D}^0 \rightarrow K^+ \pi^-$  mode; these possibilities occur at the per mill level and are neglected here.

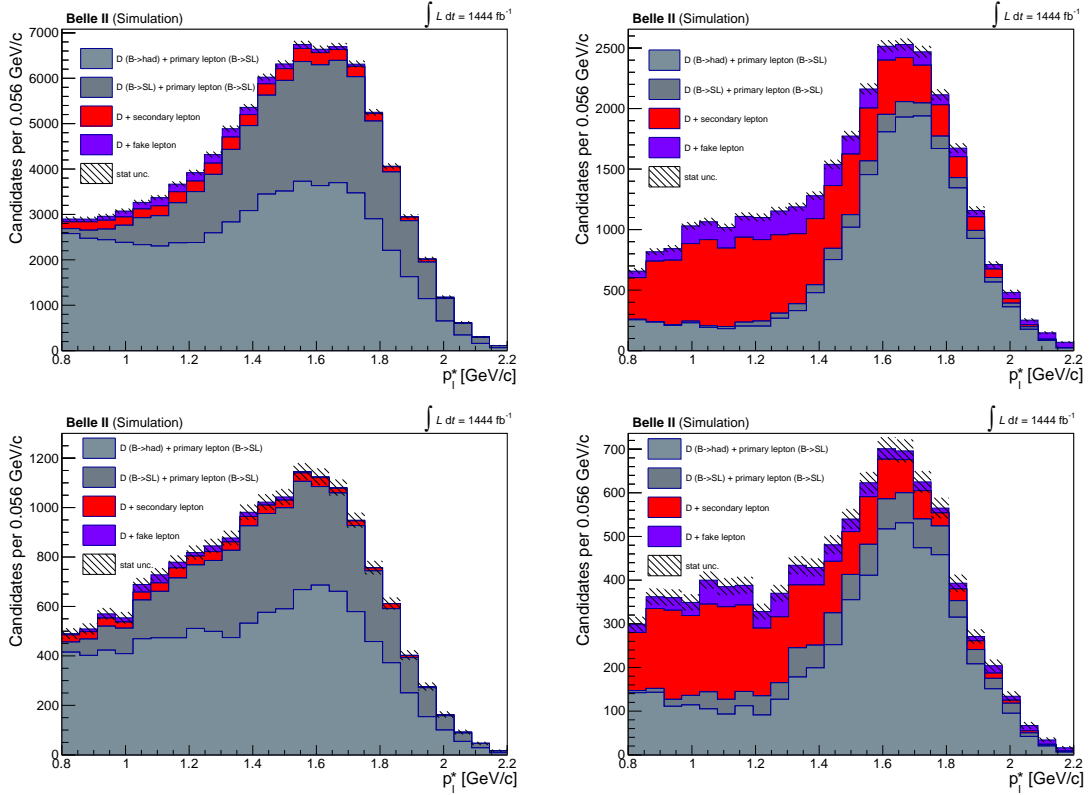


Figure 5.5: Distribution of  $p_l^*$  for the real- $D$  components (primary leptons, secondary leptons, and fake leptons) for the (left) WC and (right) RC electron samples, with (top)  $\overline{D}^0 e^\mp$  or (bottom)  $D^- e^\mp$  candidates. For primary leptons, I distinguish between the cases where the  $D$  meson originates from a semileptonic or hadronic decay. The WC muon samples exhibit a composition similar to that of the electron modes, whereas the RC samples differ between the electron and muon cases, with the latter dominated by fake leptons, as shown in Tab. 5.2.

- **secondary lepton:** a true lepton originating from a semileptonic decay of a hadron (primarily charm mesons) that belongs to the same  $B$  decay as the  $D$  candidate;
- **fake leptons:** a misidentified particle, originating from either the same or a different  $B$  decay of the  $D$  candidates, that mimics a lepton signature.

Figure 5.5 shows that the three categories exhibit different fractions between the RC and WC electron samples, as well as different lepton momentum distributions. The fractions of the categories are reported in Tab. 5.2.

Primary leptons almost saturate the WC samples, while they are less abundant in RC samples. Their momentum distribution peaks around  $1.6 \text{ GeV}/c$  and  $1.7 \text{ GeV}/c$  for the WC and RC samples, respectively, with a broader shape for WC candidates.

Secondary leptons make up only a few percent of the WC samples, while they constitute a significant fraction of the RC samples (see Tab. 5.2). They are mostly distributed at low momenta. Given the non-negligible contribution of this component in the RC sample, and since it is primarily driven by decays with large uncertainties in their branching fractions, a systematic uncertainty will be assigned to the composition assumed for this background, as detailed in Chapter 7.

lepton category	$D^0$ sample		$D^-$ sample	
	WC [%]	RC [%]	WC [%]	RC [%]
primary electron	94	60	95	68
secondary electron	4	30	4	25
fake electron	2	10	1	7
primary muon	85	26	89	36
secondary muon	3	23	3	20
fake muon	12	51	8	44

Table 5.2: Fractions of the lepton categories in the RC and WC samples.

Fake leptons represent a small fraction in the WC samples for all cases (see Tab. 5.2), whereas in the RC samples, they account for a minor fraction in the electron samples but constitute a significant component in the muon samples. They are almost uniformly distributed across the momentum range. This further highlights the discrepancy in sample composition between the WC and RC channels. The conclusions discussed next regarding the primary leptons will remain valid for the muon samples as well. Given the considerable differences in sample composition, there is no guarantee that the data-simulation discrepancy observed for the WC samples is also present in the RC samples.

Since primary leptons are dominant in the WC samples, I will further investigate this category. The purpose is to understand whether there is a commonality between primary leptons in the WC and RC samples in order to constrain the primary-lepton component in the signal region from the WC data.

Of the two  $B$  decays produced in an event with a primary lepton, either both decay semileptonically or one decays semileptonically while the other decays hadronically. The former case is less frequent in both WC (about 30%) and RC (about 7%) samples; however, it is the case where the kinematics are well known and well simulated, consisting mostly of  $B \rightarrow D^{(*)} \ell \nu_\ell$  decays. For the second case, I distinguish the three following subcomponents:

- decays with one charm meson (*i.e.*,  $B \rightarrow D(n)X$ ),
- decays with two charm mesons (*i.e.*,  $B \rightarrow D_{(s)}D(m)X$ ),
- decays with no charm mesons (*i.e.*,  $B \rightarrow (n)X(m)X$ ),

where  $X$  can be pions and kaons, and  $n$  and  $m$  are integers. The  $p_D^*$  distribution of the three subcategories in the WC and RC samples is shown in Fig. 5.6.

Charmless decays constitute a small fraction, while the first two subcomponents are dominant in both the WC and RC samples. Upon checking the composition in more detail, I find that the decays of the  $B \rightarrow D_{(s)}D(m)X$  subcomponents are simulated in Belle II using branching fractions compatible within 10% of known values [14]. Notably, in the WC samples, there are two different contributions for the  $B \rightarrow D_{(s)}D(m)X$  decays: one peaks at about 0.8 GeV/ $c$  and the other at 1.5 GeV/ $c$ . The contribution at lower momenta includes  $D_s$  meson in the final state; these decays almost saturate the  $B \rightarrow D_{(s)}D(m)X$  subcomponent in the RC samples. For  $B \rightarrow D(n)X$ , many decays have branching fractions that are either poorly known (because they rely on measurements done with small samples, such as those of  $B^+ \rightarrow \bar{D}^0 \pi^+ \pi^+ \pi^- \pi^0$  decays from CLEO [128] and  $B^- \rightarrow \bar{D}^+ \pi^- \pi^- \pi^0$  from ARGUS [129]) or unknown altogether; the latter are generated by Pythia. Due to

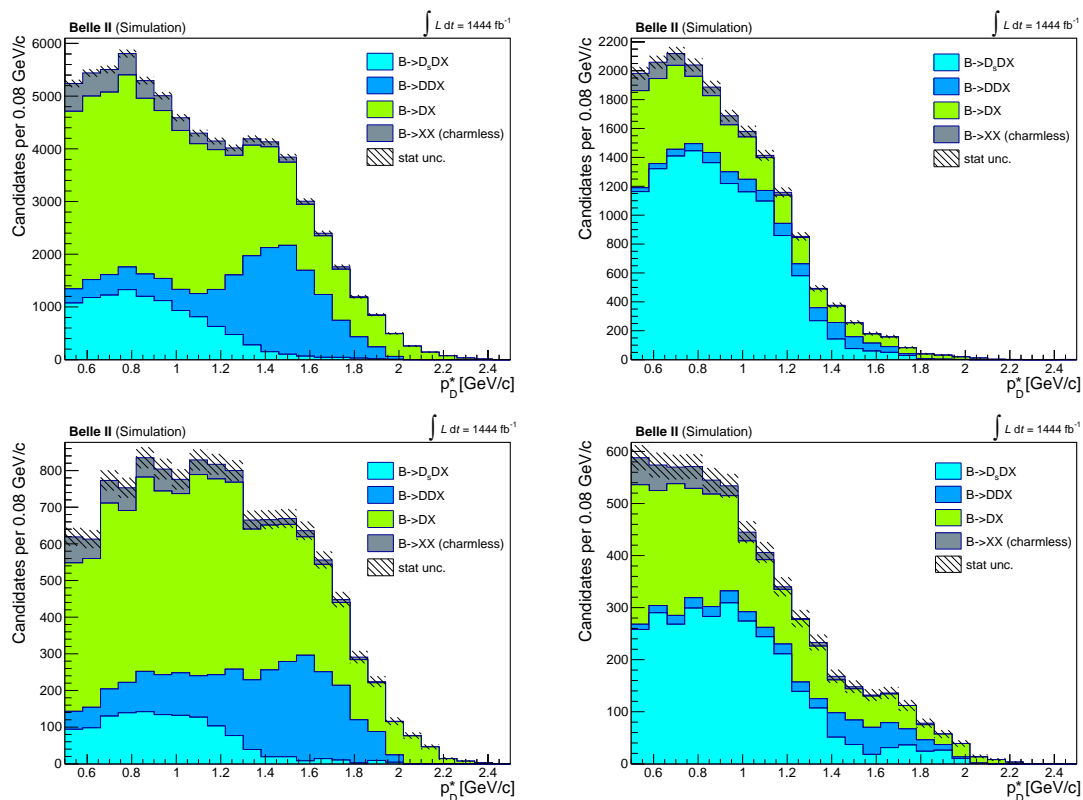


Figure 5.6: Distribution of  $p_D^*$  for the primary leptons of the real- $D$  background, where the  $D$  originates from a hadronic  $B$  decay. Plots are for the (left) WC and (right) RC electron samples with (top)  $\bar{D}^0 e^\mp$  or (bottom)  $D^- e^\mp$  candidates. For  $B \rightarrow D_{(s)} D(m) X$  decays, I distinguish two peaking components: at low momenta there are decays with a  $D_s$  meson, *i.e.*,  $B \rightarrow D_s D$  decays; at higher momentum, decays without it.

non-negligible uncertainties in the experimental information on  $B \rightarrow D_{(s)} D(m) X$  and  $B \rightarrow D(n) X$  decays, the discrepancy between data and simulation observed in the WC samples could be attributed to a mismodelling of these decays.

From this investigation of the real- $D$  background, I conclude that the WC and RC samples differ significantly in their composition, to the extent that little to no information from the WC samples can be transferred to the RC samples. This observation was also noted in previous analyses [91, 127]. Nonetheless, effective corrections for the data-simulation disagreement in the WC samples have been applied to the real- $D$  simulated candidates of the RC samples to address some of the mismodelling observed in the signal region; systematic uncertainties associated with these corrections have been considered in those analyses.

My approach is different. I have decided not to apply corrections obtained from the WC samples to the RC samples. Instead, based on the detailed understanding of the real- $D$  background composition presented in this section, I consider systematic uncertainties that reflect the current knowledge of the branching fractions of the decays comprising this background (see Chapter 7).

It is important to note that the real- $D$  background is the smallest component of the signal sample. This is done by design to minimise the impact of such systematic uncertainties: the requirement on the invariant mass of the  $Y$  system is very effective in reducing this background component, as shown in Fig. 4.4.

### 5.3 $X\ell\nu_\ell$ background

The  $X\ell\nu_\ell$  background is composed of semileptonic decays other than those of the signal. The largest fraction of these, between 65% and 70%, arises from excited charm-meson cascade decays to the  $D$  ground states, *i.e.*, the so-called  $B \rightarrow D^{**}\ell\nu_\ell$  decays introduced in Sect. 4.1.2. In addition, contributions from non-resonant  $B \rightarrow D^{(*)}\pi(\pi)\ell\nu_\ell$  decays and other yet-unknown semileptonic  $B$  decays with multi-body hadronic states, *i.e.*,  $B \rightarrow D^{(*)}\eta\ell\nu_\ell$  decays must be considered. The latter account for between 25% and 30% of the  $X\ell\nu_\ell$  background according to the latest models. I focus on all these backgrounds in this section. The remaining part, *i.e.*, semitaquonic and semileptonic decays of  $B$  with a misidentified lepton, totals only a few percent and will be further discussed in Chapter 7.

#### 5.3.1 Corrections on the cascade decays background

A clear understanding of the decomposition of the semileptonic decay width of the  $B$  meson is still lacking. The inclusive branching fraction for semileptonic  $B$  decays has been measured by Belle and Babar; the current averages [50] are  $(10.26 \pm 0.16)\%$  and  $(11.04 \pm 0.17)\%$  for  $B^0$  and  $B^+$  decays, respectively. Branching fractions of exclusive decays have also been measured. The  $B \rightarrow D\ell\nu_\ell$  and  $B \rightarrow D^*\ell\nu_\ell$  branching fractions, which are the focus of this thesis, account for about 70% of the inclusive value. For  $B \rightarrow D^{**}\ell\nu_\ell$  decays the picture is much less clear, with an additional unknown component of the inclusive rate for which there is no experimental information available.

The orbitally excited charmed mesons, categorised by their quantum numbers ( $L = 1$ ), comprise four primary states:  $D_0^*(2300)$ ,  $D_1(2420)$ ,  $D_1'(2430)$ , and  $D_2^*(2460)$  (see Tab. 5.5). These states are measured by inspecting the  $D^{(*)}\pi$  invariant-mass distribution in semileptonic decays [49, 130, 131]. The interpretation of the reconstructed distribution is challenging due to the small samples available so far. Reconstructed efficiencies are usually low, as  $B$ -tagging is employed to suppress backgrounds, and identifying soft pions from the signal is difficult. Additionally, the broad widths of two states ( $D_0^*(2300)$  and  $D_1'(2430)$ ), possible tails from  $D^*$  extending to high  $D\pi$  mass values [132], and potential non-resonant  $D^{(*)}\pi(\pi)$  contributions complicate the separation of individual states.

Recently, phenomenological analyses using information from corresponding hadronic  $B$  decays (such as  $B \rightarrow D\pi\pi$  [133]), point out that the observed  $D_0^*(2300)$  structure could be an overlap of two states [134–136]. A recent measurement from Belle [137], found no evidence of this state in data. In addition, not all branching fractions of  $D^{**}$  decays have been measured, and some must be deduced from available information, assuming isospin symmetry [50]. Finally, analyses of the  $B \rightarrow D^{(*)}\pi\pi\ell\nu_\ell$  [138] decay have also been carried out, but uncertainties remain large in this case.

The result of this unclear and evolving picture is that the sum of the measured branching fractions for exclusive decays does not saturate the inclusive branching fraction. There is a missing *gap*. Its value, as well as its significance, depends on the model used to interpret the measurements. This gap has changed significantly with the addition of the recent Belle results [137], which are in tension with earlier measurements due to the lack of evidence found for the  $D_0^*(2300)$  resonance. To reduce this gap, so-called *gap modes*, *i.e.*, yet unobserved decay channels, are hypothesised based on some educated guesses [139]. An overview of the models that have been considered so far in Belle II is presented in Tab. 5.4.

Note that poor to none experimental information is also available for the form factors of the  $B \rightarrow D^{**}\ell\nu_\ell$  decays. The model employed in Belle II is LLSW from EvtGen [120], which has been recently challenged in Ref. [140]. According to the same reference, the

Decay	HFLAV 2018 [%]		HFLAV 2021 [%]		HFLAV 2024 [%]	
	$B^0$	$B^+$	$B^0$	$B^+$	$B^0$	$B^+$
Inclusive	$10.10 \pm 0.40$	$10.80 \pm 0.40$	$10.26 \pm 0.16$	$11.04 \pm 0.17$	$10.27 \pm 0.15$	$11.05 \pm 0.16$
$B \rightarrow D\ell\nu_\ell$	$2.24 \pm 0.07$	$2.41 \pm 0.07$	$2.18 \pm 0.06$	$2.35 \pm 0.06$	$2.11 \pm 0.04$	$2.27 \pm 0.06$
$B \rightarrow D^*\ell\nu_\ell$	$5.11 \pm 0.11$	$5.50 \pm 0.11$	$5.03 \pm 0.11$	$5.41 \pm 0.11$	$4.90 \pm 0.11$	$5.27 \pm 0.12$
$B \rightarrow D_0^*(2300)\ell\nu_\ell$	$0.39 \pm 0.07$	$0.42 \pm 0.08$	$0.39 \pm 0.07$	$0.42 \pm 0.08$	$0.12 \pm 0.18$	$0.13 \pm 0.19$
$B \rightarrow D_1(2420)\ell\nu_\ell$	$0.62 \pm 0.10$	$0.66 \pm 0.11$	$0.61 \pm 0.10$	$0.65 \pm 0.11$	$0.59 \pm 0.10$	$0.64 \pm 0.10$
$B \rightarrow D_1'(2430)\ell\nu_\ell$	$0.39 \pm 0.08$	$0.42 \pm 0.09$	$0.26 \pm 0.07$	$0.29 \pm 0.08$	$0.26 \pm 0.04$	$0.28 \pm 0.04$
$B \rightarrow D_2^*(2460)\ell\nu_\ell$	$0.27 \pm 0.03$	$0.29 \pm 0.03$	$0.27 \pm 0.03$	$0.29 \pm 0.03$	$0.30 \pm 0.03$	$0.32 \pm 0.03$
$B \rightarrow D\pi\pi\ell\nu_\ell$	$0.06 \pm 0.08$	$0.06 \pm 0.09$	$0.06 \pm 0.08$	$0.07 \pm 0.09$	$0.07 \pm 0.08$	$0.07 \pm 0.09$
$B \rightarrow D^*\pi\pi\ell\nu_\ell$	$0.20 \pm 0.10$	$0.22 \pm 0.10$	$0.20 \pm 0.10$	$0.22 \pm 0.10$	$0.20 \pm 0.10$	$0.22 \pm 0.10$
$B \rightarrow D\eta\ell\nu_\ell$	$0.41 \pm 0.41$	$0.38 \pm 0.38$	$0.63 \pm 0.63$	$0.65 \pm 0.65$	$0.86 \pm 0.86$	$0.90 \pm 0.90$
$B \rightarrow D^*\eta\ell\nu_\ell$	$0.41 \pm 0.41$	$0.38 \pm 0.38$	$0.63 \pm 0.63$	$0.65 \pm 0.65$	$0.86 \pm 0.86$	$0.90 \pm 0.90$

Table 5.3: Branching fractions assumed in Belle II over time. The values are taken from the HFLAV Group [46]: for 2018 from Ref. [141]; for 2021 from Ref. [50]; for 2024 from Ref. [71]. Branching-fraction decays for  $B^+$  and  $B^0$  mesons are linked assuming isospin symmetry. The gap modes are the decays  $B \rightarrow D\eta\ell\nu_\ell$  and  $B \rightarrow D^*\eta\ell\nu_\ell$ . Their branching fractions are calculated as the difference between the inclusive and the sum of the measured exclusive modes; the division of the branching fractions between the  $D$  and  $D^*$  for gap modes is arbitrary. An uncertainty of 100% is assumed for the gap branching fraction. Note also how the branching fraction of  $B \rightarrow D_0^*(2300)\ell\nu_\ell$  changes in the last column; this is mainly due to the recent results from Belle [137]. The uncertainty for the latter was assessed to account for the significant difference observed in the branching fraction for  $D_0^*(2300)$  between the Belle and BaBar [142] measurements. It was determined by taking half of the difference between the branching fraction values obtained when considering only the Belle or BaBar measurement. The central value of the average is closer to the Belle measurement due to its higher precision, and an uncertainty of 0.19% covers the BaBar measurement within  $1.5\sigma$ .

branching fraction of  $B \rightarrow D\eta\ell\nu_\ell$  decays (used to fill the gap) is calculated to be less than  $10^{-5}$ .

In the official Belle II simulation, the values and models of exclusive semileptonic  $B$  decays have been assumed based on information available a few years ago. These need to be updated to reflect the most recent developments in the field. Corrections to the simulated data must be applied; I explain these corrections below, along with an overview of the models used.

### Branching fraction corrections

Branching fractions of  $B \rightarrow D^{**}\ell\nu_\ell$  decays listed in Tab. 5.4 are those used in the official Belle II simulation; they have all been updated according to the last (HFLAV 2024) of Tab. 5.3. Note that, using Tab. 5.3, the  $B \rightarrow D^{(*)}\pi\ell\nu_\ell$  decays with non-resonant  $D^{(*)}\pi$  present in the Belle II simulation have been removed, since their branching fractions are saturated by production of non-resonant final states via the  $D^{**}$  resonances (see Tab. 5.6).

Decay	$\mathcal{B}_j^{\text{sim}}(B^+) [10^{-3}]$	$\mathcal{B}_j^{\text{sim}}(B^0) [10^{-3}]$	EvtGen model [120]
$B \rightarrow D_1(2420)\ell\nu_\ell$	7.57	7.04	LLSW
$B \rightarrow D'_1(2430)\ell\nu_\ell$	4.31	4.01	LLSW
$B \rightarrow D_0^*(2300)\ell\nu_\ell$	3.89	3.62	LLSW
$B \rightarrow D_2^*(2460)\ell\nu_\ell$	3.73	3.47	LLSW
$B \rightarrow D\pi\pi\ell\nu_\ell$	0.53	0.49	PHSP
$B \rightarrow D^*\pi\pi\ell\nu_\ell$	2.63	2.45	PHSP
$B \rightarrow D\pi\ell\nu_\ell$	1.50	1.38	GOITY_ROBERTS
$B \rightarrow D^*\pi\ell\nu_\ell$	1.50	1.38	GOITY_ROBERTS
$B \rightarrow D\eta\ell\nu_\ell$	2.01	2.17	PHSP
$B \rightarrow D^*\eta\ell\nu_\ell$	2.01	2.17	PHSP

Table 5.4: Summary of semileptonic  $D^{**}$  branching fractions and decay models used in the Belle II simulation.

The corrections of the branching fractions are calculated as follows:

$$N_j = N_j^{\text{sim}} \frac{\mathcal{B}_j^{\text{new}}}{\mathcal{B}_j^{\text{sim}}}, \quad (5.1)$$

where  $N_j^{\text{sim}}$  and  $N_j$  are the number of candidates before and after the branching-fraction correction, and  $\mathcal{B}_j^{\text{sim}}$  and  $\mathcal{B}_j^{\text{new}}$  are the old and the updated branching fractions.

### Broad $D^{**}$ modelling

Two of the four  $D^{**}$  mesons, the  $D_0^*(2300)$  and the  $D'_1(2430)$ , have a very large width (see Tab. 5.5). Due to the non-converging properties of a naive Breit-Wigner curve used to model these resonances, a significant amount of  $B \rightarrow D^{**}\ell\nu_\ell$  decays is generated with a  $D^{**}$  mass comparable to that of the  $B$  meson (Fig 5.7).

Although these cases are not necessarily forbidden, they should naturally be highly suppressed due to the available phase space. This situation serves as a good example where the assumption of a Breit-Wigner curve is overly simplistic and does not accurately describe the properties of the particles.

To address this issue, I reject  $D_0^*(2300)$  meson candidates for which the generated mass exceeds its central value by more than 3 times the width (about  $700 \text{ MeV}/c^2$ ), and  $D'_1(2430)$  candidates for which the mass exceeds 2.5 times the width (about  $1 \text{ GeV}/c^2$ ). The remaining events are upscaled to preserve the total number of candidates.

	$D_0^*(2300)$	$D'_1(2430)$	$D_1(2420)$	$D_2^*(2460)$
Mass [ $\text{MeV}/c^2$ ]	2343	2412	2422	2461
Width [ $\text{MeV}/c^2$ ]	229	314	31.3	47.3

Table 5.5: The central mass values and widths of the different  $D^{**}$  states [14].

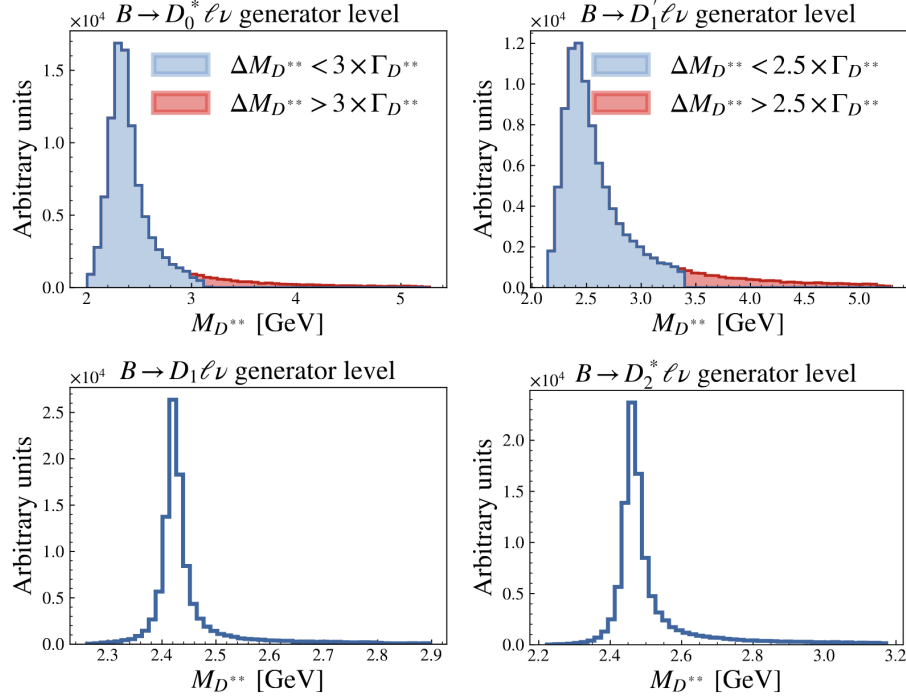


Figure 5.7: The mass spread of the different  $D^{**}$  mesons on generator level due to their intrinsic width. For the two broad  $D^{**}$ , their masses spread up to values close to the  $B$  meson mass (top row) which leads to questionable distributions in physics quantities [143].

### Non-resonant and gap modes

The decays  $D^{(*)}\pi\pi\ell\nu_\ell$  and  $D^{(*)}\eta\ell\nu_\ell$  have been generated with final state particles equally distributed in phase space, leading to a very soft lepton momentum distribution. However, a decay kinematics that is completely driven by phase space seems physically less plausible than one in which the hadronic particles are more correlated to each other. Therefore, the models are corrected by using BLR [144], in which the final state hadrons are produced via intermediate broad  $D^{**}$  resonances:

$$B \rightarrow [D^{**} \rightarrow D^{(*)}\pi\pi]\ell\nu_\ell, \quad B \rightarrow [D^{**} \rightarrow D^{(*)}\eta]\ell\nu_\ell. \quad (5.2)$$

This approach is used in the Belle simulation as well [145] and it is considered to yield a more realistic description of the underlying physics. A specific generation of these decays has been performed according to the parameters reported in Tab. 5.6.

Process	Simulated events [ $10^6$ ]	Luminosity [ $ab^{-1}$ ]	FF model
$B \rightarrow D_1'(2430)[\rightarrow D\pi\pi]\ell\nu_\ell$	8	$B^0 : 16, B^+ : 14$	BLR
$B \rightarrow D_1'(2430)[\rightarrow D^*\pi\pi]\ell\nu_\ell$	8	$B^0 : 3.2, B^+ : 2.8$	BLR
$B \rightarrow D_1'(2430)[\rightarrow D^*\eta]\ell\nu_\ell$	8	$B^0 : 1.8, B^+ : 1.8$	BLR
$B \rightarrow D_0^*(2300)[\rightarrow D\pi\pi]\ell\nu_\ell$	8	$B^0 : 16, B^+ : 14$	BLR
$B \rightarrow D_0^*(2300)[\rightarrow D^*\pi\pi]\ell\nu_\ell$	8	$B^0 : 3.2, B^+ : 2.8$	BLR
$B \rightarrow D_0^*(2300)[\rightarrow D\eta]\ell\nu_\ell$	8	$B^0 : 1.8, B^+ : 1.8$	BLR

Table 5.6: Generated samples with updated models for the  $D^{(*)}\pi\pi\ell\nu_\ell$  and  $D^{(*)}\eta\ell\nu_\ell$  decays.

Due to the intermediate  $D^{**}$  resonances, the lepton momentum distribution becomes harder, leading to more candidates surpassing the required thresholds in the selection.

## 5.4 Background control region

The majority of the background, including fake- $D$  and continuum, can be directly constrained and modelled from data with minimal input from simulation. On the other hand, I could not find a suitable control sample for the real- $D$  background, given the dissimilarity between the WC and RC samples. However, some of its subcomponents are well known, and for those that are not, this background is sufficiently small that the impact in terms of biases and systematic uncertainties on the signal should be limited (as discussed further in Chapter 7). This is not the case for the  $X\ell\nu_\ell$  background: it can be as large as 10% of the signal, and the knowledge of its largest contributors is much less established. Therefore, any possible information from data is highly valuable.

I identify a control region in data that is contaminated by this background. The control region is the  $\cos\theta_{BY}$  sideband, defined by the range  $[-12, -3]$  (see Fig. 5.8). This control region features a significant contamination from the  $X\ell\nu_\ell$  background. The expected amount of this background is sufficiently large to enhance the information on this component for the signal region, where this background is smaller. The signal  $B \rightarrow D\ell\nu_\ell$  and  $B \rightarrow D^*\ell\nu_\ell$  decays are negligible in this region for all samples, except for the  $D^*$  component in the  $\bar{D}^0 e^+$  sample. Real- $D$  is also present, allowing me to test the simulation's description of this component using data from this control region.

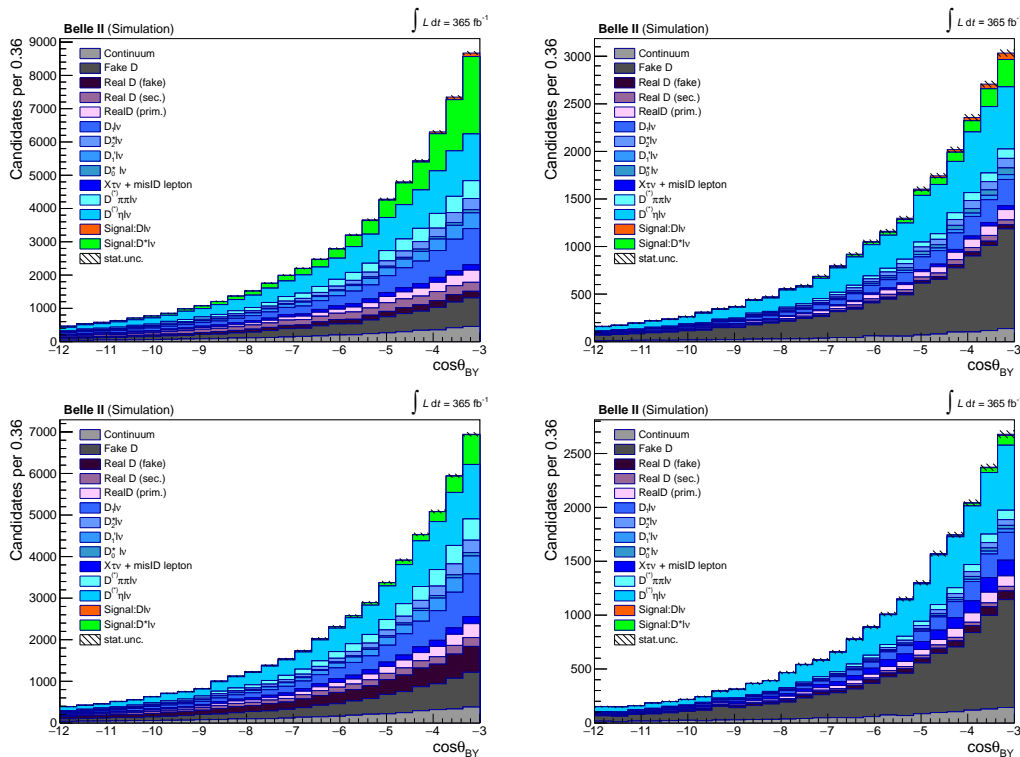


Figure 5.8: Sample composition of the  $\cos\theta_{BY}$  control region for the samples (top-left)  $\bar{D}^0 e^+$ , (top-right)  $D^- e^+$ , (bottom-left)  $\bar{D}^0 \mu^+$ , and (bottom-right)  $D^- \mu^+$ . These regions are enriched of  $X\ell\nu_\ell$  background.

I use the control data provided by the  $\cos\theta_{BY}$  control region in a simultaneous fit with the signal region. With this approach, I can constrain the branching fraction of  $B \rightarrow D^{**}\ell\nu_\ell$  (decays with the four resonance states, non-resonant  $D^{(*)}\pi\pi$  and gap modes), by employing Gaussian penalties based on inputs from HFLAV 2024 in Tab. 5.3. This allows me to gain information from the control data to determine the background yields in the signal region and minimise uncertainties associated with these components. This simultaneous fit is the core of the analysis, and the next chapter is entirely devoted to its detailed description.



## Chapter 6

# Novel approach: the global fit

*In this chapter, I present the core of the analysis: a multidimensional  $\chi^2$  fit, simultaneous to all  $D\ell$  samples, to measure the model-independent observables and  $f_{+-}/f_{00}$ . I introduce how I access the signal decay rates by means of reconstructed variables which are employed in the fit. After a general overview, I delve into the details of each fit component, describing its templates and parameters. Then, I present a fit to the data in the  $\cos\theta_{BY}$  control region, which improves information on the  $X\ell\nu_\ell$  background. With the results of this fit, I adjust the simulation to generate a realistic data set that reproduces the Run I Belle II sample. I run the fit on this data set to demonstrate the feasibility of the measurement. Finally, I inspect the fit properties by running it over hundreds of simulated samples.*

### 6.1 Accessing the differential decay rates

To measure the model-independent observables  $a'_n$ ,  $b'_n$ ,  $c'_n$  and  $G'_m$ , defined in Eqs. 2.30–2.32 and 2.34, I need to analyse the differential decay rates of the signal as a function of kinematics variables defined in the  $B$  rest frame. For  $B \rightarrow D\ell\nu_\ell$ , the key variable is the recoil energy  $w$  (see Eq. 2.33); for  $B \rightarrow D^*\ell\nu_\ell$ , they are both  $w$  and the helicity angle  $\cos\theta_\ell$  (see Eq. 2.26)<sup>1</sup>. I refer to these three variables as *B-kinematics* variables. To reconstruct them, one needs to know the  $B$ -momentum vector.

In semileptonic decays with undetected neutrinos,  $B$ -tagging algorithms are crucial for reconstructing the  $B$ -momentum vector but generally have low efficiency (below 1%), known with insufficient precision for high-accuracy measurements like  $|V_{cb}|$  [82]. Therefore, untagged analyses are preferred. Without  $B$ -tagging, the  $B$ -momentum is approximated using the vector sum of visible particle momenta, excluding those from the signal [91]. Additional constraints can be imposed from the signal kinematics or  $B$  meson angular distributions. Although untagged methods are fully efficient, they yield lower resolution for  $B$ -kinematic measurements, and rely on accurate ROE particle descriptions to obtain migration matrices to address experimental effects.

For a global analysis of  $B \rightarrow D\ell\nu_\ell$  and  $B \rightarrow D^*\ell\nu_\ell$  decays, there is an additional complication. In the case of  $B \rightarrow D^*\ell\nu_\ell$  decays, the neutrino is not the only missing particle, as the  $D^*$  decay is partially reconstructed. This further degrades the resolution of  $w$  and  $\cos\theta_\ell$ , since only kinematics information and constraints on the  $D$  and the lepton are available. Therefore, to access the differential decay rates, I adopt another approach: I use *proxy* variables that are highly correlated with the  $B$ -kinematic variables and are

---

<sup>1</sup>In the following, I use the notation  $w$  to denote both  $w_D$  and  $w_{D^*}$  when the intended variable is clear from context; similarly with  $\cos\theta_\ell$  for  $\cos\theta_\ell^D$  and  $\cos\theta_\ell^{D^*}$ , and with  $q^2$  for  $q_D^2$  and  $q_{D^*}^2$ .

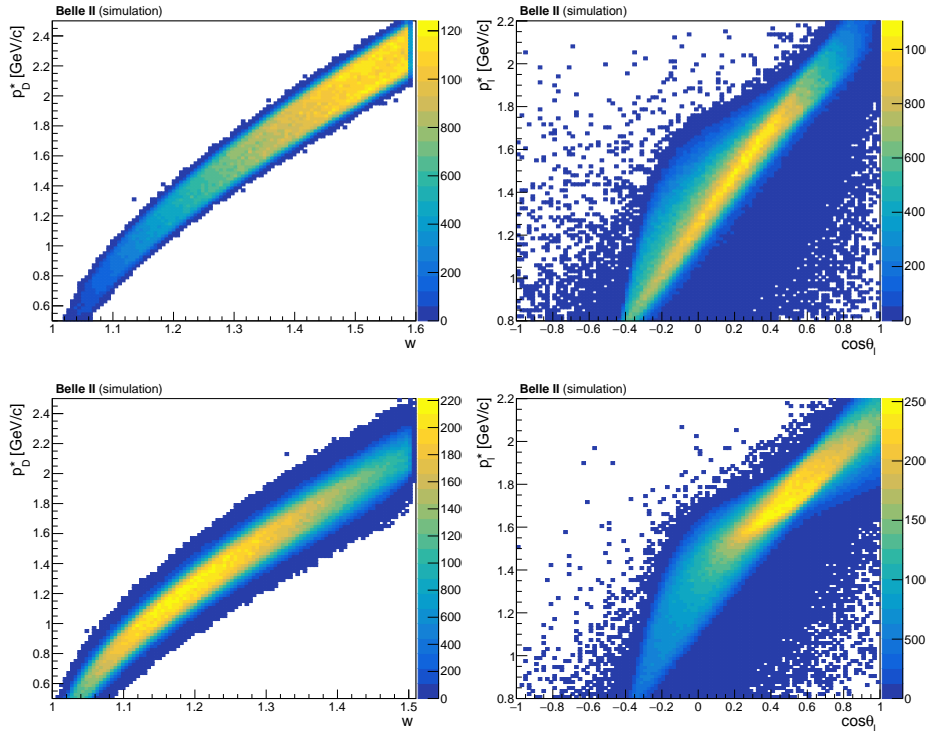


Figure 6.1: Two-dimensional distributions from simulation of: (top left)  $p_D^*$  versus  $w$ , (top right)  $p_\ell^*$  versus  $\cos\theta_\ell$  for  $B \rightarrow D l \nu_\ell$  candidates; and (bottom left)  $p_D^*$  versus  $w$ , (bottom right)  $p_\ell^*$  versus  $\cos\theta_\ell$  for  $B \rightarrow D^* l \nu_\ell$  candidates.

reconstructed solely from the visible particles of the signal. This approach has already been exploited in Ref. [62] and [146] for  $B$  and  $B_s^0$  decays, respectively.

I identify  $p_D^*$  and  $p_\ell^*$ , the momenta of the  $D$  meson and that of the lepton, both measured in the centre-of-mass frame, as proxy variables. In Fig. 6.1, I show the two-dimensional distributions of  $(p_D^*, w)$ , and  $(p_\ell^*, \cos\theta_\ell)$  for the signal decays. The distributions are obtained from simulation, where the momenta  $p_D^*$  and  $p_\ell^*$  are those reconstructed, while the  $B$ -kinematics variables ( $w$ ,  $\cos\theta_\ell$ ) are derived from the *true* information of the same candidate. These distributions show that the differential decay rate as a function of the  $B$ -kinematics variables can be accessed through  $p_D^*$  and  $p_\ell^*$ . Some dilution of the information on the decay rate occurs, as there is no one-to-one correspondence between the  $B$ -kinematic variables and the proxy variables; however, the proxy variables still capture sufficient information to assess the decay dynamics.

Since proxy variables give access to the differential decay rates, they preserve information on the form factors: the distributions of the proxy variables change depending on the form factors. For example, using the CLN parametrisation for simplicity, different values of the parameters  $\rho_D^2$  and  $\rho_{D^*}^2$  lead to different shapes of the  $p_D^*$  distribution of the signal decays, as depicted in Fig. 6.2.

In turn, these distributions allow the measurement of the form factors and, consequently, of the model-independent variables  $a'_n$ ,  $b'_n$ ,  $c'_n$  and  $G'_m$ . It is important to note that I do not attempt to reconstruct the  $B$ -kinematic variables using the proxy variables. Therefore, no unfolding of “reconstructed  $B$ -kinematic distributions” is required. Instead, I use the proxy variables directly to obtain the model-independent variables, using the fitting method explained in the next section.

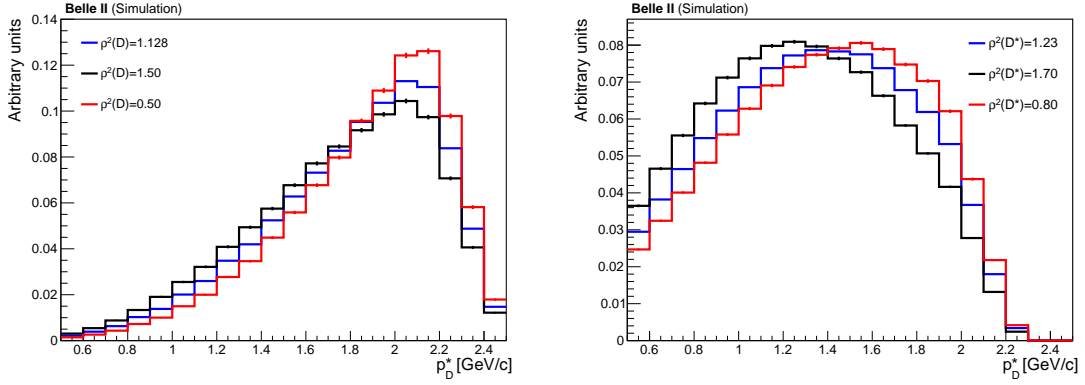


Figure 6.2: Impact of form-factor variations on the  $p_D^*$  distributions for the signal decays. (Left) Variation of  $\rho_D^2$  for the  $B \rightarrow D l \nu_l$  decay, and (right) variation of  $\rho_{D^*}^2$  for the  $B \rightarrow D^* l \nu_l$  decay. The distributions are normalised to a unit integral.

## 6.2 The $\chi^2$ fit

The core of the measurement is a multivariate fit to the binned distribution of the proxy variables, which are sensitive to the model-independent observables:  $a'_n$ ,  $b'_n$ ,  $c'_n$  and  $G'_m$ . In addition, I use a third variable,  $\cos \theta_{BY}$ , to enhance signal-to-background separation. An example of the separation of the sample components in the space  $(\cos \theta_{BY}, p_D^*)$  is shown in Fig. 6.3 for the  $\bar{D}^0 e^+$  and  $D^- e^+$  samples. The components accumulate in different regions, enabling their statistical discrimination in a fit to the data. Thus, the data are binned in three dimensions,  $p_D^*$ ,  $p_\ell^*$ , and  $\cos \theta_{BY}$ , with an histogram.

The fit is based on the method of least squares, with a  $\chi^2$  function defined as

$$\chi^2 = \sum_i \frac{[N_i - \bar{N}_i]^2}{\sigma_{N_i}^2 + \sigma_{\bar{N}_i}^2}, \quad (6.1)$$

where  $N_i$  and  $\sigma_{N_i}$  are the number of candidates and its Poisson uncertainty in the three-dimensional bin  $i$  of the data histogram;  $\bar{N}_i$  and  $\sigma_{\bar{N}_i}$  are the predicted number of candidates and its uncertainty in the same bin.

The predicted number of candidates is calculated as

$$\bar{N}_i = \sum_k n_k f_i^k \quad (6.2)$$

where  $n_k$  is the predicted yield of the sample component  $k$ , which has a fraction  $f_i^k$  of candidates in the bin  $i$ . These fractions are obtained from the three-dimensional histogram of the  $(\cos \theta_{BY}, p_\ell^*, p_D^*)$  distribution of each component, normalised to unit integral. The histograms are called *templates* and are obtained using simulated candidates or control data.

I fit simultaneously the signal region and the  $\cos \theta_{BY}$  control region. The former is defined by the selection reported in Tab. 4.2, which considers candidates with  $\cos \theta_{BY} \in [-2, 1.1]$ ; the latter has the same selection but with a different  $\cos \theta_{BY}$  requirement, as it considers the candidates with  $\cos \theta_{BY} \in [-12, -3]$ , to constrain the  $X l \nu_l$  background as explained in Sect. 5.4. In total, the fit is carried out simultaneously on eight samples:  $\bar{D}^0 e^+$ ,  $\bar{D}^0 \mu^+$ ,  $D^- e^+$ , and  $D^- \mu^+$ , for the signal region, and the same four samples for the

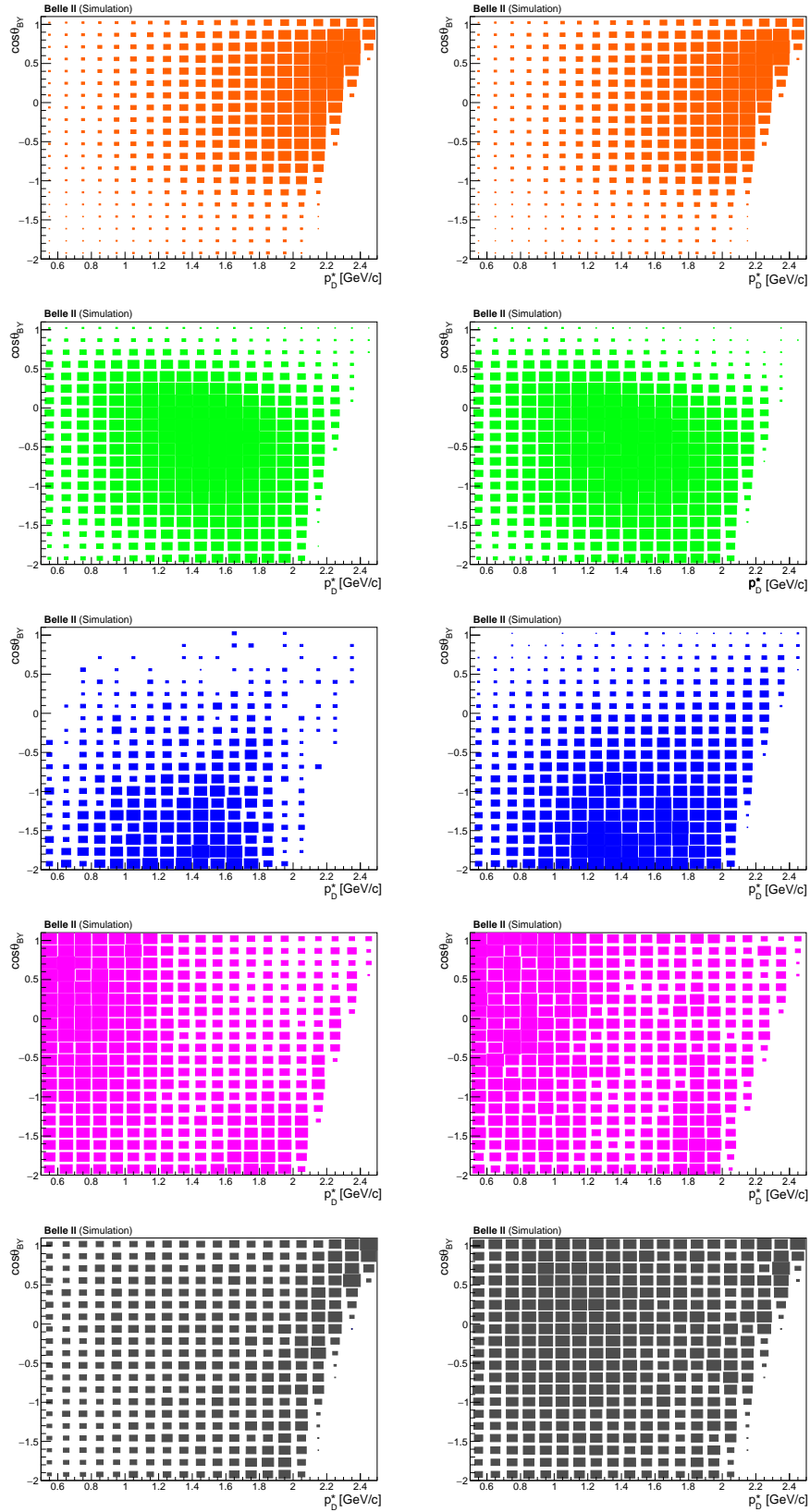


Figure 6.3: The space  $(\cos\theta_{BY}, p_D^*)$  for different sample components of the (left column)  $\overline{D}^0 e^+$  and (right column) of  $D^- e^+$  samples: (orange) signal  $B \rightarrow D l \nu_\ell$ ; (green) signal  $B \rightarrow D^* l \nu_\ell$ ; and backgrounds (blue)  $X l \nu_\ell$ , (magenta) real- $D$ , (grey) fake- $D$  and continuum. Similar distributions hold for the muon samples.

control region. Each samples features its own  $\chi^2$  function; they are all summed into a global  $\chi^2$  function.

Note that in the  $\chi^2$  fit I decided to skip a bin if  $N_i$  is less than 30, to prevent calculating the  $\chi^2$  with insufficient candidates to assume a Gaussian distribution (an assumption intrinsic to the  $\chi^2$  fit). It is key to find an adequate binning scheme that minimises these skipped bins, but, at the same time, that has enough bins to keep information on the template shape for discriminating between the components. In the signal region, I split the three-dimensional space in 90 bins: 3 bins for  $\cos\theta_{BY}$  in the range  $[-2, 1.1]$ ; 6 bins for  $p_\ell^*$  in the range  $[0.8, 2.2]$  GeV/ $c$ ; and 5 bins for  $p_D^*$  in the range  $[0.5, 2.5]$  GeV/ $c$ .

In the control region, I use only the two-dimensional distributions of  $(p_D^*, p_\ell^*)$ , as in this case the  $\cos\theta_{BY}$  distributions do not provide any additional separation of the sample components. Removing one dimension enables to increase the number of bins for the other two, resulting in a better modelling of the  $(p_D^*, p_\ell^*)$  distributions. I split the two-dimensional space into 100 bins: 10 bins for  $p_D^*$  in the range  $[0.5, 2]$  GeV/ $c$  for both the electron and muon samples, and 10 bins for  $p_\ell^*$  in the range  $[0.8, 1.9]$  GeV/ $c$  for the electron sample and  $[1.1, 1.9]$  GeV/ $c$  for the muon sample. For the latter, a tighter cut is applied to further suppress real- $D$  decays and obtain a purer  $X\ell\nu_\ell$  sample. For both the signal and control regions, the bins in a given dimension all have equal width. In the signal region, the fraction of skipped bins is less than 5% for any sample; in the control region, less than 10%.

The  $\chi^2$  is a function of a vector of parameters, which are detailed later. The best-fit parameters are those that minimise the global  $\chi^2$ . I use the numerical minimiser MINUIT with the algorithm MIGRAD to find them and HESSE to calculate their uncertainties [147]. MIGRAD employs an iterative optimisation technique that estimates the function gradient and Hessian (second derivatives) to guide the search for the minimum.

Through Eq. 6.2, the data samples are described as the sum of several components. Each component has a yield, which can be either a fit parameter or fixed, and a template, which can either depend on fit parameters or have a fixed shape. All components and their parameters are detailed in the following sections. Their division follows the sample components introduced in Chapter 4.

### 6.2.1 Signal

The signal decays  $B^+ \rightarrow \bar{D}^0 \ell^+ \nu_\ell$ ,  $B^+ \rightarrow \bar{D}^{*0} \ell^+ \nu_\ell$ , and  $B^0 \rightarrow D^{*-} \ell^+ \nu_\ell$ , contribute the yields

$$N_{\bar{D}^0 \ell^+} = N_{B\bar{B}} \frac{f}{1+f} \varepsilon_{\bar{D}^0 \ell^+} \mathcal{B}(B^+ \rightarrow \bar{D}^0 \ell^+ \nu_\ell) \mathcal{B}(\bar{D}^0 \rightarrow K^+ \pi^-), \quad (6.3)$$

$$N_{D^* \ell^+} = N_{B\bar{B}} \left[ \frac{f}{1+f} \varepsilon_{\bar{D}^{*0} \ell^+} \mathcal{B}(B^+ \rightarrow \bar{D}^{*0} \ell^+ \nu_\ell) \right. \\ \left. + \frac{1}{1+f} \varepsilon'_{D^{*-} \ell^+} \mathcal{B}(B^0 \rightarrow D^{*-} \ell^+ \nu_\ell) \mathcal{B}(D^{*-} \rightarrow \bar{D}^0 X) \right] \mathcal{B}(\bar{D}^0 \rightarrow K^+ \pi^-), \quad (6.4)$$

in the  $\bar{D}^0 \ell^+$  samples, while the decays  $B^0 \rightarrow D^- \ell^+ \nu_\ell$  and  $B^0 \rightarrow D^{*-} \ell^+ \nu_\ell$  contribute the yields

$$N_{D^- \ell^+} = N_{B\bar{B}} \frac{1}{1+f} \varepsilon_{D^- \ell^+} \mathcal{B}(B^0 \rightarrow D^- \ell^+ \nu_\ell) \mathcal{B}(D^- \rightarrow K^+ \pi^- \pi^-), \quad (6.5)$$

$$N_{D^{*-} \ell^+} = N_{B\bar{B}} \frac{1}{1+f} \varepsilon_{D^{*-} \ell^+} \mathcal{B}(B^0 \rightarrow D^{*-} \ell^+ \nu_\ell) \mathcal{B}(D^{*-} \rightarrow D^- X) \mathcal{B}(D^- \rightarrow K^+ \pi^- \pi^-), \quad (6.6)$$

in the  $D^-\ell^+$  samples. Here,  $N_{B\bar{B}}$  is the number of  $B\bar{B}$  pairs;  $f = f_{+-}/f_{00}$ ;  $\varepsilon_i$  is the efficiency for a given signal  $i$  with branching fraction  $\mathcal{B}(i)$ . Note that the two efficiencies,  $\varepsilon_{\bar{D}^{*0}\ell^+}$  and  $\varepsilon'_{D^{*-}\ell^+}$  in Eq. 6.4, are nearly identical, allowing the yield  $N_{D^{*}\ell^+}$  to be parametrised with a single global efficiency. In addition, the signal decays  $B^+ \rightarrow \bar{D}^{*0}(\rightarrow \bar{D}^0 X)\ell^+\nu_\ell$  and  $B^0 \rightarrow D^{*-}(\rightarrow \bar{D}^0 X)\ell^+\nu_\ell$  have the same  $(\cos\theta_{BY}, p_\ell^*, p_D^*)$  distribution, hence I cannot disentangle them in the  $\bar{D}^0\ell^+$  sample. By fitting simultaneously the  $\bar{D}^0\ell^+$  and  $D^-\ell^+$  samples, the branching fractions of the four signal decays can be determined.

I can impose a symmetry to link the branching fractions of  $B^+$  and  $B^0$  decays. By neglecting the tiny difference in  $u$  and  $d$  quark masses (isospin symmetry), the semileptonic decay widths for  $B^+$  and  $B^0$  decays are the same. Therefore, the branching fractions of  $B^0$  decays are related to those of  $B^+$  decays as

$$\mathcal{B}(B^0 \rightarrow D^{(*)-}\ell^+\nu_\ell) = \frac{\tau_{B^0}}{\tau_{B^+}} \mathcal{B}(B^+ \rightarrow \bar{D}^{(*)0}\ell^+\nu_\ell), \quad (6.7)$$

where  $\tau_{B^0}$  and  $\tau_{B^+}$  are the  $B^0$  and  $B^+$  lifetimes.

Considering the number of  $B\bar{B}$  pairs, the efficiencies, and the charm branching fractions as inputs, and by invoking isospin symmetry, there are three unknowns to be determined from the four Eqs. 6.3–6.6: two signal branching fractions and  $f$ , which can also be obtained from the fit to data. This, however, comes at the cost of an additional uncertainty due to possible isospin-breaking contributions. Isospin-breaking arises from the mass difference between the  $u$  and  $d$  quarks, as well as potentially different electromagnetic interactions between final-state particles in  $B^0$  and  $B^+$  decays (see Sect. 2.1). The former is negligible, as the difference in the masses of  $B^+$  and  $B^0$  mesons is much smaller than a fraction of a per mille. The latter, instead, cannot be neglected.

Decays of a  $B^+$  meson result in a neutral charm state and a lepton, which cannot interact electromagnetically. In contrast,  $B^0$  meson decays lead to a charged charm meson, which can interact electromagnetically with the lepton, introducing contributions to the  $B^0$  decay amplitudes that are absent in  $B^+$  decays. These contributions are encapsulated in the so-called ‘‘Coulomb factor’’ (see for instance Chapter 3 of Ref. [30]), a correction to the electroweak parameter  $\eta_{EW}$  (see Sect. 2.1), which is multiplied by a factor

$$(1 + \alpha\pi/2), \quad (6.8)$$

where  $\alpha$  is the electromagnetic coupling constant. This correction affects the  $B^0$  branching fraction, and therefore the extraction of  $|V_{cb}|$ . Finally, the four signal yields of Eqs. 6.3–6.6 are expressed in terms of two signal branching fractions, assuming isospin symmetry while also accounting for possible isospin-breaking effects through the Coulomb factor.

To parametrise the signal yields as a function of the model-independent observables, I decompose the signal branching fractions, as

$$\mathcal{B}(B \rightarrow D^{(*)}\ell\nu_\ell) = \frac{\Gamma(B \rightarrow D^{(*)}\ell\nu_\ell)}{\Gamma_{\text{total}}} = \frac{\Gamma(B \rightarrow D^{(*)}\ell\nu_\ell)\tau_B}{\hbar}, \quad (6.9)$$

where  $\Gamma(B \rightarrow D^{(*)}\ell\nu_\ell)$  is the decay width of the process,  $\Gamma_{\text{total}}$  is the total decay width for a  $B$  meson and  $\hbar \simeq 65.821 \times 10^{-14}$  GeV·ps is the reduced Planck constant. The  $B \rightarrow D^{(*)}\ell\nu_\ell$  decay width is obtained by integrating the differential decay rate. For  $B \rightarrow D^{(*)}\ell\nu_\ell$ , this is the two-dimensional decay rate in Eq. 2.26 integrated in  $w$  and  $\cos\theta_\ell$ ,

$$\Gamma(B \rightarrow D^*\ell\nu_\ell) = \int_1^{w^{\text{max}}} dw \int_{-1}^1 d\cos\theta_\ell \frac{d^2\Gamma(B \rightarrow D^*\ell\nu_\ell)}{dw d\cos\theta_\ell}, \quad (6.10)$$

while for  $B \rightarrow D\ell\nu_\ell$ , it is the one-dimensional decay rate in Eq. 2.33,

$$\Gamma(B \rightarrow D\ell\nu_\ell) = \int_1^{w^{\max}} dw \frac{d\Gamma(B \rightarrow D\ell\nu_\ell)}{dw}. \quad (6.11)$$

The maximum values  $w^{\max}$  are obtained at maximum recoil energy (see Eq. 2.3, with  $q^2 = 0$  and the mass values of the  $B$ ,  $D$  and  $D^*$  mesons). The two differential decay rates are functions of the model-independent variables  $a'_n, b'_n, c'_n$  and  $G'_m$  as shown in Eqs. 2.30–2.32 and 2.34. The signal yield can now be expressed in terms of these variables. However, the signal templates are still fixed from the simulation; they need to be modified to also depend on the model-independent observables, as explained in the next section.

In the control region, I parametrise the signal yields in the same way as in the signal region, by changing only the efficiencies. In the control region, the signal accounts for only 15% of the  $\overline{D}^0 e^+$  sample and less than 5% of the other samples.

### 6.2.1.1 Dynamical signal templates

The signal templates are generated assuming a specific model for the form factors, as reported in Tab. 4.1, which leads to fixed values of  $a'_n, b'_n, c'_n$  and  $G'_m$ . I need a method to adjust the shape according to new values of the model-independent observables, which should change during the  $\chi^2$  minimisation to adapt the template (and the signal yield) to the data. This is achieved through a weighting technique applied at every MINUIT call during the scan of the parameter space in search for the minimum of the  $\chi^2$  function.

The weighting acts on the simulated data to change the underlying physics model used to generate the sample. Let us consider the template for the  $B \rightarrow D^*\ell\nu_\ell$  decays as an example. The signal template must contain the information on the  $w$  and  $\cos\theta_\ell$  distributions of the original model. Therefore, the three-dimensional template in  $(\cos\theta_{BY}, p_\ell^*, p_D^*)$  is extended to a five-dimensional template with  $(\cos\theta_{BY}, p_\ell^*, p_D^*, w, \cos\theta_\ell)$ . I then calculate a weight by evaluating the following quantity

$$p_i = \left[ \frac{1}{\Gamma_{\text{new}}} \int_{\Delta x_i} \frac{d\Gamma_{\text{new}}}{dx} dx \right] / \left[ \frac{1}{\Gamma_{\text{gen}}} \int_{\Delta x_i} \frac{d\Gamma_{\text{gen}}}{dx} dx \right], \quad (6.12)$$

where  $x$  represents the space  $(w, \cos\theta_\ell)$ ;  $\Delta x_i$  is the  $i$ -th bin in  $(w, \cos\theta_\ell)$  of the template histogram;  $d\Gamma_j/dx$  and  $\Gamma_j$  are the differential decay rate and its integral over the full phase space, with  $j = \text{gen}$  for the decay model used in the generation of the simulated data, and  $j = \text{new}$  for the new decay-model with the parameters  $a'_n, b'_n$ , and  $c'_n$  to be determined in the fit.

The five-dimensional histogram, with entries modified by the weights in the  $(w, \cos\theta_\ell)$  bins, is marginalised to obtain the three-dimensional template in  $(\cos\theta_{BY}, p_\ell^*, p_D^*)$ : the shape of the three-dimensional distribution is altered according to the new underlying physics model. Note that this weighting method accounts for resolution effects and efficiency variations as a function of the reconstructed variables, which making the template independent from the form-factor model assumed in the generation of the simulated data.

A similar procedure is adopted for the  $B \rightarrow D\ell\nu_\ell$  decay, with the only difference being that I need to add only the dimension  $w$  to the  $(\cos\theta_{BY}, p_\ell^*, p_D^*)$  template and use the one-dimensional decay rate to compute the weight of Eq. 6.12<sup>2</sup>.

---

<sup>2</sup>For the  $B \rightarrow D\ell\nu_\ell$  decay, the weight is calculated using only the information from  $w$  and not from  $\cos\theta_\ell$ , as the form factor  $\mathcal{G}$  depends solely on  $w$  and  $\cos\theta_\ell$  does not provide an additional information about it.

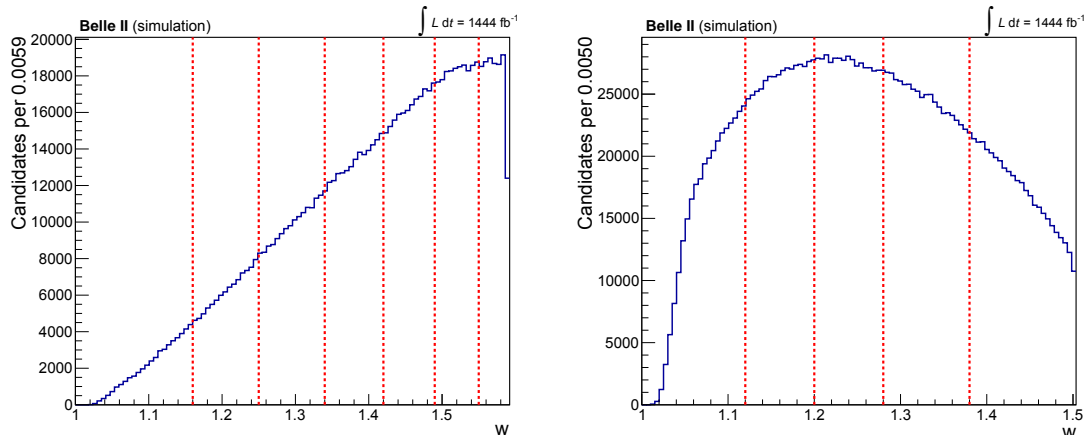


Figure 6.4: Distributions of  $w$  for (left)  $B \rightarrow D l \nu_\ell$  and (right) for  $B \rightarrow D^* l \nu_\ell$  decays. The vertical dotted red line indicates the bin edges chosen for this analysis.

Note that the weighting is not dependent on how populated the space of the  $B$ -kinematics variables is in the templates, (*i.e.*, the number of bins defined for the extra dimensions added to the original template of the reconstructed variables). The weight can be always computed, and if there are no candidates in a particular bin, the weight will not modify the (zero) content. By marginalising the distribution to project only onto the space of reconstructed variables, the weights are summed, and for the  $\chi^2$  fit, only the bin content of the template of the reconstructed variables matters.

The number of model-independent observables to fit is determined by the division of the  $w$  range into bins. It ultimately depends on the shapes of the expected distributions of  $w$ , which are shown in Fig. 6.4. I choose a binning scheme that ensures sufficient statistical precision for each observable by iterating for different schemes a simplified version of the analysis with simulated data and inspecting the results. For  $B \rightarrow D l \nu_\ell$ , I decide to measure  $G'_m$  in 7 bins of  $w$ ; for  $D^* l \nu_\ell$ , I measure  $a'_n$ ,  $b'_n$  and  $c'_n$  in 5 bins of  $w$ . Note that this binning scheme determines the minimum number of bins to be employed in the weighting of the templates.

By imposing isospin symmetry, the same form factors for  $B^+$  and  $B^0$  decays are assumed, and the fit is performed using a single set of 22 model-independent observables.

### 6.2.2 $X l \nu_\ell$ background

The  $X l \nu_\ell$  background is divided into three subcomponents, as introduced in Sect. 4.1.2, for both the signal and control regions:  $D^{**} l \nu_\ell$  decays, semitaupic decays, and semileptonic decays with misidentified leptons. The latter two subcomponents represent a small contribution (approximately 1-3% of the total  $X l \nu_\ell$  background), in both the signal and control regions across all samples.<sup>3</sup> For the analysis, I combine these contributions into a single template with yields fixed based on the simulation, and I assess a systematic uncertainty for this simplification in Chapter 7.

The  $D^{**} l \nu_\ell$  subcomponent, which contributes the largest fraction, is addressed separately. According to the study in Sect. 5.3.1, it is further divided into more subcomponents: decays with a  $D^{**}$  resonance, non-resonant  $D^{(*)} \pi \pi$ , and the gap modes. The yield of these

<sup>3</sup>One exception is the  $D^- \mu^+$  sample in the control region, where the misidentified leptons are about 20% of the  $X l \nu_\ell$  background. However, this contribution accounts for only 1.6% of the total  $D^- \mu^+$  sample.

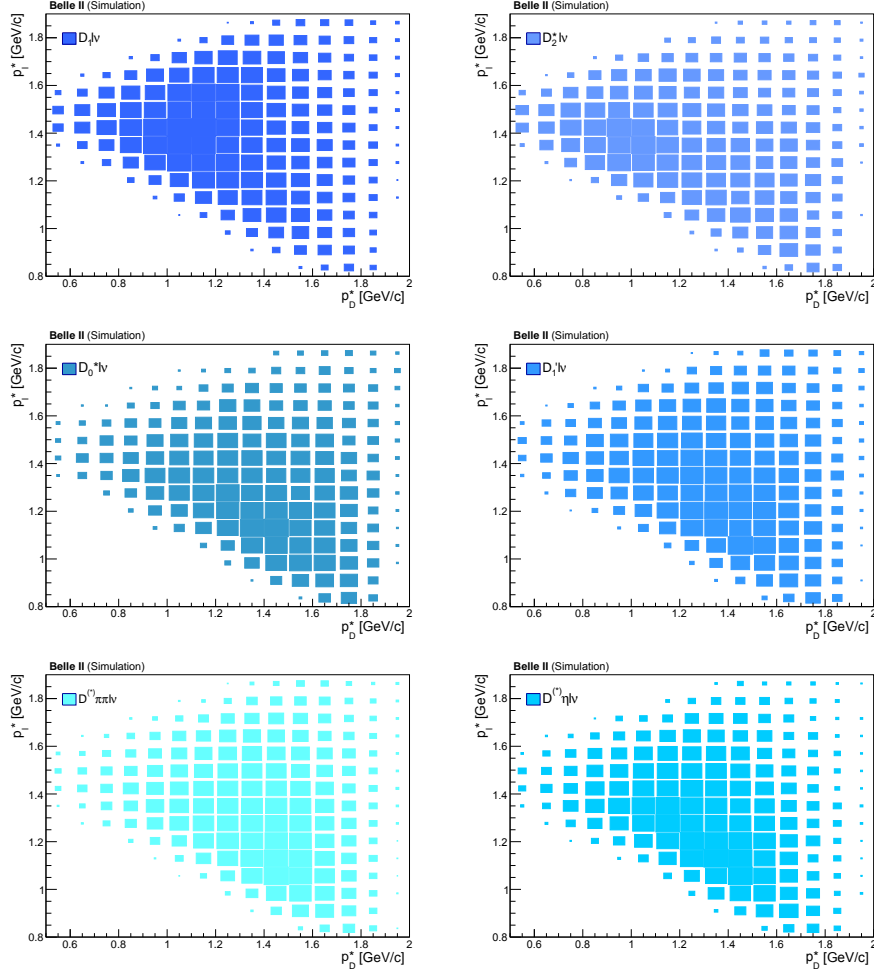


Figure 6.5: Two-dimensional distributions of  $(p_D^*, p_\ell^*)$  of the  $D^{**} l \nu_\ell$  decays for the  $\overline{D}^0 e^+$  sample in the control region. Similar distributions are observed in the other samples. For comparison, the same distributions for the  $\overline{D}^0 e^+$  sample in the signal region can be found in Appendix B.

subcomponents in the samples  $j = \overline{D}^0 \ell^+, D^- \ell^+$  is expressed as

$$N_j^i = N_{B\overline{B}} \varepsilon_j^i \mathcal{B}^i \left[ \frac{f}{1+f} K_j^{+,i} + \frac{1}{1+f} \frac{\tau_{B^0}}{\tau_{B^+}} (1 + \alpha\pi) K_j^{0,j} \right] \mathcal{B}_j(D), \quad (6.13)$$

where  $\mathcal{B}^i$  is the branching fraction of the subcontribution  $i$ ;  $\varepsilon_j^i$  is its selection efficiency in the sample  $j$ ;  $\mathcal{B}_j(D)$  is the branching fraction of  $\overline{D}^0 \rightarrow K^+ \pi^-$  and  $D^- \rightarrow K^+ \pi^- \pi^-$  for  $j = \overline{D}^0 \ell^+$  and  $j = D^- \ell^+$ ;  $K_j^{+,i}$  and  $K_j^{0,i}$  are the relative fractions of  $B^+$  and  $B^0$  decays. The latter are derived assuming the branching fractions of the  $D^{**}$  decays as used in Belle II simulation. Note that in Eq. 6.13 I assume isospin symmetry to link  $B^+$  and  $B^0$  decays as done for the signal component.

Different yields are obtained for the signal and control regions (according to the corresponding efficiencies  $\varepsilon_j^i$ ) which are linked through the branching fractions  $\mathcal{B}^i$ . Thus, the control region enables constraining the contribution of these subcomponents in the signal region. Each yield is multiplied by a template. The shapes of the various templates show small differences, as can be observed in Fig. 6.5 from the two-dimensional distributions of

$(p_D^*, p_\ell^*)$  in the control region. The statistical discrimination of each subcontribution is challenging. Thus, I apply Gaussian penalties, using the inputs from HFLAV 2024 in Tab. 5.3, to incorporate information on the branching fractions from previous measurements.

I lump in a single template the  $B \rightarrow D\pi\pi\ell\nu_\ell$  and  $B \rightarrow D^*\pi\pi\ell\nu_\ell$  decays, as well as the  $B \rightarrow D\eta\ell\nu_\ell$  and  $B \rightarrow D^*\eta\ell\nu_\ell$  decays, with constraints on their branching fractions of  $(0.30 \pm 0.13)\%$  and  $(1.80 \pm 1.80)\%$ , respectively, obtained by summing their contributions in Tab. 5.3. This is because their branching fractions have large uncertainties and for the  $D^{(*)}\eta\ell\nu_\ell$  final state, the fraction of  $D$  and  $D^*$  decays is arbitrary.

I emphasise that the purpose of using the control region is not to measure the branching fractions of the decays of the  $D^{**}\ell\nu_\ell$  component, but to build confidence in the cocktail used to model them, given the limited *a priori* knowledge available. This approach should reduce the systematic uncertainty on the signal due to the poor information available on these decays, as detailed in Sect. 5.3.1.

### 6.2.3 Real- $D$ background

From the study presented in Sect. 5.2, the real- $D$  background cannot be constrained using the WC sample, as the latter has a very different composition compared to the RC sample. For this reason, I fit the yield of the real- $D$  background directly from data in the signal region.

Here, the real- $D$  background is not decomposed into the three subcomponents discussed in Chapter 5 (primary, secondary, and fake leptons), as their separation is irrelevant given the small contribution of the real- $D$  background in all samples. The overall templates of the signal region are built from the two-dimensional distributions of  $(p_D^*, p_\ell^*)$  shown in Fig. 6.3.

In the control region, instead, the separation into the three subcomponents improves the modelling of the data and enhances the discrimination from the  $X\ell\nu_\ell$  background. An example of the separation in the  $(p_D^*, p_\ell^*)$  space of the free real- $D$  subcomponents for the  $\bar{D}^0 e^+$  sample is shown in Fig. 6.6.

Not all subcomponents have free yields, though. The ones that do are: primary leptons in the  $\bar{D}^0 e^+$  and  $D^- e^+$  samples; secondary leptons in the  $\bar{D}^0 e^+$  sample; fake leptons in the  $\bar{D}^0 \mu^+$  sample. For each lepton category, I link the yields in the electron and muon samples through efficiency ratios and fit them with a single parameter. Other categories have fixed yields based on simulation, as they contribute very small fractions. These categories include secondary and fake leptons in both the  $D^- e^+$  and  $D^- \mu^+$  samples. A systematic uncertainty for this assumption is accounted for in Chapter 7.

### 6.2.4 Fake- $D$ and continuum

The fake- $D$  and continuum backgrounds in the signal region are determined using the  $D$ -mass sideband and off-resonance data, as explained in Chapter 5; their yields and templates are fixed in the fit accordingly. I assess a systematic uncertainty related to this analysis strategy in Chapter 7.

For the control region, I cannot apply the same procedure described for the signal region, as the simulation shows significant differences between the  $(p_D^*, p_\ell^*)$  distributions for candidates in the  $D$ -mass signal region and the sideband. Therefore, I decide to constrain the two backgrounds using a different approach. I leverage information from the off-resonance data to set the yields of the continuum background, while the yield of the fake- $D$  background is determined from data by using the  $D$ -mass sideband and subtracting

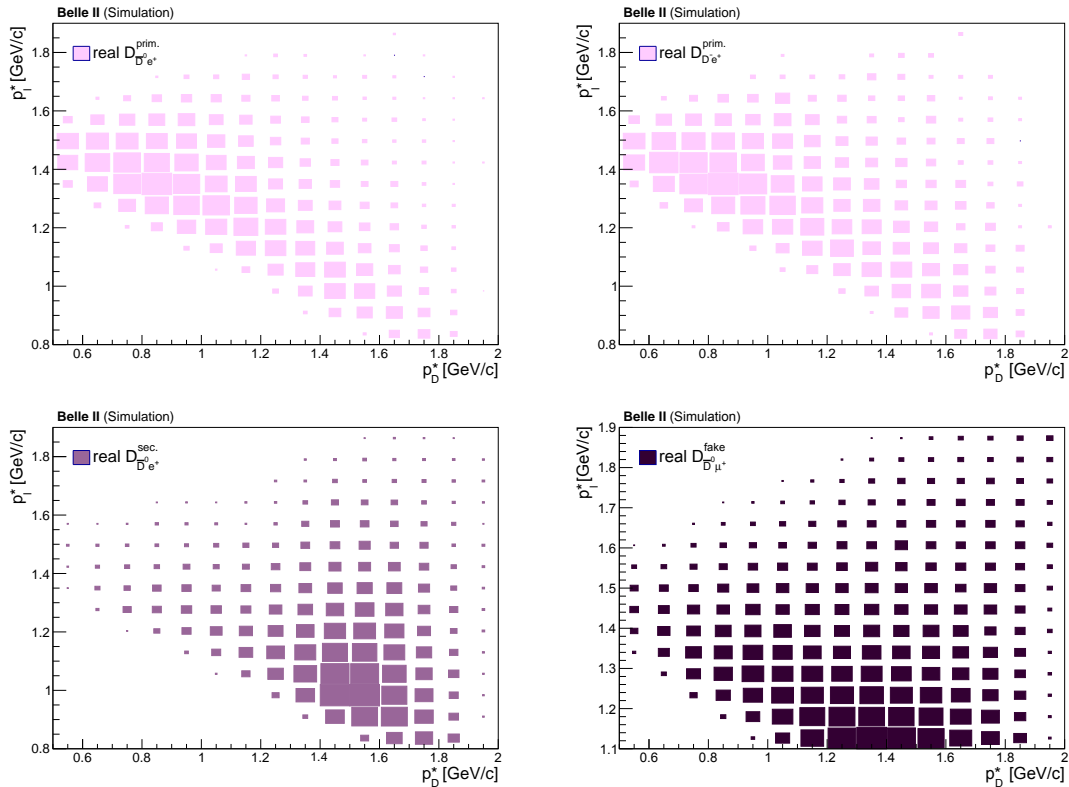


Figure 6.6: Two-dimensional distribution of  $(p_D^*, p_\ell^*)$  of the real- $D$  subcomponents left free in the fit in the control region: primary leptons in the (top left)  $\bar{D}^0 e^+$  and (top right)  $D^- e^+$  samples, secondary leptons (bottom left) in the  $\bar{D}^0 e^+$  sample and fake leptons (bottom right) in the  $\bar{D}^0 \mu^+$ .

the continuum contribution. The yields are constrained in the fit, and the templates are derived from simulation. I checked in  $D$ -mass sideband that the simulation reproduces the experimental data distributions, assuming that the same holds for the  $D$ -mass signal region. Continuum and fake- $D$  backgrounds are separated into two different templates to simplify the evaluation of the systematic uncertainty associated with them, as discussed in Chapter 7.

### 6.2.5 Fit parameters

I provide a summary of the fit parameters in Tab. 6.1. I also report those that are fixed from simulation in the fit, as previously discussed for each component. Additionally, I include several nuisance parameters using Gaussian penalties, some of which have already been introduced. The complete list of Gaussian-constrained parameters is as follows:

- the number of  $B\bar{B}$  pairs,  $N_{B\bar{B}} = (387 \pm 6) \times 10^6$ , as provided by the Belle II performance group;
- the correction for the tracking efficiency (see Sect. 4.1.1.5), which is included as a multiplicative factor on the signal efficiency,  $(1 + 0.0024 \cdot K)^N$ , with  $N$  the number of tracks and  $K$  a Gaussian-constrained parameter with a normal distribution;<sup>4</sup>

<sup>4</sup>I do not include this correction for the background  $D^{**} \ell \nu_\ell$  decays, as this is negligible compared to

Component	Decay	Parameters	Comments
Signal	$B \rightarrow D\ell\nu_\ell$	$G'_1, G'_2, G'_3, G'_4, G'_5, G'_6, G'_7$	free
		$\varepsilon_{j,r}^D$	fixed
	$B \rightarrow D^*\ell\nu_\ell$	$a'_1, a'_2, a'_3, a'_4, a'_5$	free
		$b'_1, b'_2, b'_3, b'_4, b'_5$	free
		$c'_1, c'_2, c'_3, c'_4, c'_5$	free
		$\varepsilon_{j,r}^{D^*}$	fixed
$X\ell\nu_\ell$	$B \rightarrow D_1(2420)\ell\nu_\ell$	$\mathcal{B}(B \rightarrow D_1(2420)\ell\nu_\ell)$	constrained
		$\varepsilon_{j,r}^{D_1(2420)}$	fixed
	$B \rightarrow D'_1(2430)\ell\nu_\ell$	$\mathcal{B}(B \rightarrow D'_1(2430)\ell\nu_\ell)$	constrained
		$\varepsilon_{j,r}^{D'_1(2430)}$	fixed
	$B \rightarrow D_0^*(2300)\ell\nu_\ell$	$\mathcal{B}(B \rightarrow D_0^*(2300)\ell\nu_\ell)$	constrained
		$\varepsilon_{j,r}^{D_0^*(2300)}$	fixed
	$B \rightarrow D_2^*(2460)\ell\nu_\ell$	$\mathcal{B}(B \rightarrow D_2^*(2460)\ell\nu_\ell)$	constrained
		$\varepsilon_{j,r}^{D_2^*(2460)}$	fixed
	$B \rightarrow D^{(*)}\pi\pi\ell\nu_\ell$	$\mathcal{B}(B \rightarrow D^{(*)}\pi\pi\ell\nu_\ell)$	constrained
		$\varepsilon_{j,r}^{D^{(*)}\pi\pi\ell\nu_\ell}$	fixed
$B \rightarrow D^{(*)}\eta\ell\nu_\ell$	$\mathcal{B}(B \rightarrow D^{(*)}\eta\ell\nu_\ell)$	constrained	
	$\varepsilon_{j,r}^{D^{(*)}\eta\ell\nu_\ell}$	fixed	
$X\tau\nu_\tau$	$N_{j,r}^{X\tau\nu_\tau}$	fixed	
mis-ID leptons	$N_{j,r}^{\text{mis-ID leptons}}$	fixed	
real- $D$		signal region: $N_j^{\text{real-}D}$	free
		control region: $N_{\bar{D}^0 e^+}^{\text{prim.}}, N_{\bar{D}^0 e^+}^{\text{sec.}}, N_{D^- e^+}^{\text{prim.}}, N_{\bar{D}^0 \mu^+}^{\text{fake}}$	free
		control region: $(\frac{\varepsilon_{\bar{D}^0 \mu^+}}{\varepsilon_{\bar{D}^0 e^+}})^{\text{prim.}}, (\frac{\varepsilon_{\bar{D}^0 \mu^+}}{\varepsilon_{\bar{D}^0 e^+}})^{\text{sec.}}, (\frac{\varepsilon_{D^- \mu^+}}{\varepsilon_{D^- e^+}})^{\text{prim.}}, (\frac{\varepsilon_{\bar{D}^0 e^+}}{\varepsilon_{\bar{D}^0 \mu^+}})^{\text{fake}}$	fixed
		control region: $N_{D^- e^+}^{\text{sec.}}, N_{D^- \mu^+}^{\text{sec.}}, N_{D^- e^+}^{\text{fake}}, N_{D^- \mu^+}^{\text{fake}}$	fixed
fake- $D$ + continuum		signal region: $N_j^{\text{fake-}D+\text{cont.}}$	constrained
		control region: $N_j^{\text{fake-}D}, N_j^{\text{cont.}}$	constrained
common parameters		$f_{+-}/f_{00}$	free
		$N_{B\bar{B}}$	constrained
		$\mathcal{B}(\bar{D}^0 \rightarrow K^+\pi^-), \mathcal{B}(D^- \rightarrow K^+\pi^-\pi^-), \mathcal{B}(D^{*-} \rightarrow \bar{D}^0 X)$	constrained
		lifetime ratio: $\tau_{B^0}/\tau_{B^+}$	constrained
		Coulomb factor: $\theta$	constrained
		track. eff. correction: $K$	constrained

Table 6.1: Summary of the parameters from the simultaneous fit of the eight samples (where  $r$  indicates either the signal or control regions and  $j = \bar{D}^0 e^+, \bar{D}^0 \mu^+, D^- e^+$  and  $D^- \mu^+$ ). In total there are: 31 (free) + 25 (Gaussian constrained) + 80 (fixed) parameters.

- the lifetime ratio between  $B^0$  and  $B^+$  mesons,  $\tau_{B^0}/\tau_{B^+} = 0.929 \pm 0.004$ , taken from Ref. [14];
- the branching fractions  $\mathcal{B}(\bar{D}^0 \rightarrow K^+\pi^-) = (3.95 \pm 0.03)\%$ ,  $\mathcal{B}(D^- \rightarrow K^+\pi^-\pi^-) = (9.38 \pm 0.16)\%$  and  $\mathcal{B}(D^{*-} \rightarrow \bar{D}^0 X) = (67.7 \pm 0.5)\%$ <sup>5</sup>, taken from Ref. [14];
- the branching fractions of the decays in the  $D^{**}\ell\nu_\ell$  component described in Sect. 6.2.2, using the latest HFLAV 2024 averages (see Tab. 5.3);
- the yields of the fake- $D$  and continuum backgrounds in both the signal and control regions, as estimated in Sect. 6.2.4 using off-resonance data and  $D$ -mass sideband;

the uncertainties on their branching fractions.

<sup>5</sup>The branching fraction  $\mathcal{B}(D^{*-} \rightarrow D^- X)$  is parametrised as  $1 - \mathcal{B}(D^{*-} \rightarrow \bar{D}^0 X)$ .

- an uncertainty on the Coulomb factor of Eq. 6.8. Since there is no consensus on the exact value of the correction, I assign a 100% uncertainty by modifying the correction to the lifetime ratio, Eq. 6.7, as  $(1 + \alpha\pi\theta)$ , with  $\theta$  a Gaussian-constrained parameter with a normal distribution.

### 6.3 Fit to the control region

As mentioned in Sect. 5.4, the  $\cos\theta_{BY}$  sideband is enriched with the  $D^{**}\ell\nu_\ell$  component, providing an opportunity to gain direct information on this background—the least understood in the sample—directly from data. I fit the control region simultaneously with the signal region to that purpose. Before analysing the full sample, I perform a fit to the data in the control region alone, for two reasons: it allows for testing the fit directly on data without gaining information on the signal and thus violating the blinding protocol; and it provides an initial test of the background modelling directly on data. Using the results of this fit, I can also fine-tune the simulated sample to better validate the full analysis with a background composition closer to what we expect from data. With a more realistic sample, I can also accurately assess the expected systematic uncertainties of the analysis.

First, I compare data and simulation distributions of the fitting variables; observing a large discrepancy as shown in Fig. 6.7. The primary cause of this discrepancy could be a mismodelling of the  $D^{**}\ell\nu_\ell$  component, which features the largest uncertainties. This hypothesis is supported by the fact that the other components are either better known (as the signal  $B \rightarrow D^{(*)}\ell\nu_\ell$  contamination in the control region), or already constrained from data (as for the fake- $D$  mesons and continuum backgrounds).

The configuration of the simultaneous fit between the signal and control region has been presented in detail in the previous sections. Let me summarise it here for the control region alone: I fit the two-dimensional distribution of  $(p_\ell^*, p_D^*)$ , with the binning discussed in Sect. 6.2, simultaneously between the  $\bar{D}^0\ell^+$  and  $D^-\ell^+$  samples. The yields of the  $D^{**}\ell\nu_\ell$  component are Gaussian-constrained, as reported in Sect. 6.2.2. The real- $D$  subcomponents (primary, secondary and fake leptons) have free yields, which are linked between the electron and muon channels through the ratio of efficiencies. The remaining small subcomponents (semitauonic decays, semileptonic decays with misidentified leptons, and secondary and fake leptons for the real- $D$  background in the  $D^-e^+$  and  $D^-\mu^+$  samples) are fixed in the fit. Only for this fit, the signal yields and templates in the control region are also fixed based on expectations, their contribution is minimal nonetheless.

The results of the fit are summarised in Tab. 6.2 and fit projections are reported in Fig. 6.8. The  $\chi^2$  is 107 with 350 degrees of freedom. The small  $\chi^2$  value is attributed to the statistical uncertainties on the templates, which are included in the  $\chi^2$  calculation (see Eq. 6.1). Without accounting for these uncertainties, I obtain a  $\chi^2$  value of 404 for the same degrees of freedom.

I observe that all the branching fractions of  $D^{**}\ell\nu_\ell$  decays are compatible with the central values of the corresponding Gaussian constraints. However, the  $D^{(*)}\eta\ell\nu_\ell$  branching fraction is much smaller than the nominal value ( $-0.01\%$  versus  $1.8\%$ ), with an uncertainty significantly reduced compared to that of the original constrain ( $0.12\%$  versus  $1.8\%$ ). Thus, the data suggest a configuration with a substantially smaller fraction of gap modes. Since the branching fractions of the other  $D^{**}\ell\nu_\ell$  decays are not increased accordingly, this reduction increases the tension between the inclusive branching fraction and the sum of the exclusive branching fractions (see Sect. 5.3.1). This remains an open issue, also observed in other semileptonic-decay analyses in Belle and Belle II [143, 148].

I stress that in the main fit, when including also the signal region, I still use the

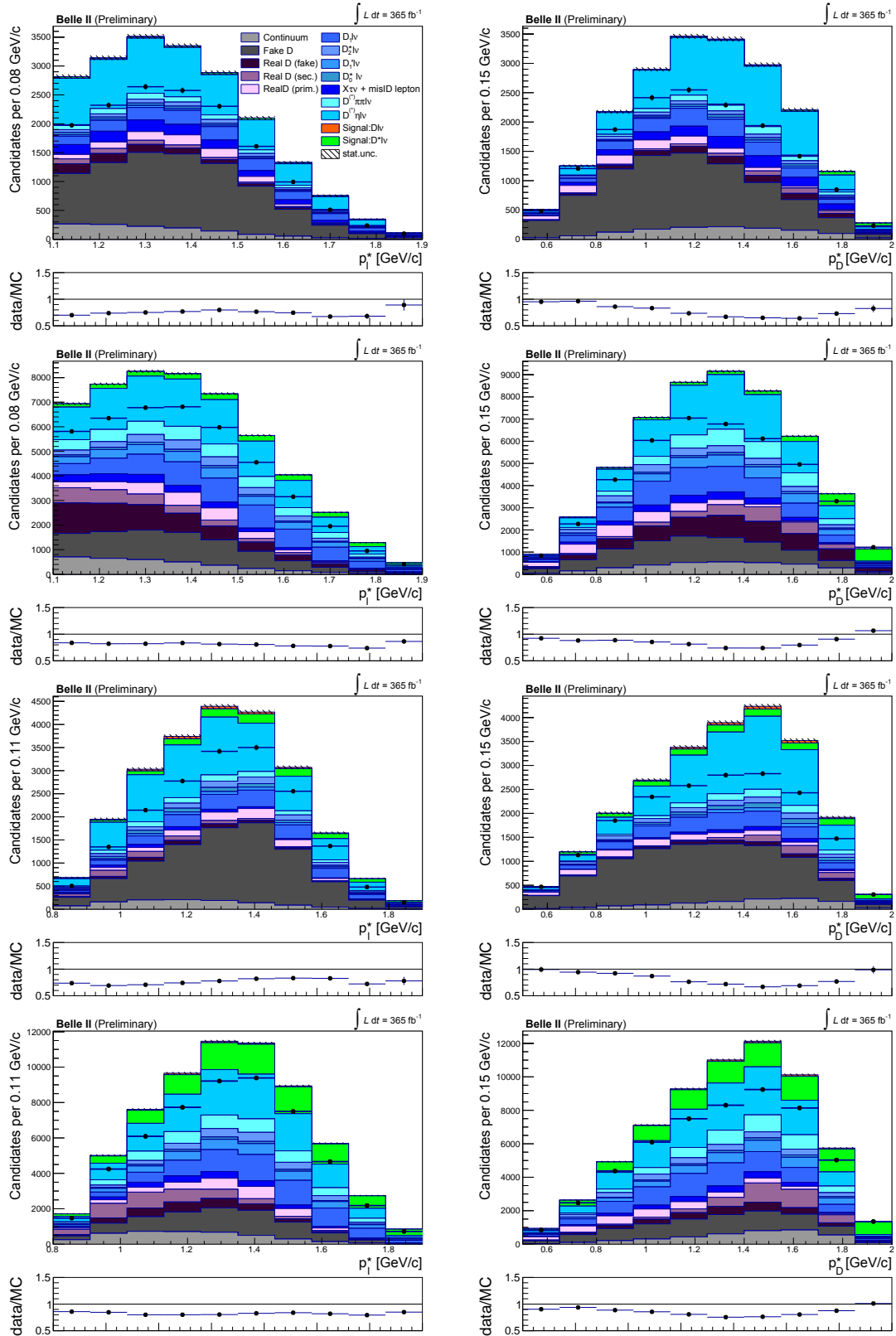


Figure 6.7: Data-simulation comparison of the (left column)  $p_\ell^*$  and (right column)  $p_D^*$  distributions in the control region for: (from top to bottom)  $D^-\mu^+$ ,  $\overline{D}^0\mu^+$ ,  $D^-e^+$ , and  $\overline{D}^0e^+$  samples.

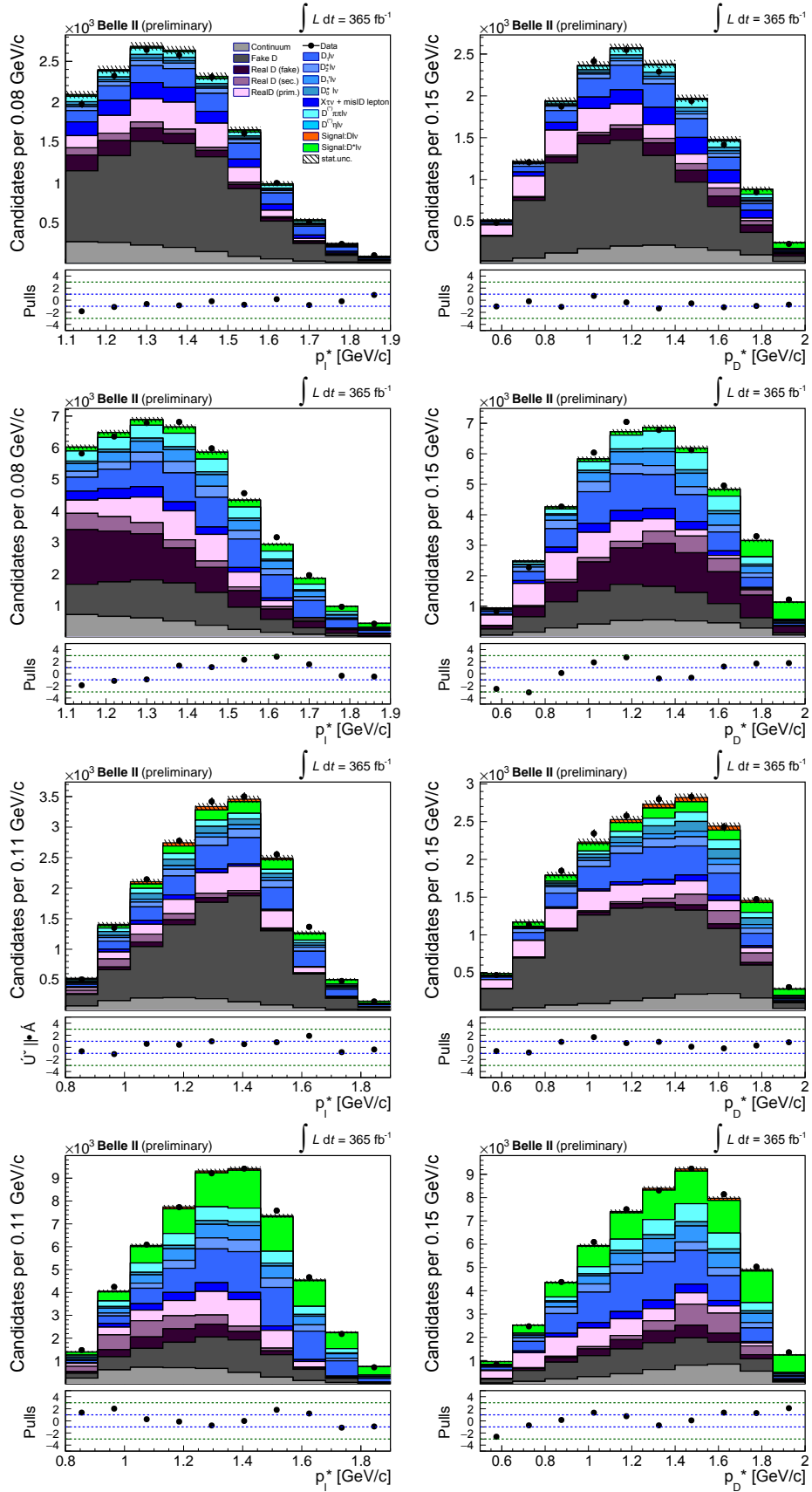


Figure 6.8: Control-region fit results. Distributions of (left column)  $p_\ell^*$  and (right column)  $p_D^*$  with fit projections overlaid. From top to bottom:  $D^- \mu^+$ ,  $\bar{D}^0 \mu^+$ ,  $D^- e^+$ , and  $\bar{D}^0 e^+$  samples in the control region.

Fit parameter	Gaussian constrain	Fit result
$\mathcal{B}(B \rightarrow D_1(2420)\ell\nu_\ell)$	$(0.64 \pm 0.10)\%$	$(0.79 \pm 0.07)\%$
$\mathcal{B}(B \rightarrow D_1'(2430)\ell\nu_\ell)$	$(0.28 \pm 0.04)\%$	$(0.29 \pm 0.04)\%$
$\mathcal{B}(B \rightarrow D_0^*(2300)\ell\nu_\ell)$	$(0.13 \pm 0.19)\%$	$(0.16 \pm 0.10)\%$
$\mathcal{B}(B \rightarrow D_2^*(2460)\ell\nu_\ell)$	$(0.32 \pm 0.03)\%$	$(0.33 \pm 0.03)\%$
$\mathcal{B}(B \rightarrow D^{(*)}\pi\pi\ell\nu_\ell)$	$(0.30 \pm 0.13)\%$	$(0.24 \pm 0.08)\%$
$\mathcal{B}(B \rightarrow D^{(*)}\eta\ell\nu_\ell)$	$(1.80 \pm 1.80)\%$	$(-0.01 \pm 0.12)\%$

Fit parameter	Simulation expectation	Fit result
$N_{D^0 e^+}^{\text{prim.}}$	2900	$4770 \pm 470$
$N_{D^0 e^+}^{\text{sec.}}$	3820	$3000 \pm 550$
$N_{D^- e^+}^{\text{prim.}}$	910	$1660 \pm 230$
$N_{D^0 \mu^+}^{\text{fake}}$	6670	$7910 \pm 860$

Table 6.2: Summary of the results from the fit to the control-region data. The upper table compares the results on the branching fractions of the decays in  $D^{**}\ell\nu_\ell$  component with the Gaussian constraints used in the fit. The branching fractions shown in the table pertain to  $B^+$  and are related to those of  $B^0$  through their lifetimes ratio. The bottom table compares the fit results of the real- $D$  background yields (free in the fit) with the expectation from the simulation.

Gaussian penalties with inputs from Tab. 5.3 for the  $D^{**}\ell\nu_\ell$  component. The uncertainties on their branching fractions, which address the inclusive-exclusive gap by assigning a 100% uncertainty to the  $D^{(*)}\eta\ell\nu_\ell$  branching fraction, are then propagated to the signal results, contributing to a systematic uncertainty (see Sect. 7.1). A dedicated study presented in Appendix D validates this systematic uncertainty, ensuring that the results are robust against different configurations of the  $D^{**}\ell\nu_\ell$  background. In addition, the yields of the real- $D$  background are significantly different from the expectations from the simulation for the primary leptons: this is not surprising, as this component features a large fraction of  $B$ -hadronic decays for which we have poor information (see Sect. 5.2).

To build confidence in the control-region fit results, I use them to scale the background components in simulation and examine the data-simulation agreement for several distributions of sideband data. I observe a good data-simulation agreement. This comparison can be found in Appendix B. Furthermore, to validate the results on the real- $D$  background yields, I compare data and simulation distributions of  $p_D^*$  and  $p_\ell^*$  in a region where these decays are enhanced, selecting candidates with  $m(Y)$  between 3.2–3.4 GeV/ $c^2$ . The results are shown in Figs. B.6–B.7 of Appendix B. I also find an improvement in the data-simulation agreement in this region; however, a few percent discrepancy remains, which should be covered by the uncertainty on the real- $D$  background yields obtained from the fit (about 10%).

Therefore, for all next studies, I consider a new composition to generate simulated realistic samples. I rescale the yields of the decays in the  $D^{**}\ell\nu_\ell$  background of the original simulation, both in the signal and control regions, and I also rescale the yields of the real- $D$  subcomponent in the control region, all according to the results from the control-region

fit in Tab. 6.2.<sup>6</sup> This new sample is used for validating the final fit configuration and for assessing the expected systematic uncertainties.

## 6.4 Fit to a simulated Run I data set

In this section, I carried out the full fit of the signal and control regions and demonstrate the feasibility of the simultaneous analysis of  $B \rightarrow D\ell\nu_\ell$  and  $B \rightarrow D^*\ell\nu_\ell$  decays. To this extent, I use a simulated sample of the same size of the Belle II Run I sample.

The data sample is generated using the full Belle II simulation, along with  $D$ -mass sideband and off-resonance data. The signal decays are generated using simulation, with the branching fractions and BGL models reported in Tab. 4.1. The fake- $D$  and continuum are described using the  $D$ -mass sideband and off-resonance data, as described in Sect. 6.2.4. For the real- $D$  and  $X\ell\nu_\ell$  background, I use the simulated data described in Sect. 6.2.3 and 6.2.2, but I rescale the yields and the branching fraction according to the results of the fit to the control region, as explained in the previous section.

The sample is fitted using templates built from the very simulated candidates that make up the data. Therefore, the results of the test are free from any statistical fluctuations: if the analysis is properly set up, the fit must return exactly the same values of the parameters used in the generation of the sample. Nonetheless, the parameter uncertainties should reflect those expected from a fit to the experimental data sample. This test, called ‘‘Asimov fit’’, is particularly advantageous as it provides a rapid and efficient mean to assess the accuracy and sensitivity of the analysis.

As a preliminary check, I run a fit focusing exclusively on the signal region and signal decays, *i.e.*, without including any backgrounds in the sample. In this test, the fit parameters are the 22 model-independent observables and  $f_{+-}/f_{00}$ . This provides an initial consistency check of the signal parametrisation: I obtain the generation values for all parameters. The fit results and projections are shown in Appendix C.

Then, I carry out the fit to the signal and control regions including also the background components, *i.e.*, in the same expected conditions as for the fit to the experimental data. The generated distributions for the signal and control regions are shown in Fig. 6.9–6.10 with fit projections overlaid. The Asimov fit returns the generated values for all parameters, both for the signal and the backgrounds components. The results of the model-independent observables determined from the Asimov fit are shown in Fig. 6.11 and compared to the expected functions.

The correlation matrix of the Asimov fit is reported in Fig 6.12. As expected, a high correlation is observed among the parameters of the model-independent observables,  $a'_n$ ,  $b'_n$ ,  $c'_n$  and  $G'_m$ , both across different bins of  $w$ , and between the observables of  $B \rightarrow D\ell\nu_\ell$  and  $B \rightarrow D^*\ell\nu_\ell$  decays. In addition, a strong correlation is also observed between  $f_{+-}/f_{00}$  and the Coulomb factor,  $\theta$ , as well as with the branching ratios of the  $D$  mesons:  $\mathcal{B}(\bar{D}^0 \rightarrow K^+\pi^-)$ ,  $\mathcal{B}(D^- \rightarrow K^+\pi^-\pi^-)$  and  $\mathcal{B}(D^{*-} \rightarrow \bar{D}^0 X)$ .

In Fig. 6.13, I also show the pull values of each Gaussian-constrained parameter,  $\theta_i^c$ . The pull is defined as the uncertainty-weighted residual,

$$\frac{\hat{\theta}_i - \theta_i^c}{\sigma_{\theta_i^c}}, \quad (6.14)$$

where  $\theta_i^c$  is the central value of the Gaussian constraint,  $\sigma_{\theta_i^c}$  is its uncertainty, and  $\hat{\theta}_i$  is

---

<sup>6</sup>As the  $D^{(*)}\eta\ell\nu_\ell$  branching fraction is negative and compatible with zero, I set this branching fraction to zero.

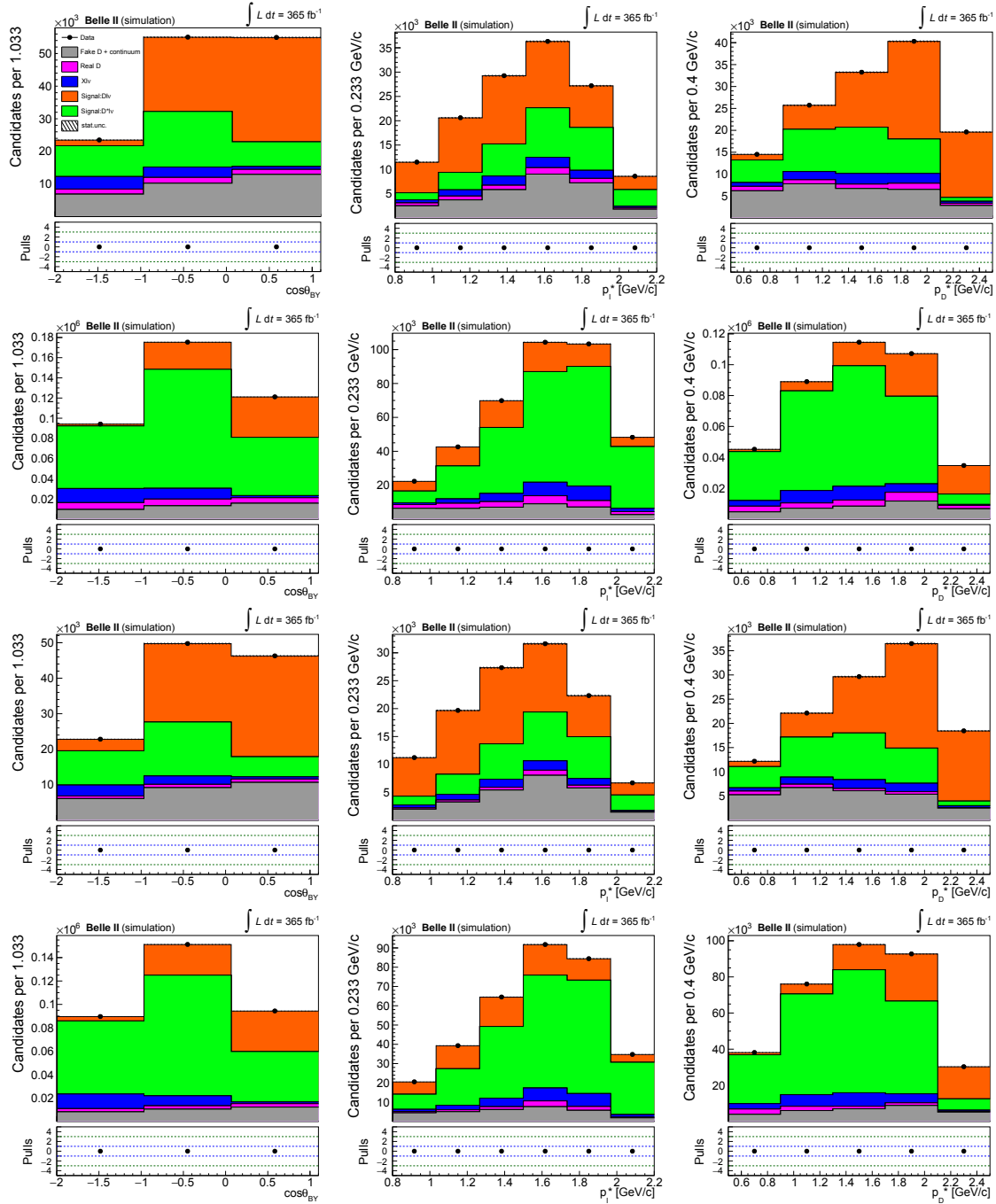


Figure 6.9: Asimov fit results. Distributions of (left column)  $\cos\theta_{BY}$ , (middle column)  $p_\ell^*$  and (right column)  $p_D^*$  with fit projections overlaid. From top to bottom:  $D^-\mu^+$ ,  $\bar{D}^0\mu^+$ ,  $D^-e^+$ , and  $\bar{D}^0e^+$  samples in the signal region. Pulls are flat as expected for an Asimov fit. The  $X\ell\nu_\ell$  backgrounds are shown as a single component.



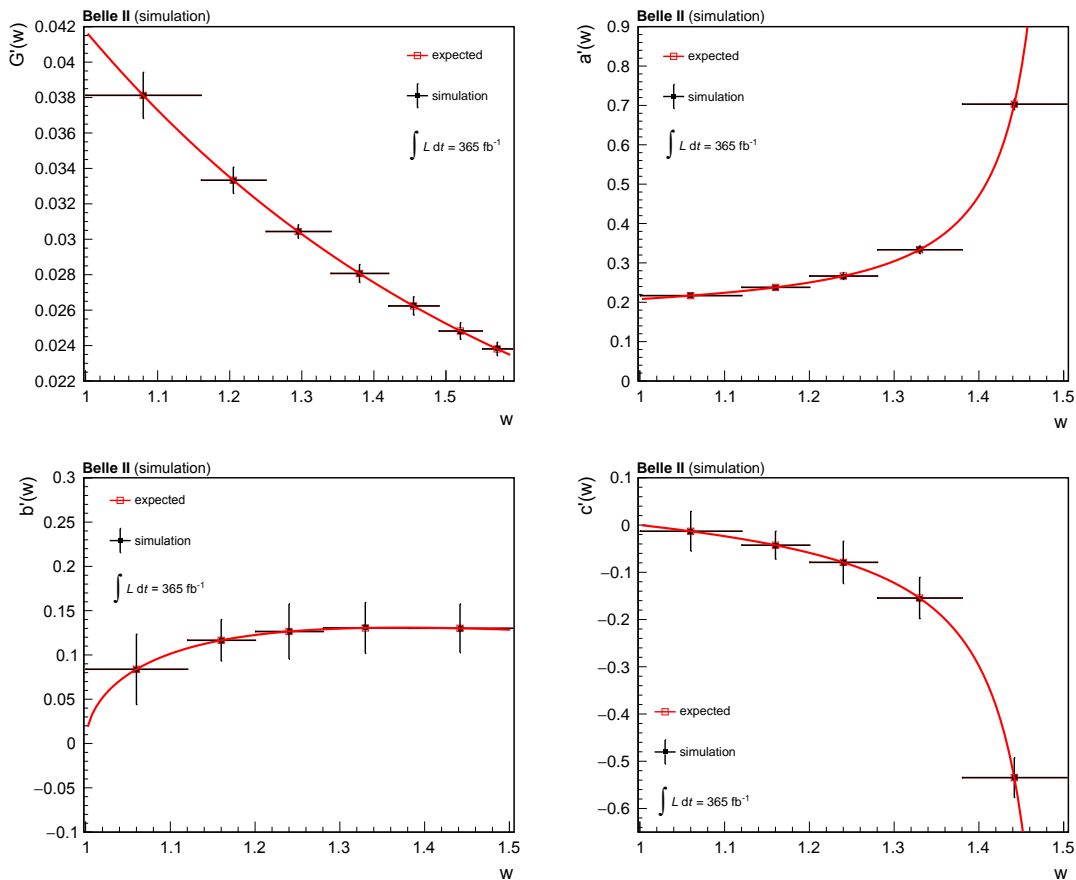


Figure 6.11: Measurements of the model-independent observables from the Asimov fit: (from top to bottom, left to right)  $G'_m$ ,  $a'_n$ ,  $b'_n$ , and  $c'_n$ . Black points are the results obtained from the fit, red points are the expected function from the model used in the signal generation. The uncertainty associated to the model-independent variables is only statistical, as the systematic uncertainty is discussed in Chapter 7.

the fit result. In the figure, I show for  $\hat{\theta}_i$  the fit uncertainty normalised to the constraint uncertainty,  $\sigma_{\hat{\theta}_i}/\sigma_{\theta_i}^c$ , to assess whether the data improve the original uncertainty of the constraint. Note that the data are generated using the results from the control-region fit, while the Gaussian constraints have values from Tab. 5.3. For instance, for the gap modes  $D^{(*)}\eta\ell\nu_\ell$ , the data are generated assuming branching fraction zero, while the Gaussian constraint has central value of 1.8%, as it will be for the fit to data.

The pulls indicate that all parameters are correctly estimated, with the expected deviation from the original constraints. In addition, the improvement on the constraint uncertainties is evident for the branching fractions of the  $D^{**}\ell\nu_\ell$  decays, and especially for the gap modes, as also observed in the fit to the control data only (see Tab. 6.2). Furthermore, the uncertainty on  $\mathcal{B}(D^{*-} \rightarrow \bar{D}^0 X)$  improves by about 30% in the fit, due to the simultaneous analysis of the  $\bar{D}^0\ell^+$  and  $D^-\ell^+$  samples using the constraint  $\mathcal{B}(D^{*-} \rightarrow D^- X) = 1 - \mathcal{B}(D^{*-} \rightarrow \bar{D}^0 X)$ .

Through this Asimov fit, the entire fit is validated in conditions similar to those expected for experimental data. In the next section, by analysing the results of 1000 different fits, I also investigate any potential bias on the estimated parameters and the coverage of their uncertainties.



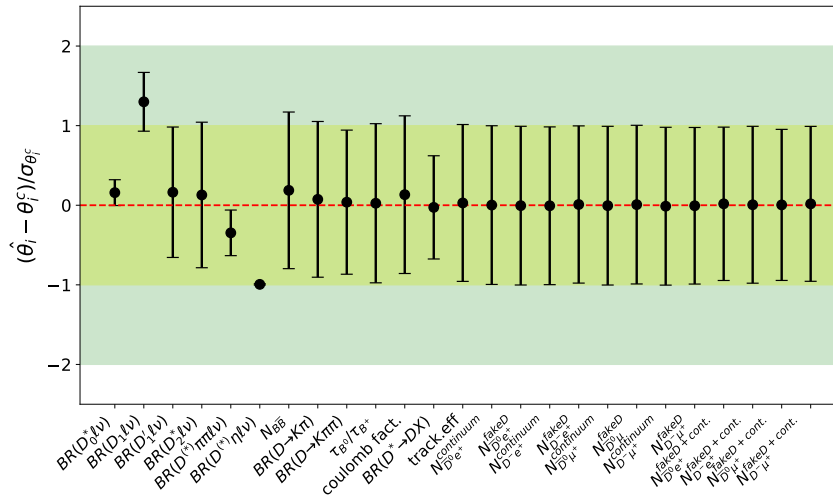


Figure 6.13: Pulls of the Gaussian constraints, described in the Sect. 6.2.5, in the final fit configuration. See the text for a discussion.

## 6.5 Check of the fit properties

I generate 1000 samples, called “toys”, each corresponding to the size of the Run I Belle II data set, by drawing variables from the template of each sample component. The yields of the components are sampled from Poisson distributions centred at the values expected either from simulation or control data: the same used to generate the sample for the Asimov fit described in the previous section.

I fit each toy data set, and calculate the pull of the parameters, defined as

$$\frac{\hat{\theta}_i - \theta_i^g}{\hat{\sigma}_{\hat{\theta}_i}}, \quad (6.15)$$

where  $\theta_i^g$  is the generation value of a fit parameter,  $\hat{\theta}_i$  is its fit value, and  $\hat{\sigma}_{\hat{\theta}_i}$  is its fit uncertainty. For an unbiased and asymptotically correct  $\chi^2$  fit, the pull distribution should be normal, *i.e.*, a Gaussian distribution centred at zero with a unit standard deviation. If the mean of the pull distribution deviates from zero, it indicates a fit bias for that parameter; a standard deviation smaller than one indicates an overestimation of the parameter uncertainty, while a standard deviation larger than one indicates an underestimation.

I summarise the results in Fig 6.14, where the mean and the standard deviation of the pull distribution for each parameter are shown. All pull distributions are reported in Appendix F. They are generally unbiased normal Gaussian distributions. Some parameters present pull mean that are significantly different from zero; however, the resulting bias is only a fraction (smaller than 20%) of the statistical uncertainty and can be accounted for as a systematic uncertainty.

From the toys analysis, I can also obtain information about the expected statistical uncertainty. To assess only this contribution, I fix all Gaussian-constrained parameters such that the uncertainties on the prior-information of these external inputs are not propagated in the fit (I account as systematic uncertainties). The average statistical uncertainties on the parameters agree with those obtained from the Asimov fit, when done under the same condition concerning the Gaussian constraints. The systematic uncertainties are calculated and discussed in the next chapter.

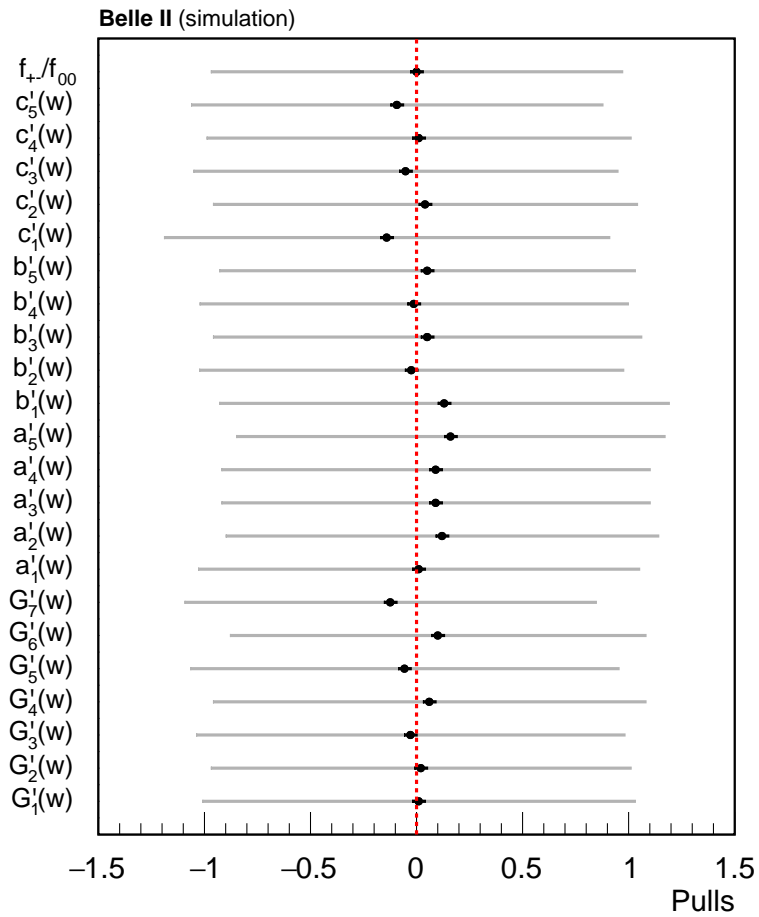


Figure 6.14: Summary of the pull analysis for the model-independent observables and  $f_{+-}/f_{00}$  measured in the fit to 1000 toy samples. The black points are the pull means, the black bars the uncertainties on the means, and the grey bars are the pull standard deviations.



## Chapter 7

# Systematic uncertainties and final measurements

*A detailed study of the sources of systematic uncertainties is essential to yield an accurate and solid measurement. In this chapter, I identify and assess those effecting  $f_{+-}/f_{00}$  and the model-independent observables. Finally, from the measured model-independent observables, I derive the  $B \rightarrow D\ell\nu_\ell$  and  $B \rightarrow D^*\ell\nu_\ell$  branching fractions and, for  $B \rightarrow D^*\ell\nu_\ell$  decays, the lepton forward-backward asymmetry and the  $D^*$  longitudinal polarisation, both as functions of the recoil energy  $w$ . The systematic uncertainties affecting these measurements are derived from those of the model-independent observables.*

### 7.1 Systematic uncertainties

Systematic uncertainties are generally a major limitation, and often the primary one, in precision measurements performed with  $B \rightarrow D^{(*)}\ell\nu_\ell$  decays. Thus, their accurate assessment is crucial. In this section, I calculate the systematic uncertainties affecting the measurement of the model-independent observables and  $f_{+-}/f_{00}$  (collectively referred to as the parameters of interest). These represent the expected uncertainties, assuming the sample composition used for the Asimov fit in Sect. 6.4, *i.e.*, using a realistic simulated sample that reproduces the Belle II Run I data set. To assess the uncertainties in the final measurements, the procedures described in the following should be repeated by replacing this simulated sample with the experimental data, or by generating toy samples using the results from the data. This will be done once I receive the permission from the Belle II Collaboration to unblind.

I categorise the systematic uncertainties into two main types: uncertainties from external inputs and uncertainties from analysis assumptions. In the following sections, I first outline the methodology to compute the contributions from the two categories. Then, I show their impact on the measurements. In general, for a given source of systematic uncertainty, I calculate a covariance matrix. The total systematic uncertainties are derived from the sum of the covariance of the fit and all the covariances of the systematic uncertainties. For each parameter of interest, the square root of the corresponding diagonal element of the resulting covariance matrix is taken as the total systematic uncertainty. The total covariance matrix is then used to derive the uncertainties on all measurements described in this and next chapter. I also split the total uncertainties in statistical and systematic (each having its own covariance). The statistical uncertainty encapsulates only the uncertainty due to the Belle II sample size.

Before proceeding further, a caveat: at the time of this writing, all uncertainties have been calculated except for one. The missing uncertainty is that related to the form-factor model for the decays in the  $X\ell\nu_\ell$  background. The calculation for this contribution is ongoing, but, based on the results in previous similar analyses, I expect a limited impact on the final uncertainty. Thus, the total expected uncertainty discussed in this thesis should be marginally affected.

### 7.1.1 External inputs

The uncertainties from the external inputs constitute the major part of the systematic uncertainties. External inputs are incorporated in the fit as Gaussian-constrained parameters, meaning their uncertainties are already included in the fit uncertainties, accounting also for possible correlations. Here, I aim to separate the contribution of each constraint to better understand the impact of each source. There is no trivial method for doing this in a correct way, but only approximations, which neglect, to some extent or another, correlations among the external inputs. Therefore, the covariance matrix from the *nominal* fit, which includes all Gaussian constraints, is used in the analysis to assess the total uncertainty.

Nonetheless, I can gain an understanding on the impact of an external input as follows. I perform an alternative Asimov fit where I fix the parameter to the value found at the minimum  $\chi^2$  of the nominal fit (*i.e.*, where the parameter is Gaussian-constrained). This approach removes the contribution of this parameter to the uncertainties of all other parameters without altering the  $\chi^2$  minimum, thereby preserving the best-fit values. Then, I calculate the difference between the covariance matrices of the nominal and alternative fits, restricting the covariances to the parameters of interest. The resulting matrix gives the contribution of the Gaussian-constrained parameter to the uncertainty of these parameters. The systematic uncertainty on a parameter is assigned as the square root of the corresponding diagonal element of this matrix.

The procedure is iterated for each Gaussian-constrained parameter. Note that, as the method to derive each contribution neglects part of the correlations between the external inputs, the sum in quadrature of the resulting uncertainties on a parameter (including its statistical uncertainty) might be different than the total uncertainty from the nominal fit with all Gaussian constraints. Although I find this difference small for all parameters, only the covariance matrix from the nominal fit with all Gaussian-constrained parameters is used in the following, as already explained before. For illustrating the measurements in the next sections, I use the covariance from the fit to the simulated Run I sample presented in Sect. 6.4; once unblinding permission is granted, this is replaced with the covariance from the fit to data.

The list of all external inputs has been provided in Sect. 6.2.5. There are 25 inputs in total: 6 for the branching fractions of  $D^{**}\ell\nu_\ell$  decays; 12 for the yields of continuum and fake- $D$  backgrounds in the signal and control regions; 3 for the branching fractions of  $D$  and  $D^*$  decays; one for the number of  $B\bar{B}$  pairs; one for the ratio of  $B^0$  and  $B^+$  lifetimes; one for the Coulomb factor; and one for the tracking-efficiency corrections.

### 7.1.2 Analysis assumptions

Analysis assumptions pertain to the modelling of the backgrounds and the accuracy of the simulation in reproducing experimental effects. Regarding the backgrounds, there is a number of parameters that are fixed, in order to simplify the fit. Additionally, aside from the signal components, shape templates are also fixed. These shapes depend on the subcomposition of each background and/or on the assumed decay model. For instance, in

the first case, the real- $D$  background template for primary leptons (a component with a free yield in the fit) depends on the relative amount of the misreconstructed  $B$  hadronic decays making up the template, hence on their assumed branching fractions. In the second case, an example is the template of the  $(p_\ell^*, p_D^*)$  distribution of the  $B \rightarrow D^{**} \ell \nu_\ell$  decays, which depends on the form-factor model used in the simulation.

Regarding the simulation, a number of corrections have been applied to fix known mis-modelling: track momentum scale, photon energy bias, lepton and hadron PID-efficiency corrections, and tracking-efficiency corrections (see Sect. 4.1.1). Such corrections introduce uncertainties that must be propagated to the parameters of interest. The uncertainty on tracking-efficiency corrections has already been included as a Gaussian-constrained parameter, and the impact of the track momentum scale and photon energy bias are negligible in this analysis. Uncertainties on PID-efficiency corrections are evaluated with the procedure described in the following.<sup>1</sup>

In general, systematic uncertainties from analysis assumptions are calculated by performing multiple alternative fits to the data, varying the assumptions made in the fit. For instance, variations may include alternative values for parameters fixed in the nominal fit. These alternative values are obtained by sampling from a Gaussian distribution, centred on the value used in the fit and with the uncertainty associated with the fixed parameter as the standard deviation. I then run the fit using the alternative value. From the results of hundreds of alternative fits, I calculate a covariance matrix by taking the covariances of the distributions of the residuals, where the residuals are the difference between the results of the alternative fits and the nominal fit. The systematic uncertainty on a parameter of interest is assigned as the square root of the corresponding diagonal element of this matrix.

To obtain a first assessment of the systematic uncertainty, I apply this procedure to the simulated Run I sample presented in Sect. 6.4; once unblinding permission is granted, this is replaced with the experimental data sample. With this method, I consider systematic uncertainties for the following sources.

- Uncertainties on the yields ( $N_{D^-e^+}^{\text{sec.}}$ ,  $N_{D^- \mu^+}^{\text{sec.}}$ ,  $N_{D^-e^+}^{\text{fake}}$  and  $N_{D^- \mu^+}^{\text{fake}}$ ) and templates of the real- $D$  subcomponents fixed in the control region. To estimate their contributions, I check the uncertainties of the branching fractions of the decays inside these subcomponents, described in detail in Sect. 5.2. I estimate that a 20% uncertainty of the expected yields of these background reflects the current knowledge on their branching fractions. I sample 300 variations.
- Uncertainties on the fixed yields of the  $B \rightarrow D^{(*)} \tau \nu_\tau$  decays and of the misidentified leptons ( $N_j^{X\tau\nu_\tau}$  and  $N_j^{\text{mis-ID leptons}}$ ), combined into a single fixed template in both the signal and control regions. I assign a generous 30% uncertainty for  $N_j^{X\tau\nu_\tau}$ , considering the tensions between the measured and expected values of  $R(D^{(*)})$  and the large uncertainties on the unknown rates of the (subdominant) semitauonic decays involving  $D^{**}$ . I assign the same uncertainty to  $N_j^{\text{mis-ID leptons}}$ , adopting a conservative approach. I sample 300 variations. The resulting systematic uncertainties are subleading given the small fraction of these backgrounds in all samples.
- Uncertainties on the PID-efficiency corrections. The PID-efficiency corrections are per-candidates weights derived as a function of the momentum and polar angle of the particle involved, as shown in Fig. 4.3. Each weight is provided with 100 variations

---

<sup>1</sup>A note on the efficiency parameters that are fixed in the fit, as shown in Tab. 6.1: the uncertainty on the efficiency are statistical and arise from the size of the simulation sample used. They are negligible compared to those on the efficiency corrections, which are included as systematic uncertainties.

that account for the correction uncertainties. I apply the different weights to the simulated samples to compute 100 different corrections and generate templates for each component, and then perform 100 Asimov fits to the data set.

- Uncertainties on the  $D^{**}\ell\nu_\ell$  form-factor models are to be calculated. One possible approach to compute these uncertainties is to consider several variations of the form-factor models to build templates for these backgrounds and use them in the fit. This contribution is expected to be subleading compared to that from the uncertainty on the branching fractions of these decays, which have already been considered as external inputs.

For the modelling of the fake- $D$  and continuum backgrounds in the signal region, I calculate an additional systematic uncertainty for the shape of the fit template, to assess potential biases arising from using the  $D$ -mass sideband and off-resonance data to model the signal region. The data-driven calculation of the templates builds confidence in the modelling of these backgrounds. However, as these two components together constitute the dominant background of the sample, analysis assumptions associated with them must be carefully inspected. Fig. 5.3 shows that differences might be present between the signal-region background and that modelled with my analysis strategy. Therefore, I generate 1000 toy samples where the template for these two components is taken from simulated candidates in the signal region, instead of the template build with the strategy described in Sect. 5.1. Then, I fit the toy samples with the template obtained using the analysis strategy (applied to simulated data instead of experimental data to avoid introducing differences due to potential data-simulation discrepancies). I consider the average residuals (*i.e.*, the average difference between the fit and generation values of the parameters) as the systematic uncertainties, and I build the covariance from these uncertainties considering the correlation between the residuals.

Finally, I include two other systematic uncertainties: that related to the fit biases discussed in Sect. 6.5 and that related to the size of the samples used to make the templates. For the former, I take the average residuals as the systematic uncertainties, and build the covariance considering the correlation between the residuals. For the latter, I run a fit to the Asimov data where the uncertainties on the templates are set to zero in the  $\chi^2$  of Eq. 6.1. I calculate the difference between covariances of the nominal fit and this fit. I consider as systematic uncertainty on a parameter the square root of the corresponding diagonal element of this matrix.

## 7.2 Measurement of $f_{+-}/f_{00}$

The systematic uncertainties on  $f_{+-}/f_{00}$  are presented in Tab. 7.1. In the table, the systematic sources are grouped as follows: in the row “ $\mathcal{B}(D)$ ”, I include together the contributions from all  $D^{(*)}$  branching fractions; in the row “ $D^{**}\ell\nu_\ell$ ”, the contributions from all branching fractions of the decays in this component; in the row “Backgr. model”, all uncertainties related to semitauonic decays and misidentified leptons, real- $D$ , fake- $D$  and continuum backgrounds, and in the row “PID”, both the uncertainties related to hadron ( $K$ ) and lepton ( $e, \mu$ ) particle identification. The row “Templates stat.” refers to the contribution from the uncertainty on the templates in the  $\chi^2$  of Eq. 6.1. The row “Total systematic” combines all systematic uncertainties of the previous rows. The contribution from the Coulomb factor is reported separately, as this is considered as a theoretical uncertainty. The statistical uncertainty is also reported for a comparison, and finally last row gives the total uncertainty.

Source	[%]
$N_{B\bar{B}}$	< 0.1
$\mathcal{B}(D)$	1.9
$\tau_{B^0}/\tau_{B^+}$	0.4
Track. efficiency	0.2
$D^{**}\ell\nu_\ell$	1.1
Backgr. model	0.4
PID	< 0.1
Templates stat.	0.3
Fit bias	< 0.1
Total systematic	2.3
Coulomb factor	2.3
Statistical	0.7
Total	3.3

Table 7.1: Expected fractional uncertainties on  $f_{+-}/f_{00}$ .

In the measurement of  $f_{+-}/f_{00}$ , the dominant source of systematic uncertainty is the Coulomb factor. The knowledge of the  $D$ -meson branching fractions contributes the second largest uncertainty, while the uncertainty arising from the knowledge of the branching fractions of the  $D^{**}\ell\nu_\ell$  decays is the third largest. A detailed study on the validation of the systematic uncertainty regarding the knowledge of the branching fractions of  $D^{**}\ell\nu_\ell$  decays can be found in Appendix D. In Tab. 7.2, my result is compared with the world's best measurement from Belle [67]. The central value of my result is not reported, as the analysis is still blind. To obtain the expected uncertainties on my result from the fractional errors reported in Tab. 7.1, I assume the central value of 1.066 used in the simulation (see Tab. 4.1).

My measurement is expected to be competitive with the Belle measurement. The statistical precision is improved by a factor of approximately 1.7. This is expected as semileptonic  $B$  decays provide larger samples than those from  $B \rightarrow J/\psi K$  decays used in the Belle measurement. The systematic uncertainty on my result is about 1.3 times larger. However, the theoretical uncertainty on my result due to possible isospin-breaking effects is nearly half that of Belle result.

This improvement is attributed to a more robust assumption of isospin symmetry in semileptonic  $B$  decays, where the dominant source of uncertainty is the Coulomb factor, in contrast to the stronger assumptions required for  $B \rightarrow J/\psi K$  decays, involving factorisation of hadronic currents in the decay amplitude.

$f_{+-}/f_{00}$	
My work	$XXX \pm 0.007(\text{stat}) \pm 0.025(\text{syst}) \pm 0.024(\text{th})$
Best measurement	$1.065 \pm 0.012(\text{stat}) \pm 0.019(\text{syst}) \pm 0.047(\text{th})$

Table 7.2: Comparison of my result of  $f_{+-}/f_{00}$  with the current world's best measurement [67]. The central value of my result is not reported, as the analysis is still blind. I assume the central value of 1.066 used in the simulation to obtain the uncertainty from the fractional errors reported in Tab. 7.1. The third uncertainty is related to possible isospin-breaking effects.

### 7.3 Measurement of the model-independent observables

The systematic uncertainties on the model-independent observables are summarised in Tab. 7.3 and their impact is displayed in Fig. 7.1. In the table, the systematic sources are grouped as explained in the previous section. Figure 7.2 shows the correlation between the total uncertainties. The main systematic uncertainties arise from the uncertainties on the templates and the background modelling, mainly from the fake- $D$  and continuum backgrounds in the signal region.

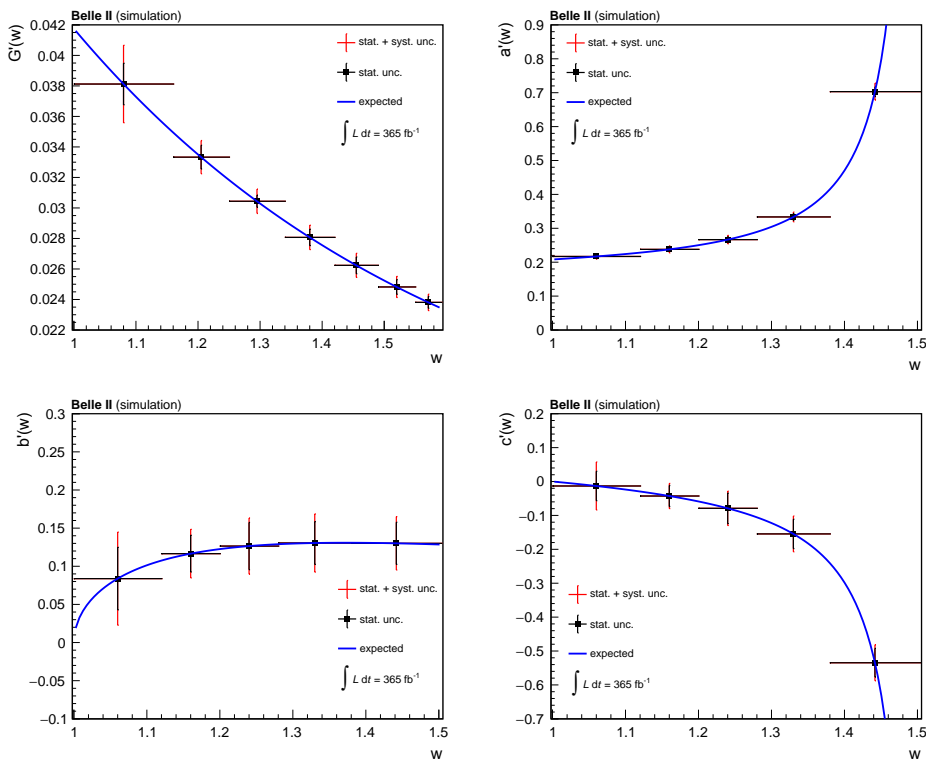


Figure 7.1: Measurements of the model-independent observables from the Asimov fit: (from top to bottom, left to right):  $G'_m$ ,  $a'_n$ ,  $b'_n$ , and  $c'_n$ . Black points are the results obtained from the fit with the statistical uncertainty only; red bars are the total uncertainty, from the sum of all uncertainties; the blue line is the expected function from the model used in the signal generation.

Source	$G_1^i(w)$	$G_2^i(w)$	$G_3^i(w)$	$G_4^i(w)$	$G_5^i(w)$	$G_6^i(w)$	$G_7^i(w)$	$a_1^i(w)$	$a_2^i(w)$	$a_3^i(w)$	$a_4^i(w)$	$a_5^i(w)$	$b_1^i(w)$	$b_2^i(w)$	$b_3^i(w)$	$b_4^i(w)$	$b_5^i(w)$	$c_1^i(w)$	$c_2^i(w)$	$c_3^i(w)$	$c_4^i(w)$	$c_5^i(w)$
$N_{B\bar{B}}$	0.027	0.025	0.022	0.021	0.019	0.019	0.018	0.322	0.352	0.395	0.500	1.050	0.123	0.177	0.181	0.199	0.188	0.018	0.072	0.110	0.249	0.803
$\mathcal{B}(D)$	0.016	0.016	0.014	0.014	0.013	0.012	0.012	0.159	0.174	0.196	0.244	0.512	0.065	0.094	0.095	0.099	0.102	<0.001	0.039	0.085	0.124	0.392
$\tau_{B^0}/\tau_{B^+}$	0.003	0.003	0.003	0.003	0.003	0.002	0.002	0.043	0.047	0.052	0.066	0.139	0.020	0.024	0.023	0.028	0.024	0.011	0.011	0.014	0.035	0.105
Track. efficiency	0.014	0.014	0.012	0.011	0.011	0.010	0.010	0.163	0.181	0.203	0.256	0.539	0.064	0.100	0.096	0.104	0.102	0.016	0.049	0.058	0.128	0.419
$D^{**}/\nu_\ell$	0.049	0.029	0.028	0.025	0.023	0.022	0.021	0.353	0.387	0.440	0.543	1.190	0.171	0.181	0.227	0.212	0.258	0.096	0.152	0.140	0.283	0.902
Backgr. model	0.191	0.050	0.054	0.038	0.040	0.033	0.015	0.352	0.528	0.266	0.449	0.720	3.710	1.780	1.100	1.900	1.260	4.830	1.770	1.610	2.230	1.790
PID	0.013	0.012	0.009	0.009	0.008	0.006	0.009	0.252	0.219	0.279	0.222	0.487	0.202	0.245	0.419	0.851	0.927	0.323	0.351	0.339	1.000	1.710
Templates stat.	0.077	0.042	0.019	0.022	0.023	0.020	0.016	0.223	0.311	0.431	0.512	0.750	2.210	1.230	1.560	1.470	1.500	2.300	1.510	2.150	2.090	2.080
Fit bias	0.004	<0.001	0.001	<0.001	0.002	0.003	0.005	0.001	0.090	0.082	0.115	0.255	0.657	0.049	0.140	0.036	0.089	0.737	0.100	0.212	0.067	0.332
Total systematic	0.214	0.077	0.068	0.055	0.056	0.049	0.037	0.671	0.832	0.820	1.020	1.940	4.380	2.190	1.980	2.560	2.190	5.410	2.360	2.720	3.240	3.470
Coulomb factor	0.019	0.018	0.016	0.015	0.014	0.013	0.013	0.227	0.249	0.279	0.353	0.743	0.088	0.125	0.128	0.140	0.133	0.019	0.051	0.077	0.176	0.568
Statistical	0.136	0.078	0.040	0.054	0.055	0.048	0.039	0.414	0.608	0.887	1.000	1.440	4.100	2.410	3.100	2.810	2.760	4.330	3.100	4.510	4.320	4.240
Total	0.254	0.109	0.080	0.080	0.079	0.069	0.054	0.821	1.050	1.240	1.450	2.500	6.110	3.190	3.690	3.820	3.500	7.090	3.710	5.070	5.290	5.330

 Table 7.3: Expected uncertainties on the model-independent observables in unit of  $10^{-2}$ .

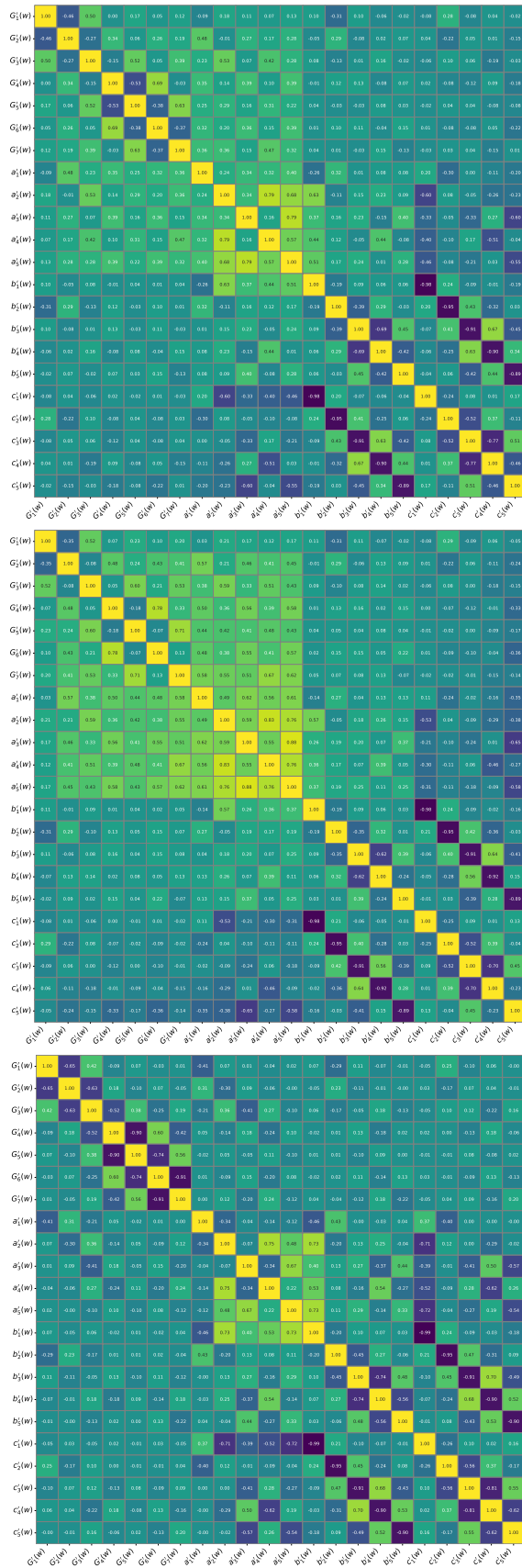


Figure 7.2: Correlation matrix of the 22 model-independent observables, from top to bottom, including statistical and systematic uncertainties, only systematic and only statistical.

Source	$\mathcal{B}(B \rightarrow D\ell\nu_\ell)$	$\mathcal{B}(B \rightarrow D^*\ell\nu_\ell)$
$N_{B\bar{B}}$	1.5	1.5
$\mathcal{B}(D)$	1.0	0.7
$\tau_{B^0}/\tau_{B^+}$	0.2	0.2
Track. efficiency	0.8	0.8
$D^{**}\ell\nu_\ell$	1.3	1.2
Backgr. model	0.8	0.9
PID	0.5	0.5
Templates stat.	0.3	0.2
Fit bias	$< 0.1$	0.1
Total systematic	2.6	2.4
Coulomb factor	1.0	1.1
Statistical	0.5	0.4
Total	2.8	2.6

Table 7.4: Expected fractional uncertainties on  $\mathcal{B}(B \rightarrow D\ell\nu_\ell)$  and  $\mathcal{B}(B \rightarrow D^*\ell\nu_\ell)$ .

As explained in Chapter 2, the model-independent observables provide a means to obtain the following measurements:

- the branching fractions of  $B \rightarrow D\ell\nu_\ell$  and  $B \rightarrow D^*\ell\nu_\ell$  decays;
- the lepton forward-backward asymmetry  $A_{\text{FB}}$ , defined in Eq. 2.35;
- the  $D^*$  longitudinal polarisation  $F_L^{D^*}$ , defined in Eq. 2.36;

I derive these measurements in the following sections.

## 7.4 Measurement of branching fractions

The signal branching fractions of  $B \rightarrow D\ell\nu_\ell$  and  $B \rightarrow D^*\ell\nu_\ell$  are determined by using Eqs. 6.10–6.11, Eqs. 2.30–2.32 and 2.34.

The uncertainties on the branching fractions can be derived from the covariance matrix of the model-independent observables, using the total uncertainties in Tab. 7.3 and the correlation in Fig. 7.2. I also provide a breakdown of all sources of uncertainty using the corresponding covariances of the model-independent observables.<sup>2</sup> This breakdown is reported in Tab. 7.4. The main systematic uncertainties affecting the branching fraction measurements are those from  $N_{B\bar{B}}$  and from the  $D^{**}\ell\nu_\ell$  background, for both  $B \rightarrow D\ell\nu_\ell$  and  $B \rightarrow D^*\ell\nu_\ell$  decays. I validate, also for the branching fraction measurements, the systematic uncertainty regarding the knowledge of the branching fractions of  $D^{**}\ell\nu_\ell$  decays (see Appendix D).

My results are compared with the world’s best measurements in Tab. 7.5, where I consider the branching fractions for both  $B^+$  and  $B^0$ . For the latter case, I use Eq. 6.7 and 6.8; the systematic uncertainties from the  $B^0$  and  $B^+$  lifetime ratio and from the

<sup>2</sup>These intermediate covariances are not reported though.

	My work	Best measurement
$\mathcal{B}(B^+ \rightarrow \bar{D}^0 \ell^+ \nu_\ell)$ [%]	$XXX \pm 0.01(\text{stat}) \pm 0.06(\text{syst})$	$2.34 \pm 0.03(\text{stat}) \pm 0.13(\text{syst})$
$\mathcal{B}(B^+ \rightarrow \bar{D}^{*0} \ell^+ \nu_\ell)$ [%]	$XXX \pm 0.02(\text{stat}) \pm 0.13(\text{syst})$	$5.40 \pm 0.02(\text{stat}) \pm 0.21(\text{syst})$
$\mathcal{B}(B^0 \rightarrow D^- \ell^+ \nu_\ell)$ [%]	$XXX \pm 0.01(\text{stat}) \pm 0.05(\text{syst}) \pm 0.02(\text{th.})$	$2.31 \pm 0.03(\text{stat}) \pm 0.11(\text{syst})$
$\mathcal{B}(B^0 \rightarrow D^{*-} \ell^+ \nu_\ell)$ [%]	$XXX \pm 0.02(\text{stat}) \pm 0.12(\text{syst}) \pm 0.05(\text{th.})$	$4.90 \pm 0.02(\text{stat}) \pm 0.16(\text{syst})$

Table 7.5: Comparison between the branching fractions from my analysis and the current world’s best measurements [45, 56, 62]. The central value of my results is not reported, as the analysis is still blind. I assume the values used in the simulation (see Tab. 4.1) to obtain the uncertainty from the fractional errors reported in Tab. 7.4. The third uncertainty for the  $B^0$  branching fraction is related to the Coulomb factor.

Coulomb factor in Tab. 7.4 are applied only to the  $B^0$  branching fractions. Moreover, the statistical uncertainty and all other systematic uncertainties in Tab. 7.4 are fully correlated between  $\mathcal{B}(B^+ \rightarrow \bar{D}^0 \ell^+ \nu_\ell)$  and  $\mathcal{B}(B^0 \rightarrow D^- \ell^+ \nu_\ell)$ , and also between  $\mathcal{B}(B^+ \rightarrow \bar{D}^{*0} \ell^+ \nu_\ell)$  and  $\mathcal{B}(B^0 \rightarrow D^{*-} \ell^+ \nu_\ell)$ . The best measurements for the  $B^+$  branching fractions are obtained by Babar [62] using a global analysis of  $B \rightarrow D \ell \nu_\ell$  and  $B \rightarrow D^* \ell \nu_\ell$  decays; those for the  $B^0$  branching fractions are from Belle [45, 56].

The branching fractions obtained from my analysis are expected to be competitive with the world’s best. The statistical uncertainties in my measurements are smaller or the same of the best measurements. Regarding systematic uncertainties, despite the contribution from the knowledge of the branching fractions of the  $B \rightarrow D^* \ell \nu_\ell$  decays, I have achieved a better control over several key sources. Specifically, compared to previous measurements, my analysis features an improvement from measuring  $f_{+-}/f_{00}$ , which is a dominant systematic in previous measurements, exploits better knowledge of tracking efficiency, and get rid of soft-pion tracking efficiency for  $D^*$  reconstruction. These improvements collectively result in competitive or higher precision compared to previous measurements.

From these measurements, the ratio of the  $B \rightarrow D \ell \nu_\ell$  and  $B \rightarrow D^* \ell \nu_\ell$  branching fractions can also be determined, as well as the ratios of the  $B \rightarrow D^{(*)} \mu^+ \nu_\mu$  and  $B \rightarrow D^{(*)} e^+ \nu_e$  branching fractions. The latter serve as tests of flavour universality for light leptons. I plan to incorporate these two measurements into the analysis during the Belle II internal review; however, they are not yet available at the time of this writing.

## 7.5 Measurements of $A_{\text{FB}}$ and $F_L^{D^*}$

For the  $B \rightarrow D^{(*)} \ell \nu_\ell$  decay, I determine the lepton forward-backward asymmetry  $A_{\text{FB}}$  and the  $D^*$  longitudinal polarisation  $F_L^{D^*}$ , both as functions of  $w$ , as per Eqs. 2.35 and 2.36. The results are shown in Fig. 7.3. These measurements are expected to be statistically limited. The main systematic uncertainties arise from the uncertainties on the templates and the background modelling, mainly from the fake- $D$  and continuum backgrounds in the signal region. I also obtain  $A_{\text{FB}}$  and  $F_L^{D^*}$  integrated in  $w$ . The uncertainties on the integrated values of  $A_{\text{FB}}$  and  $F_L^{D^*}$  are reported in Tab. 7.6.

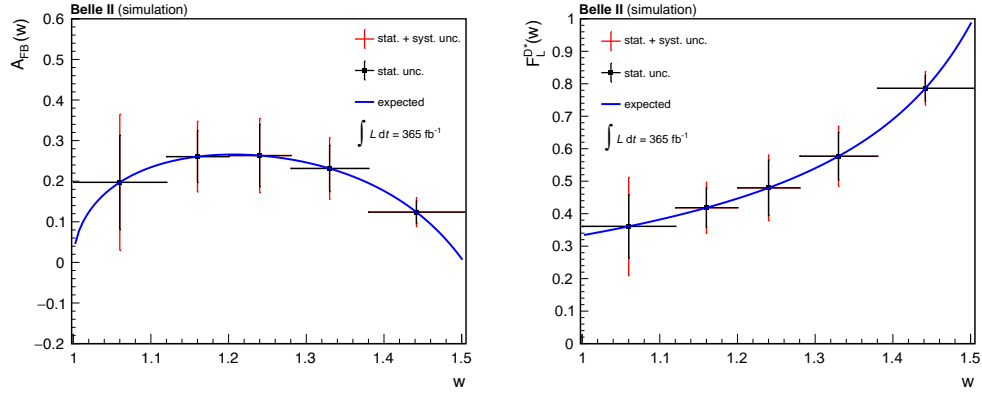


Figure 7.3: Measurements of (left)  $A_{\text{FB}}(w)$  and (right)  $F_L^{D^*}(w)$  from the Asimov fit. Black points are the results obtained from the fit with the statistical uncertainty only; red bars are the total uncertainty, from the sum of all uncertainties; the blue line is the expected function from the model used in the signal generation.

Sources	$A_{\text{FB}}$	$F_L^{D^*}$
$N_{B\bar{B}}$	$< 0.01$	$< 0.01$
$\mathcal{B}(D)$	0.01	0.01
$\tau_{B^0}/\tau_{B^+}$	$< 0.01$	$< 0.01$
Track. efficiency	$< 0.01$	$< 0.01$
$D^{**}\ell\nu_\ell$	0.03	0.02
Backgr. model	0.22	0.30
PID	0.17	0.29
Templates stat.	0.26	0.35
Fit bias	0.02	0.05
Total systematic	0.38	0.55
Coulomb factor	$< 0.01$	$< 0.01$
Statistical	0.47	0.70
Total	0.60	0.87

Table 7.6: Expected uncertainties on  $A_{\text{FB}}$  and  $F_L^{D^*}$  in unit of  $10^{-2}$ .

In Tab. 7.7, I compare the expected uncertainties on  $A_{\text{FB}}$  and  $F_L^{D^*}$  from my measurements with the Belle II analysis of  $B^0 \rightarrow D^{*-}\ell^+\nu_\ell$  of Ref. [91]. The expected precision on  $A_{\text{FB}}$  improves upon the previous Belle II measurement, combining both the electron and muon channels. This improvement is due both to a larger data set employed, which is nearly double in size, and to a reduced systematic uncertainty. On the other hand, the precision on  $F_L^{D^*}$  is lower because I cannot leverage information from the helicity angle  $\cos\theta_D$  in the  $B \rightarrow D^*\ell\nu_\ell$  decay, due to the partial reconstruction of the  $D^*$  decay; in contrast, the Belle II measurement exploits this information.

I can also obtain the differences between measurements from the electron and muon modes,  $\Delta A_{\text{FB}} = A_{\text{FB}}^e - A_{\text{FB}}^\mu$  and  $\Delta F_L^{D^*} = F_L^{D^*,e} - F_L^{D^*,\mu}$ . These enable investigations

	My work	Belle II measurement
$A_{\text{FB}}$	$XXXX \pm 0.005(\text{stat}) \pm 0.004(\text{syst})$	$0.228 \pm 0.012(\text{stat}) \pm 0.018(\text{syst})$ ( $e$ mode)
		$0.211 \pm 0.011(\text{stat}) \pm 0.021(\text{syst})$ ( $\mu$ mode)
$F_L^{D^*}$	$XXXX \pm 0.007(\text{stat}) \pm 0.006(\text{syst})$	$0.520 \pm 0.005(\text{stat}) \pm 0.005(\text{syst})$ ( $e$ mode)
		$0.527 \pm 0.005(\text{stat}) \pm 0.005(\text{syst})$ ( $\mu$ mode)

Table 7.7: Comparison between my results of  $A_{\text{FB}}$  and  $F_L^{D^*}$  integrated in  $w$  and the measurements from Belle II from Ref. [91]. The central value of my results is not reported, as the analysis is still blind.

of flavour universality violation for light leptons. I plan to incorporate also these two measurements into the analysis during the Belle II internal review; however, they are not yet available at the time of this writing.

## 7.6 Summary of the results

I report a summary of the expected measurements derived from the model-independent observables, including also  $f_{+-}/f_{00}$  for completeness:

$$\begin{aligned}
 \mathcal{B}(B^+ \rightarrow \bar{D}^0 \ell^+ \nu_\ell) &= (XXX \pm 0.01 \pm 0.06)\%, \\
 \mathcal{B}(B^+ \rightarrow \bar{D}^{*0} \ell^+ \nu_\ell) &= (XXX \pm 0.02 \pm 0.13)\%, \\
 \mathcal{B}(B^0 \rightarrow D^- \ell^+ \nu_\ell) &= (XXX \pm 0.01 \pm 0.05 \pm 0.02)\%, \\
 \mathcal{B}(B^0 \rightarrow D^{*-} \ell^+ \nu_\ell) &= (XXX \pm 0.02 \pm 0.12 \pm 0.05)\%, \\
 A_{\text{FB}} &= (XXX \pm 0.5 \pm 0.4)\%, \\
 F_L^{D^*} &= (XXX \pm 0.7 \pm 0.6)\%, \\
 f_{+-}/f_{00} &= XXX \pm 0.007 \pm 0.025 \pm 0.024.
 \end{aligned}$$

where the first uncertainty is statistical, the second systematic, and the third, when present, is related to theoretical inputs or assumptions. The measurements are expected to be competitive with the world's best measurements. In addition, Figure 7.4 reports the statistical, systematic and total correlation matrices between the measurement. Note that the statistical and systematic uncertainties between the  $B^+$  and  $B^0$  branching fractions are fully correlated.

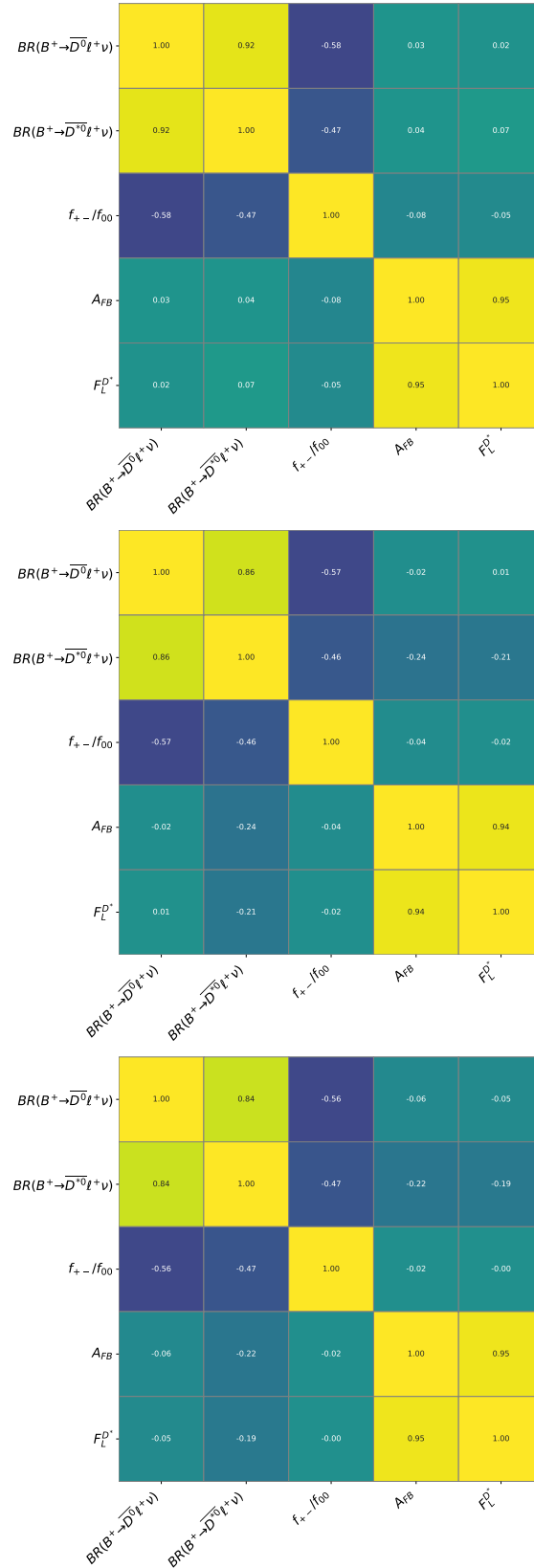


Figure 7.4: Correlation matrix between the measurements. From top to bottom: statistical, systematic and total.



## Chapter 8

# Measurement of $|V_{cb}|$

*In this chapter, I finally obtain  $|V_{cb}|$  by interpreting with a form-factor parametrisation the measurement of the model-independent observables. This is the first experimental analysis where  $|V_{cb}|$  is measured simultaneously from both  $B \rightarrow D\ell\nu_\ell$  and  $B \rightarrow D^*\ell\nu_\ell$  decays.*

### 8.1 Fit to the model-independent observables

I determine  $|V_{cb}|$  using a parametrisation of the form factors from which I calculate the model-independent observables and compare them with the measured values. This is achieved by a fit that minimises the  $\chi^2$  function

$$\chi^2 = \sum_{i,j}^{22} (x_i - x_i^{\text{model}}) C_{ij}^{-1} (x_j - x_j^{\text{model}}), \quad (8.1)$$

where  $x_i$  and  $x_j$  are the measured values of the model-independent observables,  $C_{ij}$  is their covariance matrix, and  $x_i^{\text{model}}$  and  $x_j^{\text{model}}$  are the predicted values, which depend on  $|V_{cb}|$  and the form-factor parameters of the model. Once a form-factor model is chosen, the model-independent observables for  $B \rightarrow D\ell\nu_\ell$  are calculated through Eq. 2.34, and for  $B \rightarrow D^*\ell\nu_\ell$  using Eqs. 2.30–2.32.

In the following I use the BGL parametrisation, expanded in Appendix A, which gives the more general model recommended for phenomenological analyses, as explained in Chapter 2. I show the feasibility of the analysis by using the model-independent observables obtained in Sect. 7.3 from the simulated Run I data set. I also show that unbiased results can be obtained with other parametrisations, by using a CLN model. This other analysis is reported in Appendix E.

To obtain  $|V_{cb}|$ , the form factors must be known at least in one value of  $w$ . The best precision is given by lattice-QCD calculations, as explained in Sect. 2.4, which provides form-factors values for both  $B \rightarrow D\ell\nu_\ell$  and  $B \rightarrow D^*\ell\nu_\ell$  either at  $w = 1$  and also for a number of points at  $w > 1$ . To have a better understanding of the expected sensitivity from Belle II data, I use the minimal set of required inputs from lattice-QCD, *i.e.*, the point at  $w = 1$ :

$$\mathcal{G}(1) = 1.029 \pm 0.009, \quad (8.2)$$

$$h_{A_1}(1) = 0.904 \pm 0.013, \quad (8.3)$$

for  $B \rightarrow D\ell\nu_\ell$  and  $B \rightarrow D^*\ell\nu_\ell$ , respectively (see Appendix A for their relations with the BGL parameters). These numbers are determined from the generation values of the

BGL parameters and branching fractions used in the Belle II simulation (see Tab. 4.1). Their uncertainty reflects those from the latest FLAG averages [63], in order to represent a realistic scenario. I will not employ points at  $w > 1$  in the analysis presented here, although these can be certainly considered when the analysis is applied to experimental data.

### 8.1.1 BGL fit

An arbitrary assumption of the BGL parametrisation, which might generate some model-dependence in the results, is the choice of the truncation order of the series to calculate the form factors. The truncation orders determines the fit parameters, which are the series coefficients. Different solutions have been proposed to address this issue [38, 39, 43, 79, 80], but there is not full consensus on the criteria to adopt. Ultimately, the choice also depends on the very data at hand, both from the experimental side and from the lattice-QCD calculations, which determine the sensitivity to a certain set of coefficients, and the use or not of unitarity constraints on the coefficients.

The analysis I present here has only the illustrative scope to show how my measurement of the model-independent observables can be used. I conduct a limited study to select the possible truncation orders, inspecting the configuration that minimises the Akaike Information Criterion (AIC), defined as  $AIC=2N + \chi^2$ , where  $N$  is the number of fit parameters. This approach allows for an efficient choice of parameters while balancing model complexity and goodness of fit. A more detailed study will be conducted once I have permission from the Collaboration to fit the real data, in which I will also include lattice-QCD points at  $w > 1$ .

Parameter	Generator values	Configuration 1)	Configuration 2)	Configuration 3)
$a_1^{f+}$	-0.094	$-0.069 \pm 0.002$	$-0.094 \pm 0.009$	$-0.095 \pm 0.026$
$a_2^{f+}$	0.340	truncated	$0.33 \pm 0.11$	$0.37 \pm 0.87$
$a_3^{f+}$	-0.100	truncated	truncated	$-0.34 \pm 7.99$
$a_1^f$	0.01713	$0.052 \pm 0.013$	$0.017 \pm 0.022$	$0.017 \pm 0.022$
$a_0^g$	0.02596	$0.025 \pm 0.002$	$0.026 \pm 0.003$	$0.026 \pm 0.003$
$a_1^g$	-0.06049	$-0.142 \pm 0.051$	$-0.061 \pm 0.060$	$-0.061 \pm 0.061$
$a_1^{F_1}$	0.00753	$0.0028 \pm 0.0007$	$0.0077 \pm 0.0042$	$0.0077 \pm 0.0042$
$a_2^{F_1}$	-0.09346	truncated	$-0.095 \pm 0.071$	$-0.095 \pm 0.071$
$h_{A_1}(1)$	0.9038	$0.924 \pm 0.011$	$0.904 \pm 0.012$	$0.904 \pm 0.013$
$\mathcal{G}(1)$	1.0294	$1.021 \pm 0.008$	$1.029 \pm 0.009$	$1.029 \pm 0.009$
$ V_{cb}  [10^{-3}]$	38.72	$37.29 \pm 0.68$	$38.58 \pm 0.85$	$38.59 \pm 0.90$
$\chi^2$	-	12.4	$4.7 \cdot 10^{-3}$	$2.8 \cdot 10^{-3}$
AIC	-	24.4	16.0	18.0

Table 8.1: Different configurations of the fit for various assumptions regarding the truncation of the series of the BGL form factors. The uncertainties include both statistical, systematic and lattice contributions. I also reported the  $\chi^2$  and Akaike Information Criterion (AIC) values for the three configurations. The two lattice points  $\mathcal{G}(1)$  and  $h_{A_1}(1)$  are constrained with Gaussian penalties in the fit.

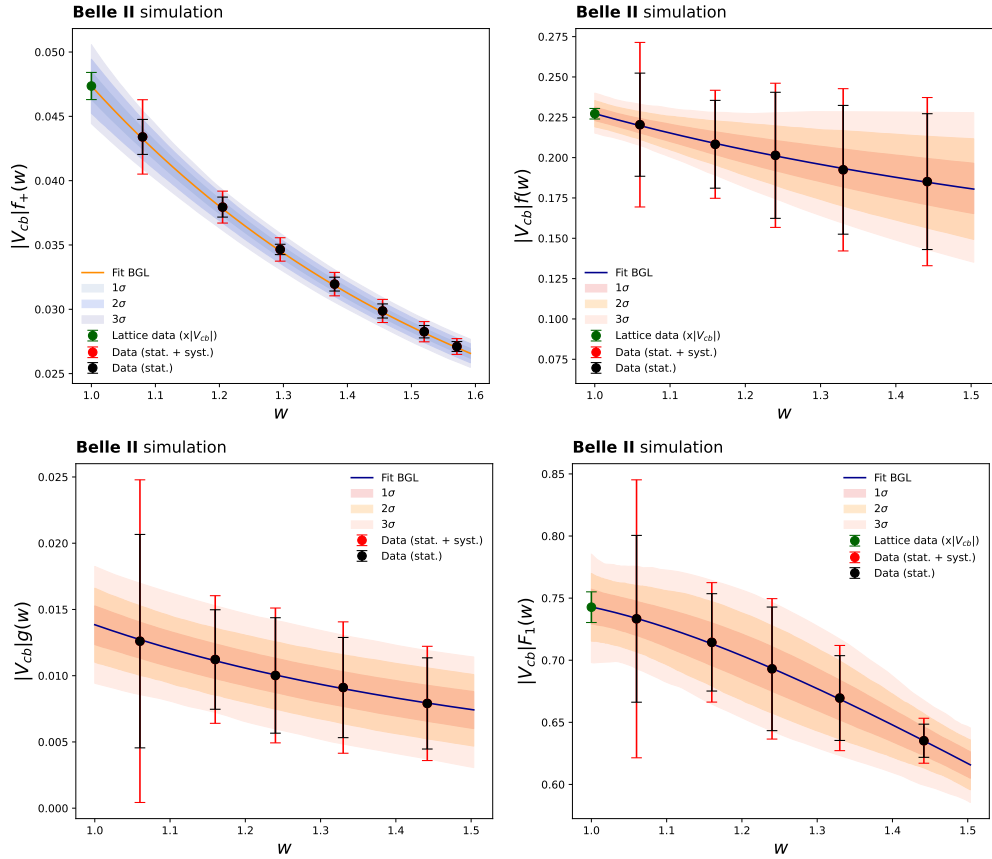


Figure 8.1: Measurements of the product of  $|V_{cb}|$  and form-factor parameters (black points) for both  $B \rightarrow D\ell\nu_\ell$  and  $B \rightarrow D^*\ell\nu_\ell$ , using configuration 2 in Tab. 8.1. The statistical (black lines) and total uncertainties (red lines) are obtained by propagating the uncertainties of the model-independent observables. The green points represent the lattice data used in the measurement multiplied by  $|V_{cb}|$ . The error bands corresponding to 1, 2, and 3 $\sigma$  are obtained using the total covariance matrix of the *a posteriori* fit.

I fit the series of the form factors using three different configurations, varying the series truncation for both  $B \rightarrow D\ell\nu_\ell$  and  $B \rightarrow D^*\ell\nu_\ell$  decays (see Tab. 4.1). The fit parameters are:  $a_1^{f+}$ ,  $a_1^{f+}$ ,  $a_2^{f+}$ ,  $a_3^{f+}$  and  $\mathcal{G}(1)$  for the  $B \rightarrow D\ell\nu_\ell$  decay; and  $a_1^f$ ,  $a_0^g$ ,  $a_1^g$ ,  $a_1^{F_1}$ ,  $a_2^{F_1}$  and  $h_{A_1}(1)$  for the  $B \rightarrow D^*\ell\nu_\ell$  decay; and  $|V_{cb}|$ , which is shared between the two decay channels.<sup>1</sup> For this test, I use the full covariance matrix included both statistical and systematic uncertainties and both the  $\mathcal{G}(1)$  and  $h_{A_1}(1)$  are constrained to the values in Eqs. 8.2 and 8.3 using Gaussian penalties in the fit.

For all the configurations analysed, I would expect  $\chi^2 \sim 0$ , as these are Asimov fits. Table 8.1 reports the results from the three configurations. Configuration 1 exhibits significant biases, along with a higher than expected  $\chi^2$ . In contrast, configurations 2 and 3 show no noticeable biases. Since configuration 2 has the lowest AIC value, I choose it for the following studies and to provide a realistic estimate of the uncertainties on  $|V_{cb}|$  and form factors.

I show the form factor parameters obtained from the model-observables in configuration

<sup>1</sup>Note that  $a_0^f$  and  $a_0^{F_1}$  are related to  $h_{A_1}(1)$  through Eqs. A.17 and A.18, and  $a_0^{f+}$  to  $\mathcal{G}(1)$  through Eq. A.24.

Parameter	Generator values	Fit scenario 1)	Fit scenario 2)	Fit scenario 3)
$a_1^{f+}$	-0.094	$-0.094 \pm 0.007$	$-0.094 \pm 0.010$	$-0.094 \pm 0.010$
$a_2^{f+}$	0.340	$0.33 \pm 0.08$	$0.33 \pm 0.12$	$0.33 \pm 0.12$
$a_1^f$	0.01713	$0.017 \pm 0.016$	$0.017 \pm 0.016$	$0.017 \pm 0.016$
$a_0^g$	0.02596	$0.026 \pm 0.002$	$0.026 \pm 0.002$	$0.026 \pm 0.002$
$a_1^g$	-0.06049	$-0.061 \pm 0.043$	$-0.061 \pm 0.044$	$-0.061 \pm 0.045$
$a_1^{F_1}$	0.00753	$0.0075 \pm 0.0028$	$0.0075 \pm 0.0028$	$0.0075 \pm 0.0028$
$a_2^{F_1}$	-0.09346	$-0.093 \pm 0.011$	$-0.093 \pm 0.048$	$-0.093 \pm 0.048$
$h_{A_1}(1)$	0.9038	$0.904 \pm 0.011$	$0.904 \pm 0.022$	$0.904 \pm 0.013$
$\mathcal{G}(1)$	1.0294	$1.029 \pm 0.009$	$1.029 \pm 0.009$	$1.029 \pm 0.028$
$ V_{cb}  [10^{-3}]$	38.72	$38.72 \pm 0.51$	$38.71 \pm 0.88$	$38.72 \pm 0.64$

Table 8.2: Comparison of the generator values of  $|V_{cb}|$  and BGL parameters with the results obtained from the fit of the model-independent observables in the three scenarios of the configuration 2 described in the text.

2 in Fig. 8.1. The error bands corresponding to 1, 2, and  $3\sigma$  are obtained using the total covariance matrix of the *a posteriori* fit. Note that, through Eq. 2.5 and Eqs. 2.9-2.11, I can directly convert the model-independent observables in a direct measurement of the form factors  $f_+$ ,  $f$ ,  $g$  and  $F_1$ , all multiplied by  $|V_{cb}|$ , in bins of  $w$ . These data are also shown Fig. 8.1: they would enable a determination of  $|V_{cb}|$  from the *direct* ratio of the experimental measurements and the lattice-QCD calculations performed in the same bins of  $w$ ; *i.e.*, through a parametrisation-free analysis. The different values of  $|V_{cb}|$  can be averaged using the methods discussed in Ref. [149].

Using configuration 2, I conducted a study involving different assumptions for the lattice points at  $w = 1$ . Three scenarios are explored:

- scenario 1: constrain  $\mathcal{G}(1)$  and  $h_{A_1}(1)$  to the values in Eqs. 8.2 and 8.3 using Gaussian penalties in the fit, enabling a better precision on  $|V_{cb}|$ ;
- scenario 2: leave  $h_{A_1}(1)$  completely free in the fit and constrain only  $\mathcal{G}(1)$ ;
- scenario 3: leave  $\mathcal{G}(1)$  completely free in the fit and constrain only  $h_{A_1}(1)$ .

For this study, I use only the information from the statistical covariance matrix for the different scenarios. The first scenario is the “nominal” configuration; the other two allow to understand how much information can be leverage from data by using only the external inputs from one channel or the other. Results of the fit in the three scenarios are reported in Tab. 8.2.

In all scenarios, I obtain values consistent with those generated. In scenario 1, I observe that the uncertainty on the Gaussian-constrained parameter  $h_{A_1}(1)$  decreases from 0.013 to 0.011, while the uncertainty on  $\mathcal{G}(1)$  remains the same (0.009). This indicates that the data provide additional information on  $h_{A_1}(1)$ .

In scenario 2,  $h_{A_1}(1)$  is determined with an uncertainty of about 0.022, which is worse than that of the external input 0.013, and also the uncertainty on  $|V_{cb}|$  increases (from  $0.51 \times 10^{-3}$  to  $0.88 \times 10^{-3}$ ). In the simultaneous analysis,  $|V_{cb}|$  is sufficiently constrained by the  $B \rightarrow D\ell\nu_\ell$  data and the external input on  $\mathcal{G}(1)$ , allowing  $h_{A_1}(1)$  to be determined in the product  $|V_{cb}|h_{A_1}(1)$ . Similar considerations hold also in scenario 3, where  $\mathcal{G}(1)$  can

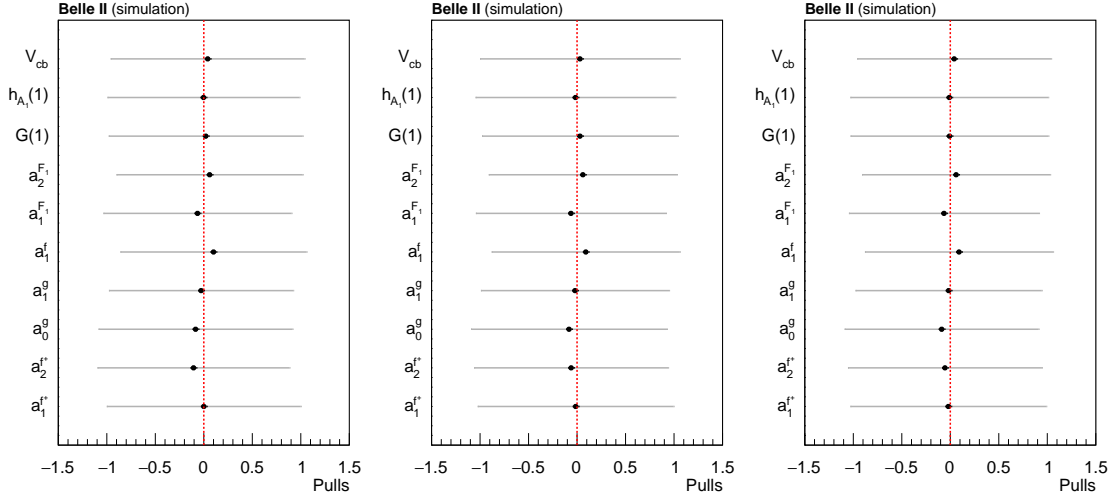


Figure 8.2: Summary of the pull analysis for  $|V_{cb}|$  and the BGL parameters in the fit configuration 2 to 1000 toy samples of the model-independent observables: (left) scenario 1, (middle) 2, and (right) 3. The black points are the pull means, the black bars the uncertainties on the means, and the grey bars are the pull standard deviations. Pull distributions can be found in Appendix F.

be determined, although with an uncertainty (0.028) much worse than that of the external input (0.009).

Scenario 2 is particularly interesting, as it could potentially lead to a first determination of the  $B \rightarrow D^* \ell \nu_\ell$  form factors directly from data, relying on external inputs from lattice calculations on  $B \rightarrow D \ell \nu_\ell$  only, thereby providing an interesting term of comparison for the lattice-QCD form-factor calculations from different collaborations [31–33], which currently feature some tensions as explained in Chapter 2.

As the measurement of the model-independent observables shows some small biases in Sect. 6.5, I test how these propagate to  $|V_{cb}|$  and the BGL parameters. I therefore run the full analysis from the measurements of the model-independent observables on 1000 toy samples. The fit *a posteriori* is then performed for each scenario over the 1000 results, including their covariances, of the model-independent observables. I inspect the pull distributions of  $|V_{cb}|$  and the BGL parameters (defined as per Eq. 6.15) and observed that they are generally unbiased normal Gaussian. Pulls distributions are reported in Appendix F and a summary plot is shown in Fig. 8.2.

Finally, I also analyse the original distributions of  $(\cos \theta_{BY}, p_\ell^*, p_D^*)$  with a 3-dimensional fit, where I use directly the BGL parametrisation in the weighting technique of the signal templates (presented in Sect. 6.2.1.1). Hence, this fit is referred to as the *direct* approach, in contrast to the *a posteriori* fit employing the measured model-independent observables. This is done to compare the sensitivity to  $|V_{cb}|$  and the form-factor parameters between the *a posteriori* and *direct* approaches, to check if there is any loss of information in the use of the model-independent observables. This study is presented in Appendix E.1.

To summarise, I demonstrated the reliability of the extraction of  $|V_{cb}|$  and the BGL parameters using the model-independent observables (showing different scenarios to use the two lattice points  $\mathcal{G}(1)$  and  $h_{A_1}(1)$ ). I also carry out a similar analysis using the CLN parametrisation, presented in Appendix E obtaining similar conclusions as reported here.

### 8.1.2 Expected uncertainties

To gain an idea on the uncertainty sources that limit the measurement, I calculate the expected uncertainties on  $|V_{cb}|$  and the BGL parameters in the configuration 2 (scenario 1) splitting between the statistical and systematic contributions; the latter is further split according to the different systematic sources as done for the other measurements described in the previous chapter. The uncertainties are reported in Tab. 8.3, while correlation matrices are shown in Fig. 8.3.

As expected, the uncertainty of  $|V_{cb}|$  is dominated by the systematic uncertainty. The sources that contribute the most are the background modelling, the number of  $B\bar{B}$  pairs, and the  $D^{**}\ell\nu_\ell$  branching fractions. For the BGL parameters, the largest systematic uncertainty is due to the background modelling, which has size similar to the statistical uncertainty for all parameters.

The expected total uncertainty on  $|V_{cb}|$  from my analysis is expected to be competitive with current world's best measurements [85, 91]. As an example, I compare in Tab. 8.4 the expected uncertainties on  $|V_{cb}|$  from my analysis with that from a Belle II analysis of the  $B^0 \rightarrow D^{*-}\ell^+\nu_\ell$  decay [91]. Note that the analyses are based on different assumptions, such as the truncation of the BGL series and the use of lattice-QCD data. In particular, I reported my result in the configuration 2 and including only two lattice-QCD points at  $w = 1$ ; in Ref. [91], additional orders are included, but lattice-QCD data for  $w > 1$  are also employed.

Source	$ V_{cb} $ [%]	$a_1^{f+}[10^{-2}]$	$a_2^{f+}[10^{-2}]$	$a_0^g[10^{-2}]$	$a_1^g[10^{-2}]$	$a_1^f[10^{-2}]$	$a_1^{F_1}[10^{-2}]$	$a_2^{F_1}[10^{-2}]$
$N_{B\bar{B}}$	0.7	< 0.01	< 0.1	< 0.01	< 0.1	< 0.1	< 0.01	< 0.1
$\mathcal{B}(D)$	0.4	0.10	1.1	< 0.01	0.2	< 0.1	< 0.01	0.1
$\tau_{B^0}/\tau_{B^+}$	0.1	< 0.01	< 0.1	< 0.01	< 0.1	< 0.1	< 0.01	< 0.1
Track. efficiency	0.4	0.01	0.1	< 0.01	< 0.1	< 0.1	< 0.01	< 0.1
$D^{**}\ell\nu_\ell$	0.6	0.05	0.7	0.02	0.3	0.1	0.02	0.3
Backgr. model	1.0	0.43	5.5	0.16	2.5	1.0	0.22	3.5
PID	0.5	0.11	1.0	0.05	1.3	0.8	0.09	1.8
Templates stat.	0.5	0.24	3.2	0.12	2.5	1.0	0.19	3.2
Fit bias	0.2	0.07	1.0	0.03	0.7	0.2	0.03	0.5
Total systematic	1.6	0.49	6.3	0.19	3.6	1.5	0.28	4.6
Coulomb factor	0.5	< 0.01	< 0.1	< 0.01	< 0.1	< 0.1	< 0.01	< 0.1
Statistical	0.7	0.39	5.5	0.18	4.2	1.5	0.27	4.6
Lattice points	1.2	0.57	6.5	0.03	0.5	0.2	0.01	0.2
Total	2.2	0.87	11.0	0.29	6.0	2.2	0.42	7.1

Table 8.3: Expected uncertainties on  $|V_{cb}|$  and the BGL parameters for configuration 2 in scenario 1. The uncertainties on  $|V_{cb}|$  are fractional.

$ V_{cb}  [10^{-3}]$	
My work	$XXX \pm 0.29(\text{stat.}) \pm 0.64(\text{syst.}) \pm 0.45(\text{latt.})$
Belle II (2023)	$40.57 \pm 0.31(\text{stat.}) \pm 0.95(\text{syst.}) \pm 0.58(\text{latt.})$

Table 8.4: Comparison between the result of  $|V_{cb}|$  from my analysis and the Belle II measurement of Ref. [91]. The central value of my results is not reported, as the analysis is still blind. I assume the values used in the simulation ( $38.72 \times 10^{-3}$ ) to obtain the uncertainty from the fractional errors reported in Tab. 8.3. The uncertainty from the Coulomb factor is included in the systematic uncertainty of my measurement; the third uncertainty is that propagated from the lattice data used.

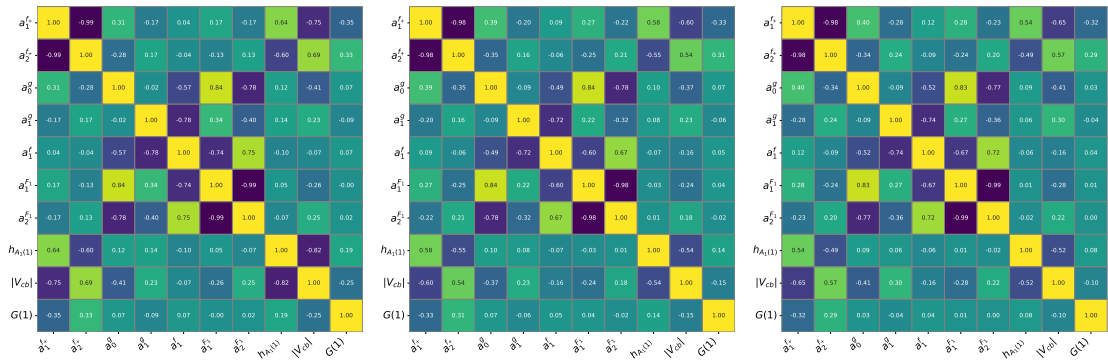


Figure 8.3: Correlation matrix between the uncertainties of  $|V_{cb}|$ , BGL parameters and lattice points at  $w = 1$  for the configuration 2 in scenario 1. From left to right: statistical, systematic and total.



# Summary

I presented an experimental particle-physics thesis that reports on the first simultaneous analysis of the  $B \rightarrow D\ell\nu_\ell$  and  $B \rightarrow D^*\ell\nu_\ell$  decays at Belle II experiment, using data collected between 2019 and 2022. The data set consists of about 387 million bottom-antibottom meson pairs from decays of the  $\Upsilon(4S)$  resonance, produced in asymmetric-energy electron-positron collisions at the SuperKEKB accelerator.

The simultaneous analysis offers a unique opportunity to explore new avenues by introducing innovative methods. I analysed the decay dynamics using a novel method that provides several key measurements, the most significant being a precise determination of the strength of the weak-interaction coupling between beauty and charm quarks,  $|V_{cb}|$ .

The core of the analysis is a multidimensional fit to measure model-independent observables sensitive to the decay dynamics, defined for the first time in this thesis. From these observables,  $|V_{cb}|$  and form-factor parameters can be determined *a posteriori* assuming any form-factor model. These observables facilitate improved determination of  $|V_{cb}|$  using any future advancement on the theoretical side, either in the calculation or modelling of the form factors. From the global analysis,  $|V_{cb}|$  can be determined by using minimal input from lattice-QCD calculations for the two decays. In particular, a determination based solely on calculations for the  $B \rightarrow D\ell\nu_\ell$  decay is possible, offering an intriguing comparison term for the  $B \rightarrow D^*\ell\nu_\ell$  form factors, which currently exhibit some tensions in lattice-QCD calculation by different collaborations.

From the same observables, I also derive measurements of the  $B \rightarrow D\ell\nu_\ell$  and  $B \rightarrow D^*\ell\nu_\ell$  branching fractions, as well as the lepton forward-backward asymmetry  $A_{\text{FB}}$ , and the  $D^*$  longitudinal polarisation  $F_L^{D^*}$ , for  $B \rightarrow D^*\ell\nu_\ell$  decays. Additionally, by assuming isospin symmetry, I obtain a new determination of  $f_{+-}/f_{00}$ , the ratio of the branching fractions of  $\Upsilon(4S)$  decays into charged and neutral  $B$  mesons pairs.

A primary challenge of the analysis has been to thoroughly investigate all potential background sources and to develop strategies for reducing or constraining them as much as possible, utilising dedicated selections and control regions in data. Specifically, I identified a control region enriched of a challenging background due to feed-down from semileptonic decays different from the signal, whose production rates and decay modelling are affected by large uncertainties. By analysing this control region along with the signal sample, I managed to bound this background from data and reduce its impact on the measurement.

The entire analysis has been fully developed using simulated and control-data samples and is currently under internal review within the Collaboration. The full analysis will be applied to the experimental data of the signal region after passing the review and defining an unblinding procedure. An in-depth study with realistic simulated samples proved unbiased

results and allowed to estimated the expected uncertainties. From this study, I obtain:

$$\begin{aligned} |V_{cb}| &= (XXX \pm 0.29 \pm 0.64 \pm 0.45) \times 10^{-3}, \\ \mathcal{B}(B^+ \rightarrow \bar{D}^0 \ell^+ \nu_\ell) &= (XXX \pm 0.01 \pm 0.06)\%, \\ \mathcal{B}(B^+ \rightarrow \bar{D}^{*0} \ell^+ \nu_\ell) &= (XXX \pm 0.02 \pm 0.13)\%, \\ \mathcal{B}(B^0 \rightarrow D^- \ell^+ \nu_\ell) &= (XXX \pm 0.01 \pm 0.05 \pm 0.02)\%, \\ \mathcal{B}(B^0 \rightarrow D^{*-} \ell^+ \nu_\ell) &= (XXX \pm 0.02 \pm 0.12 \pm 0.05)\%, \\ A_{\text{FB}} &= (XXX \pm 0.5 \pm 0.4)\%, \\ F_L^{D^*} &= (XXX \pm 0.7 \pm 0.6)\%, \\ f_{+-}/f_{00} &= XXX \pm 0.007 \pm 0.025 \pm 0.024. \end{aligned} \tag{8.4}$$

where the first uncertainty is statistical, the second systematic, and the third, when present, is related to theoretical inputs or assumptions. The measurements are expected to be competitive with the world's best and have the potential to significantly advance the precision and reliability of these quantities. This, in turn, enhances the overall understanding of semileptonic  $B$  decays for providing a more robust determination of  $|V_{cb}|$ .

# Appendices



# Appendix A

## Form-factor parametrisations

In this appendix, I provide a more detailed theoretical description of the form factors using the CLN and BGL parametrisations for both the  $B \rightarrow D\ell\nu_\ell$  and  $B \rightarrow D^*\ell\nu_\ell$  decays, in the limit of negligible lepton masses.

### A.1 $B \rightarrow D^*\ell\nu_\ell$

As explained in Chapter 2, the form factors needed to describe the hadronic part of the decay rate can be expressed using different parametrisations. Using the CLN parametrisation the three form factors of  $B \rightarrow D^*\ell\nu_\ell$  decays are written as:

$$h_{A_1}(w) = h_{A_1}(1) [1 - 8\rho_{D^*}^2 z + (53\rho_{D^*}^2 - 15)z^2 - (231\rho_{D^*}^2 - 91)z^3] , \quad (\text{A.1})$$

$$R_1(w) = R_1(1) - 0.12(w - 1) + 0.05(w - 1)^2 , \quad (\text{A.2})$$

$$R_2(w) = R_2(1) - 0.11(w - 1) - 0.06(w - 1)^2 , \quad (\text{A.3})$$

where the conformal variable  $z$  is defined as

$$z \equiv \frac{\sqrt{w+1} - \sqrt{2}}{\sqrt{w+1} + \sqrt{2}} , \quad (\text{A.4})$$

The form factors depend on four parameters:  $\rho_{D^*}^2$ ,  $R_1(1)$ ,  $R_2(1)$  and  $h_{A_1}(1)$ .

While using the BGL parametrisation, which relies only on QCD dispersion relations, the three form factors are written in terms of three functions,  $f(w)$ ,  $g(w)$  and  $\mathcal{F}_1(w)$ , as follows

$$h_{A_1}(w) = \frac{f(w)}{\sqrt{m_B m_{D^*}}(1+w)} , \quad (\text{A.5})$$

$$R_1(w) = (w+1)m_B m_{D^*} \frac{g(w)}{f(w)} , \quad (\text{A.6})$$

$$R_2(w) = \frac{w-r}{w-1} - \frac{\mathcal{F}_1(w)}{m_B(w-1)f(w)} . \quad (\text{A.7})$$

These functions are expanded as convergent power series of  $z$  as

$$f(z) = \frac{1}{P_{1^+}(z)\phi_f(z)} \sum_{n=0}^{\infty} a_n^f z^n, \quad (\text{A.8})$$

$$g(z) = \frac{1}{P_{1^-}(z)\phi_g(z)} \sum_{n=0}^{\infty} a_n^g z^n, \quad (\text{A.9})$$

$$\mathcal{F}_1(z) = \frac{1}{P_{1^+}(z)\phi_{\mathcal{F}_1}(z)} \sum_{n=0}^{\infty} a_n^{F_1} z^n. \quad (\text{A.10})$$

Here, the  $P_{1^\pm}(z)$  functions are known as Blaschke factors for the  $J^P = 1^\pm$  resonances, and  $\phi_{f,g,\mathcal{F}_1}(z)$  are the so-called outer functions. Adopting the formalism of Ref. [43], the Blaschke factors take the form

$$P_{1^\pm}(z) = C_{1^\pm} \prod_{k=1}^{\text{poles}} \frac{z - z_k}{1 - z z_k^*}, \quad (\text{A.11})$$

where the constants  $C_{1^\pm} = 1$  and

$$z_k = \frac{\sqrt{t_+ - m_k^2} - \sqrt{t_+ - t_-}}{\sqrt{t_+ - m_k^2} + \sqrt{t_+ - t_-}}, \quad (\text{A.12})$$

$t_\pm = (m_B \pm m_{D^*})^2$ , and  $m_k$  denotes the pole masses of the  $k$ -th excited  $B_c^+$  states. The outer functions are defined as

$$\phi_f(z) = \frac{4r}{m_B^2} \sqrt{\frac{n_I}{3\pi\tilde{\chi}_{1^+}(0)}} \frac{(1+z)\sqrt{(1-z)^3}}{[(1+r)(1-z) + 2\sqrt{r}(1+z)]^4}, \quad (\text{A.13})$$

$$\phi_g(z) = 16r^2 \sqrt{\frac{n_I}{3\pi\tilde{\chi}_{1^-}(0)}} \frac{(1+z)^2}{\sqrt{(1-z)}[(1+r)(1-z) + 2\sqrt{r}(1+z)]^4}, \quad (\text{A.14})$$

$$\phi_{\mathcal{F}_1}(z) = \frac{4r}{m_B^3} \sqrt{\frac{n_I}{6\pi\tilde{\chi}_{1^+}(0)}} \frac{(1+z)\sqrt{(1-z)^5}}{[(1+r)(1-z) + 2\sqrt{r}(1+z)]^5}, \quad (\text{A.15})$$

where  $n_I = 2.6$  is the number of spectator quarks (three), corrected for  $SU(3)$ -breaking effects [41]. The  $B_c^+$  resonances used in the computation of the Blaschke factors and the  $\tilde{\chi}_{1^\pm}(0)$  coefficients of the outer functions are reported in Tab. A.1.

The coefficients of the series in Eqs. A.8–A.10 are bound by the unitarity constraints

$$\sum_{n=0}^{\infty} a_n^g{}^2 \leq 1, \quad \sum_{n=0}^{\infty} (a_n^f{}^2 + a_n^{F_1}{}^2) \leq 1. \quad (\text{A.16})$$

The first coefficient of  $f(z)$ ,  $a_0^f$ , is related to  $h_{A_1}(1)$  by the expression

$$a_0^f = 2\sqrt{m_B m_D} P_{1^+}(0) \phi_f(0) h_{A_1}(1), \quad (\text{A.17})$$

while  $a_0^{F_1}$  is fixed from  $a_0^f$  through

$$a_0^{F_1} = (m_B - m_D) \frac{\phi_{\mathcal{F}_1}(0)}{\phi_f(0)} a_0^f. \quad (\text{A.18})$$

One of the actual problem of the BGL parametrisation is related to the truncation of the series in Eqs. A.8–A.10 to get an unbiased  $|V_{cb}|$  measurement [38, 39, 43, 79, 80].

Table A.1: Pole masses for the  $B_c^+$  resonances considered in the BGL parametrisation, with the  $\tilde{\chi}_{JP}(0)$  constants of the outer functions.

$J^P$	Pole mass [GeV/ $c^2$ ]	$\tilde{\chi}_{JP}(0)$ [ $10^{-4}\text{GeV}^{-2}c^4$ ]
$1^-$	6.337	5.28
	6.899	
	7.012	
	7.280	
$1^+$	6.730	3.07
	6.736	
	7.135	
	7.142	

## A.2 $B \rightarrow D\ell\nu_\ell$

For the  $B \rightarrow D\ell\nu_\ell$  decays, the form factor  $\mathcal{G}(z)$ , using the conformal variable  $z(w)$  defined in Eq. A.4, is expressed in the CLN parametrisation in terms of its value at zero recoil,  $\mathcal{G}(1)$ , and a slope parameter,  $\rho_D^2$ , as

$$\mathcal{G}(z) = \mathcal{G}(1) [1 - 8\rho_D^2 z + (51\rho_D^2 - 10)z^2 - (252\rho_D^2 - 84)z^3]. \quad (\text{A.19})$$

While using the BGL parametrisation, it is expressed as

$$|\mathcal{G}(z)|^2 = \frac{4r}{(1+r)^2} |f_+(z)|^2, \quad (\text{A.20})$$

with  $r = m_D/m_B$  and

$$f_+(z) = \frac{1}{P_{1^-}(z)\phi(z)} \sum_{n=0}^{\infty} a_n^{f_+} z^n. \quad (\text{A.21})$$

The outer function  $\phi(z)$  is defined as

$$\phi(z) = \frac{8r^2}{m_B} \sqrt{\frac{8n_I}{3\pi\tilde{\chi}_{1^-}(0)}} \frac{(1+z)^2\sqrt{1-z}}{[(1+r)(1-z) + 2\sqrt{r}(1+z)]^5}. \quad (\text{A.22})$$

The coefficients of the series in Eq. A.21 are bound by unitarity,

$$\sum_{n=0}^{\infty} a_n^{f_+^2} \leq 1, \quad (\text{A.23})$$

with the coefficient  $a_0^{f_+}$  being related to  $\mathcal{G}(1)$  through

$$a_0^{f_+} = \frac{1+r}{2\sqrt{r}} \mathcal{G}(1) P_{1^-}(0) \phi(0). \quad (\text{A.24})$$



## Appendix B

# Control region checks

Additional material regarding the fit performed on the  $\cos\theta_{BY}$  control region can be found in this appendix. Further data-simulation comparisons of the distributions, both before and after rescaling the real- $D$  and  $D^{**}$  subcomponents according to the fit results (see Tab. 6.2), are shown in Figs. B.2-B.5. The validation of the fit results for the real- $D$  background yields in the region of  $m(Y)$  between 3.2–3.4 GeV/ $c^2$ , where these decays are enhanced, are shown in Figs. B.6–B.7. A significant improvement in data-simulation comparison is also observed for the other distributions after rescaling these subcomponents.

Additionally, the shapes of the two-dimensional distributions  $(p_D^*, p_\ell^*)$  for the  $D^{**}$  decays in the signal region are shown in Fig. B.1 (see Sect. 6.2.2 in Chapter 6).

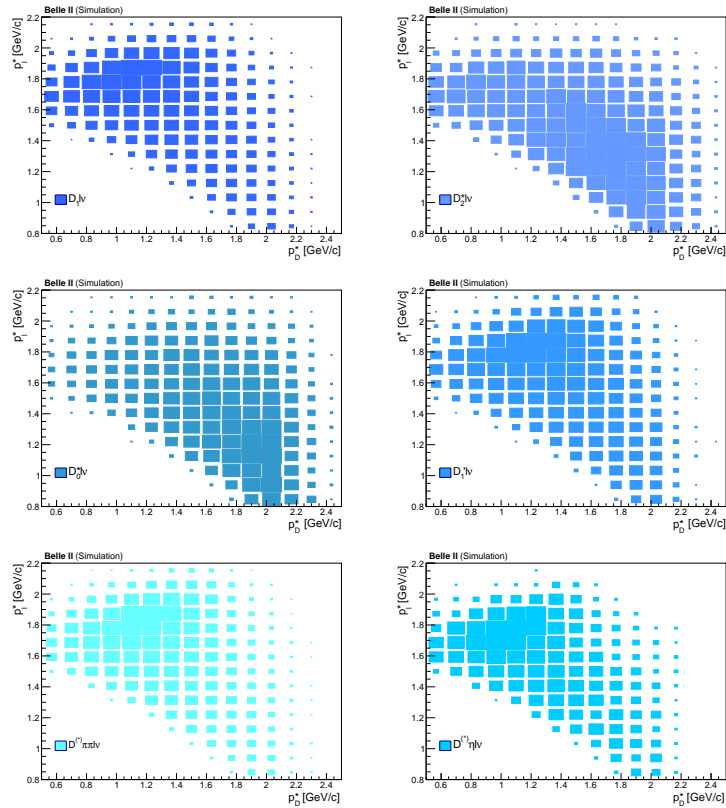


Figure B.1: Two-dimensional distributions of  $(p_D^*, p_\ell^*)$  of the  $D^{**} \ell \nu_\ell$  decays for the  $\overline{D}^0 e^+$  sample in the signal region. Similar distributions are observed in the other samples.

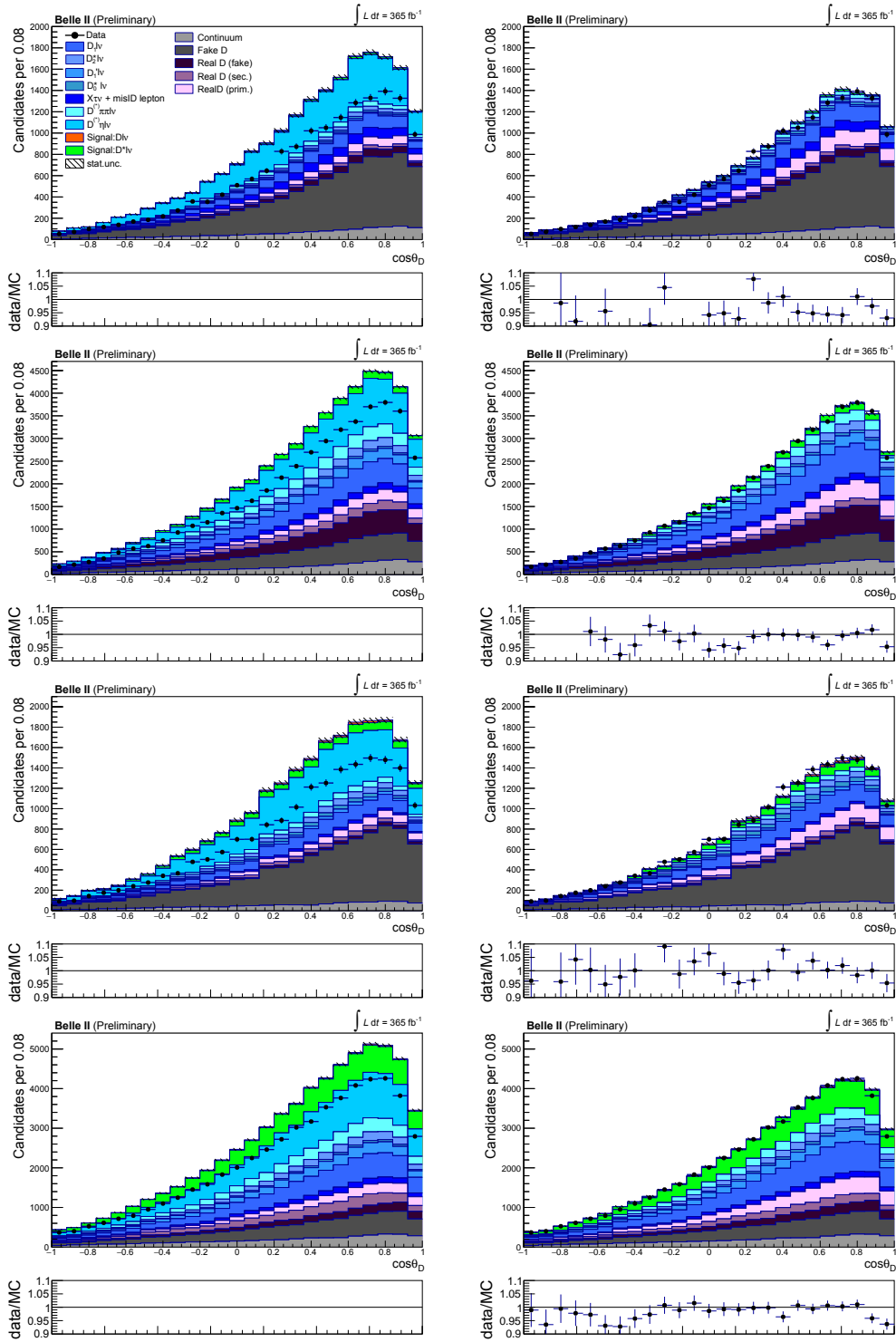


Figure B.2: Data-simulation comparison of the  $\cos \theta_D$  distributions, from top to bottom, for  $D^- \mu^+$ ,  $\bar{D}^0 \mu^+$ ,  $D^- e^+$ ,  $\bar{D}^0 e^+$  samples in the control region (left side) before and (right side) after scaling the  $D^{**}$  and real- $D$  subcomponents according to the fit results in Tab. 6.2.

## APPENDIX B. CONTROL REGION CHECKS

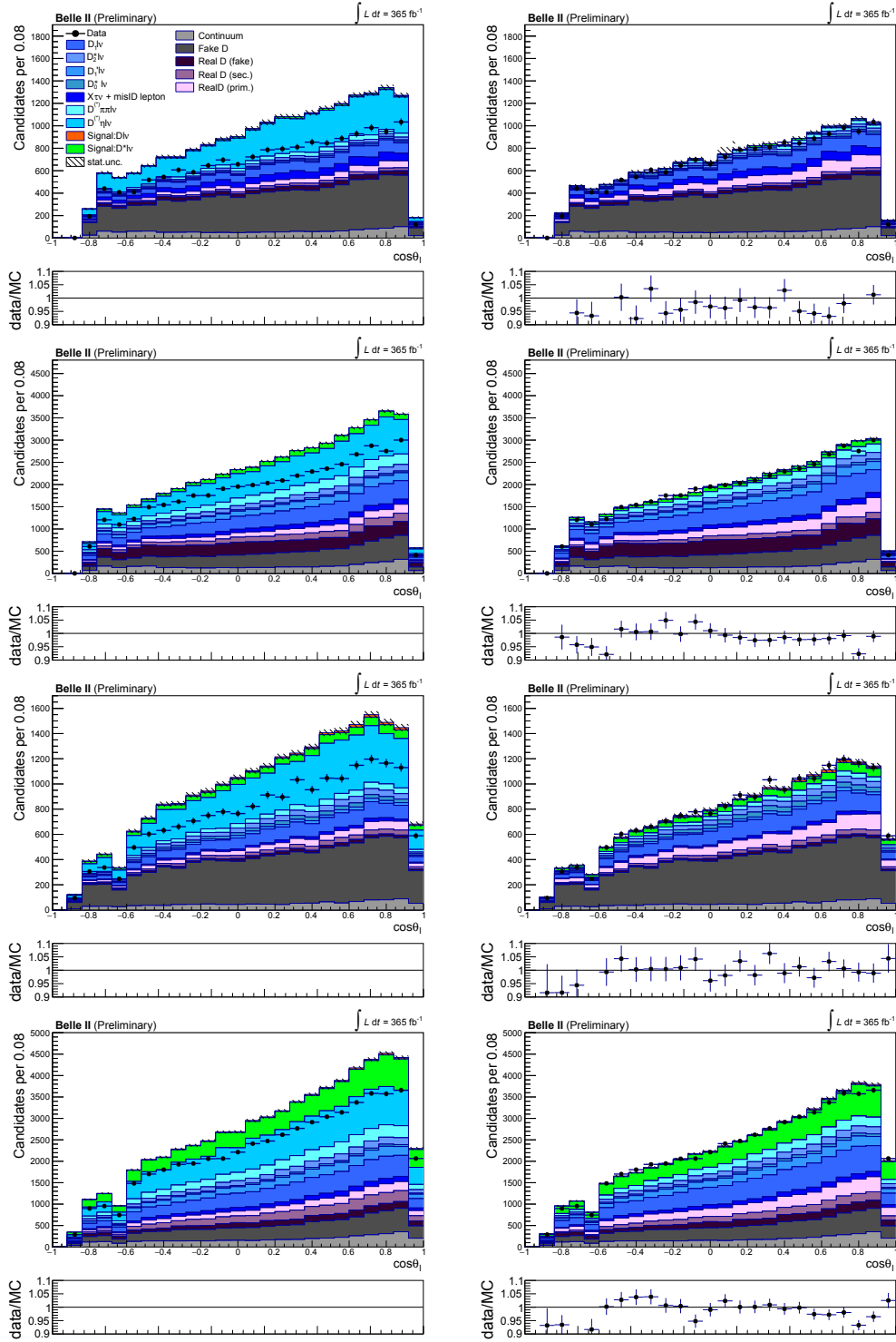


Figure B.3: Data-simulation comparison of the  $\cos \theta_\ell$  distributions, from top to bottom, for  $D^- \mu^+$ ,  $\bar{D}^0 \mu^+$ ,  $D^- e^+$ ,  $\bar{D}^0 e^+$  samples in the control region (left side) before and (right side) after scaling the  $D^{**}$  and real- $D$  subcomponents according to the fit results in Tab. 6.2.

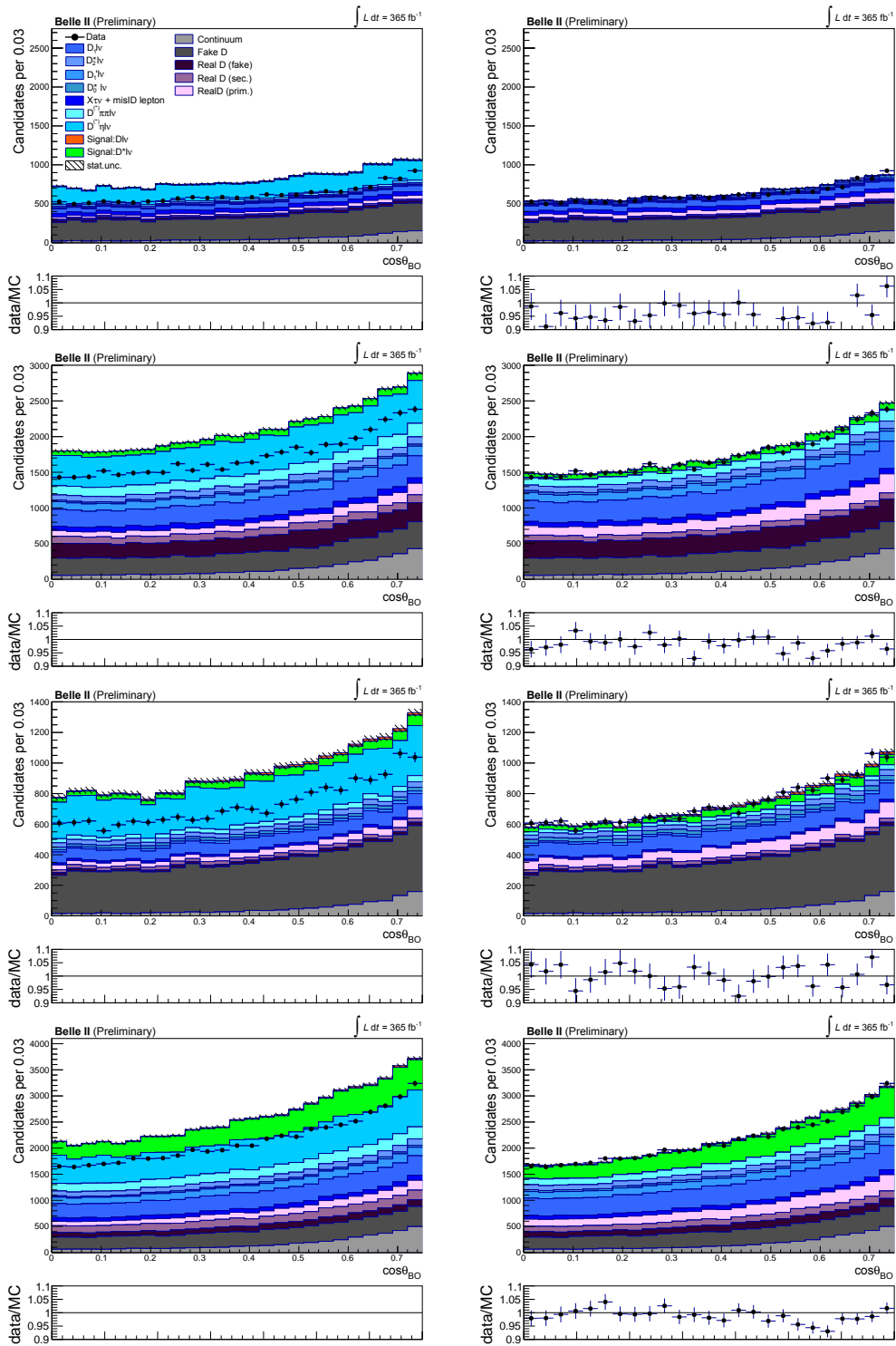


Figure B.4: Data-simulation comparison of the  $\cos\theta_{BO}$  distributions, from top to bottom, for  $D^-\mu^+$ ,  $\bar{D}^0\mu^+$ ,  $D^-e^+$ ,  $\bar{D}^0e^+$  samples in the control region (left side) before and (right side) after scaling the  $D^{**}$  and real- $D$  subcomponents according to the fit results in Tab. 6.2.

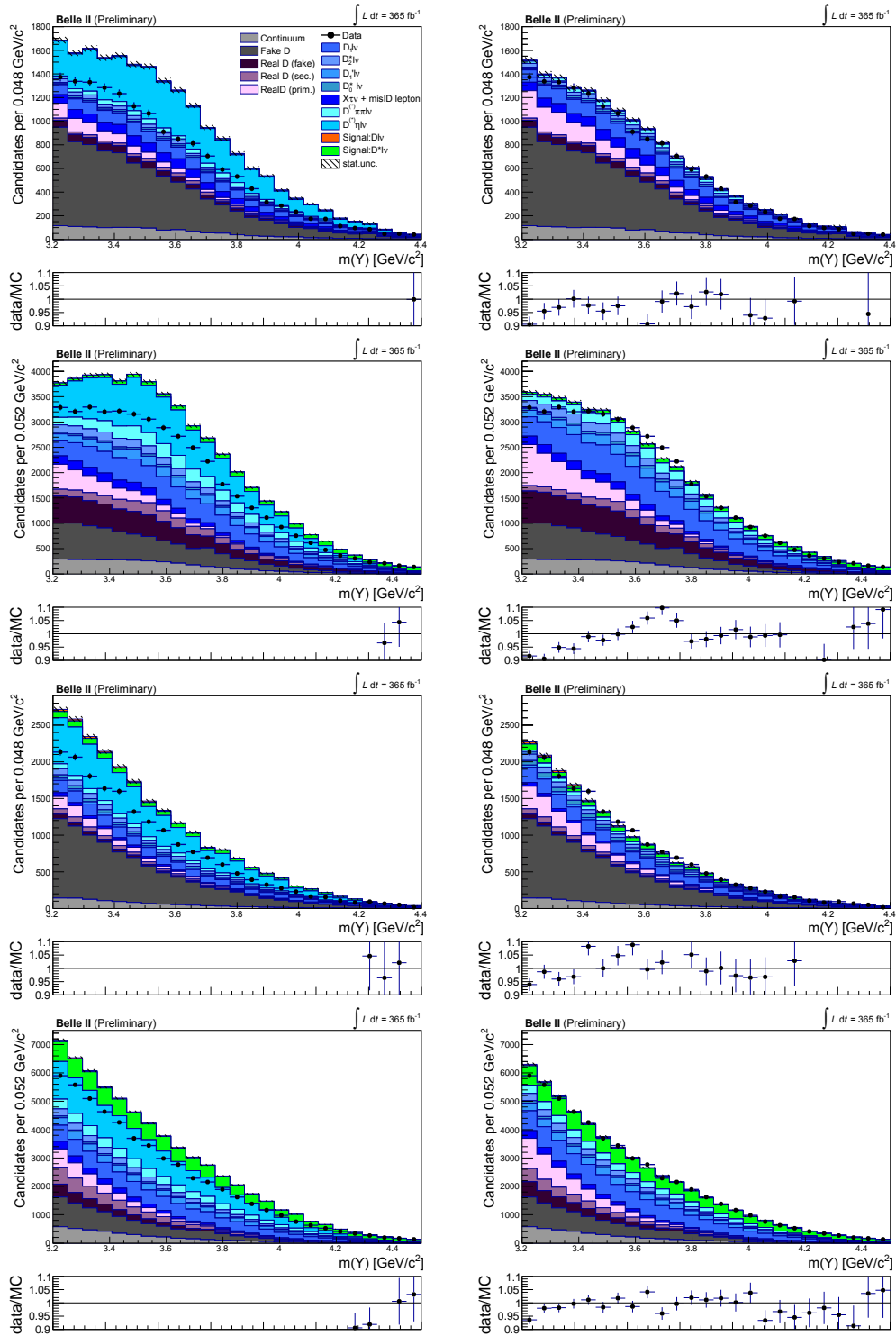


Figure B.5: Data-simulation comparison of the  $m(Y)$  distributions, from top to bottom, for  $D^- \mu^+$ ,  $\bar{D}^0 \mu^+$ ,  $D^- e^+$ ,  $\bar{D}^0 e^+$  samples in the control region (left side) before and (right side) after scaling the  $D^{**}$  and real- $D$  subcomponents according to the fit results in Tab. 6.2.

## APPENDIX B. CONTROL REGION CHECKS

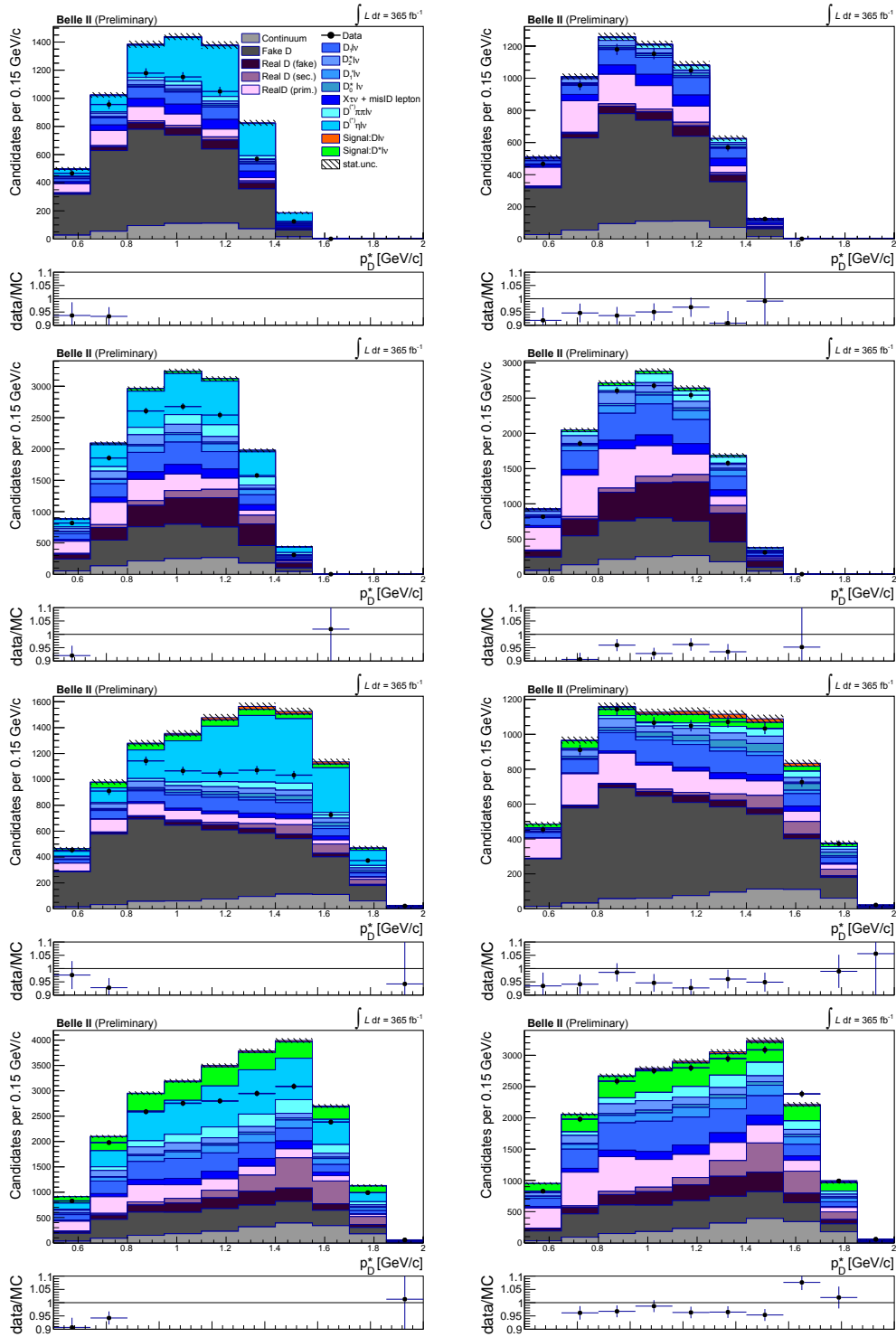


Figure B.6: Data-simulation comparison of the  $p_D^*$  distributions in the  $m(Y)$  region between  $3.2\text{--}3.4\text{ GeV}/c^2$ , from top to bottom, for  $D^-\mu^+$ ,  $\bar{D}^0\mu^+$ ,  $D^-e^+$ ,  $\bar{D}^0e^+$  samples in the control region (left side) before and (right side) after scaling the  $D^{**}$  and real- $D$  subcomponents according to the fit results in Tab. 6.2.

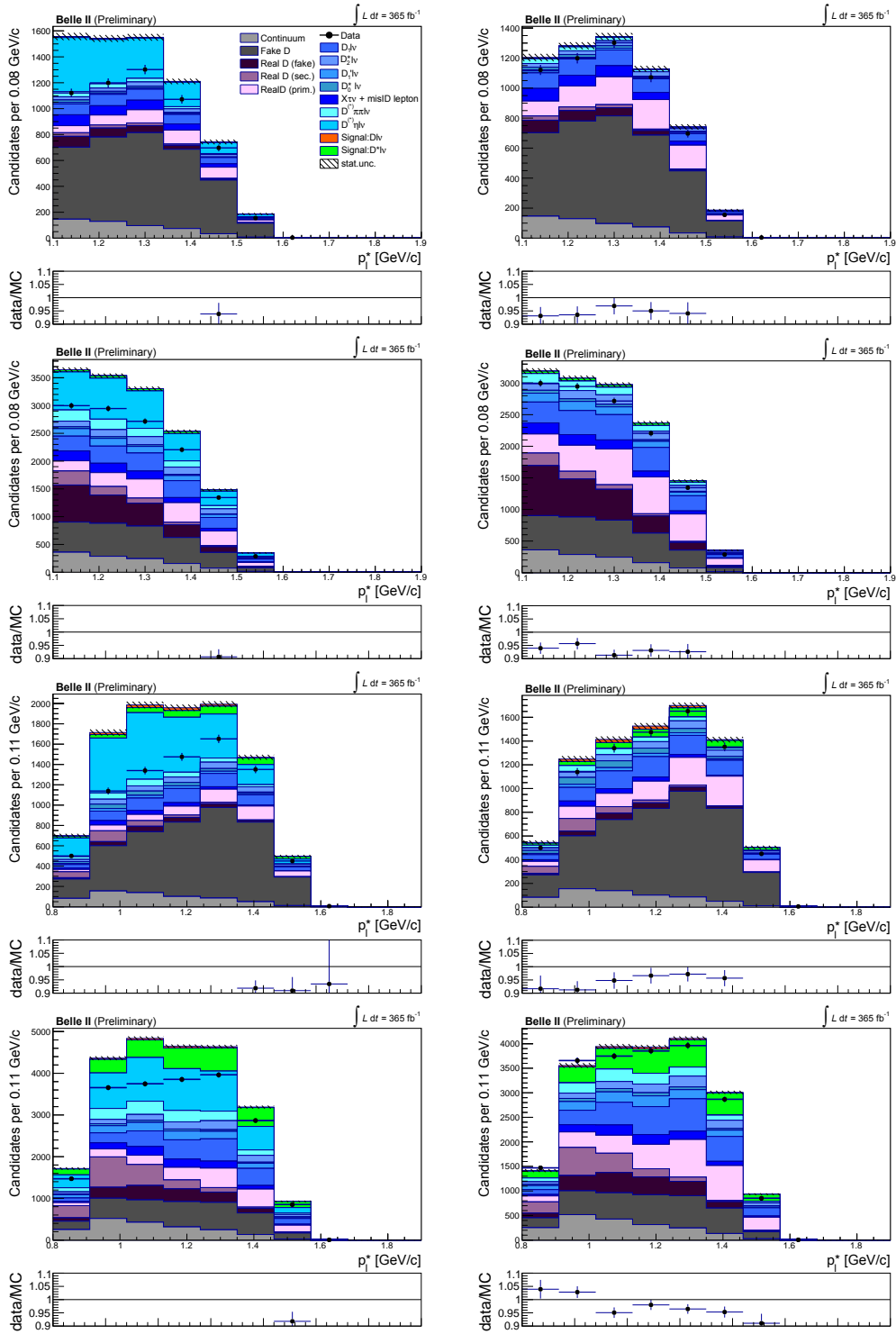


Figure B.7: Data-simulation comparison of the  $p_\ell^*$  distributions in the  $m(Y)$  region between 3.2–3.4  $\text{GeV}/c^2$ , from top to bottom, for  $D^-\mu^+$ ,  $\bar{D}^0\mu^+$ ,  $D^-e^+$ ,  $\bar{D}^0e^+$  samples in the control region (left side) before and (right side) after scaling the  $D^{**}$  and real- $D$  subcomponents according to the fit results in Tab. 6.2.



## Appendix C

### Signal-only Asimov fit

I report the results of the Asimov fit for measuring the 22 model-independent observables, defined in Sect. 2.5, simultaneously for the  $B \rightarrow D\ell\nu_\ell$  and  $B \rightarrow D^*\ell\nu_\ell$  decays. This first test involves performing the  $\chi^2$  fit, described in Sect. 6.2, focusing exclusively on the signal region and signal decays, without including any backgrounds. In this test, the fit parameters are the 22 model-independent observables and  $f_{+-}/f_{00}$ . I obtain the same generator values. A comparison between the generated values of the 22 model-independent observables and the results of the Asimov fit is shown in Fig. C.1. The fit projections are shown in Fig. C.2.

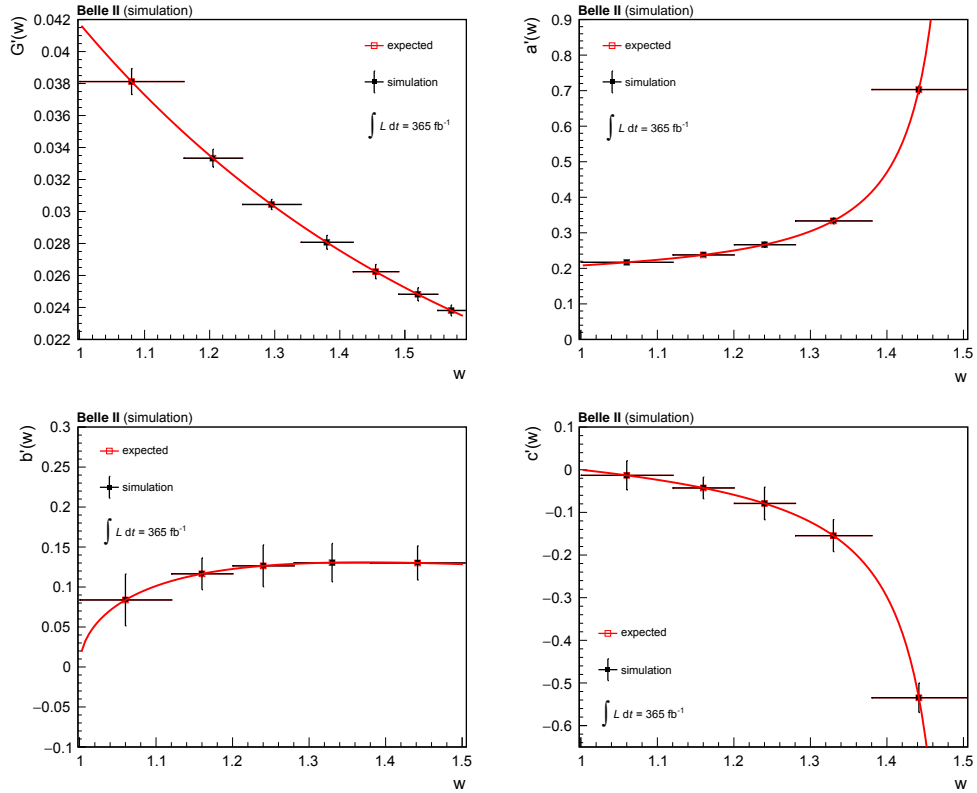


Figure C.1: (Top left) Measurements of  $G'_m$  in 7 bin of  $w$  and (top right, bottom) of  $a'_n$ ,  $b'_n$ ,  $c'_n$  in 5 bin of  $w$  obtained in the fit configuration of signal only. Black points are the results obtained from the Asimov fit, red points are the expected one from the BGL parametrisation.

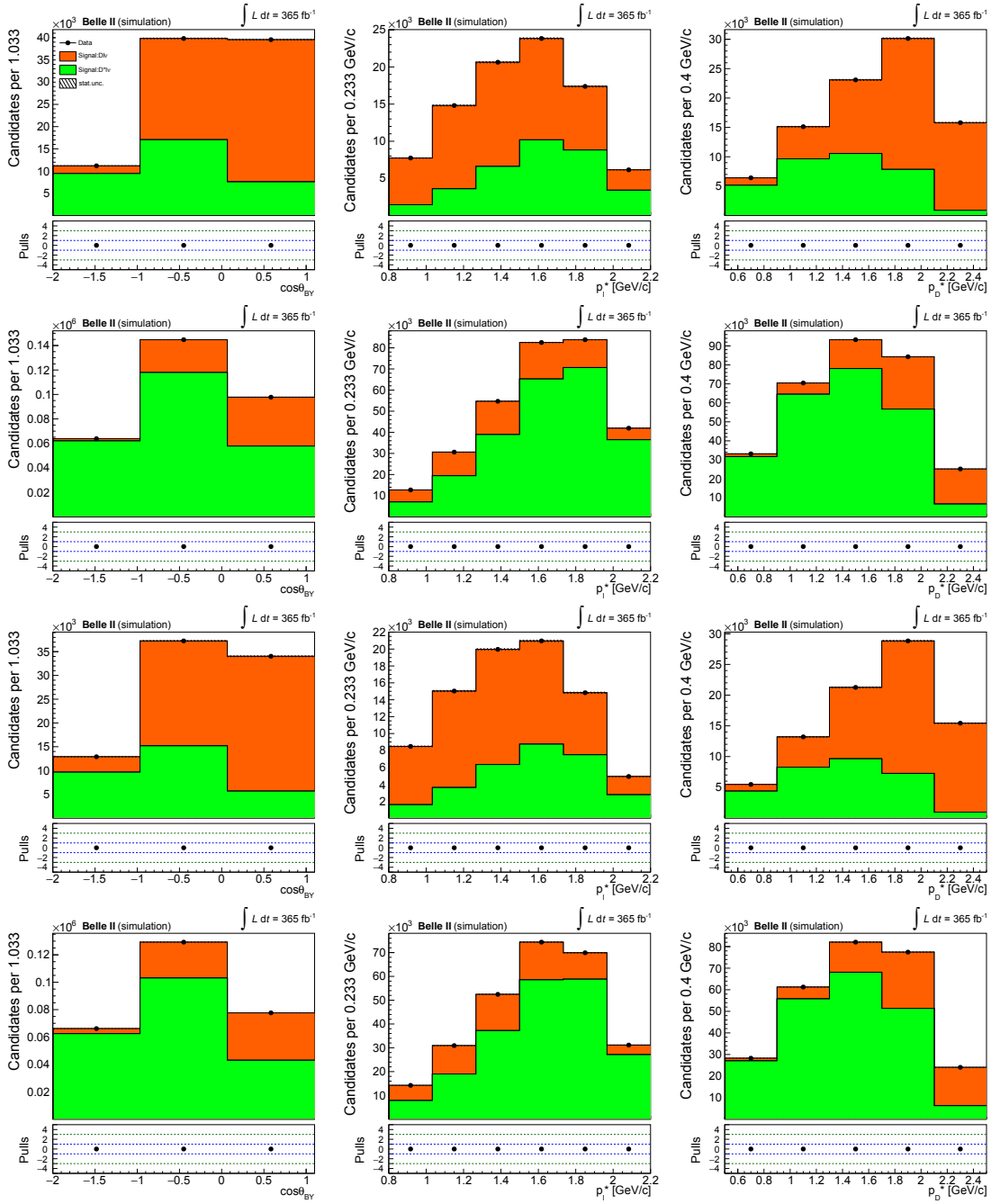


Figure C.2: Fit projections from top to bottom of  $D^- \mu^+$ ,  $\bar{D}^0 \mu^+$ ,  $D^- e^+$  and  $\bar{D}^0 e^+$  samples obtained in the fit configuration of signal only. Pulls are flat as expected for an Asimov fit.

## Appendix D

# Validation of the systematic uncertainty on the $D^{**}$ decays

From the fit conducted in the control region, I obtain results on the branching fractions of the  $D^{**}$  decays, using Gaussian penalties, which are in agreement with the latest measurements reported in Tab. 5.3, except for the branching fraction of  $B \rightarrow D^{(*)}\eta\ell\nu_\ell$  decays, which shows a large discrepancy from the expected result (see Sect. 6.3 in Chapter 6). Given this discrepancy, it is crucial to properly account for the corresponding systematic uncertainty. To address this, I perform a simultaneous fit to both the signal and control regions on three different Asimov data sets, exploring various configurations of the constraints on the  $D^{**}$  branching fractions. This allows me to assess the impact of these variations on the fit parameters and to determine whether the evaluated systematic uncertainty in the knowledge of the  $D^{**}$  decays adequately covers potential fluctuations in the fit parameters. The three configurations are reported in Tab. D.1.

Each Asimov data set is fitted using the HFLAV 2024 configuration (first column in Tab. D.1). This is done to verify whether the current constraints can accurately describe different configurations of these decays. I then analyse the results of each fit and present in Fig. D.1 the nominal values of the pulls, defined in Eq. 6.14, for the model-independent observables,  $f = f_{+-}/f_{00}$ , and the signal branching ratios. The red bands correspond to the  $1\text{-}2\sigma$  of the systematic uncertainty in the knowledge of the  $D^{**}$  decays evaluated in Chapter 7 for each fit observable. As can be seen, the assessed systematic uncertainty

Decay	Default [%]	Conf. 1) [%]	Conf. 2) [%]	Conf. 3) [%]
$\mathcal{B}(B \rightarrow D_1(2420)\ell\nu_\ell)$	$0.64 \pm 0.10$	0.75	0.55	0.80
$\mathcal{B}(B \rightarrow D_1'(2430)\ell\nu_\ell)$	$0.28 \pm 0.04$	0.30	0.40	0.40
$\mathcal{B}(B \rightarrow D_0^*(2300)\ell\nu_\ell)$	$0.13 \pm 0.19$	0.42	0.30	0.60
$\mathcal{B}(B \rightarrow D_2^*(2460)\ell\nu_\ell)$	$0.32 \pm 0.03$	0.40	0.50	0.60
$\mathcal{B}(B \rightarrow D^{(*)}\pi\pi\ell\nu_\ell)$	$0.30 \pm 0.13$	0.20	0.40	0.30
$\mathcal{B}(B \rightarrow D^{(*)}\eta\ell\nu_\ell)$	$1.80 \pm 1.80$	1.00	0.50	0.10

Table D.1: Configurations with different assumptions for the branching fractions of the  $D^{**}$  decays used to generate the Asimov data sets. The latter are fitted using the default constraints presented in the first column of the table. The branching fractions shown in the table pertain to  $B^+$  and are related to those of  $B^0$  through their lifetimes ratio.

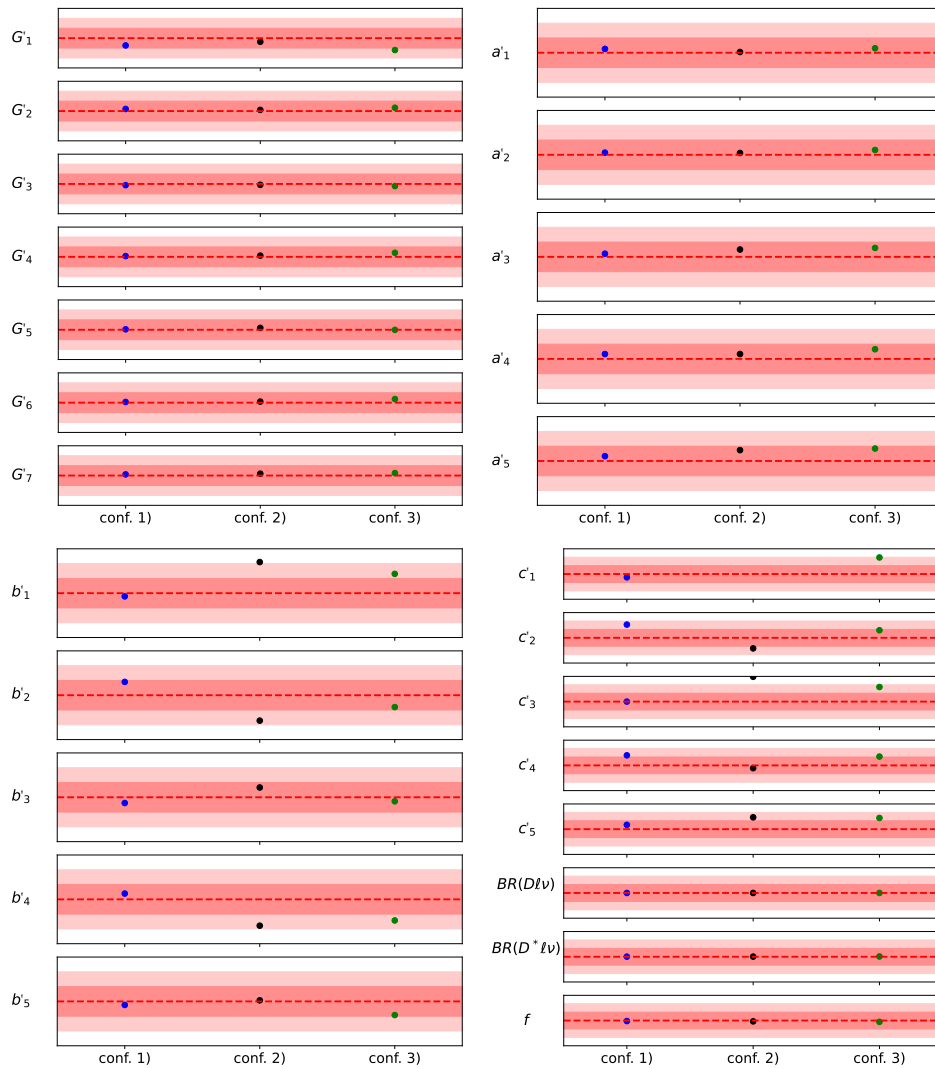


Figure D.1: Nominal values of the pulls for  $G'_m$ ,  $a'_n$ ,  $b'_n$ ,  $c'_n$ ,  $f$ , and the signal branching fractions from the three configurations in Tab. D.1. The red bands correspond to the  $1-2\sigma$  of the systematic uncertainty in the knowledge of the  $D^{**}$  decays evaluated in Chapter 7 for each fit observable.

adequately covers the potential effects of variations in these decays on the fit parameters. Only a few pulls fall outside the  $2\sigma$  range; however, given the additional statistical uncertainty, this is not a cause for concern. I do not report the pulls for  $A_{FB}$  and  $F_L^{D^*}$  because as observed in the breakdown of their uncertainties in Tab. 7.6, these observables are dominated by purely statistical effects and by the systematic uncertainties arising from the statistical uncertainties on the templates and the background modelling. The uncertainty in the knowledge of the branching fractions of the  $D^{**}$  decays is negligible as it cancels out in the ratio of the model-independent observables used to evaluate  $A_{FB}$  and  $F_L^{D^*}$  (see Eqs. 2.35-2.36). This study demonstrates that potential variations in the knowledge of the constraints for the  $D^{**}$  decays are included in the evaluated systematic uncertainty for this source.

# Appendix E

## Interpretation with the BGL and CLN parametrisations

I report the comparison between the *a posteriori* analysis of the model-independent observables, described in Chapter 8, using a BGL parametrisation, and the *direct approach*, in which the form-factor parameters are directly fitted. For this study, the comparison is made by fitting all terms of the BGL series for the  $B \rightarrow D\ell\nu_\ell$  and  $B \rightarrow D^*\ell\nu_\ell$  decays, while the higher-order terms remain fixed at their generated values, with no loss of generality in the conclusions. I demonstrate that I am able to extract the form-factor parameters and  $|V_{cb}|$  without any loss of precision compared to the *direct* approach.

I also present the *a posteriori* analysis of the model-independent observables, described in Chapter 8 and the comparison with the *direct* approach shown in Sect. E.1, using a CLN parametrisation obtaining similar conclusions to those of the BGL analysis.

### E.1 Form factors and $|V_{cb}|$ using the BGL parametrisation

I also analyse the original distributions of  $(\cos\theta_{BY}, p_\ell^*, p_D^*)$  with a three-dimensional fit, where I use directly the BGL parametrisation in the weighting technique of the signal templates (presented in Sect. 6.2.1.1). This allows to obtain  $|V_{cb}|$  and the BGL parameters directly from this fit, *i.e.*, without passing through the measurement of the model-independent observables. Hence, this fit is referred to as the *direct* approach, in contrast to the *a posteriori* fit employing the measured model-independent observables. This is done to compare the sensitivity to  $|V_{cb}|$  and the form-factor parameters between the *a posteriori* and *direct* approaches, to check if there is any loss of information in the use of the model-independent observables. I run the two approaches over 1000 toy samples. The average uncertainty between the *direct* and *a posteriori* approaches is the same in all the possible scenarios (see Tab. E.1).

I inspect for both the two approaches the pull distributions of  $|V_{cb}|$  and the BGL parameters; they are generally unbiased normal Gaussian. Pulls distributions are reported in Appendix F (see Figs. F.5-F.7 and Figs. F.9-F.11). This proves that the model-independent observables encode all information necessary for the determination of  $|V_{cb}|$  and the form-factor parameters.

To summarise, I demonstrated the reliability of the extraction of  $|V_{cb}|$  and the BGL parameters using the model-independent observables. I also carry out a similar analysis using the CLN parametrisation, presented in Sect. E.2: I obtain the similar conclusions as reported here.

APPENDIX E. INTERPRETATION WITH THE BGL AND CLN  
PARAMETRISATIONS

Fit type	$\sigma(a_1^{f+})$	$\sigma(a_1^f)$	$\sigma(a_0^g)$	$\sigma(a_1^g)$	$\sigma(a_1^{F1})$	$\sigma(h_{A_1}(1))$	$\sigma(\mathcal{G}(1))$	$\sigma(V_{cb})[10^{-3}]$
direct 1)	0.001	0.011	0.001	0.041	0.0004	0.009	0.008	0.37
a posteriori 1)	0.001	0.010	0.001	0.038	0.0004	0.009	0.008	0.36
direct 2)	0.001	0.011	0.001	0.043	0.0004	0.013	0.009	0.45
a posteriori 2)	0.001	0.011	0.001	0.040	0.0004	0.013	0.009	0.44
direct 3)	0.001	0.011	0.001	0.044	0.0004	0.013	0.019	0.66
a posteriori 3)	0.001	0.011	0.001	0.041	0.0004	0.013	0.019	0.64

Table E.1: Comparison of the average uncertainties of  $|V_{cb}|$  and the BGL parameters between the *direct* and *a posteriori* approaches from 1000 toy samples. The results in the table are shown for all the scenarios. The sensitivity to the parameters are the same between the two approaches.

## E.2 Form factors and $|V_{cb}|$ using the CLN parametrisation

I repeat the analysis of the form factors and  $|V_{cb}|$ , described in Sect. 8.1, using the CLN parametrisation, reaching similar conclusions as those presented for the BGL analysis. I generate the signal samples using the CLN form-factor parameters reported in Tab. E.2 and I construct an Asimov data set in the same configuration of that explained in the Sect. 6.4. The CLN form-factor parameters are:  $\rho_D^2$  and  $\mathcal{G}(1)$  for  $B \rightarrow D\ell\nu_\ell$ ; and  $\rho_{D^*}^2$ ,  $h_{A_1}(1)$ ,  $R_1(1)$ ,  $R_2(1)$  for  $B \rightarrow D^*\ell\nu_\ell$ .

CLN	$\rho_D^2$	$\rho_{D^*}^2$	$R_1(1)$	$R_2(1)$	$\mathcal{G}(1)$	$h_{A_1}(1)$	$ V_{cb}  [10^{-3}]$
Generator values	1.128	1.23	1.34	0.83	1.054	0.902	41.4

Table E.2: Generator values of  $|V_{cb}|$  and CLN form-factor parameters used in the generation of the signal sample.

I perform a  $\chi^2$  fit on the 22 model-independent observables obtained from the Asimov fit using the Eq. 8.1 assuming the CLN model for the form factors. This allows to extract  $|V_{cb}|$  and the CLN form-factor parameters. For this test, I use the covariance matrix that includes only the statistical uncertainties.

The form factors values at zero recoil used in the generation of the sample are:  $\mathcal{G}(1) = 1.054 \pm 0.009$  and  $h_{A_1}(1) = 0.902 \pm 0.013$ . These values are included as nuisance parameters, constrained by Gaussian penalties in the fits across the various scenarios explained in Sect. 8.1. In all scenarios, I obtain values consistent with those generated.

In scenario 1, I observe that the uncertainties on the Gaussian-constrained parameters,  $h_{A_1}(1)$  and  $\mathcal{G}(1)$ , are reduced when fitting the model-independent observables. Specifically, the uncertainty on  $h_{A_1}(1)$  decreases from 0.013 to about 0.009, while the uncertainty on  $\mathcal{G}(1)$  decreases from 0.009 to 0.008. In this study, using the CLN parametrisation, the data provide more information on the lattice points, particularly on  $h_{A_1}(1)$ , due to the smaller number of parameters employed compared to the BGL parametrisation (described in the Sect. 8.1) and the absence of assumptions regarding the truncation of the series. In particular,  $|V_{cb}|$  is sufficiently constrained by the  $B \rightarrow D\ell\nu_\ell$  observables and the external input  $\mathcal{G}(1)$ , allowing for the  $h_{A_1}(1)$  determination from the product  $|V_{cb}|h_{A_1}(1)$  with an uncertainty of about 0.012.

To test for any possible biases, I run the full analysis from the measurements of the

APPENDIX E. INTERPRETATION WITH THE BGL AND CLN  
PARAMETRISATIONS

Fit scenario	$\sigma(\rho_D^2)$	$\sigma(\rho_{D^*}^2)$	$\sigma(R_1(1))$	$\sigma(R_2(1))$	$\sigma(h_{A_1}(1))$	$\sigma(\mathcal{G}(1))$	$\sigma(V_{cb})[10^{-3}]$
direct 1)	0.013	0.037	0.054	0.037	0.009	0.008	0.37
a posteriori 1)	0.013	0.035	0.054	0.036	0.009	0.008	0.36
direct 2)	0.015	0.037	0.056	0.037	0.012	0.009	0.48
a posteriori 2)	0.015	0.036	0.055	0.036	0.012	0.009	0.47
direct 3)	0.015	0.037	0.056	0.037	0.013	0.019	0.63
a posteriori 3)	0.015	0.036	0.055	0.036	0.013	0.018	0.62

Table E.3: Comparison of the average uncertainties of  $|V_{cb}|$  and the BGL parameters between the *direct* and *a posteriori* approaches from 1000 toy samples. The results in the table are shown for all the scenarios. The sensitivity to the parameters are the same between the two approaches.

model-independent observables on 1000 toy samples. The *a posteriori* fit is then performed for each scenario using the 1000 results, including their covariances, of the model-independent observables.

To compare the sensitivity of  $|V_{cb}|$  and the CLN form-factor parameters, I also run the *direct* fit and across 1000 toy samples for the three scenarios. The average uncertainty between the two approaches is the same in the three possible scenarios as shown in Tab. E.3. I also inspect the pull (defined in Eq. 6.15) distributions of  $|V_{cb}|$  and the CLN form-factor parameters for both the two approaches and observed that they are generally unbiased normal Gaussian. Pulls distributions are reported in Appendix F (see Figs. F.16-F.18 and Figs. F.20-F.22).

With this study, I validate the conclusions obtained in the Sect. 8.1.1 and Appendix E.1, using a different form-factor parametrisation.



# Appendix F

## Pull distributions

This appendix summarises all the pull distributions obtained from the toy studies conducted in this thesis, starting with those for the Asimov fit, followed by those for the *direct* and *a posteriori* fits using both the CLN and BGL parametrisations.

### F.1 Asimov fit

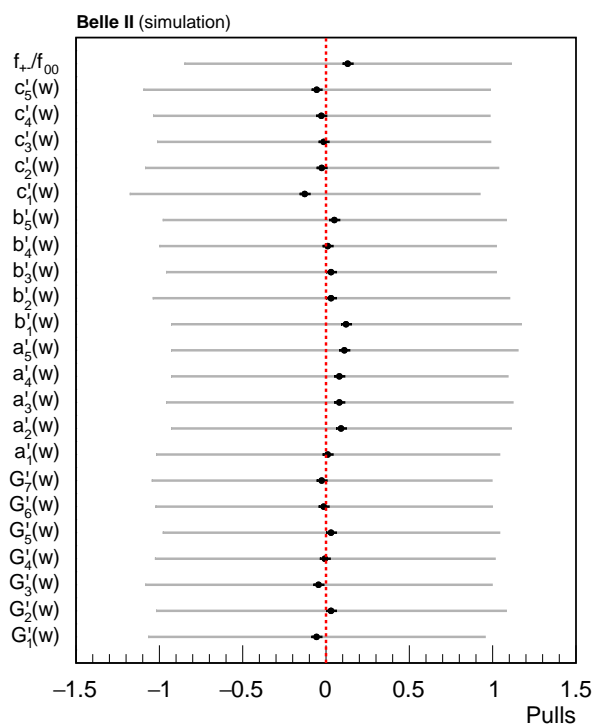


Figure F.1: Summary of the pull analysis for the model-independent observables and  $f_{+-}/f_{00}$  measured in the fit configuration of signal only to 1000 toy samples. The black points are the pull means, the black bars the uncertainties on the means, and the grey bars are the pull standard deviations. Each individual pull distribution can be found in the Fig. F.2.

## APPENDIX F. PULL DISTRIBUTIONS

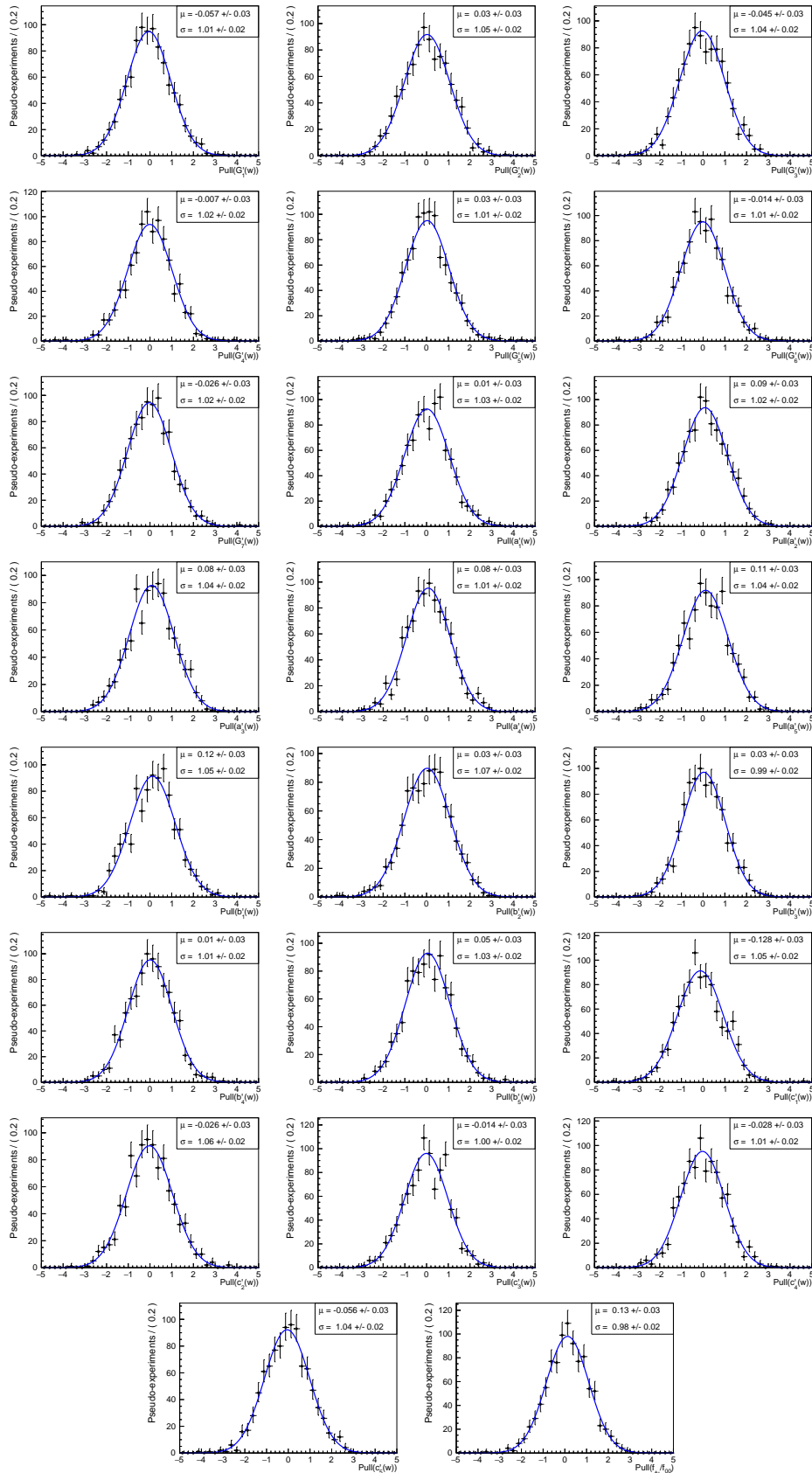


Figure F.2: Pull distributions of the model-independent observables and  $f_{+-}/f_{00}$  from 1000 toy samples in the fit configuration of signal only. Summary of the pull distributions can be found in Fig. F.1

## APPENDIX F. PULL DISTRIBUTIONS

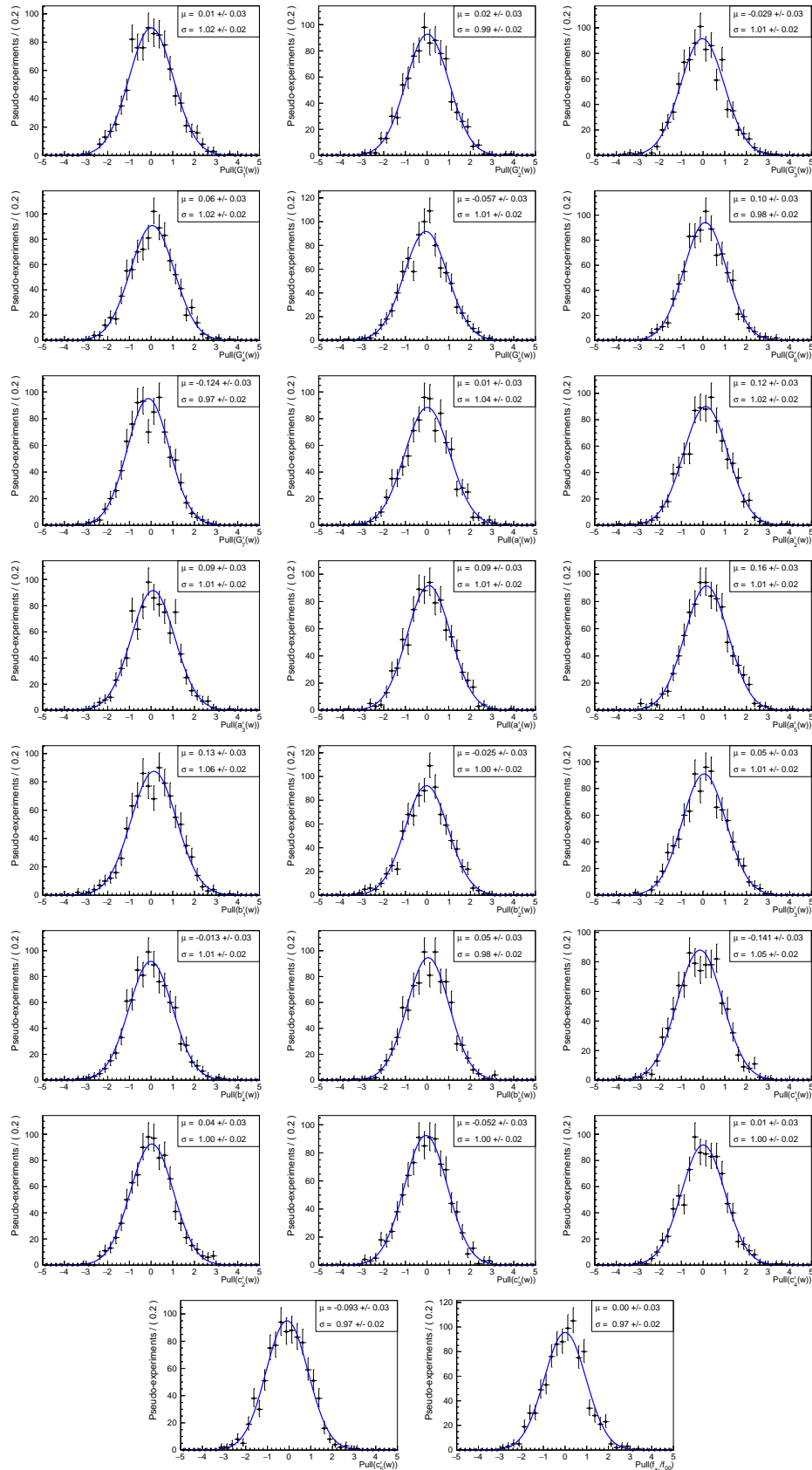


Figure F.3: Pull distributions of the model-independent observables and  $f_{+-}/f_{00}$  from 1000 toy samples in the configuration of the simultaneous fit between the signal and control regions. Summary of the pull distributions can be found in Fig. 6.14.

## F.2 Direct fit (BGL parametrisation)

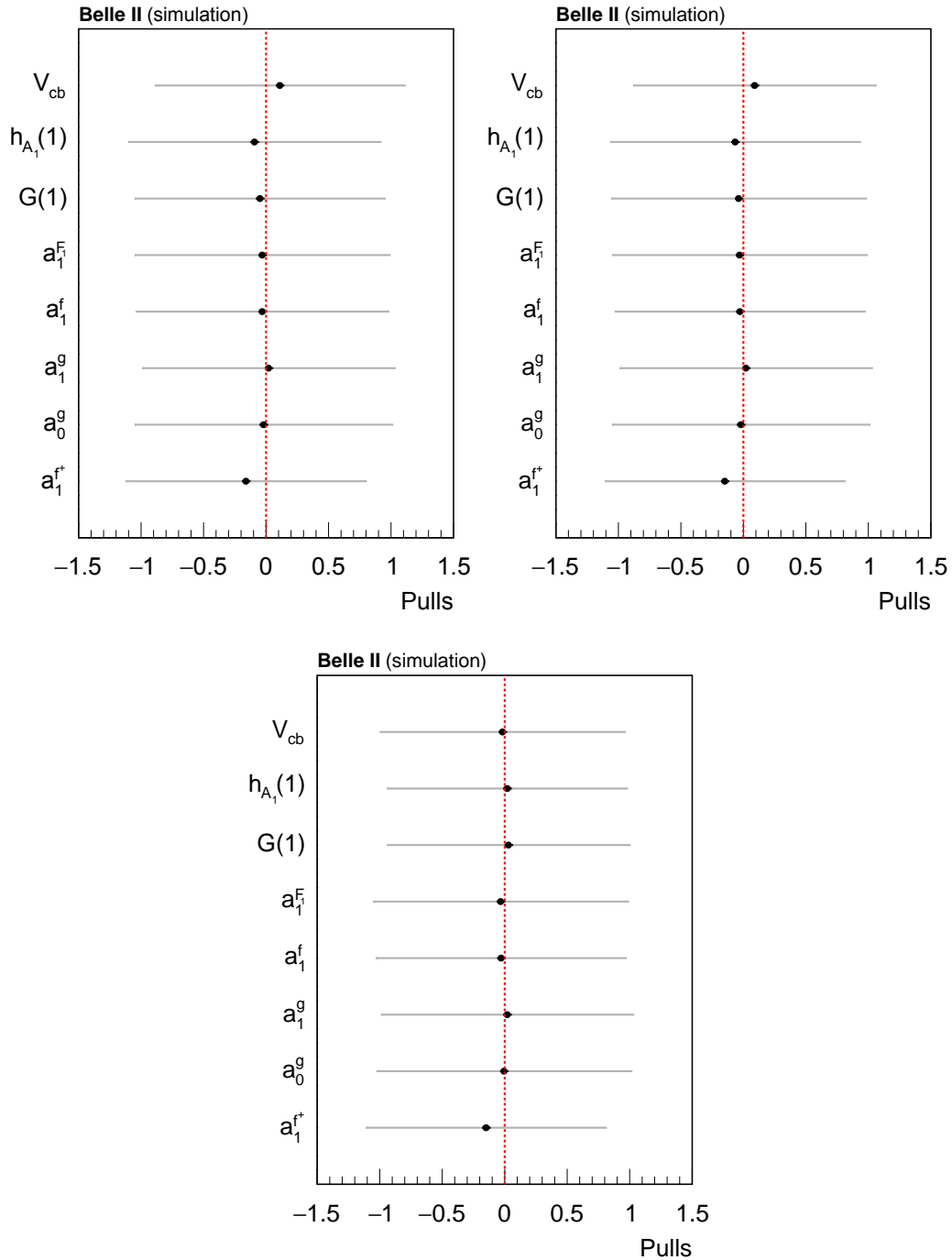


Figure F.4: Summary of the pull analysis for  $|V_{cb}|$  and the BGL parameters in the *direct* fit to 1000 toy samples of the model-independent observables: (top left) scenario 1, (top right) 2, and (bottom) 3. The black points are the pull means, the black bars the uncertainties on the means, and the grey bars are the pull standard deviations. Each pull distribution of the three scenarios can be found in Fig. F.5-F.7.

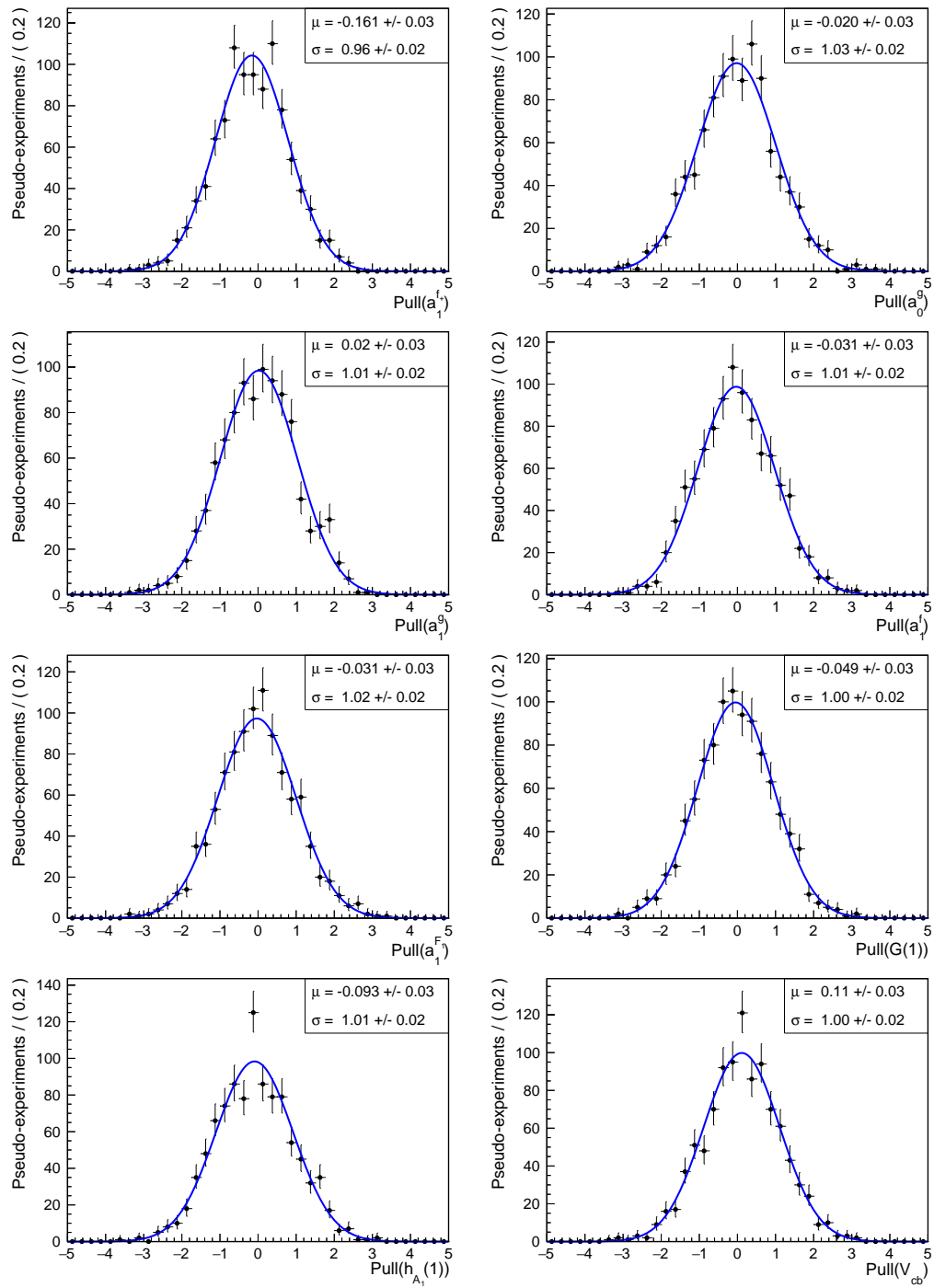


Figure F.5: Pull distributions of  $|V_{cb}|$  and the BGL form-factor parameters from 1000 toy samples obtained for the *direct* fit in scenario 1. Summary of the pull distributions can be found in Fig. F.4.

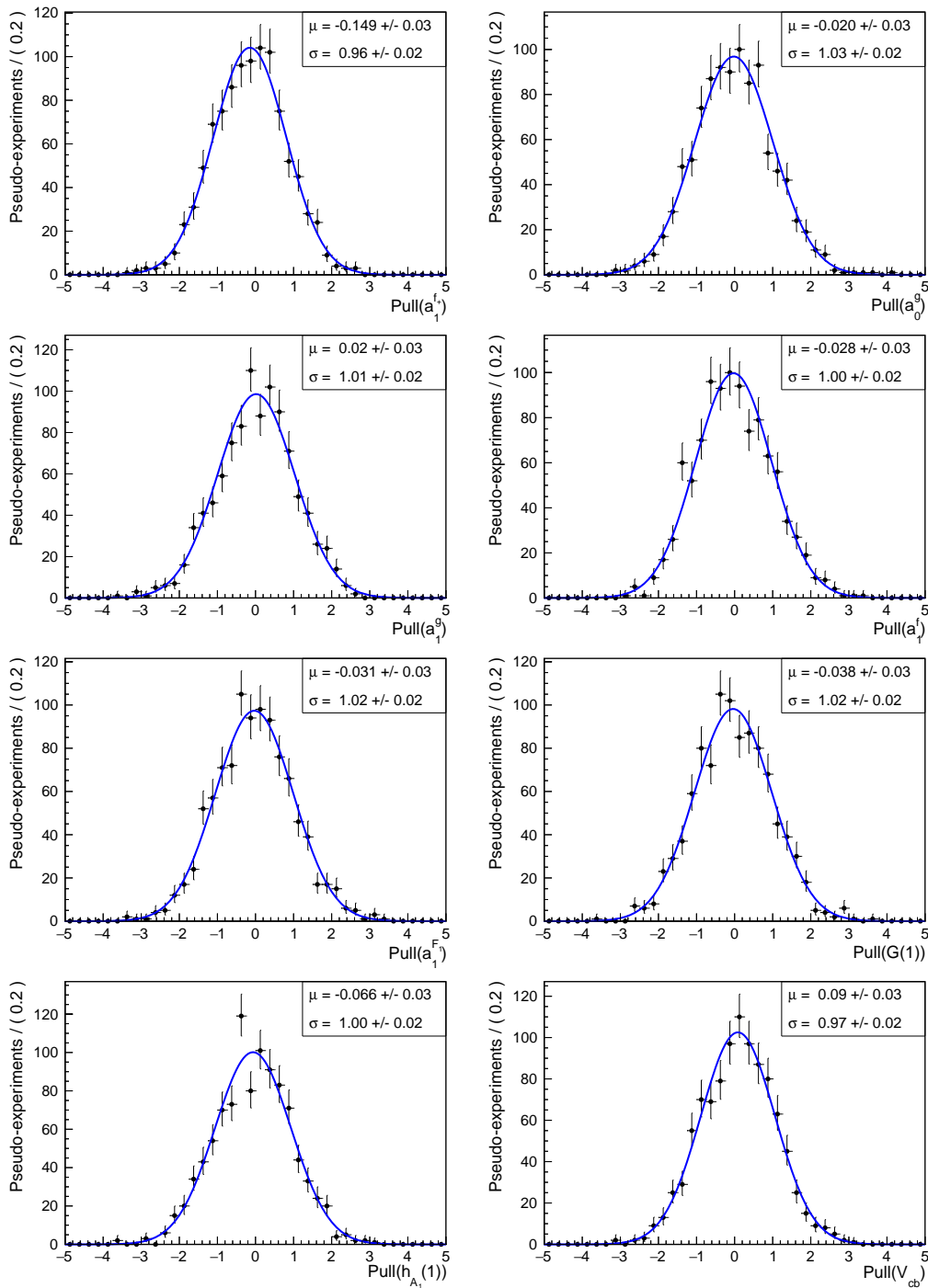


Figure F.6: Pull distributions of  $|V_{cb}|$  and the BGL form-factor parameters from 1000 toy samples obtained for the *direct* fit in scenario 2. Summary of the pull distributions can be found in Fig. F.4.

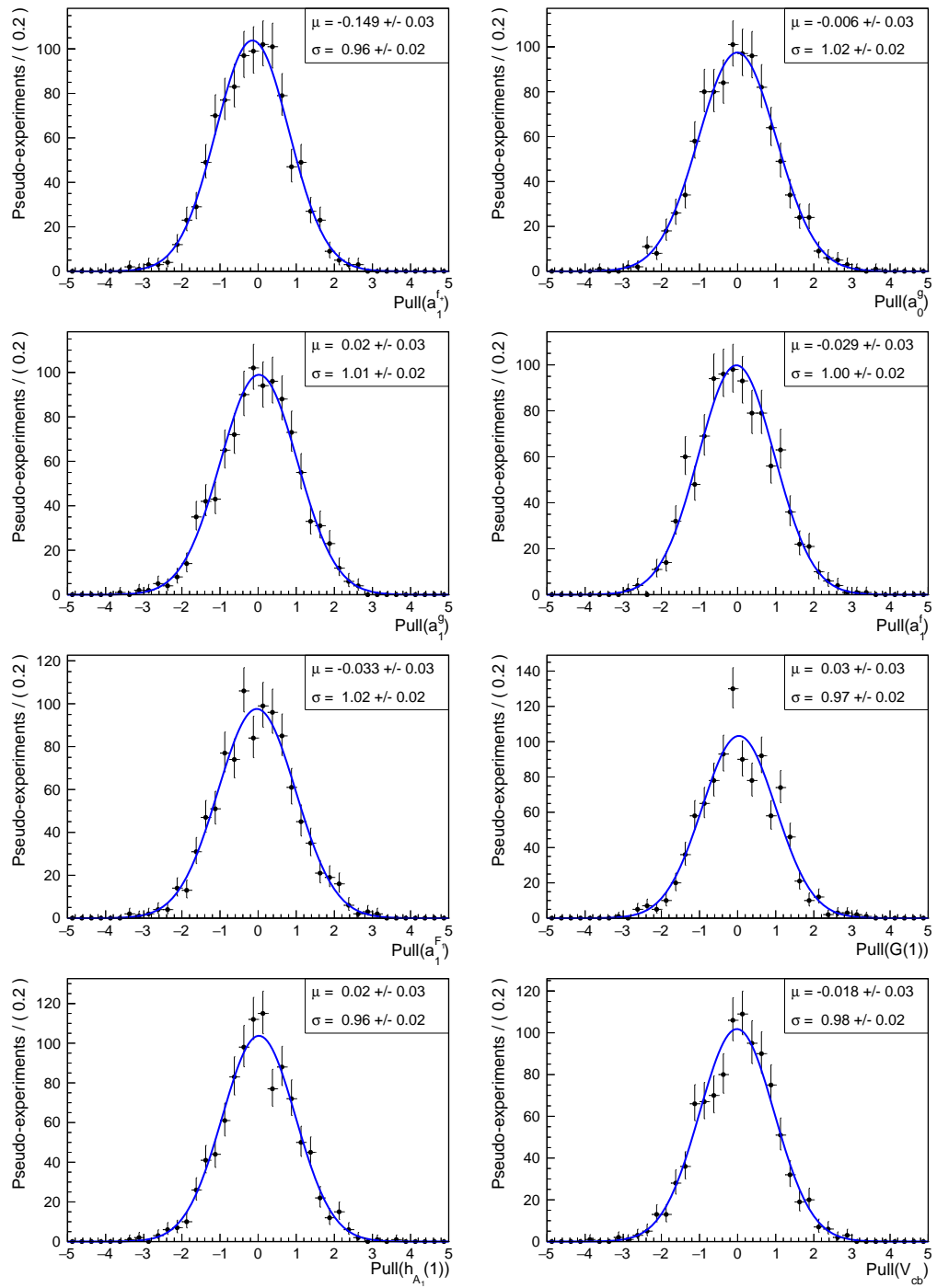


Figure F.7: Pull distributions of  $|V_{cb}|$  and the BGL form-factor parameters from 1000 toy samples obtained for the *direct* fit in scenario 3. Summary of the pull distributions can be found in Fig. F.4.

## F.3 A posteriori fit (BGL parametrisation)

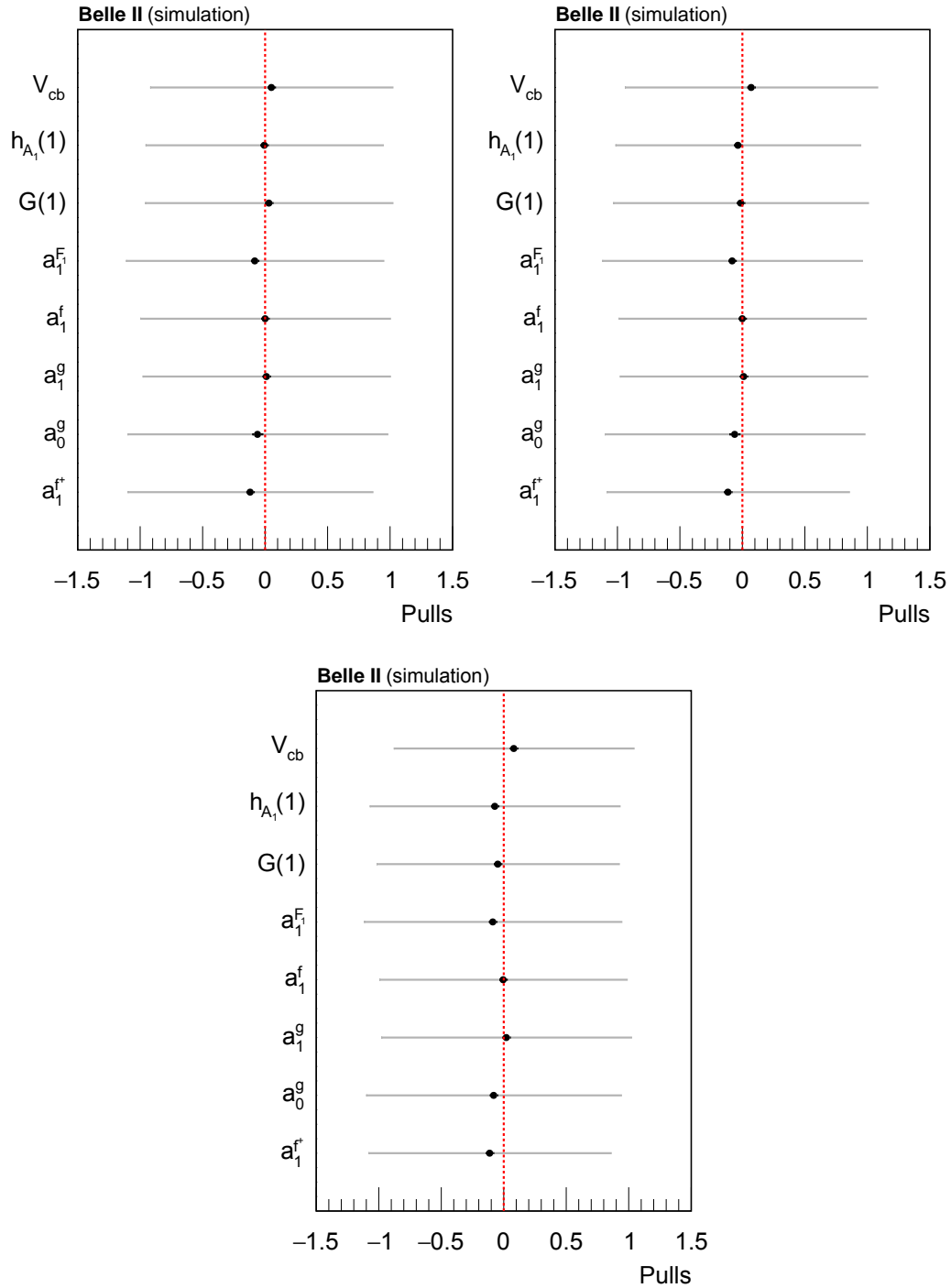


Figure F.8: Summary of the pull analysis for  $|V_{cb}|$  and the BGL parameters in the *a posteriori* fit to 1000 toy samples of the model-independent observables: (top left) scenario 1, (top right) 2, and (bottom) 3. The black points are the pull means, the black bars the uncertainties on the means, and the grey bars are the pull standard deviations. Each pull distribution of the three scenarios can be found in Fig. F.9-F.11.

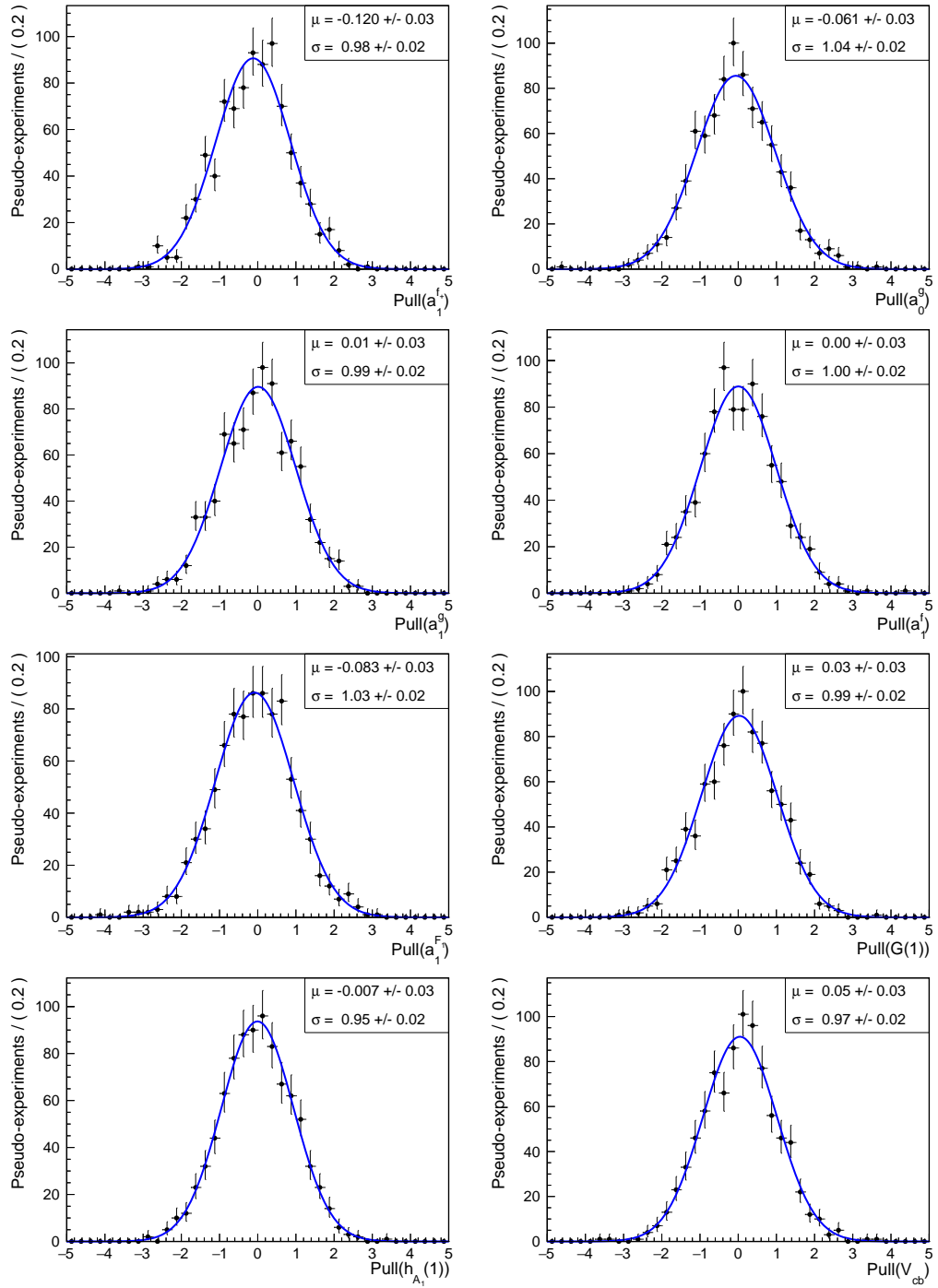


Figure F.9: Pull distributions of  $|V_{cb}|$  and the BGL form-factor parameters from 1000 toy samples obtained for the *a posteriori* fit in scenario 1. Summary of the pull distributions can be found in Fig. F.8.

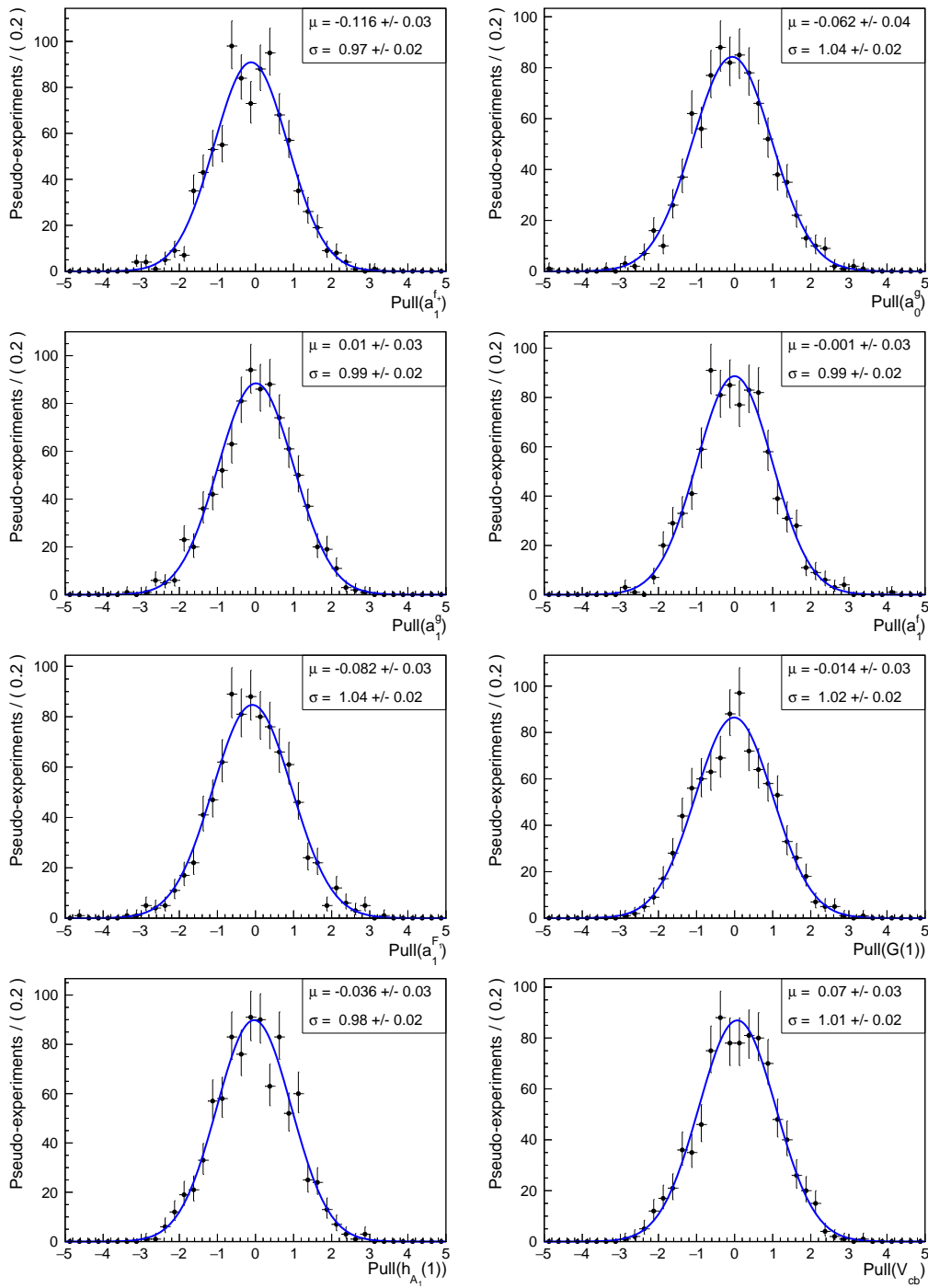


Figure F.10: Pull distributions of  $|V_{cb}|$  and the BGL form-factor parameters from 1000 toy samples obtained for the *a posteriori* fit in scenario 2. Summary of the pull distributions can be found in Fig. F.8.

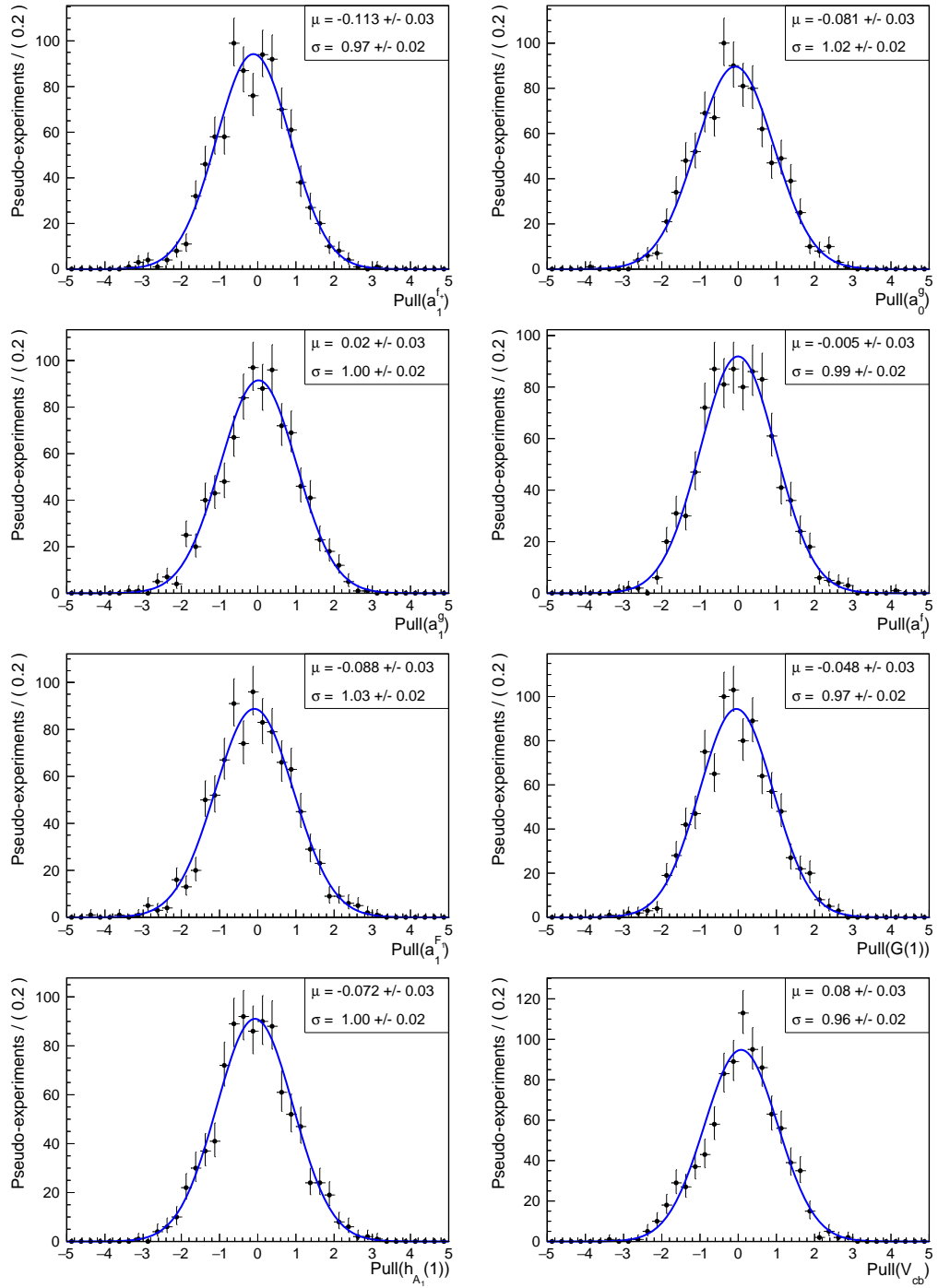


Figure F.11: Pull distributions of  $|V_{cb}|$  and the BGL form-factor parameters from 1000 toy samples obtained for the *a posteriori* fit in scenario 3. Summary of the pull distributions can be found in Fig. F.8.

## F.4 A posteriori fit (BGL parametrisation): configuration 2

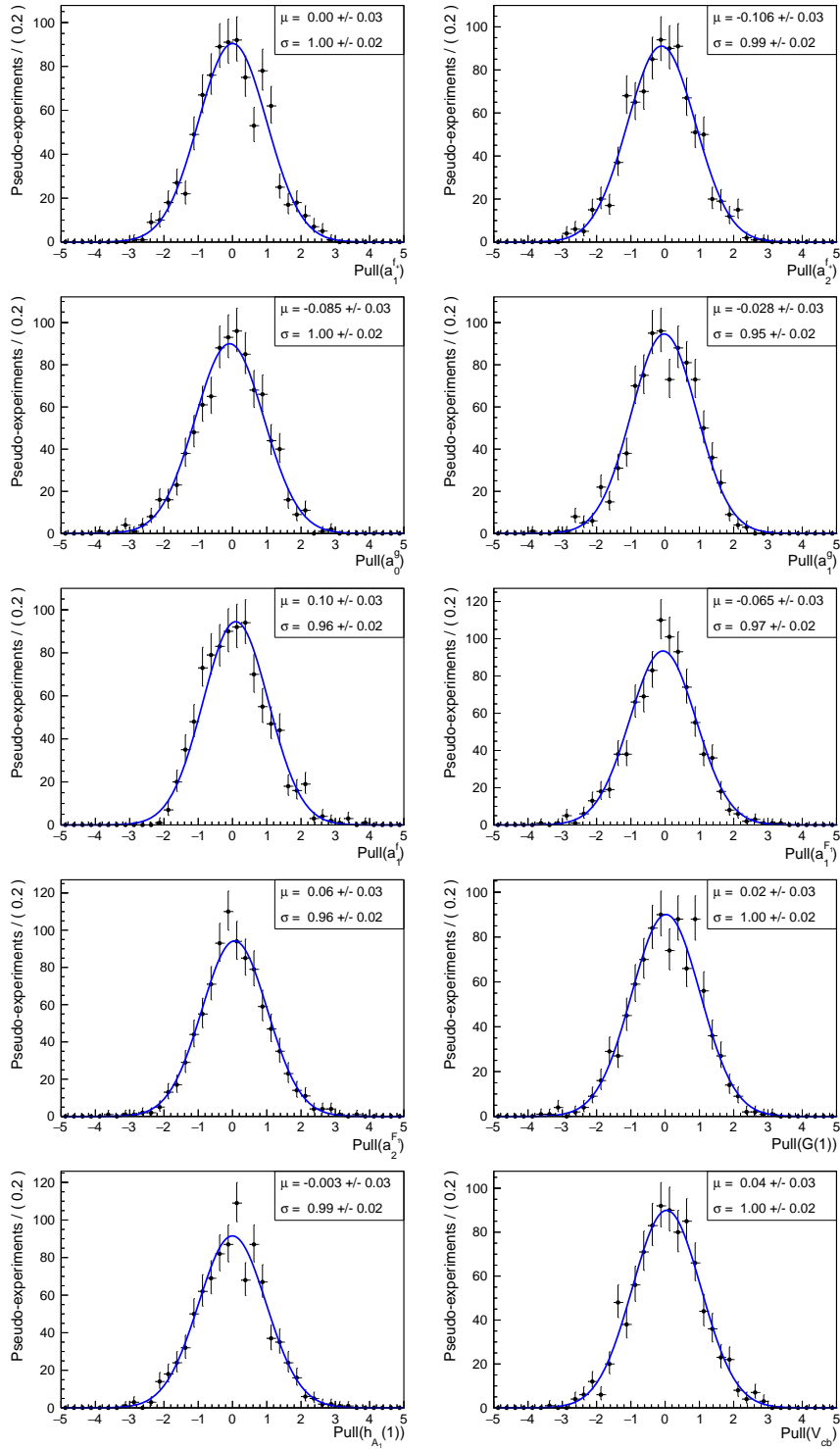


Figure F.12: Pull distributions of  $|V_{cb}|$  and the BGL form-factor parameters from 1000 toy samples obtained for the *a posteriori* fit in configuration 2 (scenario 1). Summary of the pull distributions can be found in Fig. 8.2 in Chapter 8.

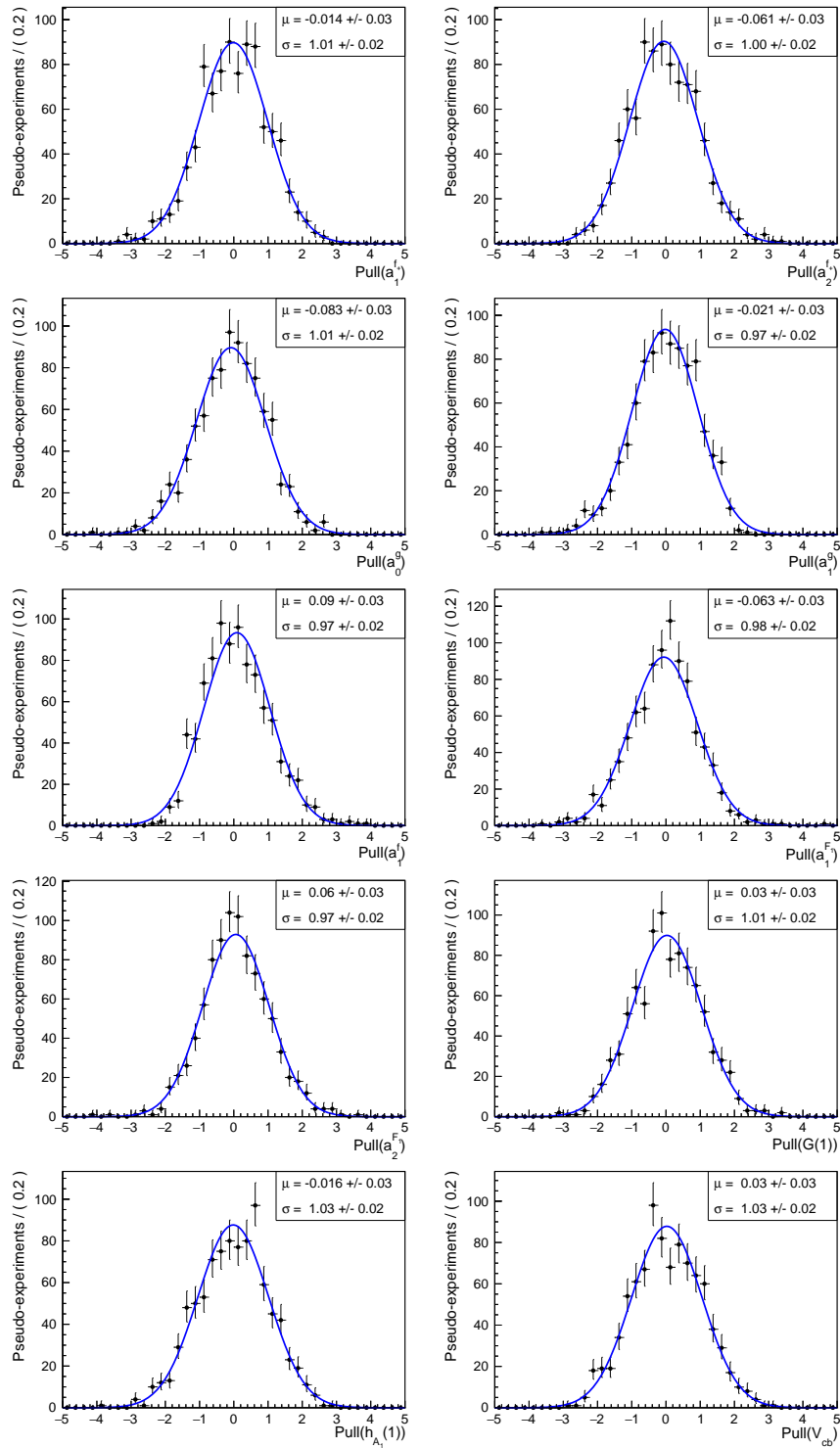


Figure F.13: Pull distributions of  $|V_{cb}|$  and the BGL form-factor parameters from 1000 toy samples obtained for the *a posteriori* fit in configuration 2 (scenario 2). Summary of the pull distributions can be found in Fig. 8.2 in Chapter 8.

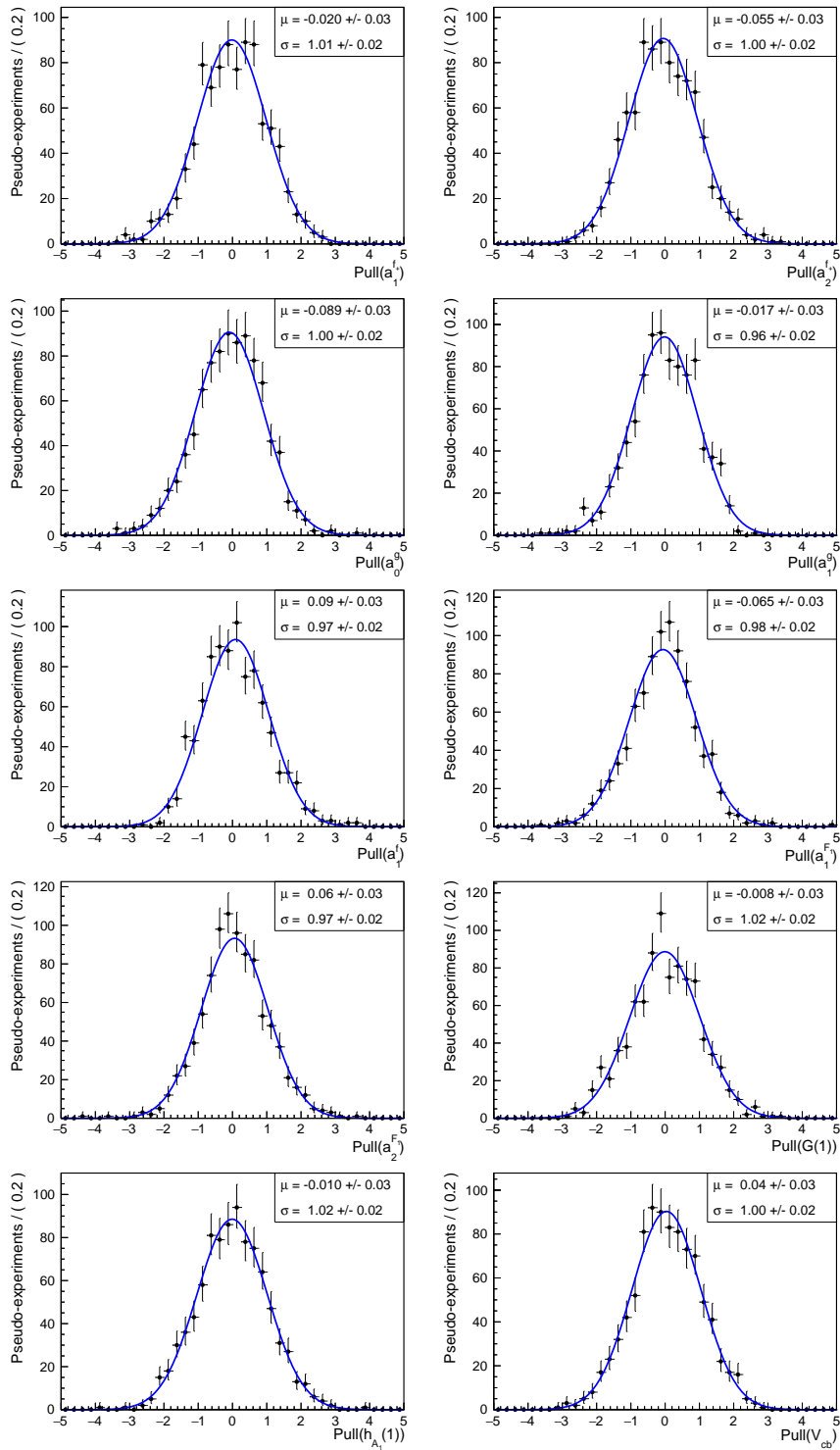


Figure F.14: Pull distributions of  $|V_{cb}|$  and the BGL form-factor parameters from 1000 toy samples obtained for the *a posteriori* fit in configuration 2 (scenario 3). Summary of the pull distributions can be found in Fig. 8.2 in Chapter 8.

## F.5 Direct fit (CLN parametrisation)

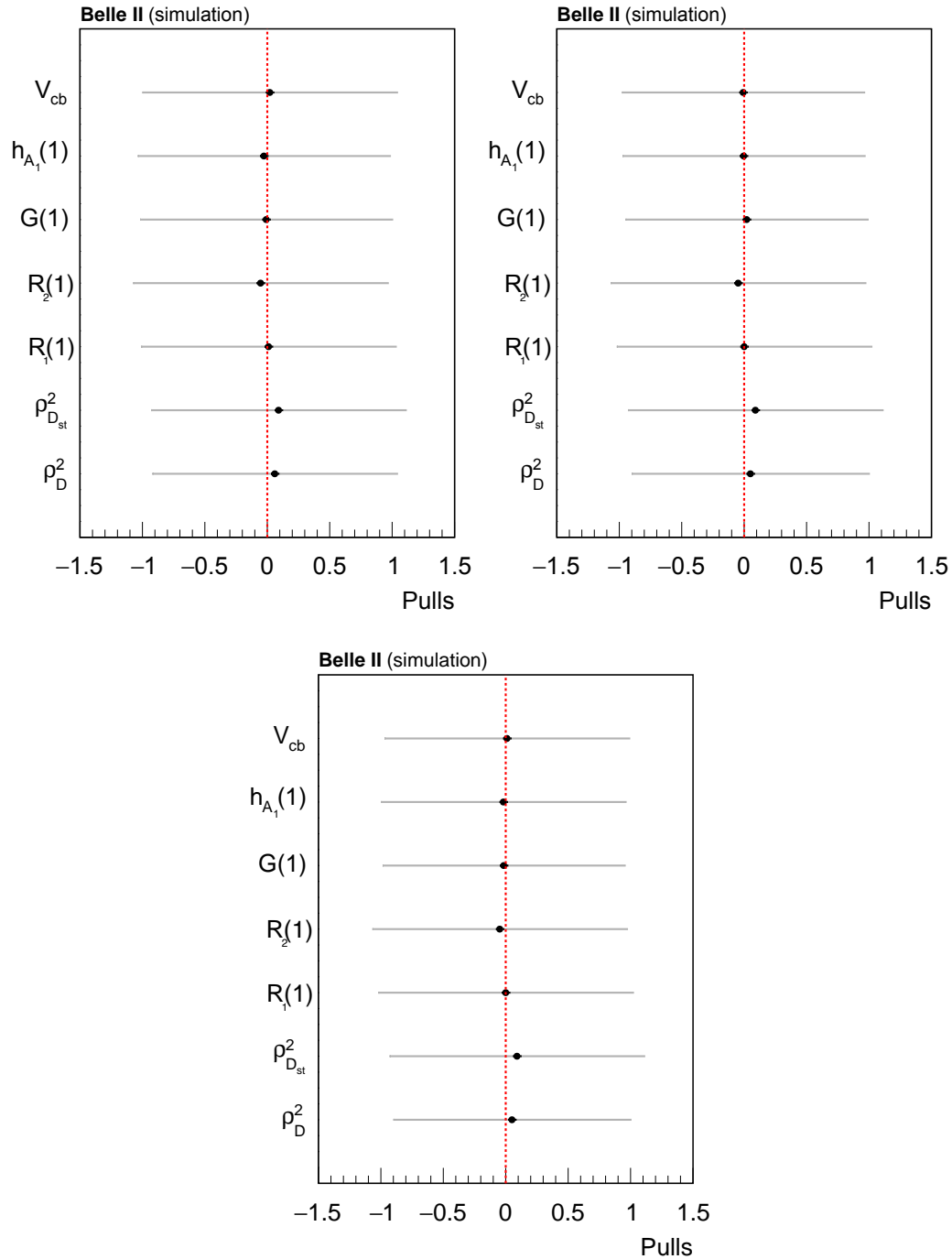


Figure F.15: Summary of the pull analysis for  $|V_{cb}|$  and the CLN parameters in the *direct* fit to 1000 toy samples of the model-independent observables: (top left) scenario 1, (top right) 2, and (bottom) 3. The black points are the pull means, the black bars the uncertainties on the means, and the grey bars are the pull standard deviations. Each pull distribution of the three scenarios can be found in Fig. F.16-F.18.

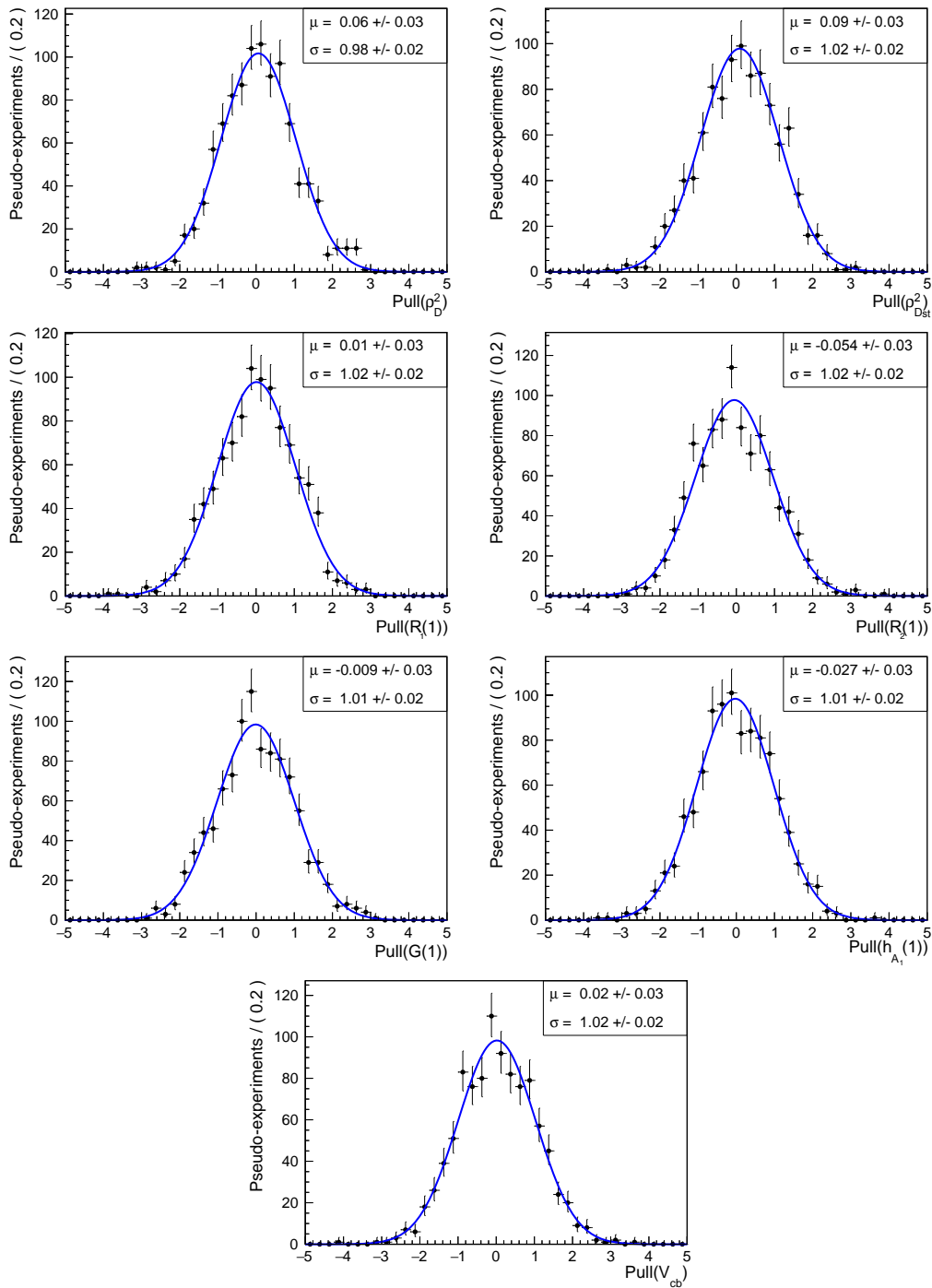


Figure F.16: Pull distributions of  $|V_{cb}|$  and the CLN form-factor parameters from 1000 toy samples obtained for the *direct* fit in scenario 1. Summary of the pull distributions can be found in Fig. F.15.

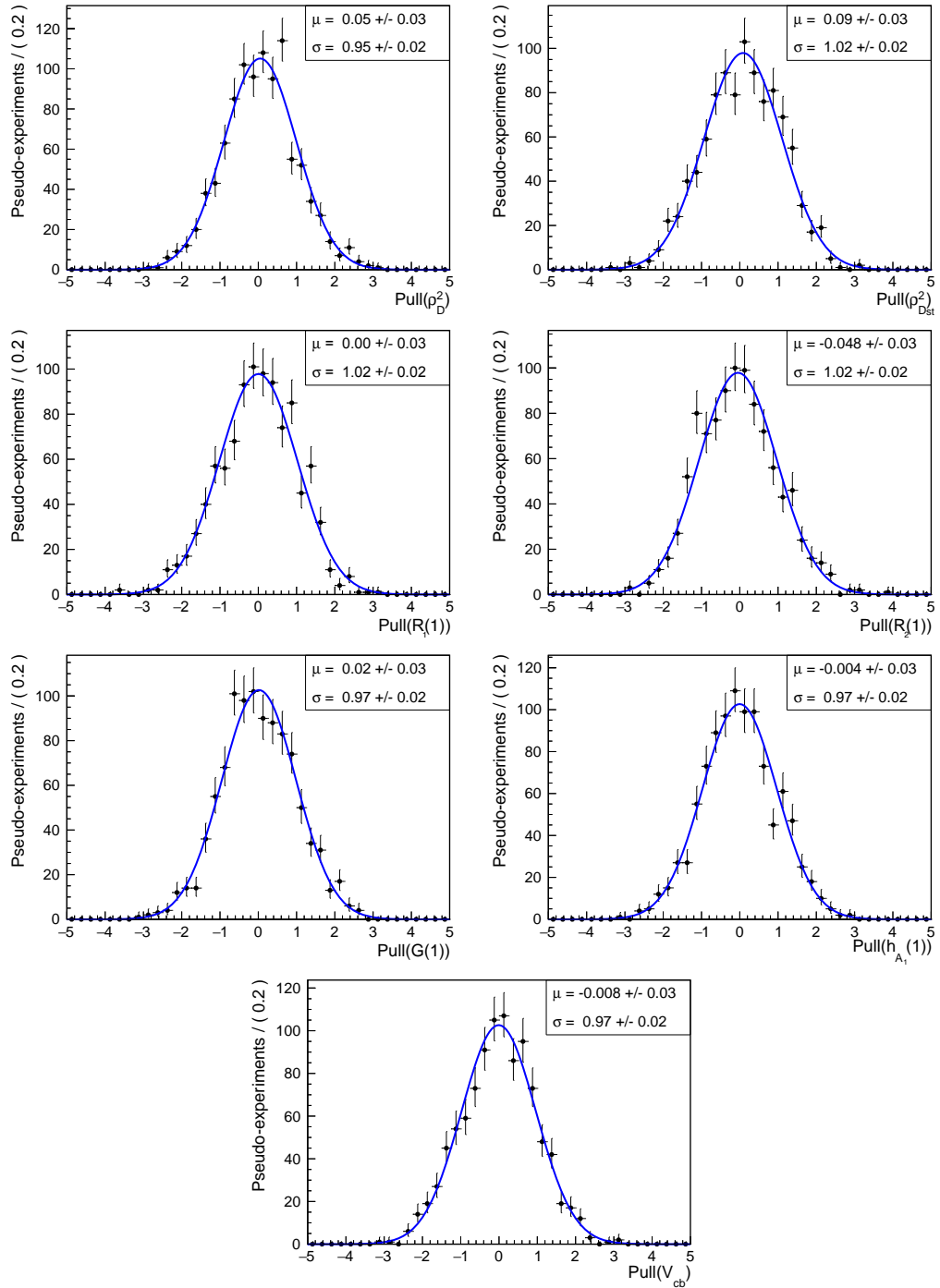


Figure F.17: Pull distributions of  $|V_{cb}|$  and the CLN form-factor parameters from 1000 toy samples obtained for the *direct* fit in scenario 2. Summary of the pull distributions can be found in Fig. F.15.

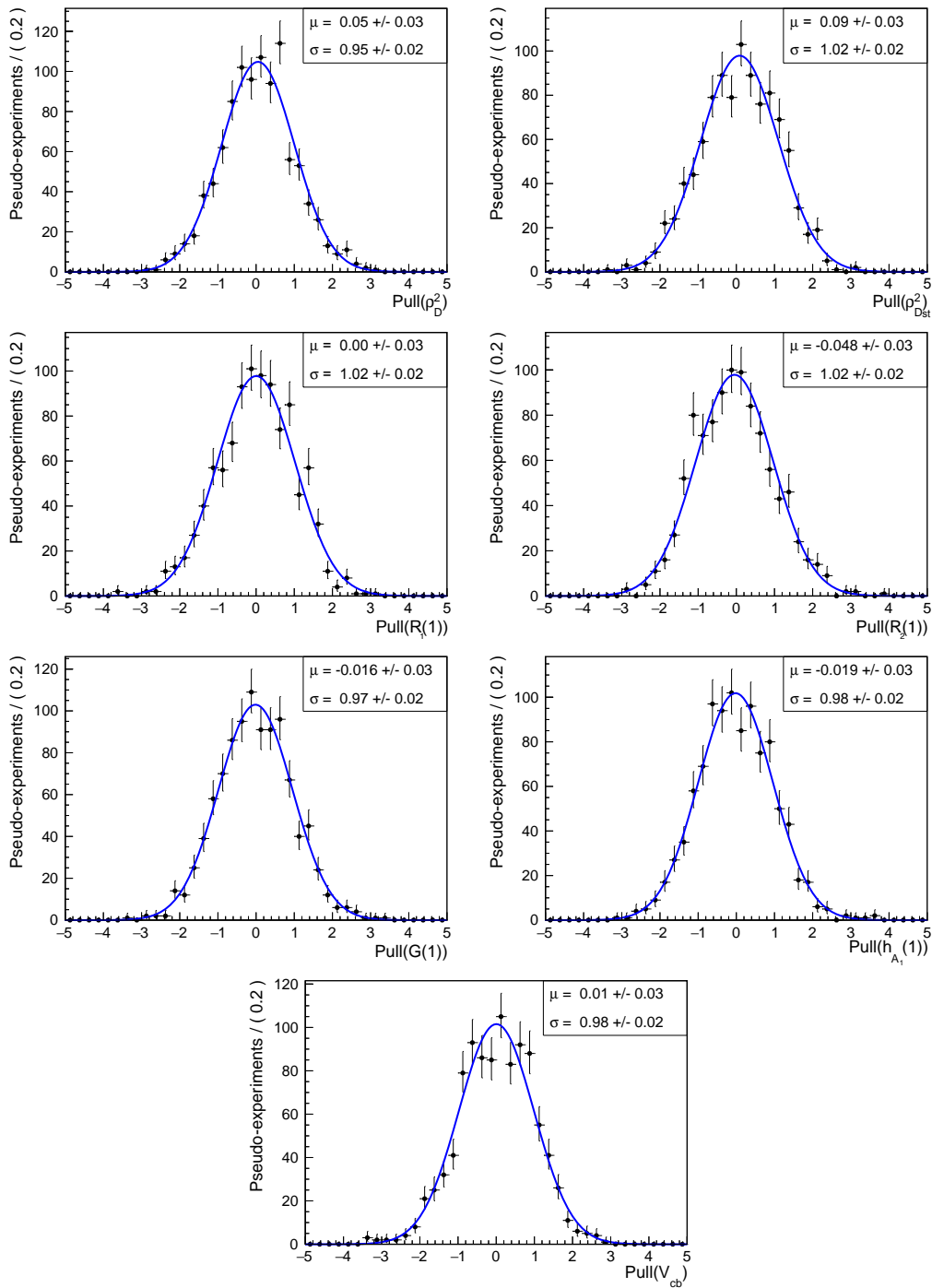


Figure F.18: Pull distributions of  $|V_{cb}|$  and the CLN form-factor parameters from 1000 toy samples obtained for the *direct* fit in scenario 3. Summary of the pull distributions can be found in Fig. F.15.

## F.6 A posteriori fit (CLN parametrisation)

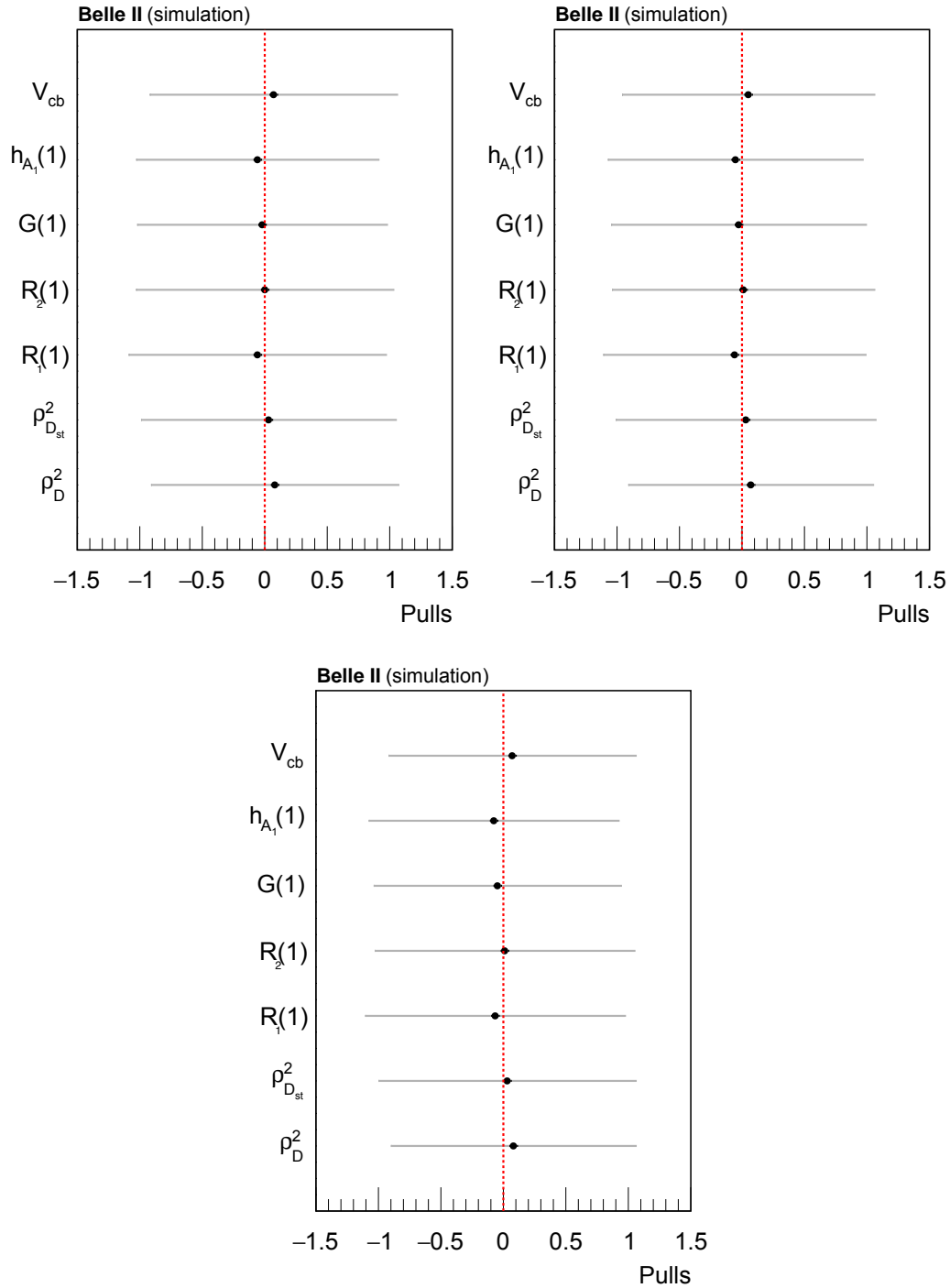


Figure F.19: Summary of the pull analysis for  $|V_{cb}|$  and the CLN parameters in the *a posteriori* fit to 1000 toy samples of the model-independent observables: (top left) scenario 1, (top right) 2, and (bottom) 3. The black points are the pull means, the black bars the uncertainties on the means, and the grey bars are the pull standard deviations. Each pull distribution of the three scenarios can be found in Fig. F.20-F.22.

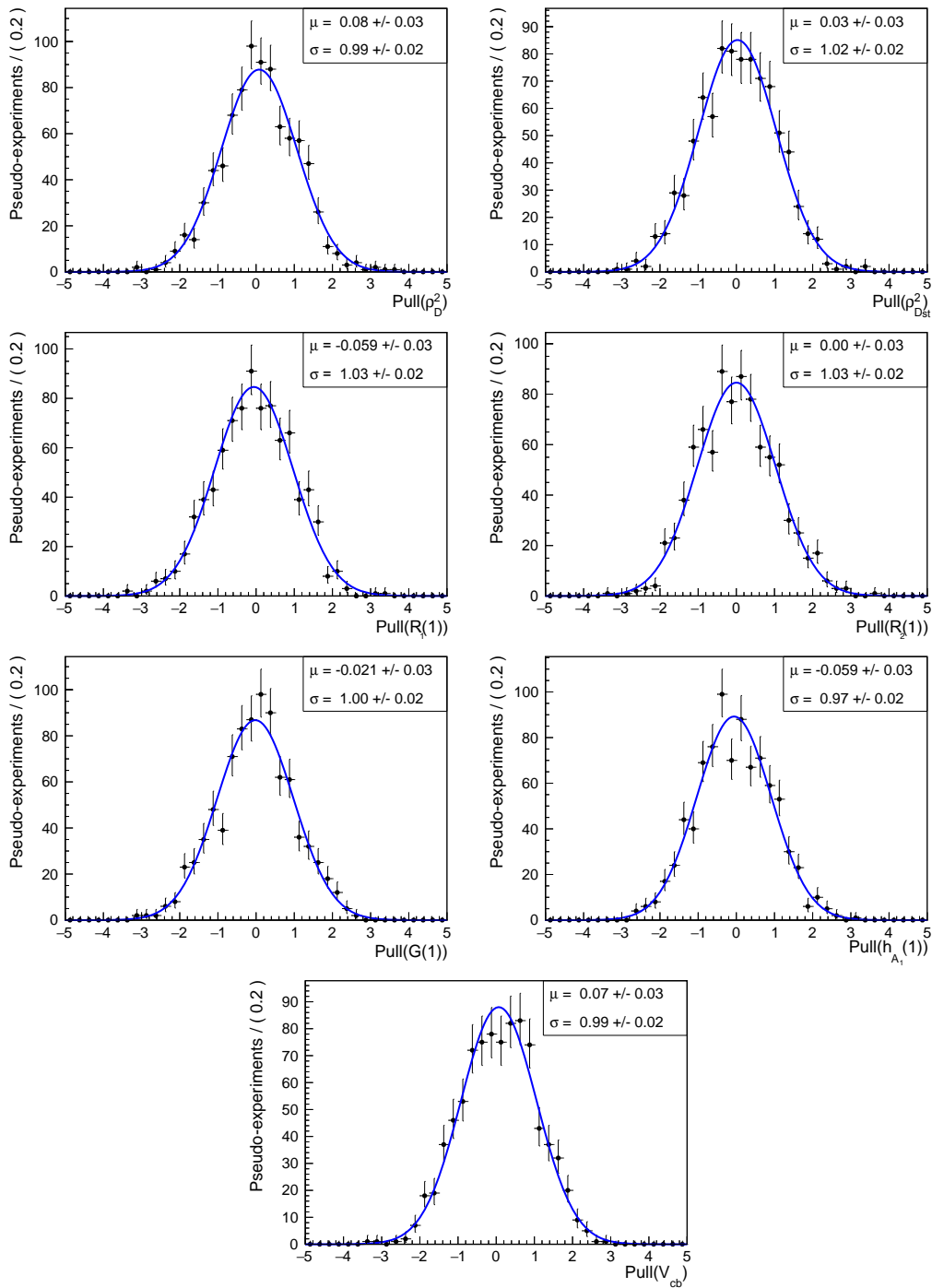


Figure F.20: Pull distributions of  $|V_{cb}|$  and the CLN form-factor parameters from 1000 toy samples obtained for the *a posteriori* fit in scenario 1. Summary of the pull distributions can be found in Fig. F.19.

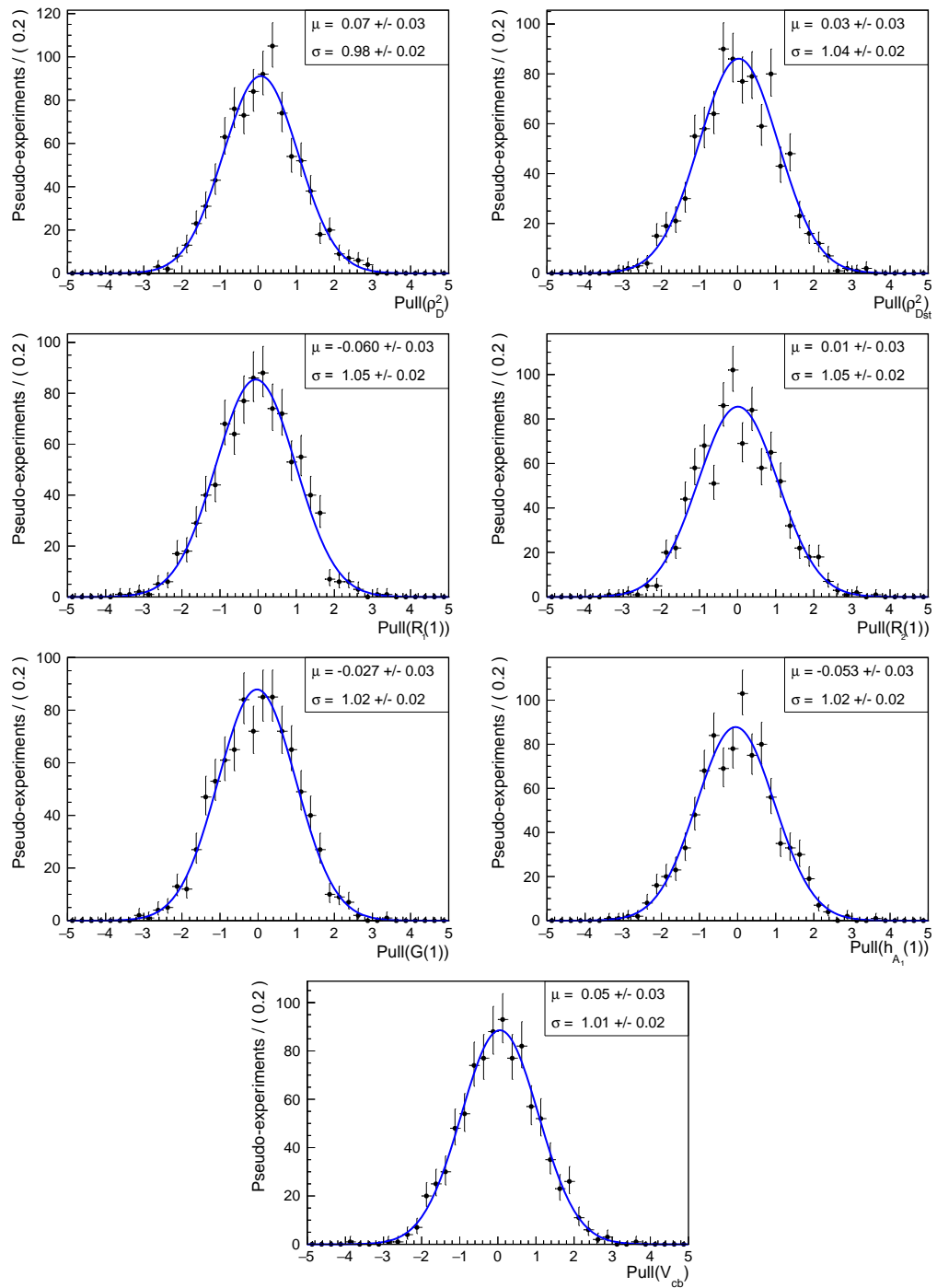


Figure F.21: Pull distributions of  $|V_{cb}|$  and the BGL form-factor parameters from 1000 toy samples obtained for the *a posteriori* fit in scenario 2. Summary of the pull distributions can be found in Fig. F.19.

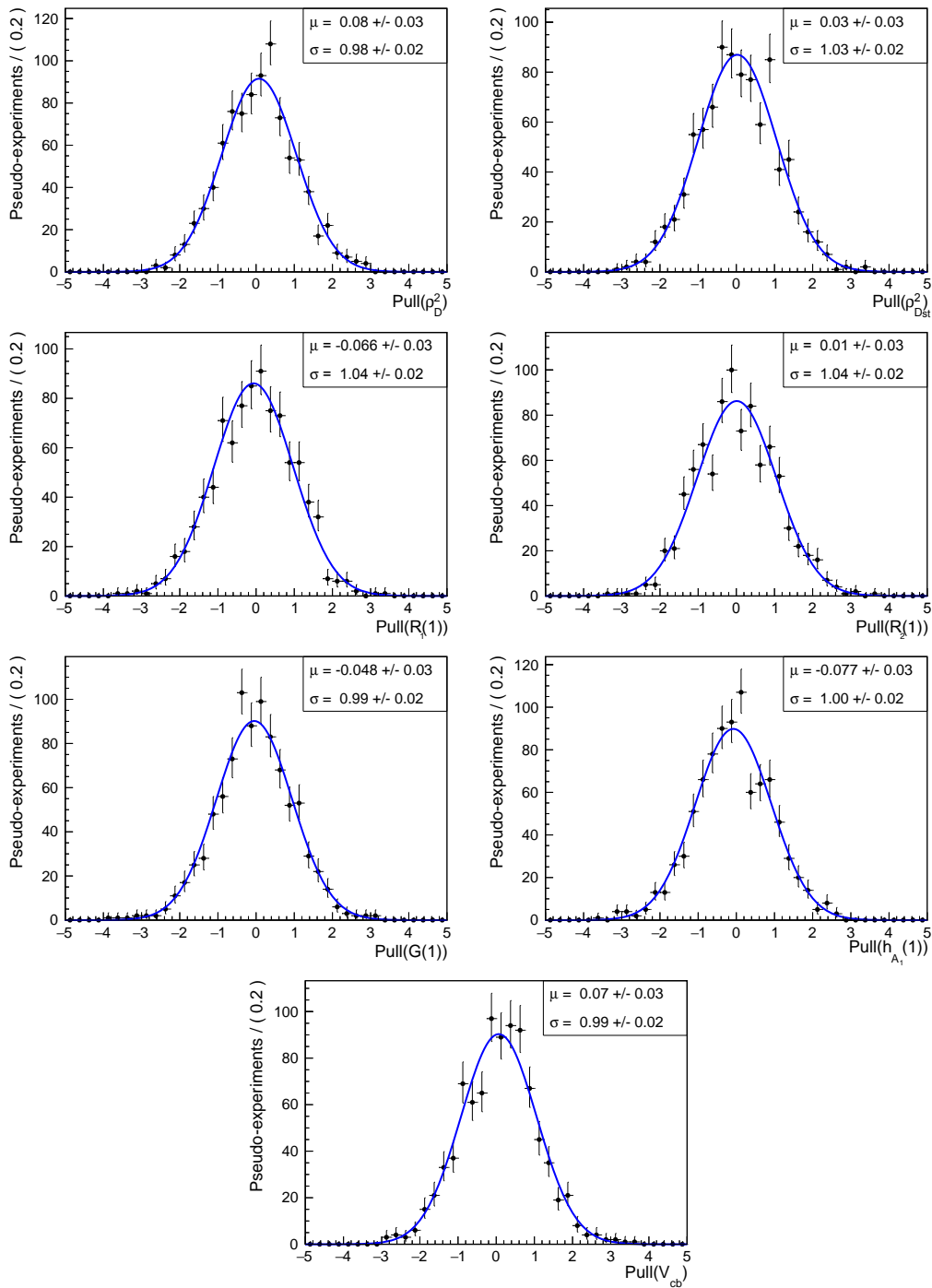


Figure F.22: Pull distributions of  $|V_{cb}|$  and the BGL form-factor parameters from 1000 toy samples obtained for the *a posteriori* fit in scenario 3. Summary of the pull distributions can be found in Fig. F.19.

# Bibliography

- [1] S. Weinberg, *A Model of Leptons*, Phys. Rev. Lett. **19** (1967) 1264.
- [2] S. L. Glashow, *Partial-Symmetries of Weak Interactions*, Nuclear Physics **22** (1961) 579.
- [3] A. Salam, *Weak and Electromagnetic Interactions*, Conf. Proc. C **680519** (1968) 367.
- [4] F. Englert and R. Brout, *Broken Symmetry and the Mass of Gauge Vector Mesons*, Phys. Rev. Lett. **13** (1964) 321.
- [5] P. W. Higgs, *Broken Symmetries and the Masses of Gauge Bosons*, Phys. Rev. Lett. **13** (1964) 508.
- [6] G. Guralnik, C. Hagen, and T. Kibble, *Global Conservation Laws and Massless Particles*, Phys. Rev. Lett. **13** (1964) 585.
- [7] M. E. Fisher, *Renormalization group theory: Its basis and formulation in statistical physics*, Rev. Mod. Phys. **70** (Apr, 1998) 653–681.
- [8] G. Aad *et al.*, ATLAS Collaboration, *Observation of a new particle in the search for the Standard Model Higgs boson with the ATLAS detector at the LHC*, Physics Letters B **716** (Sept., 2012) 1–29.
- [9] H. Greaves and T. Thomas, *On the CPT theorem*, Studies in History and Philosophy of Science Part B: Studies in History and Philosophy of Modern Physics **45** (Feb., 2014) 46–65.
- [10] M. Gell-Mann and M. Lévy, *The Axial Vector Current in Beta Decay*, Il Nuovo Cimento **16** (1960) 705.
- [11] N. Cabibbo, *Unitary Symmetry and Leptonic Decays*, Phys. Rev. Lett. **10** (1963) 531.
- [12] S. L. Glashow, J. Iliopoulos, and L. Maiani, *Weak Interactions with Lepton-Hadron Symmetry*, Phys. Rev. D **2** (1970) 1285.
- [13] M. Kobayashi and T. Maskawa, *CP-Violation in the Renormalizable Theory of Weak Interaction*, Prog. Theor. Phys. **49** (1973) 652.
- [14] R. L. Workman *et al.*, Particle Data Group, *Review of Particle Physics*, PTEP **2022** (2022) 083C01.
- [15] L. Wolfenstein, *Parametrization of the Kobayashi-Maskawa Matrix*, Phys. Rev. Lett. **51** (1983) 1945.

- [16] J. Charles *et al.*, CKMfitter Group, *Unitarity Triangle Plot*, Eur. Phys. J. C **41** (2005) . (Updated plots available at <http://ckmfitter.in2p3.fr>).
- [17] M. Bona *et al.*, UTfit Collaboration, *The UTfit collaboration report on the status of the unitarity triangle beyond the Standard Model I. Model-independent analysis and minimal flavour violation*, Journal of High Energy Physics **2006** (Mar., 2006) 080–080. (Updated plots available at <http://www.utfit.org/UTfit>).
- [18] I. Bediaga *et al.*, LHCb Collaboration, *Physics case for an LHCb Upgrade II - Opportunities in flavour physics, and beyond, in the HL-LHC era*, arXiv:1808.08865 [hep-ex].
- [19] H. Aihara *et al.*, Belle II Collaboration, *The Belle II Detector Upgrades Framework Conceptual Design Report*, arXiv:2406.19421 [hep-ex].
- [20] M. Benedikt *et al.*, *Future Circular Hadron Collider FCC-hh: Overview and Status*, 2022. arXiv:2203.07804 [physics.acc-ph].
- [21] A. de Giorgi *et al.*, *The minimal massive Majoron Seesaw Model*, Journal of High Energy Physics **2024** (Mar., 2024) .
- [22] J. Charles *et al.*, *New physics in B meson mixing: Future sensitivity and limitations*, Physical Review D **102** (Sept., 2020) .
- [23] K. De Bruyn *et al.*, *New physics in  $B_q^0-\bar{B}_q^0$  mixing: present challenges, prospects, and implications for  $B_q^0 \rightarrow \mu^+\mu^-$* , J. Phys. G **50** (2023) no. 4, 045003, arXiv:2208.14910 [hep-ph].
- [24] A. Lenz and S. Monteil, *High precision in CKM unitarity tests in b and c decays*, 2022. arXiv:2207.11055 [hep-ex].
- [25] A. J. Buras and E. Venturini, *Searching for New Physics in Rare K and B Decays without  $|V_{cb}|$  and  $|V_{ub}|$  Uncertainties*, 2022. arXiv:2109.11032 [hep-ph].
- [26] Y. Grossman and P. Tanedo, *Just a Taste: Lectures on Flavor Physics*, in *Anticipating the Next Discoveries in Particle Physics*, p. 109–295. WORLD SCIENTIFIC, May, 2018.
- [27] M. Prim, *Latest results on semileptonic and electroweak penguin decays at Belle II*, 56<sup>th</sup> Rencontres de Moriond, 2022. (Talk available at <https://moriond.in2p3.fr/QCD/2022/TuesdayMorning/Welsch.pdf>).
- [28] A. Sirlin, *Large  $m_W$ ,  $m_Z$  behaviour of the  $\mathcal{O}(\alpha)$  corrections to semileptonic processes mediated by W*, Nuclear Physics B **196** (1982) no. 4, 83–92.
- [29] D. Bigi, M. Bordone, *et al.*, *QED effects in inclusive semi-leptonic B decays*, 2023. arXiv:2309.02849 [hep-ph].
- [30] F. Bernlochner, *Determination of the CKM matrix element  $|V_{cb}|$ , the  $B \rightarrow X(s) \gamma$  decay rate, and the b-quark mass*. PhD thesis, Humboldt U., Berlin, 2011. (Ph.D. thesis available at <https://inspirehep.net/literature/1095329>).
- [31] Y. Aoki *et al.*, JLQCD Collaboration,  *$B \rightarrow D^* \ell \nu_\ell$  semileptonic form factors from lattice QCD with Möbius domain-wall quarks*, Phys. Rev. D **109** (2024) no. 7, 074503, 2306.05657.

- [32] J. Harrison and C. T. H. Davies, HPQCD Collaboration, *B* → *D*\* and *B*<sub>s</sub> → *D*\*<sub>s</sub> vector, axial-vector and tensor form factors for the full *q*<sup>2</sup> range from lattice QCD, Phys. Rev. D **109** (2024) no. 9, 094515, [arXiv:2304.03137](https://arxiv.org/abs/2304.03137) [hep-lat].
- [33] A. Bazavov *et al.*, *Semileptonic form factors for B* → *D*\**lν* at nonzero recoil from 2 + 1-flavor lattice QCD: Fermilab Lattice and MILC Collaborations, The European Physical Journal C **82** (Dec., 2022) .
- [34] M. Bordone, M. Jung, and D. van Dyk, *Theory determination of  $\bar{B} \rightarrow D^{(*)} \ell^{-} \bar{\nu}$  form factors at  $\mathcal{O}(1/m_c^2)$* , The European Physical Journal C **80** (Jan., 2020) .
- [35] C. Bourrely, L. Lellouch, and I. Caprini, *Model-independent description of B* → *πlν* decays and a determination of |*V*<sub>ub</sub>|, Phys. Rev. D **79** (Jan, 2009) 013008.
- [36] M. Wirbel, B. Stech, and M. Bauer, *Exclusive semileptonic decays of heavy mesons*, Zeitschrift für Physik C Particles and Fields **29** (Dec, 1985) 637–642.
- [37] C. G. Boyd, B. Grinstein, and R. F. Lebed, *Constraints on Form Factors for Exclusive Semileptonic Heavy to Light Meson Decays*, Phys. Rev. Lett. **74** (Jun, 1995) 4603–4606.
- [38] F. U. Bernlochner, Z. Ligeti, and D. J. Robinson, *N = 5, 6, 7, 8: Nested hypothesis tests and truncation dependence of |V<sub>cb</sub>|*, Physical Review D **100** (July, 2019) .
- [39] P. Gambino, M. Jung, and S. Schacht, *The V<sub>cb</sub> puzzle: An update*, Physics Letters B **795** (Aug., 2019) 386–390.
- [40] I. Caprini, L. Lellouch, and M. Neubert, *Dispersive bounds on the shape of B* → *D*\**lν<sub>ℓ</sub>* form factors, Nuclear Physics B **530** (1998) no. 1, 153–181.
- [41] D. Bigi, P. Gambino, and S. Schacht, *A fresh look at the determination of |V<sub>cb</sub>| from B* → *D*\**lν<sub>ℓ</sub>*, Physics Letters B **769** (2017) 441–445.
- [42] B. Grinstein and A. Kobach, *Model-independent extraction of |V<sub>cb</sub>| from  $\bar{B} \rightarrow D^* \ell \bar{\nu}_\ell$* , Physics Letters B **771** (2017) 359–364.
- [43] D. Bigi and P. Gambino, *Revisiting B* → *Dlν*, Phys. Rev. D **94** (Nov, 2016) 094008.
- [44] M. Fedele *et al.*, *Discriminating B* → *D*\**lν<sub>ℓ</sub>* form factors via polarization observables and asymmetries, Physical Review D **108** (Sept., 2023) .
- [45] R. Glattauer *et al.*, Belle Collaboration, *Measurement of the decay B* → *Dlν<sub>ℓ</sub>* in fully reconstructed events and determination of the Cabibbo-Kobayashi-Maskawa matrix element |*V*<sub>cb</sub>|, Physical Review D **93** (Feb., 2016) .
- [46] The Heavy Flavor Averaging Group. <https://hflav.web.cern.ch/>.
- [47] D. Buskulic *et al.*, ALEPH Collaboration, *Measurements of |V<sub>cb</sub>|, form factors and branching fractions in the decays B<sup>0</sup> → D\*<sup>+</sup>ℓ<sup>−</sup>ν<sub>ℓ</sub> and B<sup>0</sup> → D<sup>+</sup>ℓ<sup>−</sup>ν<sub>ℓ</sub>*, Physics Letters B **395** (1997) no. 3, 373–387.
- [48] J. Bartelt *et al.*, CLEO Collaboration, *Measurement of the B* → *Dlν* Branching Fractions and Form Factor, Physical Review Letters **82** (May, 1999) 3746–3750.

- [49] B. Aubert *et al.*, BABAR Collaboration, *Measurement of  $|V_{cb}|$  and the Form-Factor Slope in  $\bar{B} \rightarrow D\ell^-\bar{\nu}_\ell$  Decays in Events Tagged by a Fully Reconstructed B Meson*, Physical Review Letters **104** (Jan., 2010) .
- [50] Y. Amhis *et al.*, Heavy Flavor Averaging Group Collaboration, *Averages of b-hadron, c-hadron, and  $\tau$ -lepton properties as of 2021*, Phys. Rev. D **107** (Mar, 2023) 052008. (site: <https://hflav.web.cern.ch>).
- [51] F. Abudinen *et al.*, Belle II Collaboration, *Measurement of the semileptonic  $\bar{B}^0 \rightarrow D^{*+}\ell^-\nu_\ell$  branching fraction with fully reconstructed B meson decays and  $34.6\text{ fb}^{-1}$  of Belle II data*, arXiv:2008.10299 [hep-ex].
- [52] G. Abbiendi *et al.*, OPAL Collaboration, *Measurement of  $|V_{cb}|$  using  $B^0 \rightarrow D^*\ell\nu_\ell$  decays*, Physics Letters B **482** (June, 2000) 15–30.
- [53] P. Abreu *et al.*, DELPHI Collaboration, *Measurement of  $|V_{cb}|$  from the decay process  $\bar{B}^0 \rightarrow D^{*+}\ell^-\bar{\nu}_\ell$* , Physics Letters B **510** (June, 2001) 55–74.
- [54] J. Abdallah *et al.*, DELPHI Collaboration, *Measurement of  $|V_{cb}|$  using the semileptonic decay  $\bar{B}^0 \rightarrow D^{*+}\ell^-\bar{\nu}_\ell$* , The European Physical Journal C **33** (Mar., 2004) 213–232.
- [55] N. E. Adam *et al.*, CLEO Collaboration, *Determination of the  $\bar{B} \rightarrow D^*\ell\bar{\nu}_\ell$  Decay Width and  $|V_{cb}|$* , Physical Review D **67** (Feb., 2003) .
- [56] E. Waheed *et al.*, Belle Collaboration, *Measurement of the CKM matrix element  $|V_{cb}|$  from  $B^0 \rightarrow D^{*-}\ell^+\nu_\ell$  at Belle*, Physical Review D **100** (Sept., 2019) .
- [57] B. Aubert *et al.*, BABAR Collaboration, *Determination of the Form Factors for the Decay  $B^0 \rightarrow D^{*-}\ell^+\nu_\ell$  and of the CKM Matrix Element  $|V_{cb}|$* , Physical Review D **77** (Feb., 2008) .
- [58] B. Aubert *et al.*, BABAR Collaboration, *Measurement of the Decay  $B^- \rightarrow D^{*0}e^-\bar{\nu}_e$* , Physical Review Letters **100** (June, 2008) .
- [59] B. Aubert *et al.*, BABAR Collaboration, *Measurement of the Branching Fractions of Exclusive  $\bar{B} \rightarrow D^*(\pi)\bar{\nu}_\ell$  Decays in Events with a Fully Reconstructed B Meson*, Physical Review Letters **100** (Apr., 2008) .
- [60] F. Abudinén *et al.*, Belle II Collaboration, *Studies of the semileptonic  $\bar{B}^0 \rightarrow D^{*+}\ell^-\bar{\nu}_\ell$  and  $B^- \rightarrow D^0\ell^-\bar{\nu}_\ell$  decay processes with  $34.6\text{ fb}^{-1}$  of Belle II data*, arXiv:2008.07198 [hep-ex].
- [61] J. A. Bailey *et al.*, Fermilab Lattice and MILC Collaborations, *The  $B \rightarrow D\ell\nu$  form factors at nonzero recoil and  $|V_{cb}|$  from 2+1-flavor lattice QCD*, Physical Review D **92** (Aug., 2015) .
- [62] B. Aubert *et al.*, BABAR Collaboration, *Measurements of the semileptonic decays  $\bar{B} \rightarrow D\ell\bar{\nu}_\ell$  and  $\bar{B} \rightarrow D^*\ell\bar{\nu}_\ell$  using a global fit to  $DX\ell\nu_\ell$  final states*, Physical Review D **79** (Jan., 2009) .
- [63] Y. Aoki *et al.*, FLAG Review 2021, The European Physical Journal C **82** (Oct., 2022) .

- [64] J. A. Bailey *et al.*, Fermilab Lattice and MILC Collaborations, *Update of  $|V_{cb}|$  from the  $\bar{B} \rightarrow D^* \ell \bar{\nu}$  form factor at zero recoil with three-flavor lattice QCD*, Phys. Rev. D **89** (Jun, 2014) 114504.
- [65] J. Lees *et al.*, BABAR Collaboration, *Extraction of form Factors from a Four-Dimensional Angular Analysis of  $\bar{B} \rightarrow D^* \ell^- \bar{\nu}_\ell$* , Physical Review Letters **123** (Aug., 2019) .
- [66] B. Aubert *et al.*, BABAR Collaboration, *Measurement of Branching Fractions and Charge Asymmetries for Exclusive B Decays to Charmonium*, Phys. Rev. Lett. **94** (Apr, 2005) 141801.
- [67] S. Choudhury *et al.*, Belle Collaboration, *Measurement of the  $B^+/B^0$  production ratio in  $e^+e^-$  collisions at the  $\Upsilon(4S)$  resonance using  $B \rightarrow J/\psi(\ell\ell)K$  decays at Belle*, Phys. Rev. D **107** (Feb, 2023) L031102.
- [68] A. I. Milstein and S. G. Salnikov, *Coulomb effects in the decays  $\Upsilon(4S) \rightarrow B\bar{B}$* , Phys. Rev. D **104** (Jul, 2021) 014007.
- [69] S. Dubynskiy, A. Le Yaouanc, L. Oliver, J.-C. Raynal, and M. B. Voloshin, *Isospin breaking in the yield of heavy meson pairs in  $e^+e^-$  annihilation near threshold*, Phys. Rev. D **75** (Jun, 2007) 113001.
- [70] B. Aubert *et al.*, BABAR Collaboration, *Measurement of the Branching Fraction of  $\Upsilon(4S) \rightarrow B^0\bar{B}^0$* , Phys. Rev. Lett. **95** (Jul, 2005) 042001.
- [71] S. Banerjee *et al.*, *Averages of b-hadron, c-hadron, and  $\tau$ -lepton properties as of 2023*, 2024. arXiv:2411.18639 [hep-ex].
- [72] J. P. Alexander *et al.*, CLEO Collaboration, *Measurement of the Relative Branching Fraction of  $\Upsilon(4S)$  to Charged and Neutral B-Meson Pairs*, Phys. Rev. Lett. **86** (Mar, 2001) 2737–2741.
- [73] S. B. Athar *et al.*, CLEO Collaboration, *Measurement of the ratio of branching fractions of the  $\Upsilon(4S)$  to charged and neutral B mesons*, Phys. Rev. D **66** (Sep, 2002) 052003.
- [74] N. C. Hastings *et al.*, Belle Collaboration, *Studies of  $B^0 - \bar{B}^0$  mixing properties with inclusive dilepton events*, Phys. Rev. D **67** (Mar, 2003) 052004.
- [75] B. Barish *et al.*, CLEO Collaboration, *Measurement of the B Semileptonic Branching Fraction with Lepton Tags*, Phys. Rev. Lett. **76** (Mar, 1996) 1570–1574.
- [76] B. Aubert *et al.*, BABAR Collaboration, *Study of hadronic transitions between  $\Upsilon$  states and observation of  $\Upsilon(4S) \rightarrow \eta\Upsilon(1S)$  decay*, Phys. Rev. D **78** (Dec, 2008) 112002.
- [77] E. Guido *et al.*, Belle Collaboration, *Study of  $\eta$  and dipion transitions in  $\Upsilon(4S)$  decays to lower bottomonia*, Phys. Rev. D **96** (Sep, 2017) 052005.
- [78] U. Tamponi *et al.*, Belle Collaboration, *First Observation of the Hadronic Transition  $\Upsilon(4S) \rightarrow \eta h_b(1P)$  and New Measurement of the  $h_b(1P)$  and  $\eta_b(1S)$  Parameters*, Phys. Rev. Lett. **115** (Sep, 2015) 142001.

- [79] J. M. Flynn, A. Jüttner, and J. T. Tsang, *Bayesian inference for form-factor fits regulated by unitarity and analyticity*, 2024. [arXiv:2303.11285](#) [hep-ph].
- [80] M. Di Carlo *et al.*, *Unitarity bounds for semileptonic decays in lattice QCD*, Physical Review D **104** (Sept., 2021) .
- [81] S. Schmitt, *Data Unfolding Methods in High Energy Physics*, EPJ Web of Conferences **137** (2017) 11008.
- [82] T. Keck *et al.*, *The Full Event Interpretation.*, Comput Softw Big Sci **3** (2019) .
- [83] B. Aubert *et al.*, BABAR Collaboration, *Measurements of the  $B \rightarrow D^*$  form factors using the decay  $\bar{B}^0 \rightarrow D^{*+} e^- \bar{\nu}_e$* , Physical Review D **74** (Nov., 2006) .
- [84] A. Abdesselam *et al.*, Belle Collaboration, *Precise determination of the CKM matrix element  $|V_{cb}|$  with  $\bar{B}^0 \rightarrow D^{*+} \ell^- \bar{\nu}_\ell$  decays with hadronic tagging at Belle*, [arXiv:1702.01521](#) [hep-ex].
- [85] M. Prim *et al.*, Belle Collaboration, *Measurement of differential distributions of  $B \rightarrow D^* \ell \nu_\ell$  and implications on  $|V_{cb}|$* , Phys. Rev. D **108** (2023) no. 1, 012002, [arXiv:2301.07529](#) [hep-ex].
- [86] R. Gupta, *Introduction to Lattice QCD*, 1998. [arXiv:hep-lat/9807028](#) [hep-lat].
- [87] A. Vaquero, *Lattice determinations of  $B_{(s)} \rightarrow D_{(s)}^* \ell \nu_\ell$  form factors*, Talk at 12<sup>th</sup> International Workshop on the CKM Unitarity Triangle . (Talk available at <https://indico.cern.ch/event/1184945/contributions/5435458/attachments/2716793/4718929/CKM-Talk.pdf>).
- [88] M. Bordone and A. Jüttner, *New strategies for probing  $B \rightarrow D^* \ell \bar{\nu}_\ell$  lattice and experimental data*, 2024. [arXiv:2406.10074](#) [hep-ph].
- [89] C. Bobeth *et al.*, *Lepton-flavour non-universality of  $\bar{B} \rightarrow D^* \ell \bar{\nu}_\ell$  angular distributions in and beyond the Standard Model*, The European Physical Journal C **81** (Nov, 2021) 984.
- [90] F. U. Bernlochner *et al.*, *Constrained second-order power corrections in HQET:  $R(D^{(*)})$ ,  $|V_{cb}|$ , and new physics*, Phys. Rev. D **106** (Nov, 2022) 096015.
- [91] I. Adachi *et al.*, Belle II Collaboration, *Determination of  $|V_{cb}|$  using  $\bar{B}^0 \rightarrow D^{*+} \ell^- \bar{\nu}_\ell$  decays with Belle II*, Phys. Rev. D **108** (Nov, 2023) 092013.
- [92] Y. Ohnishi *et al.*, *Accelerator Design at SuperKEKB*, Prog. Theo. Exp. Phys. (2013) 03A011.
- [93] P. Oddone, *Detector Considerations*, in D. H. Stork, proceedings of Workshop on Conceptual Design of a Test Linear Collider: Possibilities for a BB Factory (1987) 423.
- [94] P. Raimondi *et al.*, *Beam-Beam Issues for Colliding Schemes with Large Piwinski Angle and Crabbed Waist*, [arXiv:physics/0702033](#).
- [95] T. Abe *et al.*, Belle II Collaboration, *Belle II Technical Design Report*, [arXiv:1011.0352](#) [physics.ins-det].

- [96] F. Forti, Belle II Collaboration, *Snowmass Whitepaper: The Belle II Detector Upgrade Program*, arXiv:2203.11349 [hep-ex].
- [97] Belle II Collaboration, *Belle II Luminosity*, 2024.  
<https://www.belle2.org/research/luminosity/>.
- [98] C. Marinas, DEPFET, *The Belle II Pixel Detector: High precision with Low Material*, Nucl. Instrum. Meth. A **731** (2013) 31.
- [99] K. Adamczyk *et al.*, Belle II Collaboration, *The Belle II Silicon Vertex Detector Assembly and Mechanics*, Nucl. Instrum. Meth. A **845** (2017) 38.
- [100] H. Hirano *et al.*, *A High-Resolution Cylindrical Drift Chamber for the KEK B-Factory*, Nucl. Instrum. Meth. A **455** (2000) 294.
- [101] V. Aulchenko *et al.*, *Electromagnetic Calorimeter for Belle II*, J. Phys. Conf. Ser. **587** (2015) 012045.
- [102] K. Inami *et al.*, *TOP Counter for Particle Identification at the Belle II Experiment*, Nucl. Instrum. Meth. A **766** (2014) 5.
- [103] S. Iwata *et al.*, *Particle Identification Performance of the Prototype Aerogel RICH Counter for the Belle II Experiment*, Prog. Theo. Exp. Phys. **2016** (2016) 033.
- [104] A. Abashian *et al.*, Belle Collaboration, *The  $K_L/\mu$  Detector Subsystem for the BELLE Experiment at the KEK B factory*, Nucl. Instrum. Meth. A **449** (2000) 112.
- [105] V. Bertacchi *et al.*, *Track Finding at Belle II*, Computer Physics Communications **259** (2021) 107610.
- [106] T. Alexopoulos *et al.*, *Implementation of the Legendre Transform for Track Segment Reconstruction in Drift Tube Chambers*, Nucl. Instrum. Meth. A **592** (2008) 456.
- [107] R. Mankel, *Pattern Recognition and Event Reconstruction in Particle Physics Experiments*, Reports on Progress in Physics **67** (2004) 553.
- [108] H. Bethe, *Theory of the Passage of Fast Corpuscular Rays Through Matter*, Annalen Phys. **5** (1930) 325.
- [109] F. Bloch, *Stopping Power of Atoms with Several Electrons*, Z. Phys. **81** (1933) 363.
- [110] M. Milesi, *Lepton Identification in Belle II Using Observables from the Electromagnetic Calorimeter and Precision Trackers*, Talk at CHEP 2019 . (Talk at CHEP 2019: [https://indico.cern.ch/event/773049/contributions/3476156/attachments/1932835/3217425/mmilesi\\_mva\\_CHEP\\_07\\_11\\_19.pdf](https://indico.cern.ch/event/773049/contributions/3476156/attachments/1932835/3217425/mmilesi_mva_CHEP_07_11_19.pdf)).
- [111] M. Starič *et al.*, *Likelihood Analysis of Patterns in a Time-of-Propagation (TOP) Counter*, Nucl. Instrum. Meth. A **595** (2008) 252.
- [112] M. Starič, *Pattern recognition for the time-of-propagation counter*, Nucl. Instrum. Meth. A **639** (2011) 252.
- [113] J. Neyman and E. S. Pearson, IX. *On the Problem of the Most Efficient Tests of Statistical Hypotheses*, Phil. Trans. R. Soc. Lond. A. **231** (1933) 289.

- [114] A. J. Bevan *et al.*, *The Physics of the B Factories*, The European Physical Journal C **74** (Nov., 2014) .
- [115] I. Adachi *et al.*, Belle II Collaboration, *Measurement of Branching Fractions and direct CP Asymmetries for  $B \rightarrow K\pi$  and  $B \rightarrow \pi\pi$  Decays at Belle II*, Phys. Rev. D **109** (2024) 012001.
- [116] F. Abudinén *et al.*, Belle II Collaboration, *Measurement of Branching Fraction and Longitudinal Polarization in  $B^0 \rightarrow \rho^+\rho^-$  Decays at Belle II*, arXiv:2208.03554 [hep-ex].
- [117] I. Adachi *et al.*, Belle II Collaboration, *Measurement of the integrated luminosity of data samples collected during 2019-2022 by the Belle II experiment*, arXiv:2407.00965.
- [118] B. Ward, S. Jadach, and Z. Was, *Precision Calculation for  $e^+e^- \rightarrow 2f$ : the KK MC Project*, Nuclear Physics B - Proceedings Supplements **116** (2003) 73.
- [119] T. Sjöstrand, S. Mrenna, and P. Skands, *PYTHIA 6.4 Physics and Manual*, Journal of High Energy Physics **2006** (2006) 026.
- [120] D. J. Lange, *The EvtGen Particle Decay Simulation Package*, Nucl. Instrum. Meth. A **462** (2001) 152.
- [121] P. Golonka and Z. Was, *PHOTOS Monte Carlo: a Precision Tool for QED Corrections in Z and W Decays*, Eur. Phys. J. C **45** (2006) 97.
- [122] D. Ferlewicz, P. Urquijo, and E. Waheed, *Revisiting fits to  $B^0 \rightarrow D^{*-}\ell^+\nu_\ell$  to measure  $|V_{cb}|$  with novel methods and preliminary LQCD data at nonzero recoil*, Physical Review D **103** (Apr., 2021) .
- [123] G. Bonvicini *et al.*, CLEO Collaboration, *Dalitz plot analysis of the  $D^+ \rightarrow K^-\pi^+\pi^+$  decay*, Physical Review D **78** (Sept., 2008) .
- [124] Belle II Collaboration, *Systematic Corrections Framework*, <https://syscorr fw.readthedocs.io/en/latest/>.
- [125] W. D. Hulsbergen, *Decay chain fitting with a Kalman filter*, Nuclear Instruments and Methods in Physics Research Section A: Accelerators, Spectrometers, Detectors and Associated Equipment **552** (Nov., 2005) 566–575.
- [126] E. Kou *et al.*, *The Belle II Physics Book*, Progress of Theoretical and Experimental Physics **2019** (Dec., 2019) .
- [127] F. Abudinén *et al.*, Belle II Collaboration, *Determination of  $|V_{cb}|$  from  $B \rightarrow D\ell\nu$  decays using 2019-2021 Belle II data*, arXiv:2210.13143 [hep-ex]. (Update to the full Run I sample ongoing: [https://indico.cern.ch/event/1345421/contributions/6040065/attachments/2933288/5157297/talk\\_240924.pdf](https://indico.cern.ch/event/1345421/contributions/6040065/attachments/2933288/5157297/talk_240924.pdf)).
- [128] J. P. Alexander *et al.*, CLEO Collaboration, *First observation of  $\bar{B} \rightarrow D^{(*)}\rho'^-$ ,  $\rho'^- \rightarrow \omega\pi^-$* , Phys. Rev. D **64** (Sep, 2001) 092001.
- [129] H. Albrecht *et al.*, ARGUS, *Exclusive Hadronic Decays of B Mesons*, Z. Phys. C **48** (1990) 543–552.

- [130] D. Liventsev *et al.*, Belle Collaboration, *Study of  $B \rightarrow D^{**}l\nu$  with full reconstruction tagging*, Phys. Rev. D **77** (May, 2008) 091503.
- [131] B. Aubert *et al.*, BABAR Collaboration, *Measurement of Semileptonic  $B$  Decays into Orbitally Excited Charmed Mesons*, Phys. Rev. Lett. **103** (Jul, 2009) 051803.
- [132] A. Le Yaouanc, J.-P. Leroy, and P. Roudeau, *Model for nonleptonic and semileptonic decays by  $\bar{B}^0 \rightarrow D^{**}$  transitions with  $\text{BR}(j = 1/2) \ll \text{BR}(j = 3/2)$  using the Leibovich-Ligeti-Stewart-Wise schem*, Phys. Rev. D **105** (2022) no. 1, 013004, arXiv:2102.11608 [hep-ph].
- [133] R. Aaij *et al.*, LHCb Collaboration, *Amplitude analysis of  $B^- \rightarrow D^+ \pi^- \pi^-$  decays*, Phys. Rev. D **94** (Oct, 2016) 072001.
- [134] M. Albaladejo *et al.*, *Two-pole structure of the  $D_0^*(2400)$* , Physics Letters B **767** (Apr., 2017) 465–469.
- [135] M.-L. Du *et al.*, *Towards a new paradigm for heavy-light meson spectroscopy*, Physical Review D **98** (Nov., 2018) .
- [136] F.-K. Guo *et al.*, *Hadronic molecules*, Reviews of Modern Physics **90** (Feb., 2018) .
- [137] F. Meier *et al.*, Belle Collaboration, *First observation of  $B \rightarrow \bar{D}_1(\rightarrow \bar{D}\pi^+\pi^-)\ell^+\nu_\ell$  and measurement of the  $B \rightarrow \bar{D}^{(*)}\pi\ell^+\nu_\ell$  and  $B \rightarrow \bar{D}^{(*)}\pi^+\pi^-\ell^+\nu_\ell$  branching fractions with hadronic tagging at Belle*, Phys. Rev. D **107** (May, 2023) 092003.
- [138] J. P. Lees *et al.*, BABAR Collaboration, *Observation of  $\bar{B} \rightarrow D^{(*)}\pi^+\pi^-\ell^-\bar{\nu}$  Decays in  $e^+e^-$  Collisions at the  $\Upsilon(4S)$  Resonance*, Phys. Rev. Lett. **116** (Jan, 2016) 041801.
- [139] F. U. Bernlochner, Z. Ligeti, and S. Turczyk, *A proposal to solve some puzzles in semileptonic  $B$  decays*, Physical Review D **85** (May, 2012) .
- [140] F. Herren *et al.*, *A model independent description of  $B \rightarrow D\pi\ell\nu$  decays*, 2023. arXiv:2311.00864 [hep-ph].
- [141] Y. Amhis *et al.*, *Averages of  $b$ -hadron,  $c$ -hadron, and  $\tau$ -lepton properties as of 2018: Heavy Flavor Averaging Group (HFLAV)*, The European Physical Journal C **81** (Mar., 2021) .
- [142] B. Aubert *et al.*, The BABAR Collaboration, *Measurement of the Branching Fractions of  $\bar{B} \rightarrow D^{**}\ell^-\bar{\nu}_\ell$  Decays in Events Tagged by a Fully Reconstructed  $B$  Meson*, Phys. Rev. Lett. **101** (Dec, 2008) 261802.
- [143] I. Adachi *et al.*, Belle II Collaboration, *First Measurement of  $R(X_{\tau/\ell})$  as an Inclusive Test of the  $b \rightarrow c\tau\nu$  Anomaly*, Phys. Rev. Lett. **132** (May, 2024) 211804.
- [144] F. U. Bernlochner, Z. Ligeti, and D. J. Robinson, *Model-independent analysis of semileptonic  $B$  decays to  $D^{**}$  for arbitrary new physics*, Phys. Rev. D **97** (Apr, 2018) 075011.
- [145] L. Cao *et al.*, Belle Collaboration, *Measurements of partial branching fractions of inclusive  $B \rightarrow X_u\ell^+\nu_\ell$  decays with hadronic tagging*, Phys. Rev. D **104** (Jul, 2021) 012008.

- [146] R. Aaij *et al.*, LHCb Collaboration, *Measurement of  $|V_{cb}|$  with  $B_s^0 \rightarrow D_s^{(*)-} \mu^+ \nu_\mu$  decays*, Phys. Rev. D **101** (Apr, 2020) 072004.
- [147] F. James and M. Roos, *MINUIT: a System for Function Minimization and Analysis of the Parameter Errors and Corrections*, Comput. Phys. Commun. **10** (1975) 343.
- [148] R. van Tonder *et al.*, Belle Collaboration, *Measurements of  $q^2$  moments of inclusive  $B \rightarrow X_c \ell^+ \nu_\ell$  decays with hadronic tagging*, Phys. Rev. D **104** (Dec, 2021) 112011.
- [149] G. Martinelli, S. Simula, and L. Vittorio, *Updates on the determination of  $|V_{cb}|$ ,  $R(D^*)$  and  $|V_{ub}|/|V_{cb}|$* , 2024. [arXiv:2310.03680](https://arxiv.org/abs/2310.03680) [hep-ph].